

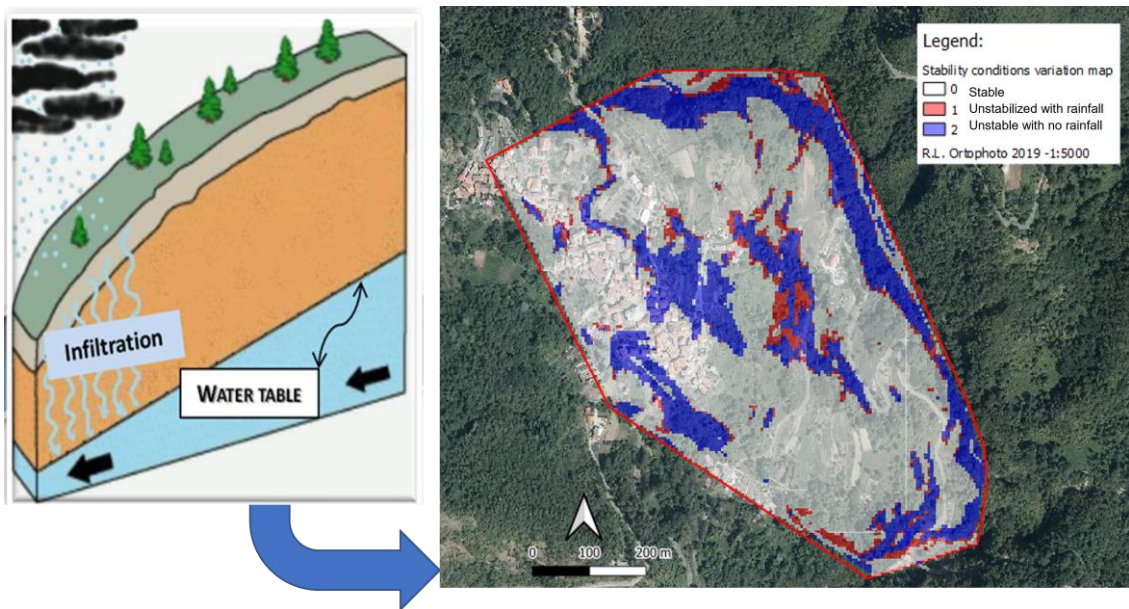
Ph.D. Program in Civil, Chemical and Environmental Engineering



Curriculum in Structural and Geotechnical Engineering, Mechanics and Materials

Department of Civil, Chemical and Environmental Engineering

Polytechnic School, University of Genoa, Italy.



Modelling for the automatic assessment of rainfall triggered landslide susceptibility due to changes in groundwater level and soil water content.

Candidate: Stefania Viaggio

MODELLING FOR THE AUTOMATIC ASSESSMENT OF
RAINFALL TRIGGERED LANDSLIDE SUSCEPTIBILITY
DUE TO CHANGES IN GROUNDWATER LEVEL AND
SOIL WATER CONTENT.

BY

STEFANIA VIAGGIO

*Dissertation discussed in partial fulfillment of
the requirements for the Degree of*

DOCTOR OF PHILOSOPHY

*Civil, Chemical and Environmental Engineering
curriculum in Structural and Geotechnical Engineering, Mechanics and Materials
Department of Civil, Chemical and Environmental Engineering, University of Genoa, Italy*



September, 2023

Advisers:

Prof. Rossella Bovolenta – Department of Civil, Chemical and Environmental Engineering, University of Genoa
Prof. Bianca Federici – Department of Civil, Chemical and Environmental Engineering, University of Genoa

External Reviewers:

Prof. Dario Peduto – Department of Civil Engineering, University of Salerno
Prof. Paolo Zatelli – Department of Civil, Environmental and Mechanical Engineering - University of Trento

Examination Committee:

Prof. Domenico Gallipoli – Department of Civil, Chemical and Environmental Engineering, University of Genoa
Prof. Paolo Bazzurro – Classe STS, Scuola Universitaria Superiore IUSS di Pavia
Prof. Federico Perotti – Department of Civil and Environmental Engineering, Politecnico di Milano

Ph.D. program in Civil, Chemical and Environmental Engineering

Curriculum in Structural and Geotechnical Engineering, Mechanics and Materials

Cycle XXXV

*To my lovely Eugenio,
to my wonderful Family.*

Acknowledgements

I would like to sincerely thank my supervisors, Professors Rossella Bovolenta and Bianca Federici, who have been a great example for me over the years and have provided me with guidance and support throughout my career.

I would like to thank Professors Anna Palla and Ilaria Gnecco for their helpful advice on the hydrological modelling.

I would like to thank all the partners involved in the AD-VITAM project for the interesting project they created and in which I was able to participate, enriching me with new knowledge and experience. My special thanks go to BRGM (Bureau de Recherches Géologiques et Minières), in the persons of Bernerdie Severine and Marçot Nathalie, who allowed me to spend my time abroad with them, giving me the opportunity to enrich my cultural background and meet interesting people.

ABSTRACT

Risk assessment of rain-triggered landslides over large areas is quite challenging due to the complexity of the phenomenon. In fact, rainfall represents one of the most important triggering factors for landslides performing an erosive action at ground level, and, through deep infiltration, increasing the soil saturation degree and feeding the groundwater table leading to fluctuations that can affect the slope stability. These phenomena represent an open challenge for technicians and authorities involved in landslide risk management and mitigation. For this reason, it is necessary to develop appropriate models for the landslides susceptibility assessment that are operationally compatible with good resolution and computational speed. Standard methods of 3D slope stability analysis are generally applied over limited areas or at low resolution. In this dissertation, two automatic procedures are proposed for estimating landslide susceptibility induced by changes in (i) groundwater levels and (ii) soil saturation conditions.

A physically based Integrated Hydrological and Geotechnical (IHG) model was implemented in GIS environment to effectively analyse areas of a few square kilometres, typically at a scale of 1:5.000. Referring to each volume element in which the whole mass under study is discretized, a simplified hydrological soil-water balance and geotechnical modelling are applied in order to assess the debris and earth slide susceptibility in occasion of measured or forecasted rainfalls. The IHG procedure allows 3D modelling of landslide areas, both morphologically and with regard to geotechnical/hydrological parameters thanks to the spatialisation of input data from in situ measurements, and renders easy-to-understand results. Critical issues inherent the discretization of quite large areas, referred to soil characterization, interpolation/extrapolation of in situ measurements, spatial resolution and computational effort, are here discussed.

Considering rain-triggered shallow landslides, the stability can be markedly influenced by the propagation of the saturation front inside the unsaturated zone. Soil shear strength varies in the vadose zone depending on the type of soil and the variations of soil moisture. Monitoring of the unsaturated zone can be done by measuring volumetric water content using low-cost instrumentation (i.e. capacitive sensors) that are easy to manage and provide data in near-real time. For a proper soil moisture assessment a laboratory soil-specific calibration of the sensors is recommended. Knowing the soil water content, the suction parameter can be estimated by a Water Retention Curve (WRC), and consequently the soil shear strength in unsaturated conditions is evaluated. The automatic procedure developed in GIS environment, named assessment of Soil Apparent Cohesion (SAC), here described, allows the estimate of the soil shear strength starting from soil moisture monitoring data (from sensor networks or satellite-derived map). SAC results can be integrated into existing models for landslide susceptibility assessment and also for the emergency management.

Some significant results concerning the automatic IHG and SAC procedures, implemented in Python, applied to landslides within the Alcotra AD-VITAM project are here presented.

INDEX

1.9	
1. INTRODUCTION.....	1
1.1. STATE OF ART ON LANDSLIDE MODELLING	4
2. CASE STUDIES	14
2.1 Mendatica site.....	18
2.1.1. Geological studies and geotechnical data.....	21
2.1.2. Monitoring activities	25
2.2. Vence site	31
2.2.1. Monitoring data	38
3. METHODOLOGY.....	42
3.1. INTEGRATED HYDROLOGICAL-GEOTECHNICAL (IHG) MODEL.....	42
3.1.1 Hydrological model.....	43
3.1.2 Calibration of the hydrological model.....	59
3.1.3 Slope stability analyses	64
3.2. ASSESSMENT OF SOIL APPARENT COHESION (SAC) INDUCED BY PARTIAL SATURATION CONDITIONS.....	68
3.2.1 Soil shear strength	69
3.2.2 Soil properties and soil moisture monitoring	74
3.2.3 Soil Apparent Cohesion (SAC) procedure in GIS.....	71
3.2.4. Shallow landslide stability analyses	73
3.3. DATA SPATIALISATION IN GIS ENVIRONMENT	74
3.3.1 Physical surfaces	74
3.3.2 IHG parameters	78
3.3.3 SAC spatial modelling.....	83
4. RESULTS AND DISCUSSION.....	85
4.1. IHG APPLICATION IN MENDATICA.....	85
4.1.1 Physical surfaces	88
4.1.2. Calibration of the hydrological model.....	98
4.1.3 Hydraulic parameter mapping	103
4.1.4 Groundwater table evolution	108
4.1.5 Slope stability analysis	109
4.1.6 In situ validation.....	117
4.2. IHG APPLICATION IN VENCE.....	125
4.2.1. Rainfall data	125

4.2.2. Physical surfaces	128
4.2.3 Calibration of the hydrological model.....	134
4.2.4 Hydraulic parameter mapping	139
4.2.5 Groundwater table evolution	143
4.2.6 Slope stability analysis	148
4.2.7 In situ validation.....	154
4.3. ASSESSMENT OF SOIL APPARENT COHESION (SAC) IN MENDATICA.....	157
4.3.1. Input data preparation.....	159
4.3.2. Results	161
4.3.3. Shallow landslide stability analyses	163
5. CONCLUSIONS	169
6. APPENDIX A	182
7. APPENDIX B	189

1. INTRODUCTION

Rainfall is one of the most important triggering factors of landslides: it can perform an erosive action at ground level, and, through deep infiltration, it can increase the soil saturation degree and feed the groundwater table leading to fluctuations that can affect the slope stability (Figure 1.1a). The importance of analysing rain-induced landslide phenomena was highlighted, once again, by the debris and earth slides occurred during the Alex storm (on 2nd – 3rd October 2020), in the Alpine territory at the border between Liguria, Piedmont and the French Department of Provence, Alpes and Côte d'Azur (PACA Region) (Figure 1.1b).

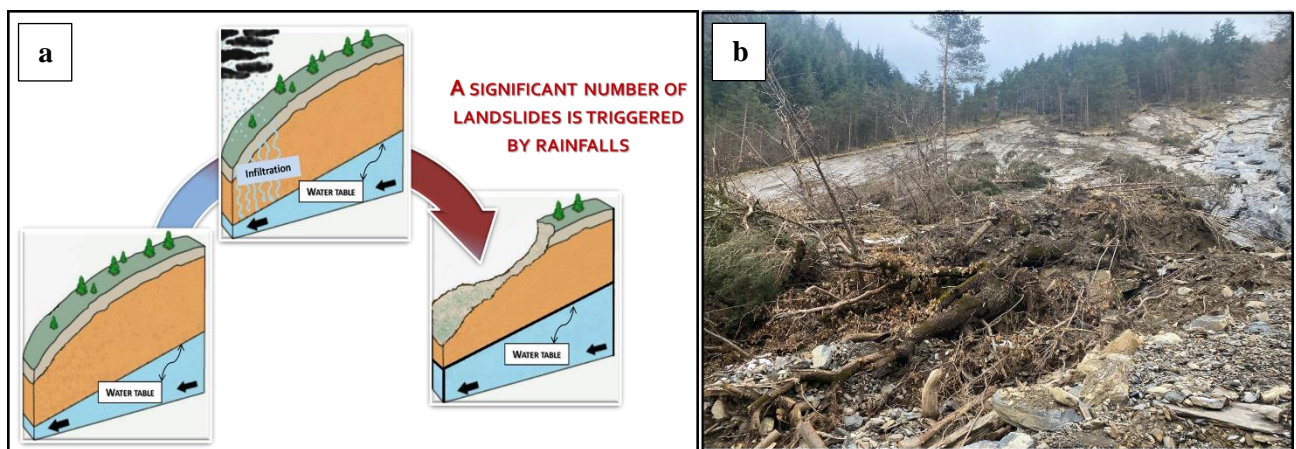


Figure 1.1. (a) rainfall effects on slope stability; (b) shallow landslide triggered by violent rainfall during the Alex storm in October 2020, in the Liguria Region (Montegrosso Pian Latte, IM).

My PhD work moves in the context of the AD-VITAM project "Analysis of the Vulnerability of Mediterranean Alpine Territories to Natural Risks", financed in the framework of the European Programme INTERREG ALCOTRA (*INTERREG V-A France-Italy ALCOTRA project 2014-2020, Axis: 2 Environment-safety, Specific objective: 2.2 Risk prevention*) for cross-border cooperation between France and Italy. This project is devoted to the ALCOTRA territories (Figure 1.2), specifically the Alpine regions located on the border between France and Italy. These territories are extremely vulnerable in relation to hydrogeological risks. These criticalities are expected to worsen in relation to climate change scenarios and increased anthropic pressure for tourism or settlement purposes. The main goal of AD-VITAM project was the improvement of the resilience of ALCOTRA territories with respect to natural risk, with particular reference to landslides triggered by rainfall, through the development of innovative operational systems. This purpose can be achieved by the design and development of physical-based models, that, fed by sensor networks, are able to provide reliable forecasting and warning systems useful in the landslide risk mitigation and management.

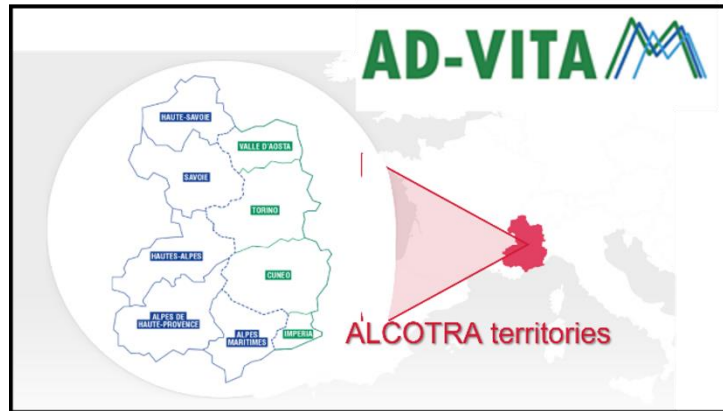


Figure 1.2. ALCOTRA territories involved in the AD-VITAM project

In this context, Geotechnical and Geomatic researchers of the University of Genoa developed the LAMP (*Landslide Monitoring and Predicting*) system. This system is composed by an Integrated Hydrological-Geotechnical model (IHG), which, fed by a sensor network, provides landslide susceptibility maps. The IHG model is developed in GIS (Geographic Information System)¹ environment and it is designed to describe in near real time the landslide susceptibility (based on LEM, Limit Equilibrium Method) over areas of a few square kilometres, typically at scale 1:5000. IHG model is fed by rainfall data observed by rain gauges or weather radar. The LAMP network consists of low-cost, self-sufficient soil water content sensors to monitor hydrological (and consequently geotechnical) soil conditions.

During my PhD I was in charge the improvement and automation of the IHG procedure for the assessment of rainfall triggered landslide susceptibility due to groundwater variations, and the implementation of another procedure for shallow landslide phenomena due to soil water content variations.

¹ The term GIS (Geographic Information System) defines a computerized information system capable of collecting, sharing, processing and displaying spatially distributed geographical information. The instrument on which a GIS software operates is numerical cartography, an evolution of traditional paper cartography, made up of sets of spatially georeferenced information and data.

There are two formats in which information and digitized data can be returned:

- *Vector format*: geometric data are stored through coordinates of significant points of the object; vector data describe the territory as a set of points, lines or polygons defined through their contours with a higher resolution on a global level; a vector map is usually associated with a database which allows each geometric entity to be linked to specific information;

- *Raster format*: data stored by creating a regular grid in which each cell (pixel) is assigned an alphanumeric value and therefore an attribute (i.e., Digital Terrain Model where the elevation value is associated with each cell of the map).

With reference to the landslide susceptibility due to fluctuations in groundwater, I worked on the improvement of the IHG model by defining the most suitable techniques for the input data spatialisation and on the automatisation of the procedure by developing a QGIS plugin, based on a Python script, that, starting from the input data allows to perform the landslide susceptibility analyses.

In particular, I focussed my attention on the input data and the 3D modelling of the parameters that allow the phenomenon to be analysed, and on the criticalities inherent in the discretization of rather large areas with good resolution and computational speed. In fact, the recently implemented improvements allow both an optimal geometry reconstruction of the model and the spatialisation of hydrological-geotechnical parameters by interpolation/extrapolation of local measurements.

The study of landslide susceptibility due to change in soil water content represents the most innovative part of my research. In fact, I proposed an innovative automatic procedure, named *SAC* (assessment of Soil Apparent Cohesion) for shallow stability analyses in partial saturation conditions. This procedure performs the estimate of (i) the soil Water Retention Curve, based on the empirical method proposed by Balzano et al. (2021), and, then, starting from the soil water content measurements provided by the LAMP network, (ii) the suction values and (iii) the apparent cohesion, based on the strength criterion proposed by Fredlund (1978) and modified by Vanapalli (1996). Shallow landslide susceptibility assessment is then based on the LEM method, where the strength contribution provided by the soil under partial saturation conditions is considered in the definition of the Factor of Safety (FS) (in the determination of which the weight of the soil at a given moisture content is also taken into account). The innovative aspect of the SAC procedure lies not only in being an operational model, allowing processing at a punctual scale, but also in the fact that it allows spatial output mapping, which is useful for characterising an entire and extensive study area.

These automatic procedures make possible to perform geotechnical analyses in GIS, in order to: (i) assess landslide susceptibility due to change in groundwater or in soil water content in near real time over areas of a few square kilometres, typically at the scale 1:5000, in short time; (ii) provide an useful tool for landslide risk mitigation and management.

The development of models for 3D stability analysis over areas of a few square kilometres, typically at the scale 1:5000, is an open challenge. This *Chapter 1* presents a general overview of some 3D LEM models proposed in the literature up to the early 2000s and then a critical description of them is attempted. It should be emphasized that the use of GIS has made a significant contribution in the development of 3D models for landslide susceptibility analysis, enabling proper data management and spatialization, working at different scales of detail in an operational manner.

In *Chapter 2* the investigated sites are presented. The physical-based IHG model, developed in a GIS environment, which allows for 3D stability analysis, will be described in *Chapter 3*. After a description the hydrological and geotechnical modelling that led to the IHG model (*Section 3.1*), the results will be

presented. *Section 3.2* will be devoted to the innovative procedure for analysing soil behaviour under partially saturated conditions. The interpolation/extrapolation techniques underlying the GIS procedures will then be described in *Section 3.3*, illustrating them on the basis of practical examples from the modelling carried out.

Subsequently, in *Chapter 4* the modelling related to the case studies will be illustrated and critically analysed.

In *Chapter 5*, some final remarks on the presented modelling will be described.

1.1. STATE OF ART ON LANDSLIDE MODELLING

Slope stability assessment is an ongoing challenge in the field of geotechnical engineering. Landslide susceptibility assessment can be carried out by applying probabilistic or deterministic approaches. The former was developed to solve problems related to uncertainty in the attribution of soil physical-mechanical parameters; therefore, this approach is more suitable for identifying critical areas on the basis of factors that are supposed be directly or indirectly related to the slope stability (Fell et al., 2008), hence more appropriate for medium (1:100000 to 1:25000) and large scale (1:25000 to 1:5000) analyses. Deterministic methods are based on the classical slope stability theory and approaches, such as limit equilibrium and finite element methods (Fell et al., 2008); standard and detailed site information (e.g. slope geometry, soil physical and mechanical properties) are required, hence deterministic methods are suggested for a detail scale (1:5000 or more). The standard two-dimensional slope stability analysis approaches, like the Limit Equilibrium Method (LEM), are usually not efficiently applied at the overall watershed scale, or on wide areas, where the kinematic phenomena have a pronounced three-dimensionality. Numerical Finite Element methods (FEM) are poorly suited to analyse wide areas for the considerable computational effort requested and for the huge amount of input data. In literature, some authors (Hongjun et al., 2012) have proposed comparative studies between the LEM and FEM methods and have shown that the LEM method is a reliable method for assessing slope stability and for general geotechnical practices. Wright et al. (1973) found that the Factor of Safety (FS) and the slide surface are reasonably accurate, and the results by LEM methods are reliably comparable with real slope behaviour. Wright et al. (1973), Spencer (1967, 1973), and Duncan (1996) indicated that the average value of FS for those LEMs that satisfy all conditions of equilibrium are accurately near to the rigorous methods by a tolerance of $\pm 6\%$ (Kalatehjari et al., 2013).

In all conventional analyses currently in use, which can be referred to the global limit equilibrium method, the behaviour of the soil is assimilated to that of a rigid-plastic medium. The analysis therefore only considers the conditions present at failure and is independent of any deformation process preceding this phase (Fredlund, 1984). The steps in calculating a limit equilibrium solution are as follows: draw an arbitrary collapse mechanism; calculate the statical equilibrium of the components of the mechanism, by

resolving forces and/or moments; examine the statical equilibrium of other mechanisms and so find the critical mechanism for which the ratio between resisting forces (moments) and driving forces (moments) has its minimum value (Bishop, 1955).

Often, the (actual or potential) sliding surface is composite, the kinematic mechanism involves different soil layers, the hydraulic conditions are not easy to schematise, and the loads applied to the slope are various, so it is necessary to resort to a procedure known in the literature as Slice Method. It consists precisely in discretizing the portion of the slope assumed to be sliding into slices. Vertical strips with a flat bottom base are generally assumed.

The problem is statically indeterminate and assumptions are necessary in order to obtain numerical results. Therefore, different LEM methods are available in the literature.

The FS (i.e. the ratio between the available shear strength and the shear strength required to maintain impeding collapse) is usually determined through an iterative process. The iterative process is commonly started by taking an initial FS and continuing to obtain the lowest acceptable value

The LEM methods most commonly used in practice are 2D methods, which simplify the geometry of the natural slope, typically with 3D characteristics, into 2D. This simplification involves very strong assumptions. In fact, the slope is idealised in the third dimension as being symmetrical and infinitely long, thus losing important information on the spatiality of soil characteristics that can vary over short distances. Furthermore, it is assumed that the Direction of Sliding (DOS) is parallel with the slope cross-section plane. This turns out to be a very strong assumption because it cannot be guaranteed in reality. However, these assumptions typically can correspond to the most critical condition for the slope examined.

Over the years, different authors have been involved in developing three-dimensional slope stability analyses to overcome the lack of characterization of the slope third dimension. Many of the 3D LEM methods are developed from 2D slice methods. The transition from 2D to 3D methods also requires varying the geometry studied adding the third dimension. In this way slices must be evolved into columns (Figure 1.3.). Consequently, the static conditions of limit equilibriums of the columns must be satisfied. The assumptions of the 3D methods are mostly derived from the corresponding 2D method. However, some new definitions are needed in 3D methods due to the added dimension. The 3D shape of the slip surface, the asymmetric slope shape, the sliding direction and the inter-column forces are some of these new meanings. With reference to Figure 1.3, the internal and external forces acting on a soil column (i,j) are present. The soil weight is denoted as $W_{i,j}$, while $L_{z,i,j}$ is external vertical load, $L_{x,i,j}$ and $L_{y,i,j}$ are respectively external horizontal loads in x- and y-directions. The inter-column normal forces are represented by $E_{x,i-1,j}$ and $E_{x,i,j}$ in x-direction and $E_{y,i,j-1}$ and $E_{x,i,j}$ in y-direction, while $X_{x,i,j}$ and $X_{y,i,j-1}$ and $X_{x,i,j}$ are vertical inter-column shear forces in x-direction in y-direction, respectively. $H_{x,i-1,j}$ and $H_{x,i,j}$ are horizontal inter-column shear forces in x-direction, $H_{y,i,j-1}$ and $H_{x,i,j}$ are the horizontal inter-column shear forces in y-direction. The

possible presence of earthquake is considered through $F_{evi,j}$, the vertical force induced by earthquake, and $F_{ehxi,j}$ and $F_{ehyi,j}$, the horizontal force induced by earthquake in x- and y-directions, respectively. Finally, $S_{i,j}$ is the shear strength force at the base of column, and $N_{i,j}$ and $U_{i,j}$ are respectively total normal force and pore water pressure at the base of the column.

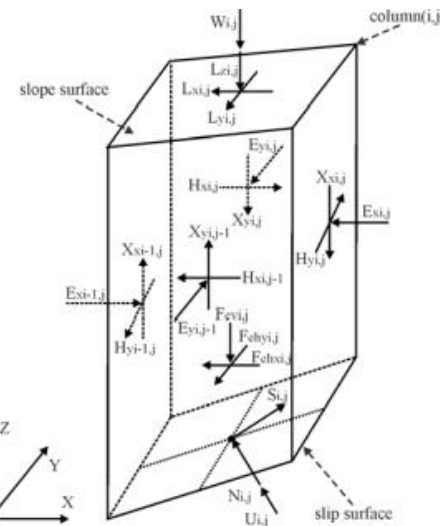


Figure 1.3. Typical 3D column scheme (Kalatehjari et al., 2013)

However, similar to 2D methods, each 3D method may rely on simplifications or neglects some additional definitions or some of these forces may be ignored, simplified or assumed.

In literature, Anagnostti (1969) proposed the first 3D model. Based on Morgenstern and Price's (1965) method, it considers a generic slip surface for which to calculate the FS. No assumptions have done on DOS direction. The limit equilibrium equations were established on vertical thin slices by assuming an interslice force function of interslice shear forces. Another model based on the method of Morgenstern and Price is that proposed by Sun et al. (2011). In analogy with Anagnostti (1969), no assumptions are made about the DOS and the sliding surface is considered generic. However, differently from this method, no assumptions are made about the internal forces. In fact, the force system follows the procedure proposed by Zheng (2009).

Zheng's (2009) method is a rigorous method that does not consider the landslide body divided into columns but considers it globally. This method satisfies, for both a generic DOS and slip surface, six equilibrium conditions and a vector of integration equations for these six conditions. The unknown values of these equations include the FS and the total normal stress on the sliding surface, defined by a distribution form that includes five unknowns. Then, the distribution function was substituted for the six mentioned equations, resulting in a system of nonlinear equations. This system was solved to find the corresponding value of FS and the distribution vector.

In analogy, in the method of Sun et al. (2011) the slip body is not divided into columns, but the equilibrium conditions are satisfied globally. A triangular mesh was used to cover the horizontal projection of the slip surface for the calculation of soil mass interpolation. Another triangular mesh was used on the slip surface to calculate the relevant integrals. In addition to Zheng's (2009) model, a more sophisticated patch-wise interpolation with a triangular mesh was used to better approximate the normal stress distribution on complicated slip surfaces (Kalatehjari et al., 2013). The minimum value of FS and other corresponding unknowns were obtained by solving the optimization problem, based on an object function.

Baligh and Azzouz (1975, 1978 and 1983) proposed a model for simple slope in which not assumptions on DOS direction were done. The first model (1975) was proposed for cohesive slope, based on the circular surface method. Differently from the models previously described the slip surface is assumed to be cylindrical in the central part with conical or ellipsoidal ends. All shear resistance forces on the slip surface were assumed to act perpendicularly to the axis of rotation. This method used the equation of moment equilibrium about the axis of rotation to find the value of FS. In 1978, they extended this model to frictional slopes, by assuming two new assumptions. The first one is related to the interslice forces. According to the Fellenius' method (1936), they supposed the neglecting of all interslice forces and calculate the normal stresses from moment equilibrium to each slice. The second assumption concerns the stress distribution. They assumed the vertical stress, coinciding with the slice weight, as the principal stress, and the horizontal stress as the minor principal stress, while the third principal stress corresponds to a slice weight coefficient, parallel to the axis of rotation. In 1983, they extend the model proposed in 1975 to consider the effect of applied loads on slope stability. The new method proposed allows the assessment of the slope stability for symmetrical slope. It is worth to underline that several methods proposed in literature are based on this assumption. The slope in the Chen's (1983) model can be cohesive or frictional with different soil water pore conditions. The sliding surface is supposed to be a combination of central cylindrical part with semi-ellipsoidal ends and the axis rotation perpendicular to the plane of symmetry. The DOS is assumed to be parallel with the symmetrical plane and this assumption made possible to neglect the shear forces in front and back sides of inter-columns. The columns are considered designed by small width and length. For each column the shear forces are divided into cohesion and frictional parts, acting on the middle section, with an arbitrary height equal to half or on third of columns height and a constant inclination equal to the base angle of the related side or the columns. In order to determine the FS and inclination of resultant inter-column forces, moment and force balance equations were considered for each column as well as the whole sliding body.

Another 3D method based on the hypothesis of symmetrical slope are proposed by Dennhardt et al., and Leshchinsky et al. in 1985. The first method considered an ellipsoidal slip surface and the presence of symmetrical external loads applied on the top of the slope. The second method is based on the limiting equations and variational analysis of Kopacsy (1957). The minimum FS value is achieved by solving three

unknown functions that includes the slip surface equation, spherical or cylindrical, the distribution function of normal stress, and the DOS direction.

In the same year Ugai proposed a 3D method for symmetrical vertical cohesive cuts based on LEM equations and variational calculus. The suitable shape of slip surface was determined by examining several arbitrary shapes including cone, ellipsoid, cylinder plus plane, combined cylinder-cone, combined-cone-plane, and combined cylinder-ellipsoid. Finally, the cylindrical slip surface attached to two curved caps was assumed as the possible shape of failure (Kalatehjari et al., 2013). The FS estimate is based on the definition of a stability factor that takes into account several variables (i.e., cut height, soil weight and length of slip surface). Another method for symmetrical vertical homogeneous cuts based on LEM equations and variational calculus has been proposed by Leshchinsky and Mullet in 1998. These methods considered vertical corners cuts and vertical cuts with longitudinal extension. The assumed shape of failure surface was an expansion of log-spiral function. This method could be able to calculate 3D FS taking into account the presence of water pore pressure.

Leshchinsky and Baker (1986) and Baker and Leshchinsky (1988) are extension of the first method proposed in 1985, both of these methods considered symmetrical homogenous slopes. The version of 1986 proposed a cylindrical slip surface and the application of two equilibrium equation along transversal and vertical axis and the moment equilibrium equation of half-sliding body about the rotation axis to assess the FS for the slope. The following version (1988) has been developed to investigate homogenous conical slopes, making some simplifications: external loads and water pore pressure are neglected¹⁸⁹⁷. In the same year, Hungr (1987, 1989) proposed another method based on the assumption of symmetrical slope, that is an extension of Bishop's method (1955). The slip surface is a rotational surface with circular central cross section assumed as failure surface. The vertical interslice shear strength forces are neglected on the column sides. The FS equation is established by imposing the vertical forces equilibrium for each column as well as the overall moment equation of the whole sliding mass around the axis of rotation. In the 1989, Hungr proposed an extension of the model proposed in 1987, based on simplified Bishop's (1955) and simplified Janbu's 1954 methods.

The hypothesis made for the extension of simplified Bishop's (1955) method were similar to the model of 1987: vertical interslice shear strength forces neglected and horizontal shear strength parallel to the plane of symmetry. The slip surface shape was assumed rotational, while for non-rotational failure surface the proposed approach of Fredlund and Krahn (1977) is applied. The FS values is found by applying the vertical force equilibrium equations for each column and the moment equation overall the sliding body. The FS values found showed that the 3D FS obtained by extended Bishop's method found to be smaller than the results of 3D rigorous methods. The results of the extended Janbu's method has been found to be even more conservative than extended Bishop's method.

Gens et al. (1988) proposed a 3D method for homogeneous, isotropic and purely cohesive soils. According to Azzouz et al. (1987), the slip surface shape is cylindrical in the central part, but differently from this method, at the ends it is attached to a planar or curved shape. The equation of 3D FS was established by considering the moment equilibrium of sliding mass about the axis of rotation of cylindrical surface.

In the same year Ugai proposed a series of 3D method for symmetrical slopes, based on several 2D method of slices (i.e., Spencer's (1967), Fellenius' (1936), simplified Janbu's (1954), and simplified Bishop's (1955) methods). The slip surface depends by the applied method. Xing (1988) proposed a simple 3D method for analysing the stability of symmetrical concave slopes with elliptic slip surface. All inter-column forces perpendicular to the sliding direction were neglected due to the assumption of movement in parallel with vertical plane. Therefore, the resultant of the forces acting on each column was assumed to have a constant inclination over the sliding mass. For each column as well as overall sliding body, the FS values are obtained by applying the LEM equilibrium equations along x- and y- axis and moment equilibrium equation of sliding body about the axis of rotation. An iterative process was utilized to estimate the value of FS. The process ends when the assumed inter-column angle satisfies both force and moment equilibriums equations at the same values of FS. Leshchinsky and Huang (1992) proposed a generalized 3D method for log-spiral or a general symmetrical slip surface. The estimate of the FS is done by an interactive mathematical process. While Cavounidis et al. (1992) proposed an extension of the Azzouz et al. (1978) method to examine vertical cuts in cohesive soil.

The FS is defined by applying moment equilibrium equation around the axis rotation. The slip surface is cylindrical in the central part and conical at the ends. Lam and Fredlund (1993) proposed a 3D method based on general LEM of Fredlund and Krahn (1977). A single direction of movement is imposed, and the inter-columns force were used to calculate the inclination of the resultants. The definition of this forces is close to the Morgenstern and Price's (1965) function including five relationships between normal and shear inter-column forces. They also established two different equations of FOS based on moment and force equilibriums to determinate the condition of problem. The overall value of FOS was determined to simultaneously satisfy moment and force equilibriums.

In the method of Yamagami and Jiang (1996 & 1997) no assumptions are made on the symmetry of slope or on the DOS. The method is an extension of the simplified Janbu's method (1954). The FS is estimated by using an interactive process by using the LEM equilibrium equations.

Huang and Tsai (2000) established a 3D method based on two-directional limit equilibriums to find the 3D FOS for possible sliding directions. The slip surface was assumed semi-spherical or partly spherical shape with an axis of rotation parallel with longitudinal axis. The sliding body was discretized by using a grid parallel to x and y-axis. In this method all horizontal inter-column forces were neglected, while other inter-column forces were decomposed with reference to the main axis. The DOS definition and the

corresponding FS was carried out by applying two equations of moment equilibriums in x and y directions and one equation of moment equilibriums overall sliding body. An interval calculation similar to Yamagami et al. (1996, 1997) was used to find the DOS and the Directional Factors of Safety (DFOS). The overall FS was calculated from the third equation by using the achieved DFOS.

In 2003, Chen et al. proposed a method based on the 2D Spencer' method (1967), using a rotational slip surface. The horizontal and two of the vertical inter-column forces have been neglected and the inclination of the resultant force was assumed to be constant. LEM equilibrium equations have been applied to assess the FS value by using the Newton-Raphson method. Another method based on Spencer' method (1967), is the one proposed by Jiang at al. (2004). This method is also based on a variational analysis to find the FS value by applying two different horizontal equations and an overall moment equation. The DOS is assumed to be perpendicular to the longitudinal direction of slope and the internal forces were supposed acting on the sides of the columns assuming both direction and inclination. FOS was defined by simultaneous solving of equations with different inclination of inter-column force values.

Cheng and Yip (2007) proposed a series of 3D methods by developing the simplified Bishop's (1955), simplified Janbu's (1954), and Morgenstern and Price's (1965) methods. They formulated a 3D asymmetrical problem as an extension of Morgenstern-Price's method and then reduced it to simplified Bishop's and simplified Janbu's methods (Kalatehjari et al., 2013). The slip surface is assumed to be spherical for all the methods defined. The inter-column forces are estimated by assuming the inter-column force function proposed in the Morgenstern-Price's method. The FS is detected through an interactive process for which the moment equilibrium has to must guarantee in x- and y-directions. The process ends when a unique FS value is detected in both directions.

The description of 3D methods proposed by Kalatehjari et al. (2013) highlights the effort that various authors have made over the years to propose 3D analysis methodologies based on the LEM method. These methods are summarized in chronological order Table 1.1, where the main assumptions (i.e., 2D method from which they were developed, slip direction assumptions (DOS), and defined slip surface shape) are highlighted.

All of the above authors agree that such models, although simplified, are able to more adequately characterize the 3D nature of the natural slope, achieving more reasonable results with safety factors close to or higher than 2D models.

However, there are still some limitations in the practical application of these 3D methods. In fact, most of these methods assume a plane of symmetry for the slope and the slip surface is usually imposed. These assumptions deviate significantly from the real nature of the slope, which has strongly non-symmetrical characteristics and presents a sliding surface that is difficult to assimilate to a precise geometric shape. The application of these methods is therefore limited. In addition, the position and direction of the DOS are

sensitive to the symmetry assumption on which the equilibrium equations for FS estimation are set. Therefore, the procedure for its definition can be time-consuming. As for the internal forces of the sliding mass, they are largely simplified or ignored in the FS equations.

3D Method	Source	DOS	Application	Slip Surface
Anagnosti (1969)	Morgenstern-Price's method	No	Generalized	Generalized
Baligh and Azzouz (1975)	Circular arc	No	Simple slopes	Cylindrical center part with conical or ellipsoidal ends
Hovland (1977)	Fellenius' method	No	Symmetrical	Cone/wedge sha
Azzouz and Baligh (1978)	Circular arc	No	Simple slopes	Cylindrical center part with conical or ellipsoidal ends
Chen and Charneau (1983)	Spencer's method	No	Symmetrical	Cylindrical center part with conical or ellipsoidal ends
Azzouz and Baligh (1983)	Circular arc	No	Simple slopes	Cylindrical center part with conical or ellipsoidal ends
Dennhardt and Forster (1985)	LEM	No	Symmetrical	Ellipsoidal
Leshchinsky et al. (1985)	LEM and variational analysis	No	Symmetrical	Spherical and cylindrical
Ugai (1985)	LEM and variational analysis	No	Vertical cuts	Cylindrical center part with conical or ellipsoidal ends
Leshchinsky and Baker (1986)	LEM and variational analysis	No	Symmetrical	Cylindrical center part with conical or ellipsoidal ends
Baker and Leshchinsky (1987)	LEM and variational analysis	No	Conical heaps	Cylindrical with cap ends/ expansion of 2D log-spiral
Hungr (1987)	Bishop's modified method	No	Symmetrical	Rotational with circular central section
Gens et al. (1988)	Swedish circle	No	Simple slopes	Cylindrical with planar or curved ends
Leshchinsky and Mullet (1998)	LEM and variational analysis	No	Vertical cuts	Expansion of log-spiral function
Ugai (1988)	Simplified Bishop's and Junbu's methods	No	Symmetrical	Based on the method
Xing (1988)	Spencer's method	No	Symmetrical	Symmetrical elliptic surface with circular vertical cut
Hungr et al. (1989)	Simplified Bishop's and Junbu's methods	No	Symmetrical	Symmetrical rotational
Leshchinsky and Huang (1992)	2D method of Leshchinsky and Huang	No	Symmetrical	General symmetrical/extension of log-spiral
Cavounidis and Kalogeropoulos (1992)	3D method of Azzouz and Baligh (1978)	No	Symmetrical	Cylindrical with conical end caps
Lam and Fredlund (1993)	2D general LEM	No	Symmetrical	Generalized rotational surfaces
Yamagami and Jiang (1996, 1997)	Simplified Junbu's methods	Yes	Generalized	Generalized
Huang and Tsai (2000)	LEM and two-directional FOS	No	Complicated	Semispherical/ partly spherical composite
Huang et al. (2002)	Junbu's method and two-directional FOS	Yes	Generalized	Generalized
Chen et al. (2003)	Spencer's method	No	Generalized	Generalized rotational
Jiang and Yamagami (2004)	Spencer's method based on variational analysis	No	Symmetrical	Rotational surfaces
Cheng and Yip (2007)	Bishop's, Junbu's and Morgenstern- Price's methods	Yes	Generalized	Spherical
Zheng (2009)	LEM	No	Generalized	Generalized
Sun et al. (2011)	Morgenstern-Price's method	No	Generalized	Generalized

Table 1.1. 3D LEM Methods and key features (Kalatehjari et al.,2013).

In literature, existing models show that the development of three-dimensional LEM methodologies for landslide susceptibility estimation is an open challenge.

Moreover, the new challenge is related to the design and development of 3D models that, although simplified, represent a useful tool for landslide risk management. In particular, attention should be paid to the estimate of susceptibility to rainfall triggered landslides. In fact, continuous climate change, abandonment of the countryside, and excessive urbanization, sometimes poorly managed, of parts of the territory are some of the critical issues that local authorities have to face today. For this reason, it is necessary to develop appropriate models that are operationally compatible with good resolution and computational speed.

GIS is an excellent tool for developing models for analysing landslide susceptibility. GIS is recommended in the 'Guidelines for landslide susceptibility, hazard and risk zoning for land-use planning' (Fell et al., 2008a). However, the need for field validation of GIS modelling results is also highlighted. This is crucial for the production of maps that best reflect the reality on site. In literature, there are several deterministic models for landslide susceptibility assessment developed in GIS environment and based on the safety factor computation and spatialisation.

In particular, the use of free and open source software is considered to be the best solution due to its strength, versatility and the possibility of developing new codes and modules to be applied to digital data. The main free open source software on which the IHG was developed is GRASS (Geographic Resources Analysis Support System) GIS, used to manage the numerical cartography and all the data (surveys, piezometers, inclinometers, groundwater levels, stratigraphy). However, also QGIS was used, to easily render, validate and share the results of modelling, superimposing them on georeferenced photographic documentation or WebMapService (WMS) maps.

For the sake of brevity, I will mention the models for landslide susceptibility assessment developed in GIS environment, which have the greatest relevance for the IHG model.

Most of them use Mohr-Coulomb theory to achieve geotechnical modelling, as TRIGRS (Baum et al., 2002 based on the Iverson model, 2000) or SLIP (Montrasio & Valentino, 2008); the soil is usually assumed isotropic and homogeneous, accounting for the horizontal heterogeneity varying the parameters from cell to cell. From the hydrological point of view, these simplified methods combine the infinite slope equation with the steady state hydrological conditions, as in SHALSTAB (Montgomery & Dietrich, 1994) and Lu & Godt (2008) or with physically based models adopted to simulate the time or quasi-time dependent groundwater processes, as in dSLAM (Wu & Sidle, 1995) and Qiu et al. (2007), or transient infiltration models (Baum et al. 2002, 2008, 2010).

An innovative physically based model, developed in a GRASS GIS environment to assess slope stability, is here presented. It performs both a water balance (Passalacqua, 2002) and a stability analysis in the volume of soil studied (which is appropriately discretized into columns). However, it is based on a simplified assumption: the geotechnical cells are considered independent, for this reason the adjacent soil portions are not considered as interacting from the mechanical point of view. This means that the instability of the downstream portions does not influence its contiguous upstream portions and vice versa, leaving their safety factors unchanged.

The Integrated Hydrological-Geotechnical Model (called IHG model) is able to establish a cause-effect relationship between observed rainfall and the possible occurrence of landslides (Federici et al., 2014; Passalacqua et al, 2015 and 2016). Currently, IHG model is able to describe the soil slide susceptibility over areas of a few square kilometres, typically at scale 1:5000, discretizing the 3D dominium in vertical volume elements, eventually composed of several voxels. The GIS-based approach allows the

interpolation/extrapolation of in situ measurements, descriptive of the groundwater and stratigraphy surfaces and of the relevant hydrological-geotechnical parameters. Last, but not of least importance, the low computing time allows to achieve fast and reliable results for real time analyses and forecasts of the landslide susceptibility over wide areas.

More details on the IHG model and its applications will be described in the following Chapters.

2. CASE STUDIES

In the frame of the AD-VITAM project five sites in the ALCOTRA territories have been chosen as case studies for their well-known rainfall-triggered landslide susceptibility (Figure 2.1). Four sites (Mendatica, Ceriana-Mainardo, Monesi di Triora, Ville San Pietro) are in the Province of Imperia (western Liguria, Italy) while the fifth site (Vence) is in the neighbouring district of the PACA Region (Region of Provence-Alpes-Côte d'Azur, Department 06, France).

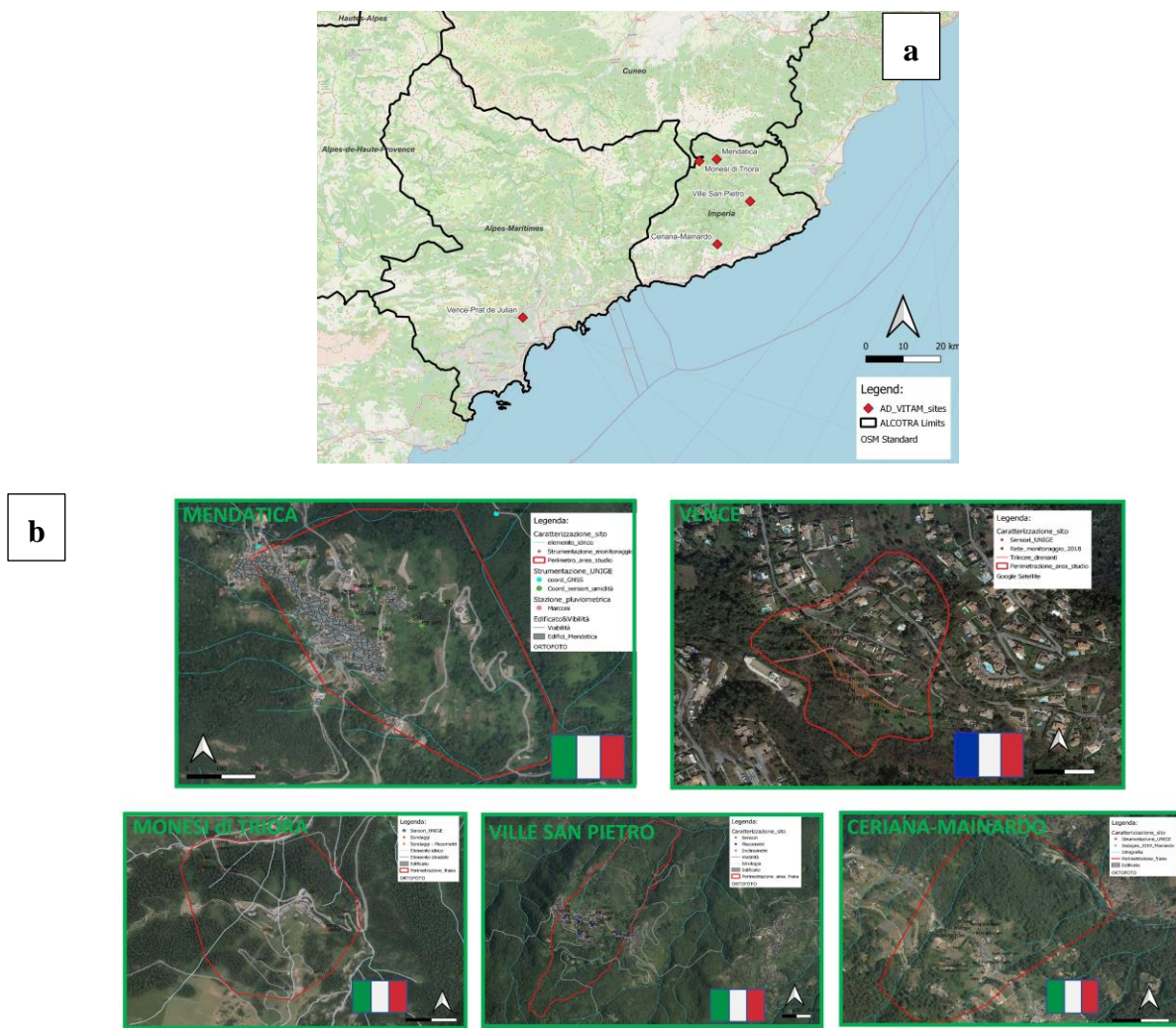


Figure 2.1: (a) Geographical location of the AD-VITAM sites (on a OSM background: <https://www.openstreetmap.org/copyright>), (b) landslide boundary of the five study areas.

In this dissertation, particular attention will be paid to the sites of Mendatica and Vence. Considering the slope volumes involved, the landslides that affect these sites are the most important on a provincial, if not

regional, scale: the former for the Imperia Province (Macciò, 2007), the latter for the PACA Department (Palis, 2017).

The geological context of the study area

The Imperia region and western Liguria in general present a geological and structural complexity that has been highlighted only over the last years (Federici et al., 2007), thanks to the studies of several geologists. The large Geological Map of Liguria at a scale of 1:200000 (Giammarino et al., 2002) represents the most complete work available, also due to the lack of geological maps at a greater scale of detail, both at a regional and at a national level. A rich literature can be found on the Italian side, by researchers from Pavia, Genoa and Milan (Vanossi et al., 1984), as well as on the French (e.g. Lugeon, 1902, Du Bois et al., 1990, Ricou et al., 2009) and German sides (e.g. Schmidt, 1907, Schmid et al., 1996, 2004, Pfiffner, 2009). The Alpine Arc extends for a length of about 1200 km from Nice to Vienna with a thickness varying between 200 and 500 km, and its formation is due to the collision between the African and Eurasian plates (Palis, 2017). In the Jurassic era, around 200 million years ago, the separation of Pangaea and the shifting of the European plate away from the African plate led to the formation of the Ligurian-Piedmont Ocean.

The shifting of the two plates and the consequent thinning and tearing of the oceanic crust allowed volcanic materials to escape and give rise to basaltic-type beds; these basalts can be recognized in some parts of the Alpine chain such as Monviso, the Ligurian Alps and the Susa Valley.

At the end of the Cretaceous, there was a reversal in the movement between the two plates, which began to converge, creating the conditions for the Alpine formation. When the Ligurian-Piedmont Ocean was completely closed, the collision of the two plates gave rise to the Alpine orogenesis. During this process of collision and overlapping of the continental margins of the two plates, some of the oceanic sediments were trapped inland, first occupying deep positions, and then later resurfacing on the surface after undergoing metamorphic and erosive processes. This is one of the reasons why traces of basaltic oceanic floors can be found along the Alpine arc.

Geologically, it is possible to subdivide the Alpine arc by considering the position of its major structural elements in relation to the main tectonic lineation (Insubric line) (Figure 2.2.), which is clearly recognizable on a regional scale; in the context of the Western Alps and the Maritime Alps, this line is defined as the Penninic Front (P.F.) or Penninic Basal Contact (P.B.C.) (Maino et al., 2016).

With reference to the Penninic Front (P.F.), it is possible to define two different geological areas:

- to the east of the P.F., the Internal domain, the axial sector of the Austroalpine and Penninic continental domains, separated by oceanic units of the Piedmont and Briançonnais nappes, that correspond to strongly deformed and transformed soils, belong to this geological area Piedmont, Piedmont-Ligurian and Briançonnais domains, so-called Western Internal Alps;

- to the west of the P.F., the external domain, consisting of the Provençal-Dauphinois, Helvetic and External Massif domains, characterised by soils corresponding to the Mesozoic series of flysch and molasse zones and crystalline basement, so-called Western External Alps (Maino et al., 2016).

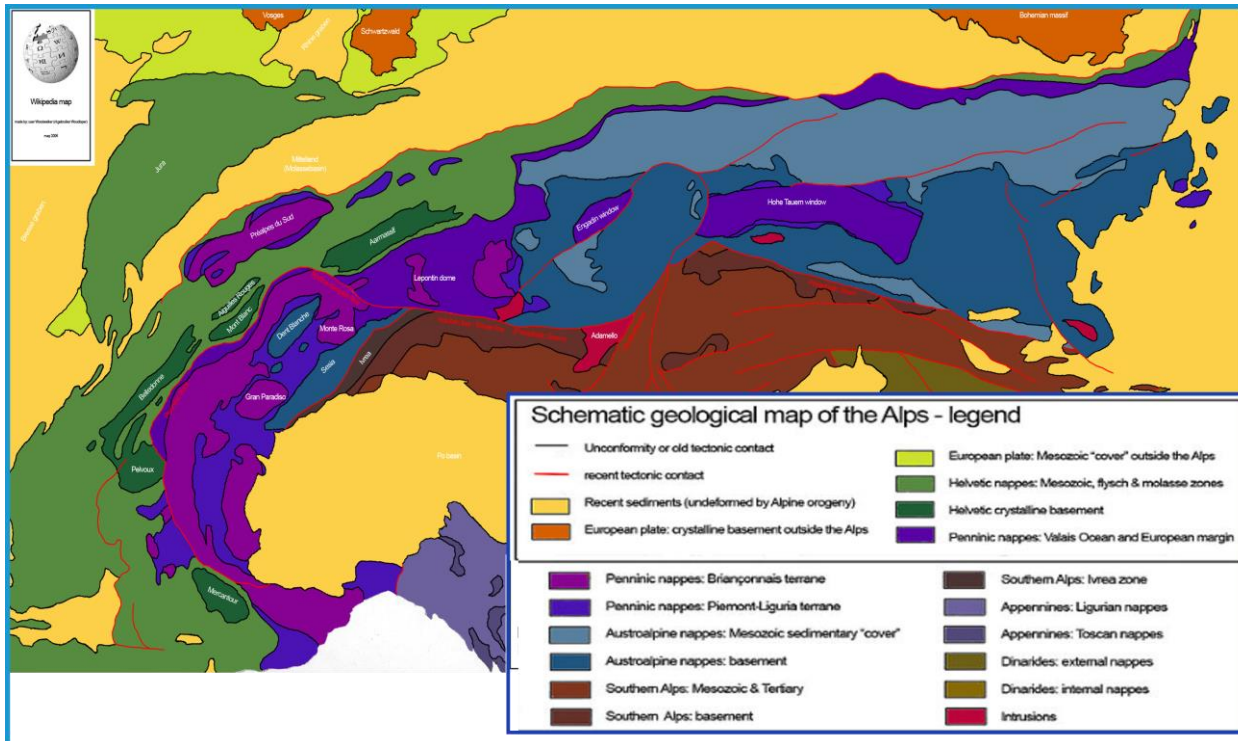


Figure 2.2. Geologic structure of Alps (Public Domain, <https://commons.wikimedia.org/w/index.php?curid=4380219>).

A more detailed description of the geological structure of this region is provided in Figure 2.3., it is possible to define: 1) Helvetic-Dauphinoise domain delimited by the Penninic Frontal Thrust (P.F.T.) with (1a) external Crystalline Massifs (Arg: Argentera-Mercantour; Mt Bl.: Mont Blanc) and (1b) the Mesozoic sedimentary cover; (2) Upper Cretaceous flysch; 3) metamorphic oceanic units of the Piedmont and Briançonnais nappes, including the Internal Crystal Massifs (D.M.: Dora Miara; G.P.: Gran Paradiso; M.R.: Monte Rosa) with (3a) the European ridge and (3b) the Tethys Ocean Domain 4) Austroalpine and Penninic continental domains with the Dent Blanche (D.B.), the Sesia Lanzo area (S.L.) and the Canavese line (Ca), representing the Adriatic continental margin 5) the Molasse basin belonging to the Quaternary Oligocene, located on the edge of the Alps, while the dotted lines represent the main active faults systems (Palis, 2017).

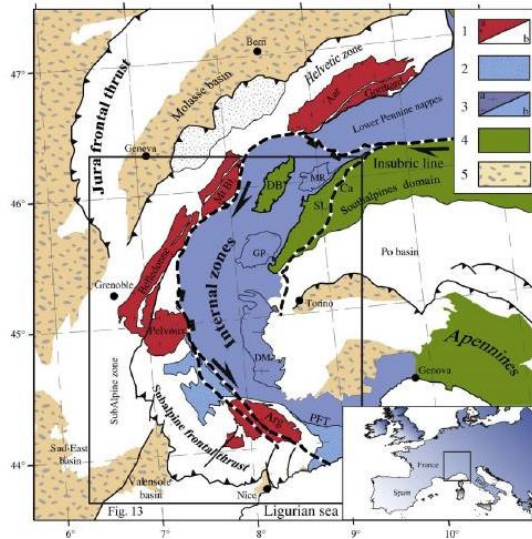


Figure 2.3. Simplified geological map of the Alps (Sanchez 2010, modified after Bigi et al, 1990 and Polino et al, 1990).

The Alpes-Maritimes department is in the southern part of the External Western Alps. It is included in the areas outside the Penninc front belonging to the Helvetic domain and contains the Pelvoux and Argentera-Mercantour massifs. The Ligurian sector belongs to the Internal Wester Alps domain, including the Monte Saccarello Massif.

Climate and Hydrology of the ALCOTRA territories

The climate of ALCOTRA territories ranges, in the space of a few kilometers, from a Mediterranean coastal climate to a mountain one. This transition is mainly due to the orography and the Mediterranean Sea closeness. Indeed, due to the Alpine geomorphology, the presence of natural barriers (e.g., the Alpine massifs to the north and the Massif des Moors to the west) lead to a sunny and warm climate with relatively mild winters, protecting the southern Alpine areas (PACA region and province of Imperia) from northern and Atlantic currents.

Annual rainfall has a geographical distribution depending on the distance from the sea, the elevation and the orientation of the reliefs with respect to the direction of origin of the disturbances (Federici et al., 2007). The mitigating action due to the presence of the sea gradually decreases moving away from the coastal to internal areas and with increasing altitude. For this reason, rainfall distribution is irregularly distributed over the year, reaching the highest rainfall height in autumn and decreasing considerably in summer. In fact, the rainfall regime can be defined bimodal, with a monthly maximum in November and a secondary maximum in December or October (Figure 2.4). The most pronounced meteorological drought is in July. With reference to the French side, Palis (2017) proposed an example of the rainfall and temperature comparison between the Nice city located in the coastal zone and Saint Etienne de Tinée in the internal areas (Figure 2.4a). The Saint Etienne de Tinée climate is characterized by very low temperature values in the autumn and winter seasons, while the maximum is recorded in the summer period. In July and August, temperature can vary between 12°-13°C and 20°-22°C (yellow zone), while coastal temperatures can reach values around 27-28 °C during the same period. Nice is characterized by low rainfall in summer,

and a period of heavy rainfall in autumn and spring, differently from the mountain area, where significant rainfall is present throughout the year, this trend is confirmed from the Ligurian side (Figure 2.4b), by a comparison between the data of Sanremo and Triora sites (Federici et al., 2007).

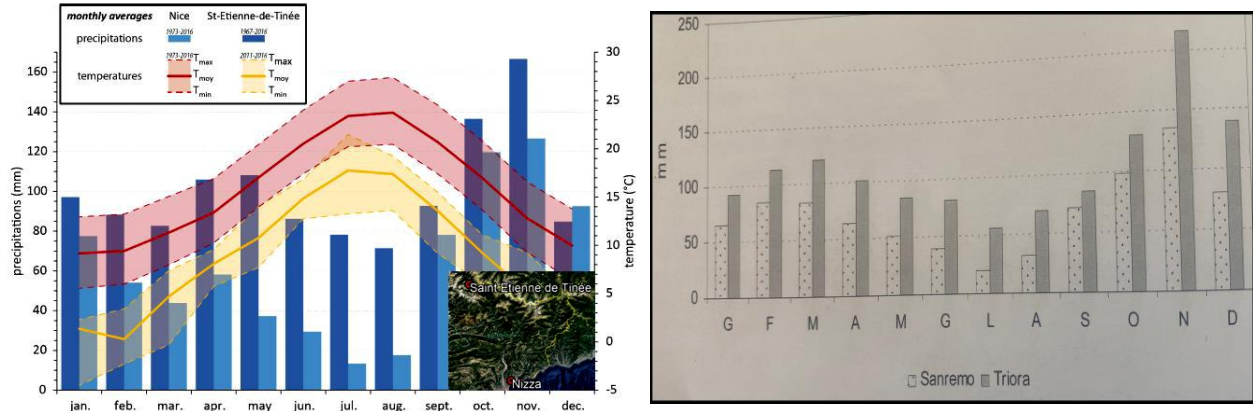


Figure 2.4. (a) Comparison of the evolution of monthly climatic averages (precipitation and temperature) between Nice and Saint-Étienne-de-Tinée sites (Palis, 2017), (b) annual temperature comparison between Sanremo and Triora sites (Federici, 2007).

In these valleys, therefore, it is possible to define the presence of different areas characterised by their own microclimate due to different altitudes, slope exposures and the presence or absence of wind. It is necessary to emphasise the importance of this aspect, since the fact of finding different climatic configurations within a radius of a few kilometres will inevitably condition the considerations made in relation to the choice of rainfall and temperature values taken as representative of the case studies proposed in the present dissertation.

The territories of the Alps are crossed by a dense hydrographic network of streams and coastal rivers, that are mainly characterized by a torrential regime and fed by both precipitation and late spring snowmelt; they present large flows and rapid flooding in spring and autumn. The hydraulic behaviour of the soil in the studied areas is strongly influenced by annual rainfall regime. In fact, the alternance of dry summers followed by autumns with heavy rainfall events can significantly affect the slope stability conditions. Therefore, rainfall triggered landslide occurrence is linked to extreme weather events (e.g. cumulative rainfall exceeding 500 mm in a week) that may follow wet periods, for which the soil had already exploited most of its infiltration capacity.

2.1 Mendatica site

Mendatica is a town in Liguria region, in north-western Italy, and belongs to the Province of Imperia, which borders Piedmont to the north and France to the east. Mendatica is in the upper Arroscia Valley, between 750 and 850 m above sea level, at the foot of Mount Frontè - the second highest peak in Liguria (2152 m a.s.l.) after Mount Saccarello; the Arroscia river is one of the most important watercourses in the western area (Figure 2.5.).

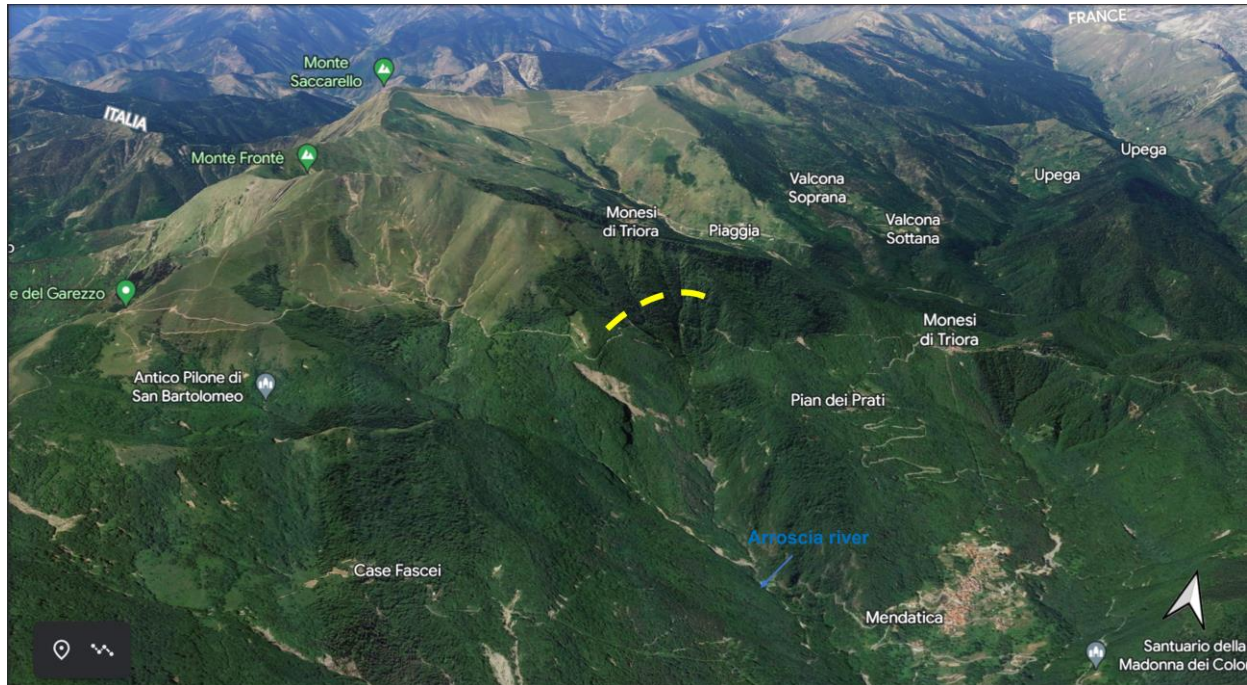


Figure 2.5. Overview of the alpine ridge behind Mendatica, with the landslide crown (yellow dashed line)
(Google Earth)

The origins of the village probably date back to the mid-7th century, during the Longobard invasions that forced the coastal towns (i.e., Albenga, in Savona Province) to flee and take refuge in mountainous territory. However, there is evidence of continuous occupation as early as the pre-Roman phase, due to the importance of the site in terms of roads and pastoral activities (Occelli, 2008). Today, the Mendatica territory is sparsely populated, with a population density of about 8 persons/km².

Mendatica was entirely built within a large relict landslide of about 250 ha, the largest in the Arroscia Valley and probably in the Province of Imperia. Quiescent or active landslide areas are present within relict landslides, as demonstrated by damages on buildings. The magnitude of this landslide has been highlighted by a geognostic campaign conducted in 2006, aimed at defining the geological and hydrological model of the slope. Through the acquisition of new data and the installation of monitoring instrumentation, the stable layer, on which the landslide flows, has been identified at a depth varying between 18 and 40 m below the ground level (Macciò, 2007). The crown of the landslide is located at the Costa Pian dei Prati ridge (about 1800 m a.s.l.); from the crown the main scarp develops downstream to about 1600 m a.s.l. The displaced mass is about 2.8 km long and its surface is about 2.2 km² (Pepe et al., 2021): the landslide body is bounded to the south by the Costa delle Forche ridge, while it borders directly on the path of the Creuso stream to the north. To the east, the accumulation zone extends up to an average altitude of 600 m a.s.l., where the tip of the landslide is bordered by the Passo Cagnasso and Arroscia stream courses (Figure 2.6).

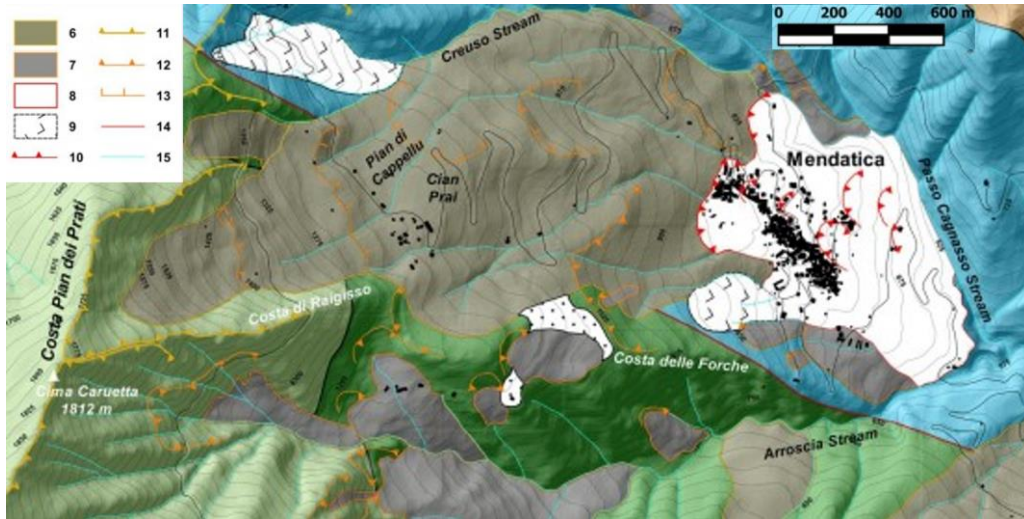


Figure 2.6.: (6) relict landslide deposit; (7) dormant landslide deposit; (8) active landslide deposits; (9) rock slide (potential); (10) edge of main active landslide scarp; (11) edge of main relict landslide scarp; (12) edge of main dormant landslide scarp; (13) edge of secondary dormant land-slide scarp; (14) tectonic contact; (15) hydrographic network (extracted from Pepe et al., 2021).

A more detailed examination of the entire landslide deposit revealed that it consists of several small coalescent bodies, suggesting a rather complex evolution (Federici et al., 2007).

According to the existing standard on hydrological risk management, the Mendatica area is classified with high geomorphological risk (Law Decree 180/1998 converted into Law 267/1998: Basin Plan - regional area n.9). The geomorphological hazard of the site is illustrated in the landslide susceptibility map (Figure 2.7.), where the urban area is classified in an active landslide zone (Pg4, red), that corresponds to a very high susceptibility, while the other part is classified as high susceptibility zone, that corresponds to quiescent (Pg3a in pink) and relict (Pg3b, beige) landslides. The area corresponding to active and/or quiescent landslide is approximately of 60 hectares, and it is located within a very large relict landslide (light brown area).

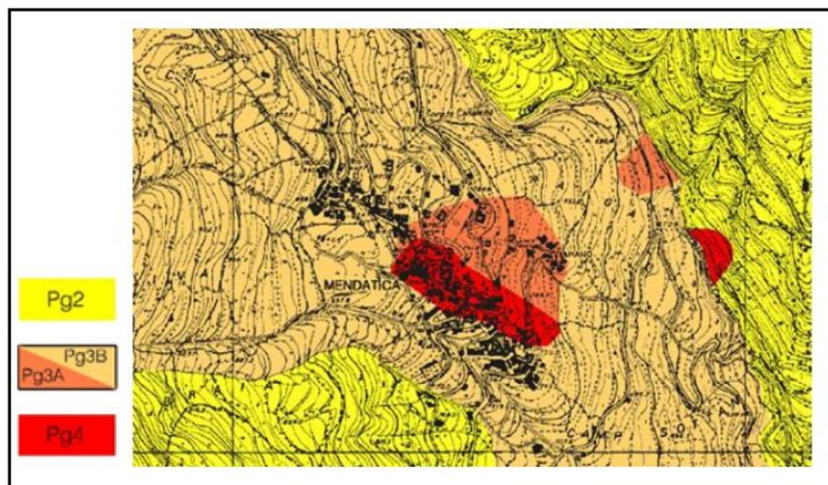


Figure 2.7. Geomorphological hazard classification based on the Law 267/1998 Basin Plan - regional area n.9

The territory represents the highest sector of the Arroscia basin (305 km^2 in total), which connects the Neva upstream of Albenga (SV) to form the Centa River. Mendatica is known for the water richness of the subsoil, which feeds several perennial springs used for irrigation and/or aqueduct. This peculiarity is typical of the thick relict landslide deposits located in areas characterized by a significant rainfall regime. Studies and on-site interventions have found outflow of groundwater, both deep and superficial, at different depths from ground level, both interconnected and isolated, and areas of stagnation and widespread imbibition on sub-surface areas. Groundwater level subsurface flow is one of the main causes affecting the slope stability, but due to the site geomorphology, an important role is also played by surface flow, which performs erosive action along the riverbanks. In fact, minor streams, such as the Creuso stream and the Cagnasso stream, have a narrow and heavily submerged bed, typical of torrential beds, and produce an intense erosive action on both sides. This phenomenon can trigger a regressive behaviour of the slope, already unstable (Macciò, 2007). Figure 2.8. shows hydrographic network that characterizes the landslide boundaries.



Figure 2.8. Hydrographic network: natural landslide boundaries

2.1.1. Geological studies and geotechnical data

Although the morphology of the Mendatica relict landslide has been strongly modified by subaerial erosion processes and partially hidden by vegetation, many morphological features can be still identified (Macciò, 2007). From a geological point of view, this portion of the Arroscia Valley is geologically characterised by the tectonic units that characterise western Liguria, belonging to the so-called Helmintoid Flysch Nappe, also named Western Liguria Flysch complex, made up of thick Cretaceous non-metamorphic turbiditic deposits (Pepe et al., 2021). These geological complex (Figure 2.9) overlays both the soils of the Delphinian-Provençal domain, belonging to the so-called External Western Domain (Maino et al., 2016) to the west and the soils of the Briançonnais and Piedmont domains to the west and north (Federici et al.,

2007). Two are the main tectonic units, belonging to the Western Liguria Flysch complex, that characterized the landslide area: the Sanremo-Monte Saccarello Unit (FSR) and the Moglio-Testico Unit, both mainly consisting of calcareous and sand-rich turbidite sequences (i.e., Bordighera Sandstones Fm. (AOB) and Testico Fm.) that overlay abyssal plane pelitic complexes (i.e., San Bartolomeo Fm. And Peliti di Moglio Fm.). The Sanremo-Monte Saccarello Unit (Upper Campanian) outcrops with the San Bartolomeo Fm. (FBA), mainly consisting of thin-bedded and very-fine-grained varicoloured shales, and with the above-standing Bordighera Sandstone Fm. Which is prevalently composed by medium to thick-bedded, coarse to fine-grained, siliciclastic sandstones and conglomerates (Maino et al., 2016). The Moglio-Testico Unit outcrops with the Pieve di Teco Member (Lower Cretaceous–early Upper Cretaceous), which is constituted by an irregular alternation of thin to medium turbiditic beds made up of marls, calcareous marls and sandy marls (Pepe et al., 2021). The geologic age of the sequence was attributed to the Palaeocene by Boni and Vanossi, (1972).

In the landslide area, this lithology outcrops (Figure 2.8) extensively along the Rio Creuso and Passo Cagnasso (eastern sector), along their main tributaries and Provincial Road 3 (northern sector), along the Arroscia River channel (southern sector), and thus traces the perimeter of the landslide (Macciò, 2007).

It is possible to define the geology of landslide area as structurally complex, characterized by a complex mechanical behaviour (Pepe et al., 2015).

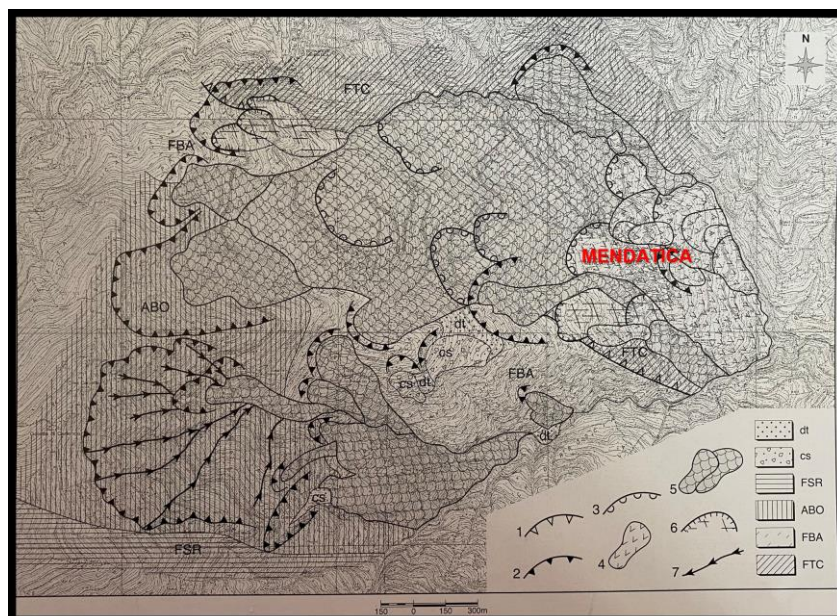


Figure 2.9. Geomorphological scheme of the Mendatica territory (Mendatica Municipality). Legend:

(dt) shapeless detrital deposit, debris-colluvial deposit; (cs) debris stratum or cone, also originated by rockfalls, or residual flap of relict ancient landslides; Helmintoid Flysch Nappe: Sanremo Monte Saccarello Unit; -FSR Sanremo Flysch; -AOB Arenaire di Bordighera; - FBA San Bartolomeo Formation; Helmintoid Flysch Nappe: Moglio-Testico Unit. 1 Tectonic contact; - 2. Edge of landslide and/or degradation scarp; 3- rotational sliding in the landslide body; -4 Recent and current landslide; -5. Active and relict landslide; 6-Deep Gravitational Slope deformation and/or block rock sliding; -7. Concentrated Erosion Pit.
(Federici et al., 2007)

Since 2005, a geological survey for the definition of geo-hydrological soil model has been carried out, due to a reactivation of the paleolandslide. In the autumn of 2005, a surface geological survey was carried out to assess the landslide boundaries and the depths to which subsequent investigations should be conducted. Then, attention was focused on the buildings, assessing their internal and external crack condition. In the second half of 2006, the geognostic survey was carried out, which revealed the soil stratigraphic structure and a greater thickness of the blanket than initially expected. An inclinometer and piezometric monitoring network have been installed, but in the following years, due to slope movements triggered by violent rainfalls (2013), new instrumentation had to be added to replace the broke down instrumentation and to support the remaining ones. Between 2013 and 2014, 3 draining wells and 3 new piezometer standpipes were installed, while in 2015, 4 new PVC inclinometer tubes were inserted. In addition, 105 crack gauges were installed between 2010 and 2015 throughout the center and a rain gauge station has been installed in January 2015 (Macciò, 2015).

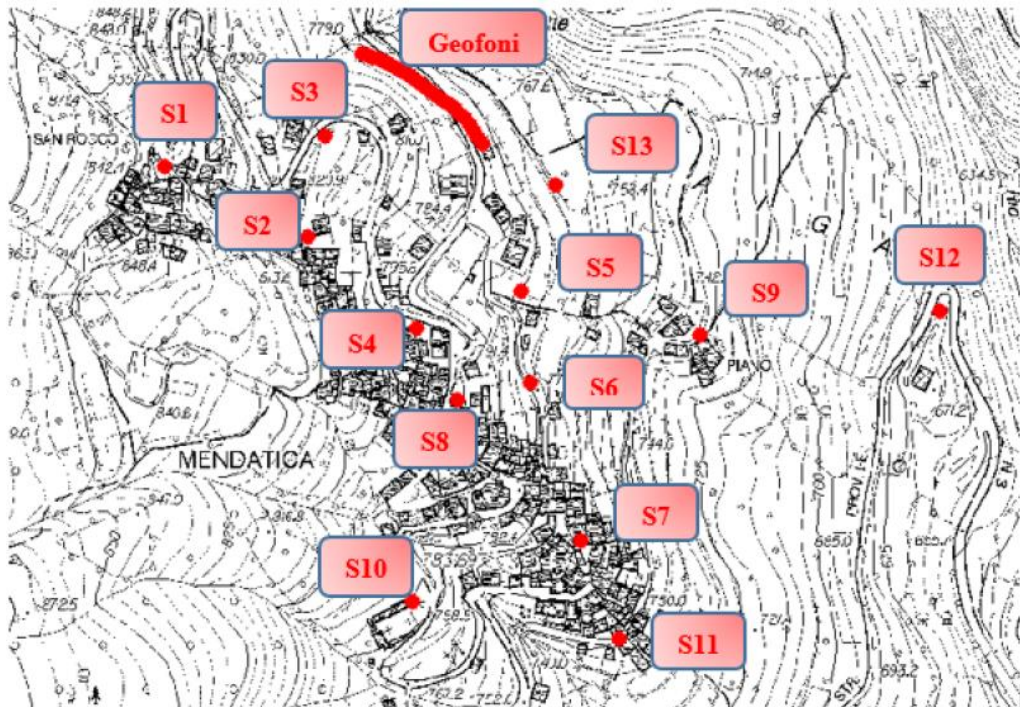


Figure 2.10. Monitoring network installed on Mendatica site in 2006.

Figure 2.10 shows the monitoring network designed in 2006. The instrumentation installed in 2006 consisted of 9 inclinometers, 4 piezometers, 13 rotary drilling cores for stratigraphy definition. For each of the 13 boreholes, SPT tests were performed at different depths. For each instrumented borehole, Table 2.1 resumes the investigated depth, the instrumentation type (i.e., inclinometer or piezometer) and the bedrock depth (Balestero, 2015).

Survey	z_drilling [m]	Inclinometer/Piezometer	z_bedrock [m]
S1	45	I	33
S2	24	I	19.5
S3	45	P	40.5
S4	40	P	33
S5	40	I	28.4
S6	45	P	37
S7	52.5	I	38.5
S8	50	I	37.8
S9	35	I	27.8
S10	40	I	29.7
S11	38.3	P	36
S12	25	I	18
S13	33	I	19.4

Table 2.1. Description of on-site instrumentation.

The Rock Quality Designation (RQD) test highlights a very variable bedrock rock quality, ranging from poor quality ($25\% < RQD < 50\%$) to fairly good quality ($50\% < RQD < 75\%$). Stratigraphic data revealed the occurrence of silty and clayey gravels with sand and clayey sand with gravel. However, the occurrence of interbedded and strong sandstone boulders was revealed.

Moreover, 3 down-hole tests and 1 refraction seismic survey were carried out. The down-hole tests were conducted in boreholes S2, S5 and S7 to obtain information on the subsurface physical-mechanical condition. The refraction seismic test, on the other hand, was used to verify if the claystone outcrops identified in the landslide deposit were rock portions involved in kinematic movement or stable portions that emerged due to post-erosion. It was conducted by means of 24 channel refraction seismic spreading of 125 meters; the results of the processing were obtained both with traditional method and by tomographic method for a better definition of the subsurface. It was therefore possible to identify a bedrock structural condition ranging from fairly good to good.

4 Lefranc tests have been performed to estimate the soil permeability (k_s). The tests have been carried out at S5, S6, S8, S9 and the results highlight a strong variability due to the soil heterogeneity (Table 2.2).

Survey	z [m]	k_s [m/s]
S5	13.5-14	3.82e-06
S6	33.1-34.2	1.35e-05
S8	18-19	1.60e-07
S9	16-16.5	3.37e-03

Table 2.2. Soil permeability values detected by Lefranc tests.

Geotechnical laboratory tests have been performed on S13 and S4 samples. Grain size distribution and Atterberg limits have been defined to classify the soil, according to the Casagrande plasticity chart. From the direct shear tests conducted, the friction angle obtained was 28° in S13, at depths between 8.65 and 9.0 m and between 16.35 and 16.70 m, and 30° in S4 (depths between 10.55 and 10.9 m and between 17.65 and 18.0 m). The synthesis of the laboratory results is shown in Table 2.3 (Macciò, 2007).

CAMPIONE			ANALISI GRANULOMETRICHE			CARATTERISTICHE INDICE					TAGLIO DIRETTO		
Sondaggio	Sigla	Profondità (m)	Ghiaia (%)	Sabbia (%)	Limo/Argilla (%)	Limite Liquido LL (%)	Limite Plasticoo LP (%)	Contenuto in acqua W (%)	Indice di Plasticità IP=LL-LP (%)	Indice di Consistenza IC=(LL-W)/IP	Peso di Vol.Nat. γ (kN/m ³)	Angolo d'Attrito ϕ' (°)	Coesione Efficace c' (kPa)
S4-Pz	C11	10,55+10,90	46,55	28,97	24,48	31,2	19,2	8,67	12,0	1,88	23,02	32,5	4,7
	C12	17,65+18,00	<i>Classificazione USCS: GC</i>			31,4	18,6	8,64	12,7	1,79	22,29	29,8	9,4
			32,13	39,77	28,10								
S13-I	C11	5,65+6,00	51,67	27,59	20,75	31,7	24,8	10,40	6,9	3,09	23,11	-	-
			<i>Classificazione USCS: GM</i>			<i>Carta della Plasticità di Casagrande:</i> Limi inorganici di media compressibilità e limi organici					<i>Prova di Compressione Semplice Ell.:</i> Resistenza a compressione $\sigma = 446,20$ kPa		
	C12	8,65+9,00	20,38	39,90	39,72	34,8	22,4	10,78	12,4	1,13	22,53	28	1,6
			<i>Classificazione USCS: SC</i>			<i>Carta della Plasticità di Casagrande:</i> Argille inorganiche di media plasticità							
	C13	16,35+16,70	24,48	35,71	39,81	31,4	23,5	9,28	7,9	2,8	22,42	28	5,1
			<i>Classificazione USCS: SM - SC</i>			<i>Carta della Plasticità di Casagrande:</i> Limi inorganici di media compressibilità e limi organici / Argille inorganiche di media plasticità							

Table 2.3. Laboratory results (Macciò, 2007).

In 2013, as a continuation of the geognostic investigation and to support the executive design of a new risk mitigation intervention, based on the use of automatic deep drainage techniques by means of Electro Pneumatic (ED) (Bomont 2008), pumping tests were conducted. The investigation was conducted in a dry period, in the absence of significant rainfall, in order to detect the groundwater level under critical conditions. The results obtained for the transmissivity, varying between 1e-06 and 1e-07, and the permeability coefficient, varying between 1e-06 and 1e-08, reveal the presence of sandy and clayey silts in the landslide deposit.

2.1.2. Monitoring activities

Inclinometer monitoring:

Since the inclinometer monitoring system was operational (2006), readings have not been made regularly, and the system presents some criticalities. In fact, in 2009 the breakage of several instruments placed in the active zone was detected, from 2009 to 2013 data were missing, in the subsequent period measurements recorded by the still active instrumentation, located in the dormant zone, are taken every 4-5 months. Moreover, in the first year of measurements, movements associated with instrumental errors are shown. The only exceptions were related to S1, S2, S5 and S9 boreholes, placed in the active area according to an alignment that starts from the Church of S. Rocco reaches Borgata Piano, where displacements of a few centimetres are recorded. In addition, few measurements recorded in 2008 indicated a deep movement, absent in S1 and present in S2, confirming the local positioning of the crown of the active landslide area in an intermediate position with respect to the two borehole locations. The southern portion of the historic center is outside the region of active landslide, since it has been subjected to effective consolidation works. Inclinometers S2, S5, S9, S12, aligned along the line of the maximum slope gradient, suggest the existence

of two sliding surfaces: the first one passing through S2 (-14.00), S5 (-20.00), S9 (-12.50) having the toe downstream of Borgata Piano (Section CC in Figure 2.11), and the second one passing through S2 (-14.00), S5 (-20.00), S9 (-27.50) and S12 (-13.5) having a toe in the Rio Cagnasso riverbed (Section AA in Figure 2.11).

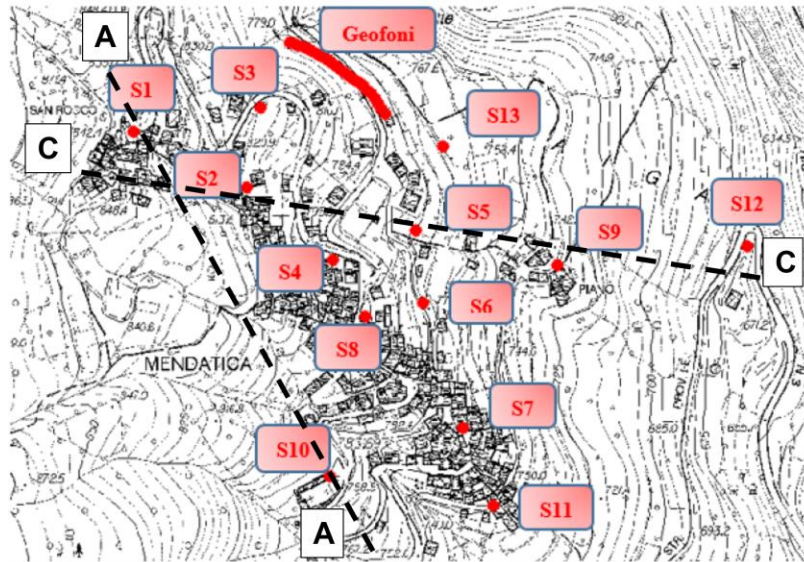


Figure 2.11. Most critical sections of the landslide.

The latter results to be more critical due to the erosive action carried out by the watercourse. In addition, the detected movement in correspondence of S10 borehole indicates an isolated, and probably secondary, kinematism in correspondence to the cemetery area, with a south direction, according to the river stream location (Section AA in Figure 2.11). The recorded data from the monitoring network allows to estimate a potential landslide area of approximately 550000 m², with a potential volume of approximately 9000000 m³. Furthermore, S12 breakdown between April and May 2013, in occurrence of intense rainfall, highlights the active state of landslide. However, the still working instrumentation appears to be located in the quiescent landslide zone and this can affect the obtained results. For this reason, new inclinometers were installed in 2015 in active zones.

Piezometer monitoring:

The instrumentation installed in 2006 consisted of 4 piezometers. In 2007, less than a year after the installation, the presence of two different oscillation frequencies was already noted: one was regular and independent from rainfall, with groundwater variations between 0.5 and 2 m, the other one was irregular and closely connected to rainfall, with variations between 5 and 11 m. All the piezometers recorded the presence of water, with groundwater levels falling into the landslide blanket.

A distinction can be made between the groundwater levels measured respectively in the piezometers S3 and S6 and those in piezometers S4 and S11 boreholes. In fact, the formers denote a deep steady groundwater level, whose variation can be correlated to the rainfall occurrence, with rising peaks relating

to particularly intense rainfall events, and also sensitive to seasonal variations, with excursions of the order of 20 m. The second group shows a groundwater level closer to the ground level, less subject to seasonal variations, but in occurrence of rainfall sudden GWT oscillations happen.

The hydrogeological model therefore presents different groundwater levels, separated or connected at different depths according to the investigated verticals. They are located in the more permeable soil, and they are recharged by infiltration during intense meteoric events. However, the low number of on-site instrumentations does not allow to perform a more accurate description of the hydrology conditions. In May 2013, no instrument was functioning because of instrumentation breakdown, due to landslide evolution. For this reason, new piezometers have been installed in the S4 and S11 surveys. Between June 2013 and April 2014, piezometric readings were conducted manually at intervals that did not allow adequate monitoring of the trend of the groundwater level: on average, two measurements were taken per month. From April 2014 to December 2016 measurements were carried out on the new piezometers installed in the S4 and S11 holes and in the PB and PC wells, with data acquisition at intervals of about 4 hours: they detected piezometric levels closer to the ground level due to the landslide evolution.

Figure 2.12 presents piezometric and rainfall measurements from 2007 to 2013. The stops in the measurements, due to the breakages of the instrumentation listed above, and the correlations between rainfall and groundwater variation are highlighted. Rainfall is plotted with the histogram (purple color), and refers to the scale in left ordinate; piezometric data (blue for S3, pink for S4, red for S6 and cyan for S11) are plotted with continuous line and refer to the scale in right ordinate. It is worth to underline that until 2015, no rain gauges were present on the Mendatica site. The analysis of the relationship between water table fluctuation and precipitation is carried out by choosing rain data recorded by rain gauges located in Pornassio, that is close to Mendatica.

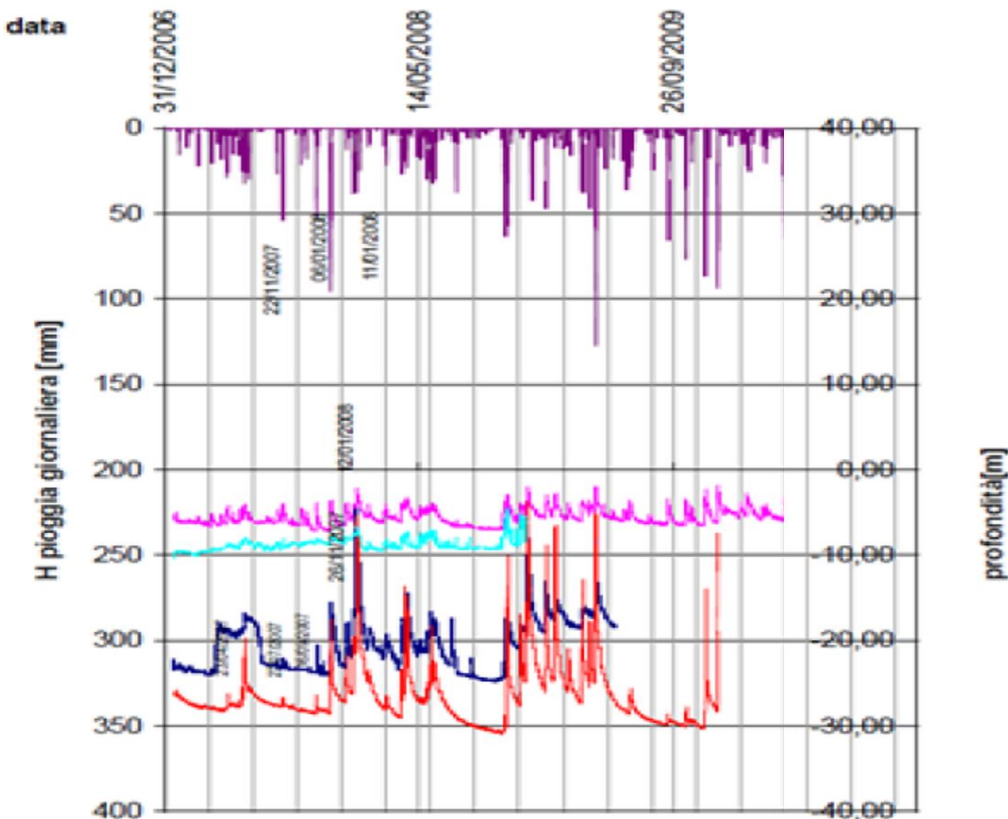


Figure 2.12. Diagram showing correlation between piezometric and rainfall measurements.

During the executive works for the construction of the deep drainage lines (Bomont, 2008), four new automated piezometers were installed, two to replace the damaged ones located in pipes S4 and S11 and two were installed in the PB and PC wells to monitor the groundwater level around the first row of vertical drains installed and activated. The PB and S11 piezometers, have been also equipped with water temperature recording. In addition, in order to monitor the water table level excursions in the area of Borgata Piano, where the second lot of sub-horizontal drains has been planned, 2 new piezometers, named S14 and S17, were realized. In addition, a geognostic campaign was carried out between March and April 2016, consisting of 10 boreholes. Automatic piezometers were installed in 8 boreholes (named S21-S24-S26-S27-S28-S29-S30-S31), which record the groundwater level in a pre-set time interval of 4 hours.

Therefore, the current overall piezometric monitoring network consists of the following instrumentation:

- n.13 automatic electric piezometers;
- n.5 hand-reading piezometers with phreatimeter;
- n.18 automatic piezometers installed in the vertical electropneumatic drains; this network is currently undergoing further development by carrying out additional draining lines in Mendatica center.

Crack gauges monitoring:

From July 2010 a system of cracking monitoring of the main structures is active. Some crack gauges have detected greater displacements in spring 2013 compared to the entire previous period (about two and a half years), proving a clear landslide reactivation. In some points located in the active zone, the crack thickness was exceeding the operable instrument range, equal to 25 mm along the horizontal and 10 mm along the vertical, making it in fact unusable.

GNSS monitoring:

In the frame of the AD-VITAM project, a single-frequency permanent GNSS monitoring system consisting of five stations (one reference and four rover) has been installed at the end of November 2019 in order to monitor the landslide displacements (Figure 2.13).

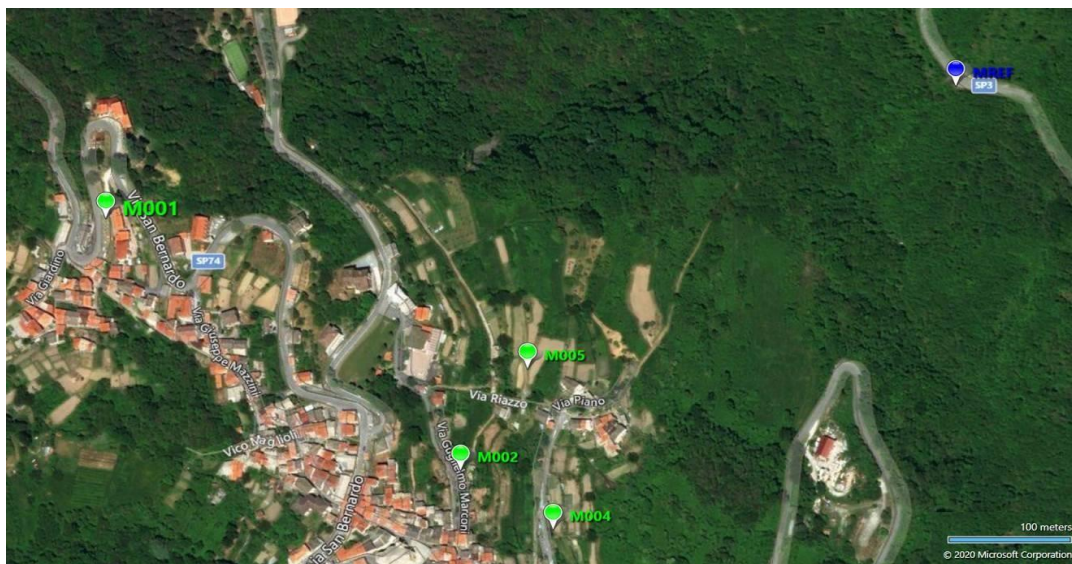


Figure 2.13. GNSS network installed on Mendatica site.

The reference station has been configured as the "gateway" of the local data transmission network via GPRS modem. The device receives GNSS observables and telemetry data from the four rover stations every 30 seconds and relays them, along with its own observables, to the remote computing software installed on a dedicated server. The computational software measures the relative displacements of the rover receivers with respect to the base in terms of offsets in the east, north, and altitude directions.

Displacements were observed after the main rainfall events, as showed in *Section 4.1* and *4.3*.

Soil Moisture monitoring:

In the framework of the AD-VITAM project, a sensor network for soil moisture measurements was installed on site by the University of Genova (Bovolenta et al., 2020). The network is composed by low-

cost and self-sufficient sensors, i.e. WaterScout SM100 capacitive probes properly calibrated and installed in the first meter of soil, at four different depths, along a vertical measuring line. This sensor arrangement corresponds to each measuring node in the network. The Mendatica network is composed of 5 instrumented nodes and one reference station (located on the church bell tower) for data storage and communication to/from the web service (Figure 2.14). The network is acquiring data from the end of November 2019.



Figure 2.14. soil moisture monitoring network installed at Mendatica.

2.2. Vence site

Vence is in the PACA (Provence-Alpes-Côte d'Azur) Region, in southern France and belongs to the Alpes-Maritimes Department. Its administrative borders coincide to the north with the Département des Alpes-de-Haute-Provence (AHP, 04), to the south-west with the Département du Var (84), to the south with the Mediterranean Sea and to the east with Italy (Figure 2.15).



Figure 2.15 Administrative boundaries of PACA Region.

The southern part of the Alpine mountain chain, due to its geographical and geomorphological configuration, is affected by a considerable number of landslides. In fact, the topography of the area is characterized by significant altimetric variations and steep slopes, while from a climatic point of view, there is a transition from typically Mediterranean to mountainous conditions within a few kilometres. Figure 2.16a shows the three different morphological zones, from north to south, that characterise the PACA region:

- the *area of the Pre-Alps of Nice and the Argentera-Mercatour massif*: a predominantly mountainous zone with altitudes of up to 3000 m a.s.l. and deeply incised valleys (zone A);
- the *middle zone* corresponding to the hinterland of Nice and Grasse, characterized by moderate-altitude reliefs oriented in an east-west direction (zone B);
- the *coastal zone*, flat and densely populated (zone C).

With reference to Figure 2.16a, the municipality of Vence is in the first hinterland of Nice, on the border between zone C and zone B. For this reason, according to the definition of landslide risk as the product between the hazard of the site, the type of exposed elements and their vulnerability, a high risk is associated with this area. This is explained by the simultaneous association between the high landslide occurrence probability and the high-density population here located Figure 2.16b.

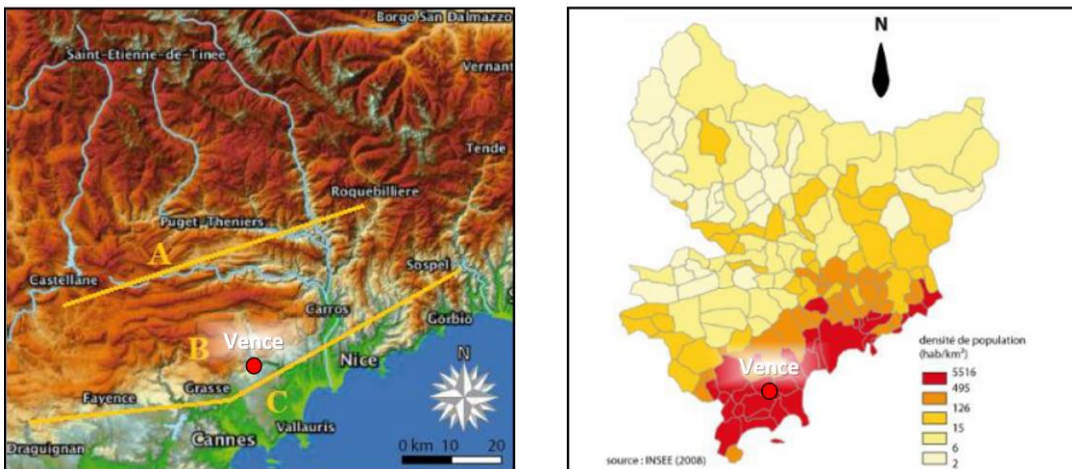


Figure 2.16 (a) Topographic map of the Maritime Alps, in which the three zones are identified: A: alpine zone, B: middle zone, C: coastal zone; (b) density population in the Alpes-Maritimes municipalities (INSEE 2008).



Figure 2.17. Hydrological network of the Southern Maritime Alps region
(<https://www.geoportail.gouv.fr/carte-IGN>).

Vence is located within the La Cagne catchment basin. The watercourse has a total length of 27.6 km and a catchment area extension of 96 km². Its main tributaries are La Lubiane and Le Malvan, with respective lengths of 7.3 km and 16.6 km. La Lubiane crosses Vence municipality and directly affects the portion under analysis, i.e., Le Prat de Julian (Figure 2.17). Concerning information on the hydraulic flow, values were obtained for the 100-year return period of 58 m³/s.

The case study here analysed concerns the neighbourhood of Prat de Julian, in Vence. The area is densely urbanised with a population density of 486 persons/ km² on 2013 (Institut National de la Statistique et des Etudes Economique, INSEE).

The Prat de Julian neighbourhood experienced its greatest urban development between the 1970s and the early 2000s, as evidenced by the installation of the sewage treatment station (STEP) in 1978 and the increasing number of houses (from 9 houses in 1970 to 17 in 1980 and 35 in 2000) until November 2000, when the most significant landslide event occurred (Figure 2.18).

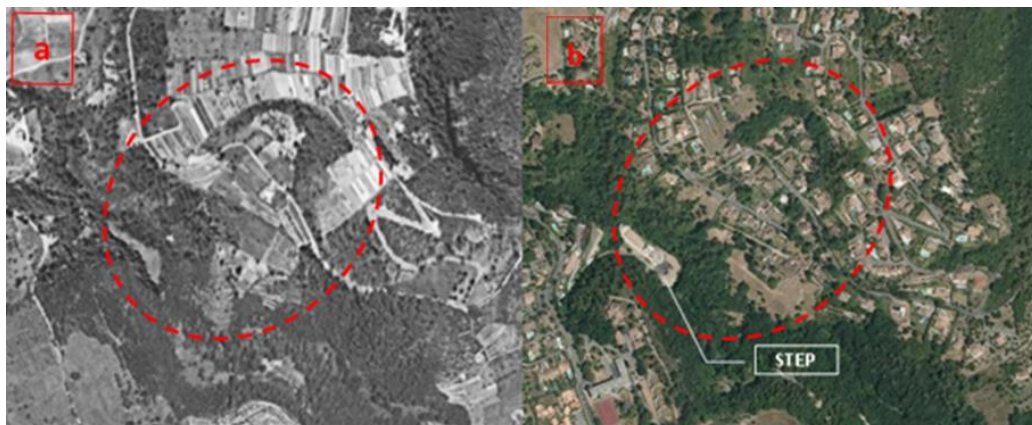


Figure 2.18 Aerial photo from 1950-1965 (a) compared with a current aerial photo (b)
(<https://www.geoportail.gouv.fr/carte-IGN>).

The acceleration of the landslide kinematics induced the obstruction of the “Lubiane” riverbed in October 1981 when an intense rainfall episode (250 mm in 24 hours) generated mud flows. Despite the observed movements, the urbanization still increased during the 90s and the sliding phases continued to occur, always associated with intense rainfall episodes (Lebourg et al., 2010)

Landslide affecting Prat the Julian can be classified as a rotational slide with a very flat sliding surface. The affected area develops with an NNE-SSW axis and is limited to the north by an escarpment varying in height between 15 and 30 m, and to the south by the course of the La Lubiane river. The landslide body involves a volume of approximately 1.2 million m³, with the main movement in the direction of the river with a mean slope angle varying from 12° to 14°; it has an almost circular shape with dimensions in plan equal to 350 m in length and 280 m in width; the highest point is located at approximately 220 m while the lowest point coincides with the bed of the Lubiane. Due to its volume, the Vence case represents one of the most important landslide movements in the PACA region.

According to the geological analysis of the site (Mangan, 1982) it can be stated that the origins of this movement are ancient and the absence of movement until the 20th century can probably be explained by a landslide dormant state. This landslide affects the Lower Eocene Biot sand formation, which rests on a Cretaceous marl and limestone bedrock and is outcropped by Middle Eocene sandstone limestone (Dardeau et al., 2010). In the study area, the facies correspond to yellowish to red continental sandy clays. These loose sandy-clay deposits show locally important facies variations in the form of clay lenses (Figure 2.19).

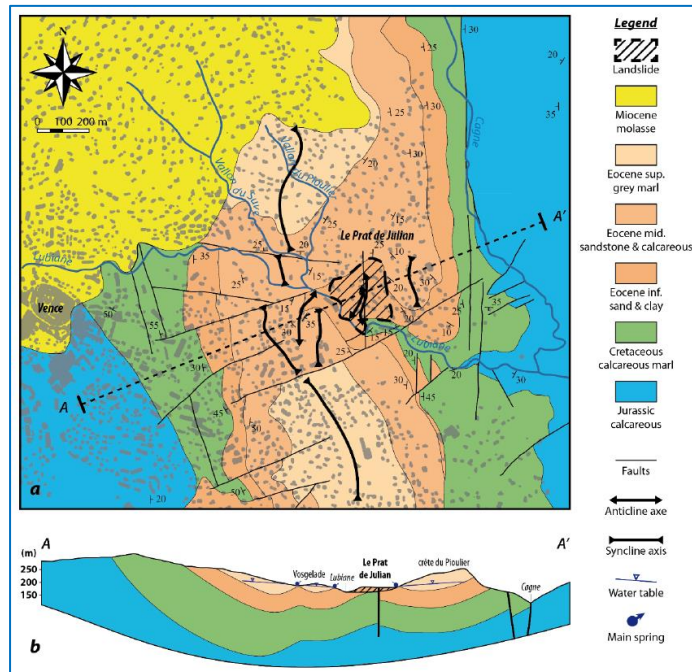


Figure 2.19. Geology of the Prat de Julian landslide area (Palis, 2017).

(a) Modified geological map after Mangan (1982) and Lebourg et al. (2010), with the distribution of the houses in the study area (source: IGN) (b) Cross-section along the AA' line with hydrological indications (main springs and groundwater location).

The landslide body (Figure 2.20) can be divided in three areas, that correspond to different degrees of activity over time, from upstream to downstream, characterized as follows:

- *zone c* (in yellow): shows a significant number of failures and represents the Landslide Detachment Zone, today strongly vegetated, and is characterised by significant inclinations (from 30° to 45°),
- *zone b* (in green): represents an intermediate plane with moderate slope (from 5° to 10°) that corresponds to the central part of the landslide body.
- *zone a* (in red): represents the zone at the slope foot, characterised by a frontal bank that locally deviates the course of the la Lubiane river that presents steep slopes (from 20° to 35°). Most of the gravity deformations observed on the Prat de Julian landslide since 1950 are concentrated in this area.

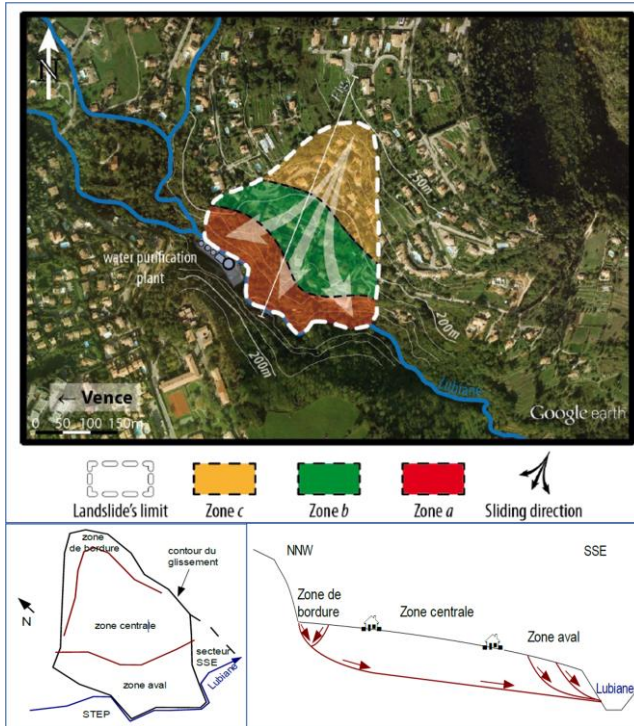


Figure 2.20. Aerial photo of the Prat de Julian landslide and areas of landslide activity (Palis, 2017).

Over the years, the correlation observed between the reactivation of the sliding and the occurrence of heavy rainfalls has made it possible to identify heavy rainfall as the main triggering factor. In fact, rainfall, through deep infiltration, can lead to changes in groundwater levels that affect slope stability conditions.

The movements that have affected the Prat de Julian since 1980 are characterised by slides, mudflows, small local landslides, obstruction of the La Lubiane river and small cracks in the houses (Figure 2.21), Figure 2.21a shows the chronology of the main damages occurred over the year. However, it was during the winter 2000-2001 that landslide activity reached the maximum intensity due to the severe rainfall event occurred (250 mm in 48 hours). Several landslides affected the upper (zone c) and lower (zone a) parts (according to the zonal definition showed in Figure 2.20) of the landslide body (Figure 2.21b). At the same time, some houses were damaged by the reactivation of slides close to the upper crown of the landslide. In the downstream area, many houses were evacuated, and some were definitively abandoned. The road suffered extensive damage. This inevitably led the Vence municipality to declare a state of calamity/natural disaster.

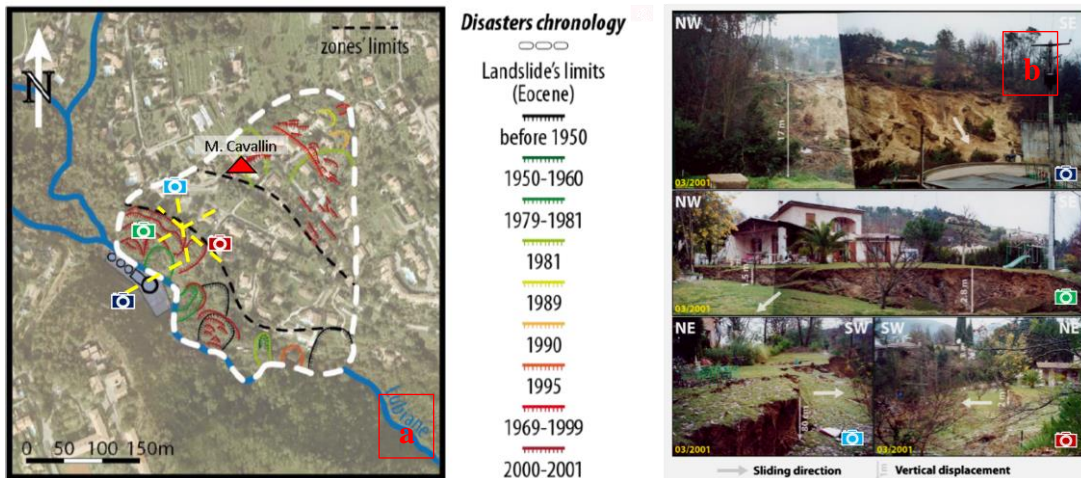


Figure 2.21. (a) Chronology of damages observed since the 1950s and (b) damages after the winter 2000-2001 rainfall event (Palis, 2017).

What happened at the beginning of 2001 confirms the importance of the landslide phenomenon and its activity. Although, overall, modest displacements are measured during relatively dry years, an intense event, e.g., one occurring every ten years, can lead to significant damages. Despite the lack of continuity in the topographic measurements, between 2002 and 2008-2010, low but not negligible displacements were observed in planimetry (4-5 mm/year depicted in plan in Figure 2.22), that show a slow drift oriented mainly in the S-SW direction.

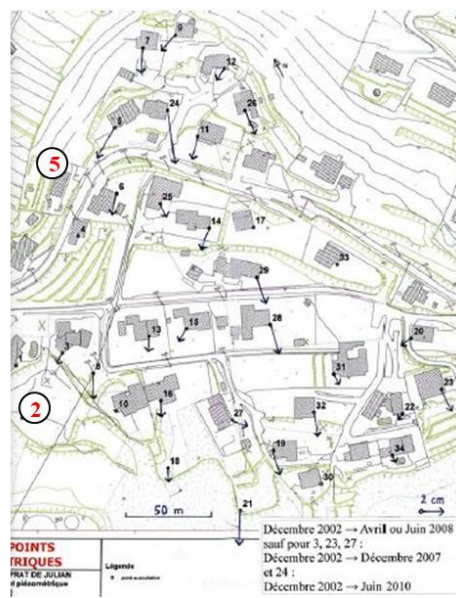


Figure 2.22. Planimetric displacement vectors of the buildings constructed in the area subject to movement (Besson & Durville 2012, Technical report).

In elevation, the results are more confusing and more difficult to be interpreted: in zone *a* at point 2, displacements of approximately 32 mm were measured, while in the upper part, zone *c* the registrations report 64 mm at point 5.

From the displacement analysis, it can be assumed that, in the presence of a new rainfall event, the dynamics of the events could be as described in the following. In *zone a* the slope could suddenly become unstable due to multiple simultaneous factors: the groundwater table rising to ground level, the total soil saturation and erosion at the foot performed by La Lubiane river. This would be followed by a continuation of the instability upstream, leading to a Prat de Julian landslide.

In 2005, in order to provide an effective solution for landslide risk mitigation, the Plan de Prévention des Risques Naturel (NPPR, Natural Hazard Prevention Plan) was approved, and the Prat de Julian district was classified as area at high landslide risk. Established in 1995, this Plan represents one of the fundamental tools for working on Natural Risk. The purpose for which it is drawn up is to establish measures of risk prevention, of vulnerability mitigation, to be implemented according to the estimated level of risk and the exposed elements considered, through the definition of one or more regulated zoning maps with annexed obligations to be fulfilled. In this contest, Prat de Julian has been zoning in red area, representing area with Major Risk (RM) with consequent regulatory restrictions: new construction is forbidden, except those devoted to risk reduction and works concerning outdoor areas (e.g., sport areas or green areas). Strict limitations are also introduced on existing building management, except in the case of maintenance works and demolitions, that can be authorised only between May and the end of September in order to avoid the wet season and the associate increasing of landslide risk. In the summer of 2015, the acquisition and demolition, by Vence municipality, of the houses located in the most critical area of the RM*, i.e., *zone a*, was carried out as can be noted by comparing Google Maps aerial photos before demolition (31/12/2004) and to the present day. In Figure 2.23a, red areas highlight the buildings demolished in July 2015 (Figure 2.23b).



Figure 2.23. Comparison of aerial photos after the PPRN (a) and before the 2015 (b).

2.2.1. Monitoring data

During the years, several experts and technicians, as well as researchers from the University of Nice and Sofia-Antipolis, have investigated and analysed the Prat de Julian landslide. Since the 2001, several study and geognostic campaigns have been carried out (1999, 2001, 2003, 2007, 2008, 2009) as well as landslide risk mitigation works have been proposed and realised (e.g., trench drains in zone a). Since 2006, monitoring instruments (meteorological station, piezometer, inclinometer) have also been permanently installed on site. In addition, several electrical tomography profiles were used to characterise the subsurface geometry of the area (Hernandez, 2009; Lebourg et al., 2010). These geological surveys allow the landslide volume characterisation in terms of both stratigraphy and physical-mechanical soil parameter definition, also performing back analysis, and hydrology.

The monitoring network installed at the end of 2009, was composed as follows (Figure 2.24)

- 5 boreholes at depths between 20 and 30 m (C1-C5);
- 12 boreholes at depths of 10 m (C10- C14, C16-C20);
- 5 drilling boreholes at depths of 10 m (C6-C7-C8i-C9i-C15i);
- drilling boreholes at depths of 30 m (D1-D5);
- permanent resistivity measurements on the lower part of the slide (ERT permanent 2006);
- ERT electrical resistivity measurements over the width of the landslide body (Lebourg et al.,2010);
- introduction of piezometers and inclinometers inside some boreholes (C7, C11, C6, C20);
- installation of an on-site meteorological station (blue point).
-



Figure 2.24 Monitoring network in 2009.

Geological and geotechnical data:

With reference to the dashed line shown in Figure 2.25, a typical geological section of the landslide volume can be observed. Thanks to the soil stratigraphy analyses, it was possible to identify three main soil layers with different geotechnical characteristics. The blanket consists of a sandy clayey soil, dating back to the Lower Eocene, with a depth of between 15 and 20 m, as demonstrated by the ERT investigations. The stable substrate appears to be composed of alternating layers of soft sandstone and limestone, belonging to the Cretaceous.

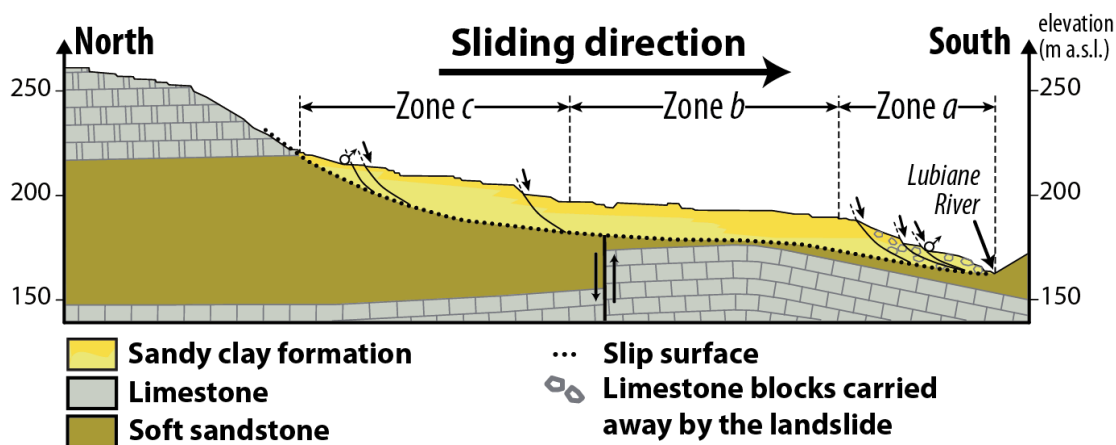


Figure 2.25 Typical geological section.

The physical-mechanical soil parameter, related to each soil layer, defined in the follows as Soil 1, Soil 2 and Soil 3, composing the slope volume are reported in Table 2.3, Table 2.4 and Table 2.5.

Soil 1	Sandy-clay formation
γ_{nat}	20 [kN/m ³]
φ'	10 [°]
φ' back analysis	14 [°]
c'	0 [kPa]
K_s	3.4×10^{-5} [m/s]

Table 2.3. Soil 1: mechanical and physical parameters

Soil 2	Soft sandstone
γ_{nat}	21 [kN/m ³]
φ'	30 [°]
c'	30 [kPa]
K_s	10^{-6} [m/s]

Table 2.4. Soil 2: mechanical and physical parameters

Soil 3	Limestone
γ_{nat}	23 [kN/m ³]
ϕ'	40 [°]
c'	50 [kPa]
Ks	10 ⁻⁶ [m/s]

Table 2.5. Soil 3: mechanical and physical parameters

Piezometric data:

The Prat de Julian area has been equipped with a continuous groundwater monitoring system since 2008, consisting by four piezometers. The piezometers named C11 and C7 were positioned in the upper part of the slope, zone c, while those named C6 and C20, in the slope downstream area, zone a. The measurements were carried out continuously over a period from mid-2008 to 2015. However, the time series are not comparable for all four instruments. In fact, piezometer C7 has not been active since the autumn of 2010, probably due to a failure, while C11 since the summer of 2012. Figures 2.26 show the time history of groundwater table (GWT) oscillation compared to the recorded rainfall. The GWT fluctuations are represented by the continuous line, one for each measurement point. It is possible to appreciate the recharge phase during the winter season and the progressive discharge until the dry summer period. Daily rainfall is represented by the histogram where the colour scale highlights the different reference rain gauge. In fact, the inconsistency in rainfall measurements is linked to the presence of rainfall measurement gaps due to breakdown of the meteorological station of the Prat de Julian. For this reason, the rainfall stations which were closest to the site were taken as reference. GeoAzur station is located about 23 km from Vence, while Carros station is 14 km away.

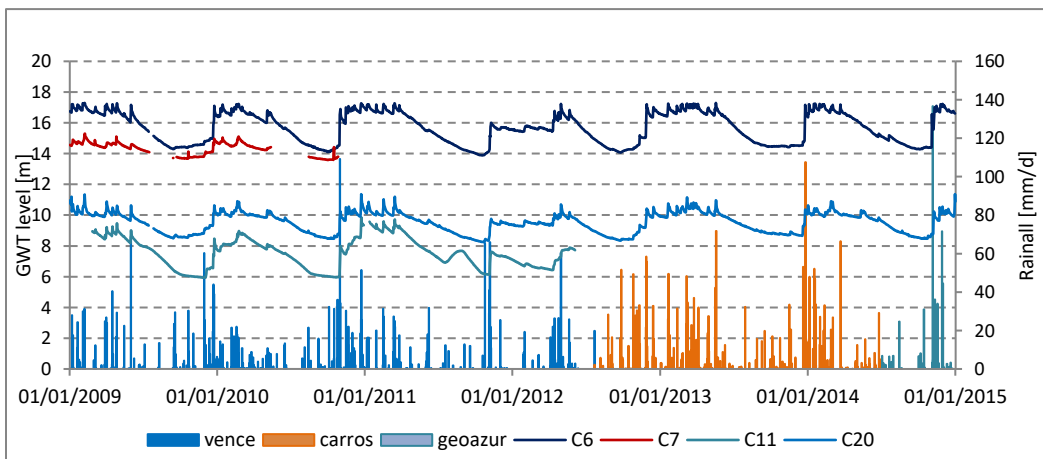


Figure 2.26 Comparison of the historical time-series of GWT variations due to rainfall.

Time history analyses allow the behaviour of the water table to be defined. First, an annual cyclic trend is revealed, characterised by a very rapid response to rainfall (at the daily scale) and indicating high soil permeability (Lebourg et al., 2010). During the winter period, due to the occurrence of several rainfall events, the groundwater level remains close to ground level for a few months, then a discharge phase to the

lowest level, is recorded in spring and summer times. Furthermore, Lebourg et al. (2010) highlighted that the groundwater oscillation is influenced by the presence of faults within the landslide body, thus playing a draining role. In fact, the probable presence of aquifers of karstic origin, in the deepest layers providing a recharge of the aquifer, reaching a saturated condition in occurrence of important rainfalls.

Installation of a new monitoring network:

The instrumentation described above is partially or totally in out of service. For this reason, in the frame of the ADVITAM project (2018), new installations have been carried out, improving the network with the development of the ERT line, the installation of a GNSS network and the replacement of the piezometers (C6 and C20) located in the zone a with two new instruments (C6 and C42).

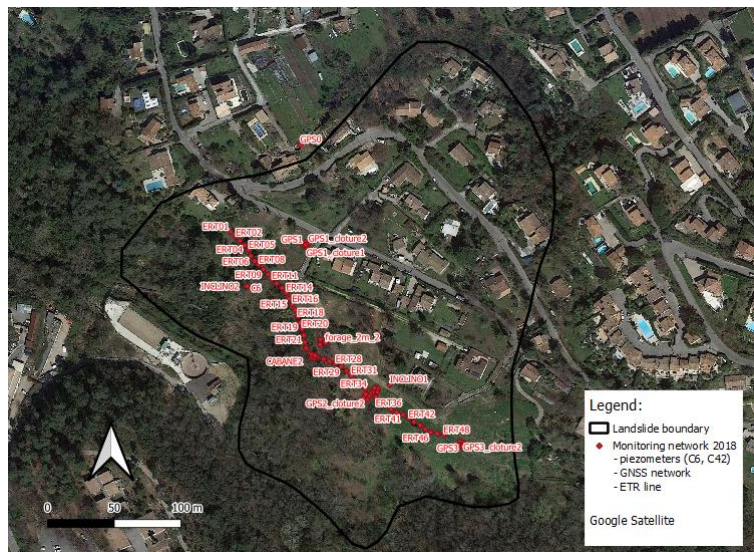


Figure 2.27 Monitoring network on 2018.

3. METHODOLOGY

3.1. INTEGRATED HYDROLOGICAL-GEOTECHNICAL (IHG) MODEL

The Integrated Hydrological-Geotechnical (IHG) model is a physically-based model that allows to assess landslide susceptibility to measured (and even forecasted) rainfalls, by establishing a cause-effect relationship between rainfalls and site-specific groundwater oscillations, hence the eventual occurrence of landslides (Federici et al., 2014; Passalacqua et al., 2015-2016).

IHG is designed to describe in near real time the landslide susceptibility (soil slides are considered) over areas of a few square kilometres, typically at scale 1:5000. The model needs to be fed by monitoring data (e.g., rainfall, temperature, soil water content), which vary both in space and time, so as to take into account the wetting condition of the soil and the water table oscillation. The IHG workflow is described in Figure 3.1.

The modelling is completely 3D, the spatialization being made possible through appropriate data interpolation and extrapolation methods from in situ investigations and geotechnical surveys (Passalacqua et al., 2013). The site characterization requires knowledge of piezometric measurements, stratigraphy, physical parameters, soil strength and permeability.

A Digital Terrain Model (DTM) discretizes the area of interest in pixels (usually 5m x 5m). The lower limit of the slope portion is given by the bedrock or stable layer surface, defined by knowing the stratigraphy and/or inclinometer monitoring, where present. Piezometric monitoring and proper interpolation/extrapolation allows to estimate the water table surface in steady conditions.

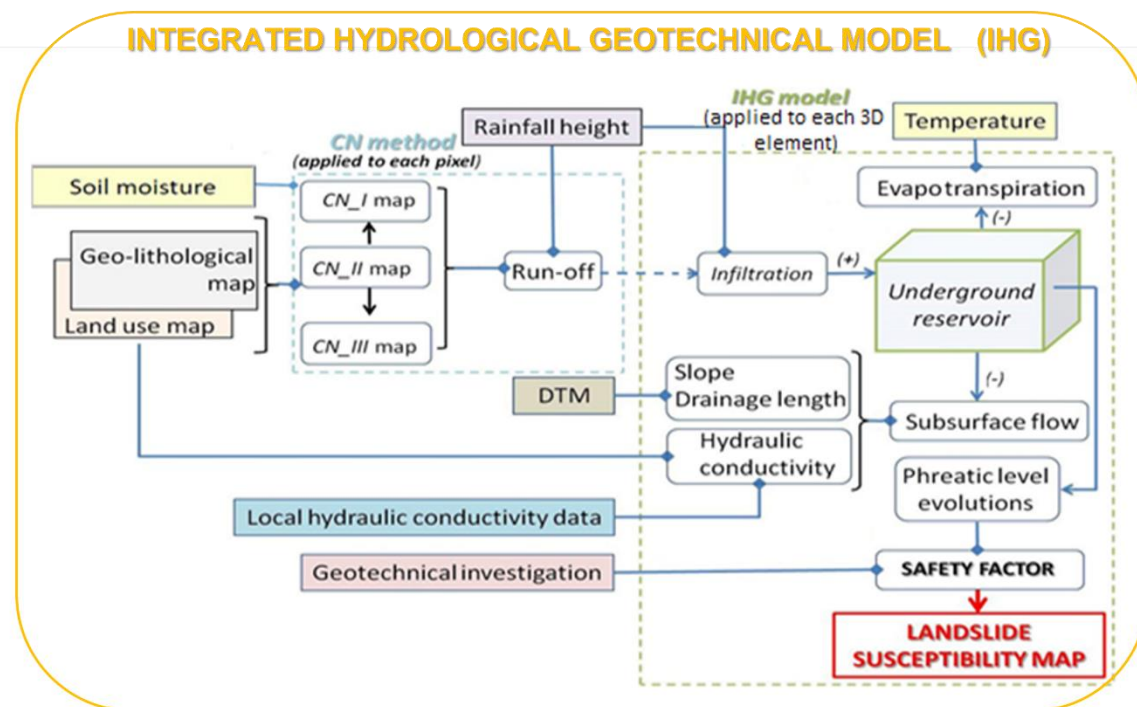


Figure 3.1. IHG workflow

The resulting landslide volume is subdivided into a series of three-dimensional elements, which behave like underground reservoirs to which a hydrological balance is applied. The input data are described by the boxes in Figure 3.1. Rainfall data can be derived from rainfall gauges or from meteorological radar. In the first case, data spatialisation on the study area is required, while in the second case the information is already spatially distributed. Infiltration, evapotranspiration and subsurface flow are estimated to reproduce the groundwater (GWT) fluctuations in response to the examined rainfall event, paying particular attention to the groundwater rising and descending phases. The infiltration into the soil is deduced by run-off evaluation applying the modified Curve Number method (Soil Conservation Service (SCS), 1972-1975; Passalacqua, 2002). Rainfall, geo-lithological/land-use maps and soil moisture are required as input data. The hydrological balance allows the hydraulic soil parameters (i.e. effective porosity and permeability) to be estimated by performing a point calibration, which will be explained in detail in *Section 3.1.2*, based on minimising the difference between measured and modelled GWT levels.

Once the water table resulting from the occurred rainfall has been determined, the model performs a stability analysis in effective stresses. The failure surface is defined by analysing the soil stability conditions with reference to each pixel and for different depths (generally every 1 m) down to the stable layer. The failure surface is defined at the depth with minimum safety factor in each pixel. Consequently, the whole failure surface can have a complex shape, determined by the failure depth pertinent to each pixel. In fact, the morphological, the hydro-geotechnical features and the loads may vary in the mass under study.

Based on the spatial variation of the safety factors, the final model products are maps of landslide susceptibility in the occurrence of a rainfall history and maps forecasting the susceptibility evolution on the expected short-term rain. In particular, maps that indicate the variation of the stability condition, enhancing the areas characterized by a safety factor < 1 after the examined event if previously stable, may be produced. All the maps in output are rendered choosing an appropriate colour table so to provide great immediacy even for not expert GIS users.

Thanks to the simplified modelling of the phenomenon, IHG is computationally light, hence applicable in near real time to model the site response to the occurring or forecasted rainfalls. A sliding mass, discretized by circa one million of voxels (5 m wide x 5 m length x 1 m depth), could be analyzed within 5–6 minutes by a standard computer.

More details on the hydrological modelling, the calibration phase and the slope stability analysis are in the following sections.

3.1.1 Hydrological model

The hydrological model is fundamentally based on a hydrological balance, which will be detailed below.

The runoff estimate is based on the empirical Curve Number (CN) method proposed by the Soil Conservation Service (SCS, 1972-1975) of the United States Department of Agriculture (USDA) and modified by Passalacqua (2002). Such method, dedicated to the evaluation of the runoff, allows also to estimate the infiltration rate.

The original Curve Number method follows the Horton method, based on a comparison between the infiltration curve and the rainfall histogram (Figure 3.2). The infiltration curve represents the characteristic

curve of the potential infiltration rate decreasing due to a complete filling of pores with water and the consequent attainment of complete soil saturation. With reference to Figure (3.2), considering a time-varying rainfall height $H(t)$, the portion of the histogram below the infiltration curve represents the initial abstraction (I_a) that corresponds to the rate of total rainfall infiltrating into the ground, for which runoff, denoted $R(t)$, does not occur.

$$R(t) = 0, \quad H(t) < I_a \quad (3.1)$$

Then, starting from the time $t > t_j$, the rainfall results to be higher than the infiltration curve and a rate of rainfall starts to runoff, while the rate F_a continues to infiltrate the soil. However, during the analysed rainfall event in Figure (3.2), in the interval $[t_{j+n}; t_{j+n} + \Delta t]$ the rainfall height does not reach the infiltration curve. In this case, runoff will not occur, only infiltration.

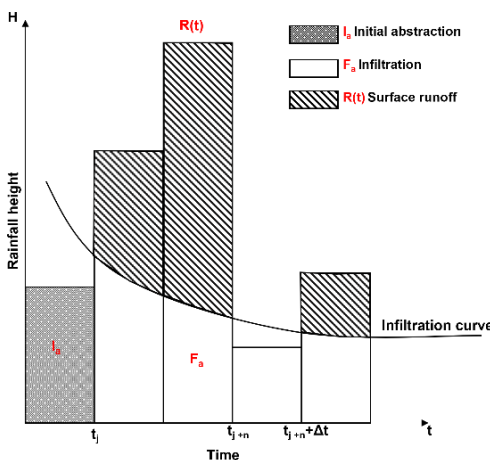


Figure 3.2 Description of the components of the Curve Number method (adapted from Horton, 1933; and SCS, 1972-1975).

The rainfall rate that infiltrates into the soil is given by the total rainfall height $H(t)$, reduced by the direct runoff quantity $R(t)$, estimated by Equation 3.2 and expressed in millimetres [mm].

$$R(t) = \frac{(H(t) - I_a)^2}{H(t) + S - I_a}, \quad H(t) > I_a \quad (3.2)$$

The runoff estimate follows the water balance equation (Equation 3.3) and the two assumptions (Equations 3.4-3.5) on which the SCS-CN method is based.

- Water balance equation:

$$H = I_a + F_a + R \quad (3.3)$$

- Proportional equality hypothesis:

$$\frac{F_a}{S} = \frac{R}{H - I_a} \quad (3.4)$$

- I_a -S hypothesis:

$$I_a = 0.2S \quad (3.5)$$

The first hypothesis establishes the equality between the ratio of infiltration (F_a) to potential maximum retention (S) and the ratio of direct surface runoff (R) to total rainfall (H) reduced by initial abstraction (I_a). The second hypothesis relates the initial abstraction (I_a) to the potential maximum retention S .

The potential maximum retention S is defined as follows:

$$S = 25.4 \left(\frac{1000}{CN} - 10 \right) \quad (3.6)$$

where:

25.4 is a value necessary to convert the result from inches to millimetres;

CN is the Curve Number value.

S is a dimensional quantity [L] that can vary in the range $[0; \infty)$. Equation 3.6 allows to calculate S as function of the Curve Number dimensionless parameter (CN), which varies in the range $[0; 100]$. Low CN values indicate vegetated areas, with a larger infiltration capacity, while high values indicate impermeable areas, where the surface run-off is more important. CN values are tabulated (e.g., Figure 3.3) according to the following site-specific characteristics: land use and hydrological soil conditions, grouped into four classes based on their minimum infiltration rate. According to SCS (1972-1975), the four Hydrologic Soil Groups (HSG) are defined as follows:

Group A. The soils exhibit high infiltration rates even when they are completely wetted, high rate of water transmission, and low runoff potential. Such soils include primarily deep, well-drained to excessively drained sands or gravels.

Group B. These soils have moderate infiltration rates when completely wet. They consist primarily of moderately deep to deep, moderately well drained to well drained, fine to moderately fine textures, e.g. shallow loess and sandy loam. These soils exhibit moderate rates of water transmission.

Group C. The soils have low infiltration rates when completely wet. These soils primarily contain a layer that prevents the downward movement of water. Such soils have a moderately fine to fine texture, such as clay loams, shallow sandy loam, and soils with low organic content. These soils exhibit slow rate of water transmission.

Group D. The soils exhibit very low rates of infiltration when they are completely wetted. Such soils are primarily clay soils of high swelling potential, soils with a permanent high-water table, soils with a claypan

or clay layer at or near the surface, and shallow soils over nearly impervious material. These soils exhibit a very slow rate of water transmission.

SCS TR-55 Table 2-2a – Runoff curve numbers for urban areas¹

Cover description		Curve numbers for hydrologic soil group			
Cover type and hydrologic condition	Average percent impervious area ²	A	B	C	D
Fully developed urban areas					
Open space (lawns, parks, golf courses, cemeteries, etc.) ³ :					
Poor condition (grass cover < 50%)		68	79	86	89
Fair condition (grass cover 50% to 75%)		49	69	79	84
Good condition (grass cover > 75%)		39	61	74	80
Impervious areas:					
Paved parking lots, roofs, driveways, etc. (excluding right-of-way)		98	98	98	98
Streets and roads:					
Paved; curbs and storm sewers (excluding right-of-way)		98	98	98	98
Paved; open ditches (including right-of-way)		83	89	92	93
Gravel (including right-of-way)		76	85	89	91
Dirt (including right-of-way)		72	82	87	89
Western desert urban areas:					
Natural desert landscaping (pervious areas only) ⁴ ..		63	77	85	88
Artificial desert landscaping (impervious weed barrier, desert shrub with 1- to 2-inch sand or gravel mulch and basin borders)		96	96	96	96
Urban districts:					
Commercial and business	85	89	92	94	95
Industrial	72	81	88	91	93
Residential districts by average lot size					
1/8 acre or less (town houses)	65	77	85	90	92

Figure 3.3. Example of CN table. The values are relative to the description of the urban area and associated according to the four different HSGs.

The CN values (hereafter CN(II)) in Figure 3.3 are referred to intermediate soil wetting conditions according to the soil Antecedent Moisture Condition (AMC) definition. The AMC estimate is based on the

knowledge of the Antecedent Precipitation Index (API) calculated over the antecedent 5-day rainfall as used in the National Engineering Handbook (SCS, 1971). AMC is categorized into three levels AMC I, AMC II and AMC III. AMC I describes a dry soil condition, which allows the highest infiltration rate and, in turn, the lowest runoff rate. On the other hand, AMC III indicates an almost completely wet soil situation, which produces the lowest infiltration rate and, in turn, the highest runoff rate. AMC II refers to the average condition, standing between the two extreme states. It is possible to describe the AMC condition as function of the tabulated CN(II), by introducing two additional CN values (Equations 3.7- 3.8): CN(I), corresponding to AMC I, refers to dry soil condition or lowest runoff potential, while CN(III), corresponding to AMC III condition, refers to wet soil condition and consequently to the highest runoff potential.

$$CN(I) = \frac{4.2 CN(II)}{10 - 0.058CN(II)} \quad (3.7)$$

$$CN(III) = \frac{23 CN(II)}{10 + 0.13CN(II)} \quad (3.8)$$

The S variation can then be calculated as function of the three CN values, using Equation 3.6, thus taking into account the wetting conditions occurring during a rainfall event. The following relationships between the CN values calculated under the three AMC conditions, and consequently between the values of S, exist:

$$CN(I) < CN(II) < CN(III), \quad S(I) > S(II) > S(III)$$

An example of produced CN(II) map is shown in Figure 3.4 referred to Vence site. The lithological map (on the left), detailed in *Section 3.1.1* and the land use map (on the right) represent the input data. CN(II) values are associated to different areas according to HSG class and land use definition, the latter defined with respect to Corine Land Cover (CLC) specifications (proposed for the Vence site in the Mode d'Occupation du Sol (MOS) by Autran J., 2007).

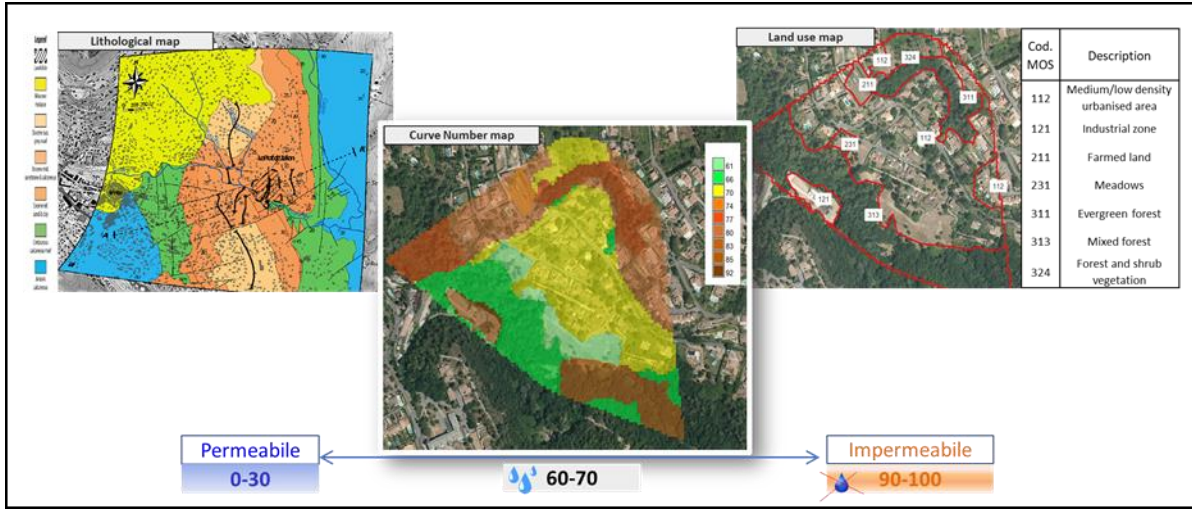


Figure 3.4. Vence: Curve Number Map (middle) generated by the lithology map (left) and of land use map (right)

The SCS method requires the use of cumulative precipitation values (USDA NRCS, 2004) when the length of the precipitation event exceeds the temporal scale of the analysis, usually daily or at most hourly. In other words, for a time step t_i rainfall is given as the sum of all rainfall heights from the beginning of the event. In this way, it is possible to calculate the runoff “having memory” of the rainfall in the previous time steps using Equations 3.9 - 3.11.

$$H_n^{cum} = \sum_{i=1}^n H_i \quad (3.9)$$

$$R_n^{cum} = \frac{[H_n^{cum} - 0.2S]^2}{H_n^{cum} + 0.8S} \quad (3.10)$$

$$R_n = R_n^{cum} - R_{n-1}^{cum} \quad (3.11)$$

The Modified Curve Number method (Passalacqua, 2002), compared to the original method, allows the estimate of the infiltration rate and the subsurface flow. Each 3D volume element, which characterises the landslide body in the GIS environment, is associated with an underground reservoir, with a thickness equal to the depth between ground level and bedrock/stable substrate, each with its own storage capacity S , depending on the associated CN value. The reservoirs are assumed to be independent and not influenced by adjacent cell subsurface flow. In accordance with the SCS method, the S value is expressed in terms of equivalent water height [mm] since, from a dimensional point of view, it corresponds to a height per unit area.

For each volume element, Figure 3.5 shows the quantities involved in the hydrological balance, rainfall is the only input data (orange arrow) and, depurated of the runoff quantity, provides the infiltration rate (blue arrows), triggering the GWT fluctuations, while the outgoing quantities (run off, evapotranspiration,

subsurface flow) are identified with a red arrow. It is worth underlining that the hydrological balance is performed in terms of water volume, as indicated in Equation 3.12.

$$V_{1+i} = V_i + \sum V_{i+1}^{in} - \sum V_{i+1}^{out} \quad (3.12)$$

where the volume of water at the end of the $i+1^{\text{st}}$ day is the result of the algebraic sum of V_i , representing the initial water volume, and the incoming ($\sum V_{i+1}^{in}$) and outgoing ($\sum V_{i+1}^{out}$) quantities at the end of the analysed day.

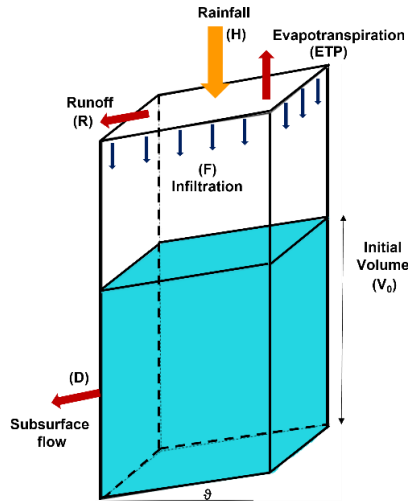


Figure 3.5. Representation of the typical volume element that discretizes the landslide body and the hydrological balance components acting on it.

In Figure 3.5, V_0 represents the initial saturation height of the reservoir draining by gravity along the maximum slope line. In the GIS procedure, V_0 is obtained as difference in height between the groundwater and bedrock 3D models.

The subsurface flow Equation 3.13 is described through an emptying function typical of linear reservoirs, ruled by an exponential function of λ (Figure 3.6), which is the discharge constant representative of the basin (Passalacqua, 2002). In Equation 2.13, Δt is the emptying time, V_t and $V_{t+\Delta t}$ are the water volumes present at the time t and $t+\Delta t$.

$$V_{(t+\Delta t)} = V_{t+\Delta t} (e^{-\lambda \Delta t}) \quad (3.13)$$

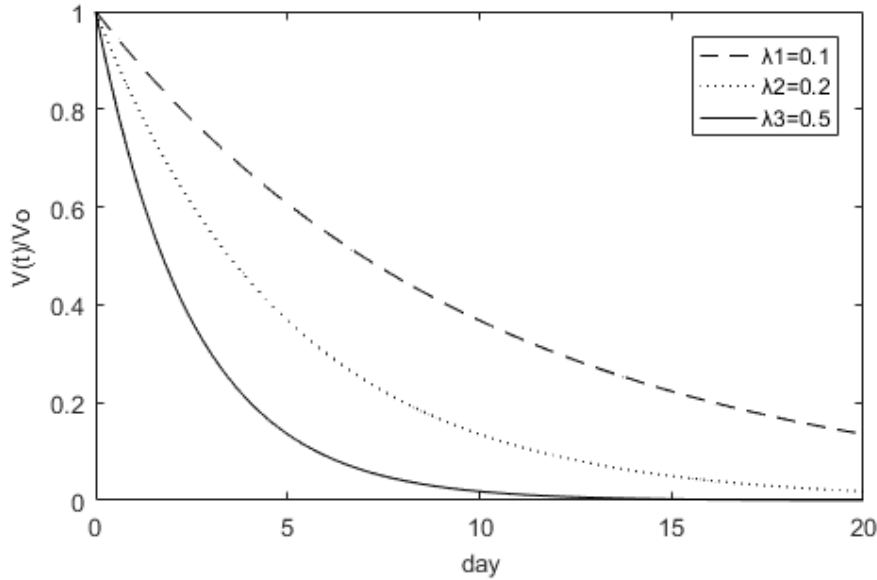


Figure 3.6. Linear reservoir discharge function varying λ - emptying constant [1/g].

The linear behaviour hypothesis is adopted, so that the time required for the linear reservoir to halve its water volume (i.e., the half-life time) in the absence of supply is a characteristic of the system, independent of the reservoir conditions. Adapting the parameters for $t_{1/2}$ to the depletion function, it is possible write Equation 3.13 as Equation 3.14:

$$\frac{V_t}{2} = V_t e^{-\lambda t_{1/2}} \quad (3.14)$$

and λ can be obtained (Equation 3.15):

$$\lambda = - \frac{1}{t_{1/2}} \ln(1/2) \quad (3.15)$$

At the basin scale, the emptying constant can be evaluated directly, either through the use of flow meters placed in the final section of the streams, or through the use of mathematical approaches, based on the continuity equation and the Darcy law. The emptying constant is thus a function of the soil permeability (K_s), the driving slope (i) and the drainage length (L). In the Passalacqua method (2002), the emptying constant is considered to be unique for the entire basin considered. However, differently from (Passalacqua, 2002), in the IHG model, the constant λ is calculated with reference to each 3D element composing the study area, through Equation 3.16:

$$\lambda = \frac{K_s i}{L} = \frac{K_s \sin \vartheta}{D \cos \vartheta} = \frac{K_s}{D} \tan \vartheta \quad (3.16)$$

here:

- K_s [m/s] is the soil permeability;
- i [$^{\circ}$] is the slope gradient, calculated by the DTM, as the sine of the angle ϑ between the maximum slope direction and the horizontal plane;
- L [m] is the drainage length that corresponds to the pixel resolution (D) multiplied to the cosine of the angle ϑ between the maximum slope direction and the horizontal plane.

According to the Modified Curve Number method, the input volume per unit area (V_{in}) is given by Equation 3.17 as the difference between rainfall height (H) and runoff estimate (R):

$$V_{in} = V_{in}^{net} = H - R = H - \frac{[H - 0.2S]^2}{H + 0.8S} \quad (3.17)$$

Equation 3.17 provides a net rainfall height, in terms of volume, without considering soil presence. The infiltrated volume, in terms of height per unit of area, will be greater if we consider the real volume employable by the water in the soil. For this reason, to evaluate the real volume height variation due to the infiltration process, the geotechnical porosity parameter is introduced in the modelling. The porosity is expressed as the ratio between the volume of voids and the total soil volume (Equation 3.18).

$$n = \frac{V_v}{V_{tot}} < 1 \quad (3.18)$$

However, it should be noted that this parameter is not able to represent the gross infiltrated rainfall height physical phenomenon. In fact, due to the porous nature of the soil, two are the present void types: the isolated voids, in which no water flow is possible, and the interconnected ones, in which water flow is permitted. In context of the infiltration processes representation, the parameter of interest is the effective porosity n_e , also called specific yield S_y , defined as the ratio of the volume of the interconnected voids to the soil total volume. Specific yield (Equation 3.19) is defined as the ratio of the volume of water that a saturated rock or soil will yield by gravity to the total volume of the rock or soil. Specific yield is usually expressed as a percentage (Johnson, 1967).

$$n_e = S_y = \frac{V_{v,con}}{V_{tot}} < n \quad (3.19)$$

The specific retention parameter (S_r) describes the amount of water in the isolated (or unconnected) voids that cannot drain. This term is defined as the ratio of the retained water volume to the total volume (Equation 3.20). The specific retention can also be computed as the difference between soil porosity and specific yield (Equation 3.21).

$$S_r = \frac{V_{uncon}}{V_{tot}} < n \quad (3.20)$$

$$S_r = n - S_y \quad (2.21)$$

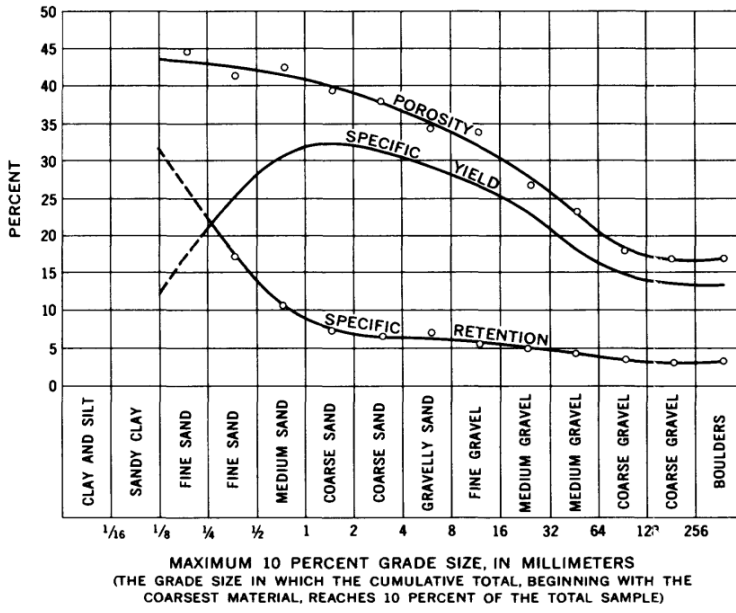


Figure 3.7. Porosity, Specific yield and Specific retention trend (Johnson, 1967)

Figure 3.7 shows the distribution of the parameter described by Equations 3.18-3.21, for different soil types. It highlights as for coarse-grained soils (e.g., clean sands or gravel) the reduction in effective porosity compared to total porosity is small. This is due to the fact that, in these types of soils, most of the voids are interconnected and allow the water drainage. On the other side, fine-grained soils are characterised by lower values of effective porosity compared to the total one. This is due to the soil structure, composed mainly by unconnected voids.

By introducing the effective specific yield (S_y), in the following defined as soil effective porosity (n_e), the infiltrated rainfall height is defined as follows (Equation 3.22):

$$V_{in}^{gross} = \frac{V_{in}^{net}}{n_e} > V_{in}^{net} \quad (3.22)$$

The application of the hydrological balance also requires the estimate of evapotranspiration (Figure 3.8), in the following named E. It is well known that the definition of this quantity may not be simple, due to the lack of observed data. In literature different models are proposed for its evaluation, based on simple associations/combinations of meteorological variables, extraterrestrial radiation or mean daily temperature. In particular, previous works have shown that temperature-based models allow a good estimate of

evapotranspiration (Oudin et al., 2005). In the IHG model evapotranspiration is estimated using the Hargreaves and Samani equation (1982), a temperature-based model where the main input data are the maximum and minimum daily temperature, deriving from local meteorological station measurements, Equation 3.23.

$$E = 0.0135K_T(T_{med} + 17.8)R_a\sqrt{T_{max} - T_{min}} \quad (3.23)$$

Where:

0.0135 is a factor for conversion from American to the International System of Units (Gafurov et al., 2018)

K_T = is the radiation adjustment. It is an empirical coefficient originally set equal to 0.17, then modified and set equal to 0.162 for internal regions and 0.19 for coastal regions.

T_{med} = average temperature of day

T_{max} and T_{min} = maximum and minimum daily temperatures

R_a =extraterrestrial radiation [mm/day], estimated by Equation 3.24

$$R_a = \frac{1440}{2.43\pi} G_{sc} d_r (w_s \sin \varphi \cos \delta + \cos \varphi \cos \delta \sin w_s) \quad (3.24)$$

where:

1440 and 2.43 are constants used to convert the results from [MJ/mq/min] to [mm/day]

G_{sc} = solar constant equals to 0.082 [MJ/mq/min]

φ = latitude [rad]

d_r = correction factor for the eccentricity of the Earth's orbit around the Sun, estimated by Equation 3.25

$$dr = 1 + 0.033 \cos\left(2\pi \frac{day}{365}\right) \quad (3.25)$$

w_s = hour angle, calculated using Equation 3.26

$$w_s = \cos^{-1}(-\tan \varphi \tan \delta) \quad (3.26)$$

where δ is the solar declination, estimate according to Equation 3.27

$$\delta = 23.45 \frac{\pi}{180} \sin \left[2\pi \frac{(284+day)}{365} \right] \quad (3.27)$$

The main quantities composing Equation 3.23 are represented in Figure 3.8, related to one year of rainfall measurements (2020) in Ceriana, represented by the histogram. Specifically, the daily maximum, average and minimum temperature values are represented by the orange, grey and yellow curves, respectively. The blue curve represents the extraterrestrial radiation (Ra) calculated through Equation 2.24 and it is described by a maximum corresponding to the summer season, followed by a decrease that reaches the minimum in the winter season with comparable average values, around 5 mm/day, between December and January. Finally, the green points represent the daily evapotranspiration value, estimated by Equation 3.23 and here multiplied by ten for a better representation, which, being a function of temperature, reaches the highest values between June and August.

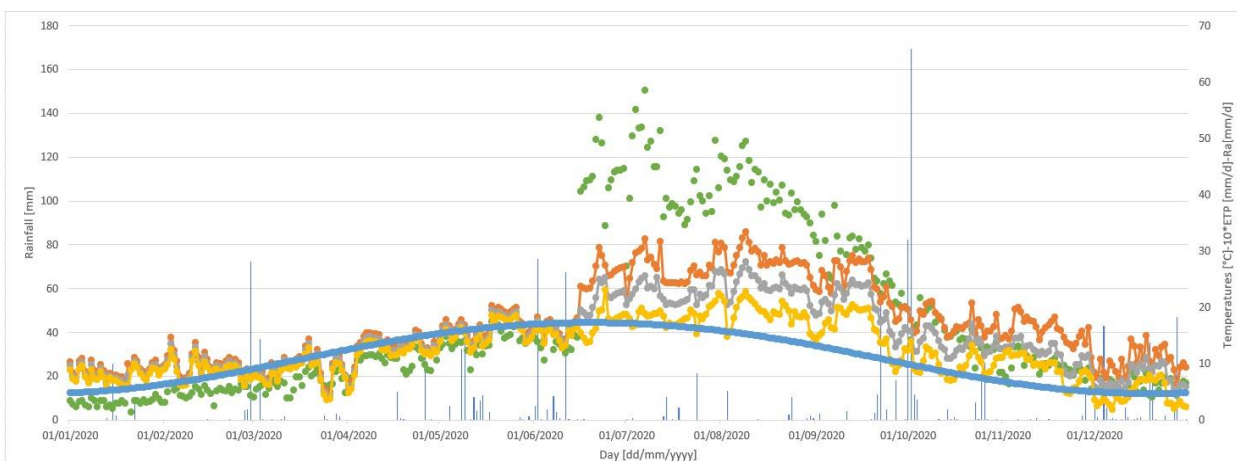


Figure 3.8. Ceriana (IM, Italy): Trend over one year (2020) of the main quantities composing the Hargreaves and Samani equation: the histogram represents the daily rainfall, the daily maximum, average and minimum temperature values are represented by the orange, grey and yellow curves, respectively; the blue curve represents the extraterrestrial radiation; evapotranspiration is represented with green points and multiplied by 10 for a better visualization.

To estimate the subsurface flow (Equation 3.28) it is necessary to transform the discharge process, which is continuous in time, into a concentrated quantity to be subtracted at a precise moment in time. Considering an analysis on a daily scale ($\Delta t = 1$ day), this instant can be made to coincide with the end of one day and the beginning of the next.

$$D_{i-1} = V_{i-1}(1 - e^{-\lambda}) \quad (3.28)$$

With reference to the i -th day, assuming that the underground flow involves the portion of the volume of water already present in the reservoir at the beginning of the day, this results in Equation 3.29:

$$V_{in,i}' = V_{in,i}^{net} - D_{i-1} \quad (3.29)$$

Hydrological modelling is based on the assumption that subsurface flow between adjacent reservoirs is neglected. In order to reduce the error associated to this assumption, together with the introduction of the effective porosity quantity, a new quantity P' is now introduced. Furthermore, an appropriate calibration of the parameters (as will be explained in the following) will make it possible to refine the simulations of the water table, compensating for the aforementioned simplifying assumption.

The fictitious rainfall P' is representative of the amount of rainfall that would have to fall during the day in order for a volume equal to V' to enter the reservoir.

Hence, the following relations, represented in Equations (3.30) -(3.31), are valid:

$$V_{in,i}' = P_1' - R_1' = H_1 - R_1 - D_0 \quad (3.30)$$

where:

P_1' = fictitious rainfall

R_1' = runoff associated to the fictitious rainfall

D_0 = initial subsurface flow, estimated by Equation (3.28)

Equation 3.30 holds the soil state in memory, allowing V_{in} to be considered uniquely as a function of Equation 3.31, where H and R are fictitious.

$$V_{in,i}' = P_1' - R_1' = P_i' - \frac{[P_i' - 0.2S]^2}{P_i' + 0.8S} \quad (3.31)$$

Isolating the parameter P' yields:

$$P_i' = H_i - R_i - D_{i-1} \quad H_i - R_i - D_{i-1} < 0.2S \quad (3.32)$$

$$P_i' = \frac{0.04S^2 + 0.8S(H_i - R_i - D_{i-1})}{1.2S - (H_i - R_i - D_{i-1})} \quad H_i - R_i - D_{i-1} > 0.2S \quad (3.33)$$

Using fictitious rainfall instead of actual rainfall makes it possible to consider the runoff contribution directly into the incident rainfall. Consequently, the fictitious rain is always lower than the actual rainfall.

At the end of the day, knowing the input and output quantities, the water volume in the reservoir is obtained by applying the continuity equation as presented in Equation 3.12.

The formulation of the modified CN method applied to rainfall events of length N days follows.

The cumulative rainfall (relative to the fictitious rainfall) over a window of N days is calculated as:

$$H_{c,N} = H_N + \sum_{j=1}^{N-1} P'_j \quad (3.34)$$

The eventual runoff on day N and cumulated to the same day is estimated as:

$$R_{c,N} = \frac{[H_{c,N} - 0.2S]^2}{H_{c,N} + 0.8S} \quad (3.35)$$

$$R_N = R_{c,N} - \sum_{j=1}^{N-1} R'_j \quad (3.36)$$

The cumulated volume actually entering the reservoir is equal to:

$$V_{in(c),N}' = H_{c,N}' - R'_{c,N} = H_{c,N} - R_{c,N} - D_{N-1} \quad (3.37)$$

The fictitious cumulative rainfall for the N-th day, knowing the value of $V_{in(c),N}'$, is derived from:

$$H_{c,N}' = H_{c,N} - R_{c,N} - D_{N-1} \quad H_{c,N} - R_{c,N} - D_{N-1} < 0.2S \quad (3.38)$$

$$H_{c,N}' = \frac{0.04S^2 + 0.8S(H_{c,N} - R_{c,N} - D_{N-1})}{1.2S - (H_{c,N} - R_{c,N} - D_{N-1})} \quad H_{c,N} - R_{c,N} - D_{N-1} > 0.2S \quad (3.39)$$

Therefore, the fictitious rainfall for the single N-th day is given by the following relation:

$$H_N' = H_{c,N}' - \sum_{j=1}^{N-1} P'_j \quad (3.40)$$

The volume infiltrated into the reservoir due to the only rainfall is equal to:

$$V_{in(c),N}' = H_{c,N} - R_{c,N} - \sum_{j=0}^{N-2} D_j \quad (3.41)$$

The water volume contained in the reservoir at the end of day N results in:

$$V_N = V_0 - D_{N-1} - \sum_{j=1}^N E_j + \frac{V_{in(c),N}'}{n_e} \quad (3.42)$$

Where:

- V_N is the water volume at the end of the pertinent N-th rainfall day
- V_0 is the initial water volume (day 0) respect to which the balance is performed
- D_{N-1} is the subsurface flow outcomes from the reservoir
- $\sum_{j=1}^N E_j$ is the summation of daily evapotranspiration contributions
- $V_{in(c)}$ is the volume of water infiltrated into the soil due to the rainfall;
- n_e is the effective porosity, introduced in the hydrological formulation to take into account the hydraulic soil properties that influenced the rainfall infiltration behaviour.

To summarized, the input data, the derived variables and the calibrated parameters involved in the hydrological model are summarized in Table (3.1).

Input Data			Derived variables			Calibrated parameters		
Parameter	Symbol	u.m.	Parameter	Symbol	u.m.	Parameter	Symbol	u.m.
Curve Number 2	CNII	[-]	Curve Number 1	CN I	[-]	Soil effective porosity	n_e	[-]
Slope angle	θ	[°]	Curve Number 3	CN III	[-]	Soil permeab	k_s	[m/s]
Rainfall	H	[mm/day]	Maximum storage capacity (CNI)	S I	[mm]			
Evapotranspiration	E	[mm/d]	Maximum storage capacity (CNII)	S II	[mm]			
Initial GWT level	H_{GWT}	[m]	Maximum storage capacity (CNIII)	S III	[mm]			
Resolution	D	[m]	Cell length	L	[m]			
			Discharge constant	λ	[1/d]			

Table 3.1. Parameters involved in the hydrological calibration

For each rainfall event identified, the analysis is carried out with reference to the groundwater level of the first day of the considered event. With reference to *Section 3.1.1.*, the equations for all variables evaluated at the time i in the modelling are given below:

- Cumulative evapotranspiration [mm]:

$$E_{cum} = E_i + E_{i-1} \quad (3.43)$$

- Cumulative rainfall (taking into account effective rainfall) [mm]:

$$H_{cum} = H_i + P'_{cum,i-1} \quad (3.45)$$

- Cumulative runoff [mm]

$$R_{cum} = \frac{[H_{cum,i} - 0.2S]^2}{H_{cum,i} + 0.8S} \quad H_{cum,i} > 0.2S \quad (3.46)$$

- Fictitious cumulative rainfall [mm]

$$P'_{cum,i} = H_{cum,i} - R_{cum,i} - D_{i-1} \quad H_{cum,i} - R_{cum,i} - D_{i-1} < 0.2S \quad (3.47)$$

$$P'_{cum,i} = \frac{0.04S^2 + 0.8S(H_{cum,i} - R_{cum,i} - D_{i-1})}{1.2S - (H_{cum,i} - R_{cum,i} - D_{i-1})} \quad H_{cum,i} - R_{cum,i} - D_{i-1} > 0.2S \quad (3.48)$$

- Fictitious rainfall for the single day [mm]

$$P' = P'_{cum,i} + P'_{cum,i-1} \quad (3.49)$$

- Infiltrated rain netted by effective porosity [mm]:

$$P_{in} = H_{cum,i} - R_{cum,i} - D_{i-2} \quad (3.50)$$

- Saturated blanket thickness [mm]

$$P_{in}/n = \frac{P_{in}}{n_e} \quad (3.51)$$

- Water Volume at the end of the day [mm]:

$$V_i = V_0 + \frac{P_{in}}{n_e} - E_{cum,i} - D_{i-1} \quad (3.52)$$

- Daily Subsurface flow [mm]

$$D = V_i(1 - e^{-\lambda}) \quad (3.53)$$

- Cumulative Subsurface flow [mm]

$$D_{cum} = D_i + D_{cum,i-1} \quad (3.54)$$

- Groundwater level at the end of the day [m]

$$H_{GWT} = \frac{V_i}{1000} \quad (3.55)$$

Working on daily time scale, the definition of a daily GWT value was required. Then, the identification of the maximum, the average and the minimum GWT position along the available time series was performed, in order to characterize the range on which the GWT can fluctuate. Due to the fact that the piezometric measurements referred to ground level (z_{DTM}) are negative quantities (Equation 3.56),

$$H_{GWT} = (z_{GWT} - z_{DTM}) \leq 0 \quad (3.56)$$

in order to apply the modified CN model, the GWT elevation were referred to the bedrock, so to be positive. Since, for each piezometer, the depth at which the bedrock is located is known, the following expression must be used:

$$\begin{aligned} H_{GWT} &= (z_{DTM} - z_{bedrock}) + (z_{GWT} - z_{DTM}) = \\ &= (z_{GWT} - z_{bedrock}) \geq 0 \end{aligned} \quad (3.57)$$

3.1.2 Calibration of the hydrological model

The hydrological balance described above is based on the definition of three parameters:

- the *Curve Number (CN)* for the runoff estimation;
- the *effective soil porosity* (n_e) or specific yield (S_y), parameter underlying the assessment of the infiltration process, which varies significantly both planimetrically and altimetrically in the thickness of the unstable blanket;
- the *soil permeability* (k_s), parameter describing the soil water filtration process, directly linked to the reservoir emptying constant (λ) and, consequently, to the subsurface flow assessment.

While the CN parameter is derived by the lithological map, the land use map and the soil wetting conditions, as described in the previous section, the hydraulic soil-specific parameters, i.e, the effective porosity and permeability, has to be estimated through a calibration between rainfall and groundwater table response, with reference to the available piezometers.

Calibration requires the application of the hydrological balance to a number of significant rainfall events, chosen for their high intensity or long duration, of which both precipitation and groundwater level must be measured. Concerning the definition of the length of a rainfall event from a hydrological point of view, the beginning and the end of a rainfall event is not univocally defined. For example, Aleotti (2004) identified the beginning of an event in correspondence of a significant change in the slope of the cumulative precipitation, Godt (2006) defined the beginning and end of an event by the identification of a 3-hour interval of no precipitation. Brunetti (2010) defined a rainfall event after a multi-day dry period (4 to 2 days), depending on the climate of the location and the seasonal period. Working on a daily scale, it was decided to adopt the latter criterion and to define the event through a dry period lasting 48 hours, also in relation to the observed groundwater response time.

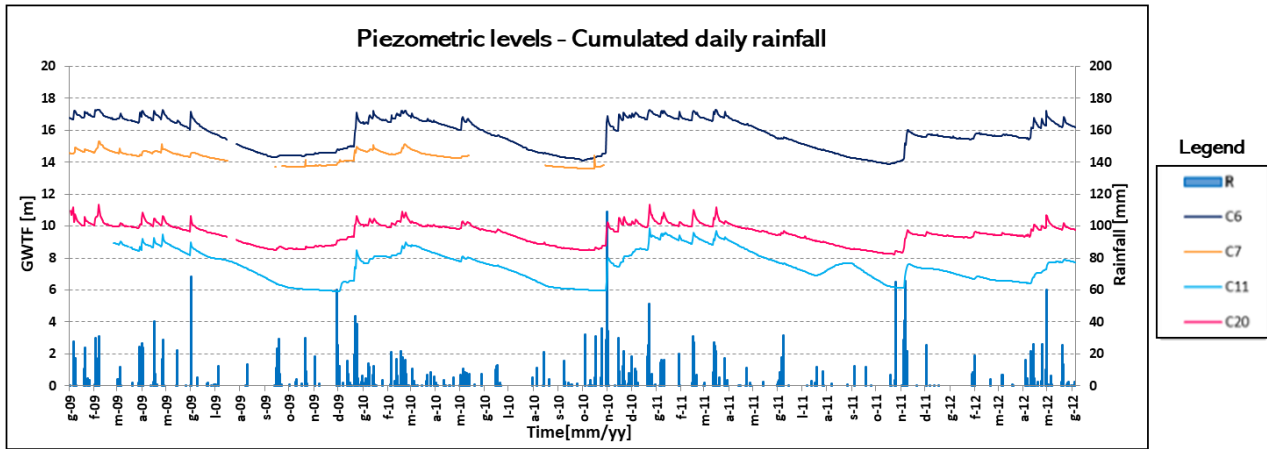


Figure 3.9. Vence (06, France). Example of rainfall-piezometric measurements correlation over a three-year period (2009-2012).

The chart in Figure 3.9 shows an example of the correlation between a rainfall history, described by the blue histogram, recorded by a rain-gauge over a period of about three years (2009-2012), and the groundwater (GWT) response. The latter has been recorded by the monitoring network installed in the Vence site, composed by four piezometers, two (C6 and C20) located in the lower portion of the slope (*zone a*), while C7 and C11 are located in the upstream zone (*zone c*). Water table raising may be observed after the most intense rainfalls in autumn, winter and spring; instead, rainfall events in summer do not influence so much the groundwater level.

The calibration is carried out using an objective function based on the minimisation of the standard deviation (Equation 3.58) resulting from the difference between the modelled groundwater levels, as a result of applying the hydrological balance, and the observed values on-site.

$$\sigma = \sqrt{\frac{1}{N} \sum_i^N (x_i - \bar{x})^2} \quad , \quad \bar{x} = \frac{1}{N} \sum_i^N x_i \quad (3.58)$$

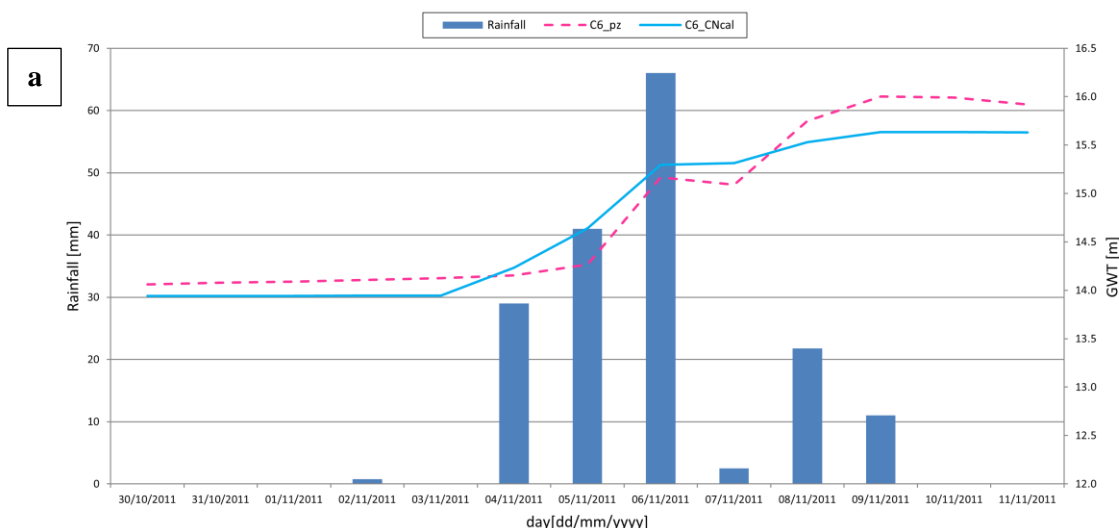
In Equation 3.58, the difference in absolute value between the water table height simulated by the model and the observed water table height represents the series of the random variable x . It has a length equal to

the entire number of simulated days (N) belonging to the different events being calibrated. It is worth underlining that the hydrological balance is carried out for a number of significant rainfall events, chosen for their high intensity or long duration over time.

Minimising the objective function leads to the evaluation of the two hydraulic parameters underlying the model calibration: the *effective soil porosity* (n_e) and the *soil permeability* (k_s).

Figure 3.10a shows the hydrological modelling applied to a short-term but intense rainfall event occurred in November 2011, while Figure 3.10b shows the balance applied to a long-lasting event occurred in November 2010, characterized by daily rainfalls ranging about 20-30 mm for several non-consecutive days in a 15-day period. In both graphs, referred to the piezometer C6 (Vence site), the rainfall history is represented by the light blue histogram, the piezometric measurements ($C6_{pz}$) by the purple dashed line, while the calibrated GWT ($C6_{cal}$) by the blue dotted one. Figure 3.10a showed a good simulation of the trend observed in field, while in Figure 3.10b the blue dotted line is not able to mimic the observed GWT variations in a satisfying manner.

Note that the volume element, in which the slope volume is discretized, may be characterised by different soil layers, and for this reason, along its height, it may consist of several voxels with different soil features. In this context, the calibration phase has to interpret the peculiar mechanisms of groundwater response to the analysed rainfall event, as the presence and the alternation of heterogeneous soil layers that influence the GWT fluctuations. Indeed, the groundwater table may show different velocities during the raising phase, linked to the presence of rainfall, and the lowering phase, linked to the absence of rainfall. For this reason, according to Equations 3.13 and 3.16, an optimisation of the calibration is performed by adding and calibrating a soil permeability value, named $k_{s_discharge}$ representing the groundwater discharge phase, due to a lack of rainfall. Figure 3.10b shows the optimised calibration for the long-time duration rainfall event, with the introduction of the $k_{s_discharge}$ parameter, compared to the previous calibration (green dotted line). This shows that the modelling implemented with the double soil permeability value allows a better representation of groundwater levels in the case of intermittent events (cyan line).



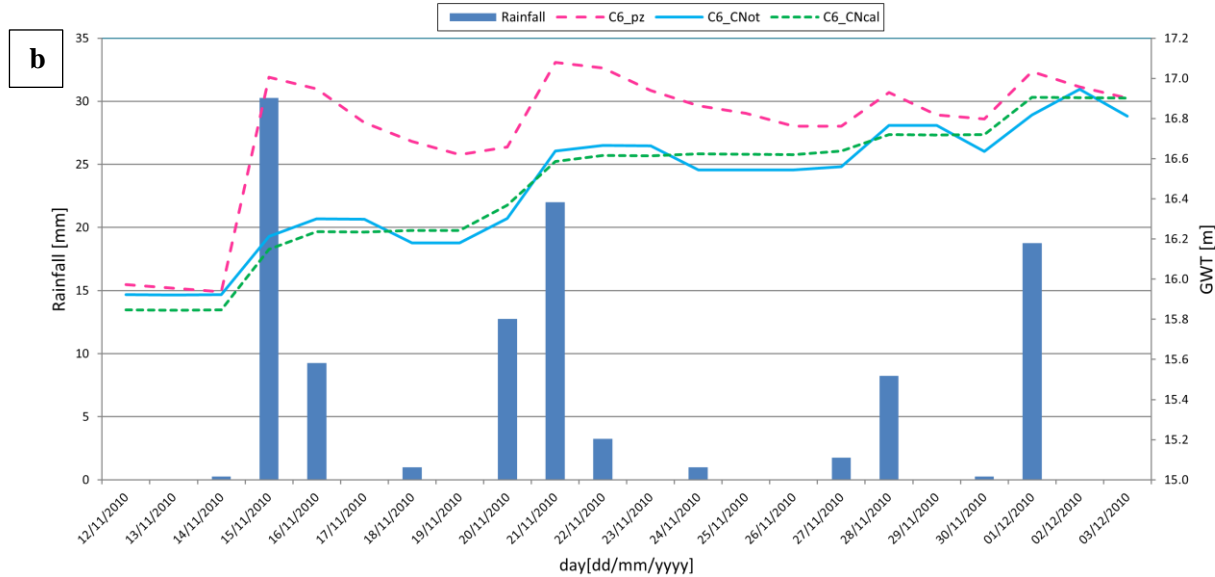


Figure 3.10. Vence (06, France). (a) Calibration of a short but intense rainfall event, and (b) of a long-time duration event.

In addition, the calibration could permit the reproduction of the presence of soils with different effective porosity that may influence the groundwater recharge and discharge phase of the water table, as in the case of Mendatica. In fact, the presence of soil layers characterised by different grain sizes, which influence the soil effective porosity (as represented in Figure 3.11), could require an optimisation of the calibration by introducing two different values (n_{e1} and n_{e2}) associated with different water table depths.

Figure 3.12 shows the results of a calibration related to a short but intense rainfall event, occurred in January 2008 in Mendatica. The green line represents the piezometric measurements. The blue line refers to “middle-optimized” calibration, by introducing the two different soil permeability values. Due to the impossibility of the blue curve to correctly mimic the piezometric line, two different values of effective soil porosity, associated to different layers, have been introduced and the “fully-optimised” calibration (in red line) was performed with results that correctly mimic the GWT phases.

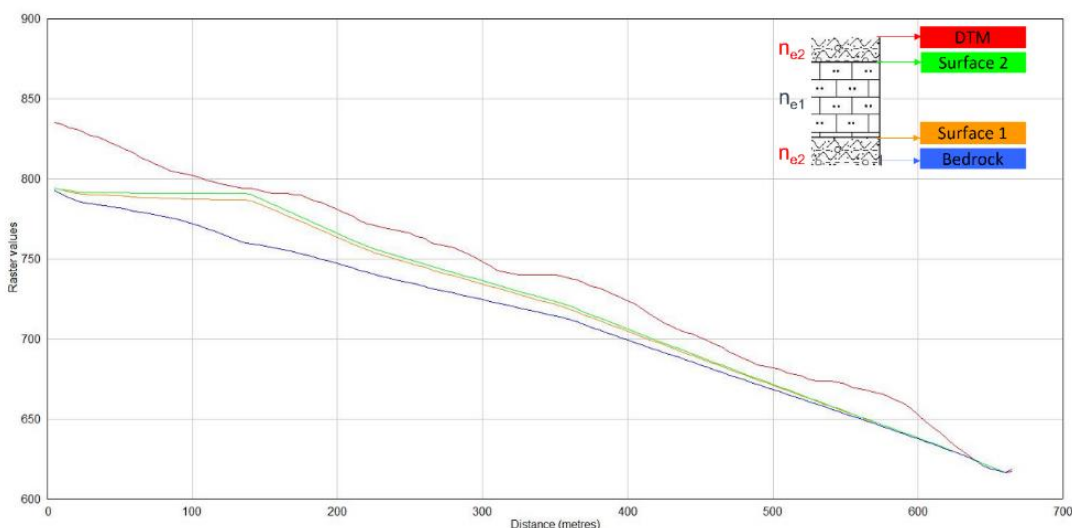


Figure 3.11. Mendatica, (IM, Italy). Section of the modelled volume showing the presence of two layers with different geological/geotechnical characteristics, reproducing the stratigraphy on the right.

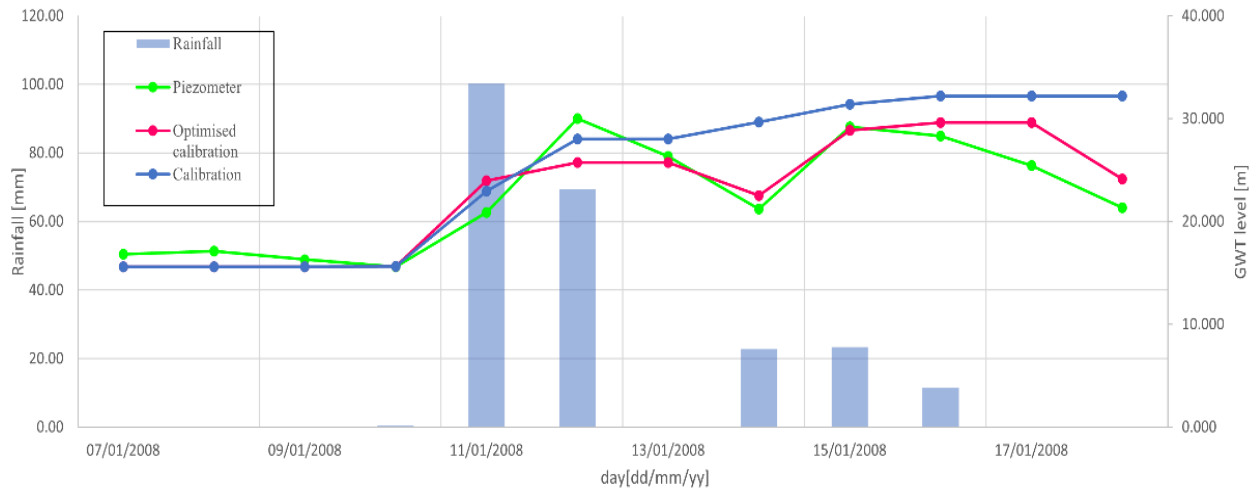


Figure 3.12. Mendatica, (IM, Italy). Calibration performed in correspondence of S6 piezometer for the Event 2008: the blue line refers to “middle-optimized” calibration, by introducing the two different soil permeability value; the red line refers to “fully-optimized” calibration, taking into account also the presence soil layers with different soil porosity.

At the end of the analysis, the reliability of the calibration is assessed by evaluating the correlation between the piezometric measurement signal (y) and the modelled groundwater signal (x), through the *correlation index* ρ_{xy} as follows:

$$\rho_{xy} = \frac{\sigma_{xy}}{\sigma_x \sigma_y} = \frac{\sum_i (x_i - \bar{x})(y_i - \bar{y})}{\sqrt{\sum_j (x_j - \bar{x})^2 \sum_k (y_k - \bar{y})^2}} \quad (3.59)$$

In Equation 3.59, σ_{xy} is the covariance and σ is the standard deviation of the considered variable. According to the coefficient value estimate, the following correlation classes are distinguished:

$0 < \rho_{xy} < 0.3$ weakly correlated signals

$0.3 < \rho_{xy} < 0.7$ moderately correlated signals

$0.7 < \rho_{xy} < 1$ strongly correlated signals

$\rho_{xy} = 0$ uncorrelated variables

$\rho_{xy} < 0$ inverse correlation

Other statistical indexes taken into account are:

- *Root Mean Square Error (RMSE)*: indicates the mean quadratic deviation between observed (x) and estimated (y) data values and depends on the variation range of these data values. The RMSE uses the same unit of measurement as the parameter of interest.

$$RMSE = \sqrt{(\bar{x} - \bar{y})^2} \quad (3.60)$$

- *Percent bias (PBIAS) [%]*: is an index that allows to measure the average tendency of the simulated values (x) to be larger or smaller than their observed ones (y). It is described by Equation (3.47)

$$PBIAS = \frac{\sum(x - y)}{\sum x} \% \quad (3.61)$$

The optimal value is zero; positive values ($PBIAS > 0$) indicate the tendency to overestimation, while negative values ($PBIAS < 0$) indicate the tendency to underestimation. This index is largely used to assess the reliability of hydrological calibration (Yapo et al., 1996).

The statistical indexes allow to estimate the goodness of calibration. With reference to the event depicted in Figure 3.12, the correlation index calculated for the calibration and its optimisation shows an important increase, rising from 0.745 to 0.878, similarly the RMSE, which goes from 5.75 to 2.56, and the PBIAS from -14% to -3.35%. This means that the possibility of considering the variation of porosity in the calibration procedure allows for a good reproduction of the groundwater table, indicating a strong correlation between modelled and measured values.

Concluded the calibration, the hydraulic soil-specific parameters (effective porosity and permeability) must be spatialized, as described in *Section 3.3*.

3.1.3 Slope stability analyses

As detailed in *Section 3.1.1*, the hydrological model is able to determine the groundwater oscillations in response to a rainfall occurrence for each analyzed time step. Then the IHG model performs a slope stability analysis in relation to the daily GWT fluctuations.

It is worth to underline that numerous approaches exist to assess the landside slope stability, which can be grouped into two main categories:

- numerical analyses of Finite Element Method (FEM) or Finite Difference Method (FDM);
- global Limit Equilibrium Method (LEM).

Stability analyses using software based on FEM or FDM allow analyses of the evolution of the landslide phenomenon to be carried out, taking into account both equilibrium and compatibility equations. Displacements and strains can be estimated. In general, numerical code analyses involve fairly high costs (not only for the software, but also for the characterization of the geotechnical parameters of interest) and modelling is also usually quite onerous, especially for complex case studies and in the case of analyses performed over quite large areas. The estimate of displacements and strains requires knowledge of the soil stiffness, the determination of which is not always straightforward.

LEM assumes that the soil behaves as a perfectly plastic rigid medium. As a result, soil strains and displacements are neglected. However, LEM can be seen as the combination of several elements derived from the Bound method, described in the following:

- **LOWER BOUND THEOREM:** if an equilibrium distribution of stress can be found which balances the applied load and nowhere violates the yield criterion, the body (or bodies) will not fail, or will be just at the point of failure.
- **UPPER BOUND THEOREM:** the body (or bodies) will collapse if there is any compatible pattern of plastic deformation for which the rate of work done by the external loads exceeds the internal plastic dissipation.

The Limit Equilibrium Method combines features of the upper and lower bound methods:

- as in the lower bound theorem, the equilibrium conditions are examined, but they refer to the forces acting on the wedge of unstable soil and the stress state within the soil is not examined.
- as in the upper bound theorem, a collapse kinematic mechanism is examined, but it does not necessarily have to be compatible and there are no restrictions to the shape of the slip surfaces.

Although there is no formal proof that the LEM leads to correct solutions, experience has shown that such method usually gives solutions that agree quite well with observations of the collapse of real structures and the method is firmly established among the techniques of geotechnical engineering.

It is possible to identify some steps on which LEM methods are based on:

- 1) Draw an arbitrary collapse mechanism (this may consist of any combination of straight lines or curves).
- 2) Impose the statical conditions of equilibrium (translation and rotation) for the portion of soil delimited by the failure surfaces.
- 3) Study other collapse mechanisms looking for the critical one, i.e. the one to which the limit equilibrium loads correspond.

The sliding surface is characterised by the minimum value of the Safety Factor (or Factor of Safety FS), defined as the ratio between the available soil shear strength τ_f and the driving shear stress τ .

The Integrated Hydrological Geotechnical (IHG) model, which I developed and employed in the analyses performed in my doctoral research, is based on the global limit equilibrium method.

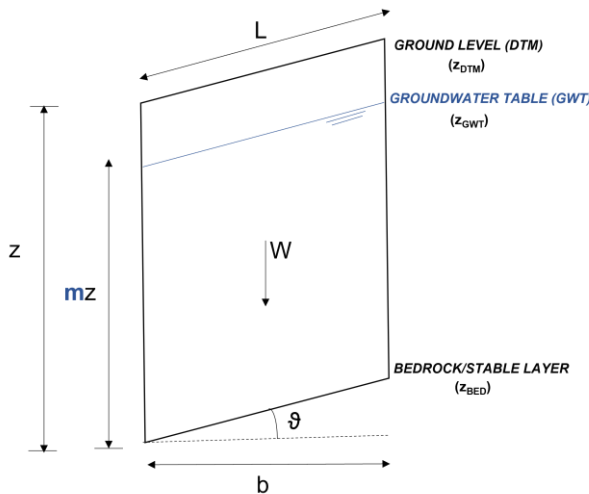
In the IHG model, with reference to each discretisation 3D volume, the sliding surface is assumed to be parallel to the ground plane, in analogy to Skempton and Delory, (1957) and other models in the literature (e.g. Alvioli and Baum, 2016, Baum et al., 2002-2008, Monrasio and Valentino, 2008). However, differently from the above cited models, this assumption is made for each volume element composing the slope mass.

With reference to each pixel (usually 5mx5m) of the ground surface, the stability conditions are evaluated for different depths (generally every 1 m) up to the stable layer, so defining soil volume elements. Consequently, the failure surface is defined at the depth with minimum Safety Factor. Since elements can vary in geometry and in terms of hydrological and physical-mechanical parameters, the whole failure surface can be irregular, having a complex shape determined by the interpolation of the failure depths pertinent to various volume elements.

In the IHG model, the Safety Factor is estimated by applying Equation. 3.49 for any discretization element. The shear strength is provided by applying the Mohr-Coulomb strength criterion, while the effective driving stress is induced by the soil weight of the pertinent volume element. A vertical cross section of the 3D element is schematized in Figure 3.13, where m is dimensionless parameter to describe the vertical position of the

groundwater table in the 3D volume. With reference to the stable layer or bedrock, m is defined as the ratio of the water table height to the DTM (Equation 3.48), thus representing the daily variations of the GWT.

$$m = \frac{z_{\Delta GWT_{BED}}}{z_{\Delta DTM_{BED}}} \quad (3.62)$$



3.13. Vertical cross section of the volume element with reference to the maximum slope plane.

$$FS = \frac{\tau_f}{\tau} = \frac{c' + z(\gamma - m\gamma_w) \cos \vartheta^2 \tan \varphi}{\gamma z \cos \vartheta \sin \vartheta} \quad (3.63)$$

where:

c' = soil cohesion in effective stress terms [kPa];

φ' = soil effective friction angle [°];

γ = soil unit weight [kN/m^3];

γ_w = water unit weight [kN/m^3];

m = dimensionless parameter to describe the groundwater table location in the 3D volume.

ϑ = maximum slope angle pertinent to each pixel assumed equal to the sliding surface inclination with respect to the horizontal [°];

z = height of volume element [m].

In the GIS procedures, the slope inclination ϑ is calculated for each pixel of the DTM, while the soil physical-mechanical parameters, such as effective cohesion c' , soil unit weight γ and friction angle φ' are derived from the interpretation of laboratory and in-situ test results and then spatialized.

The calculation of the Safety Factors in every cell allow to provide, as IHG final product, maps of landslide susceptibility in the occurrence of a rainfall history (Figure 3.14a) or maps forecasting the susceptibility evolution triggered by expected short-term rain. The maps are rendered in raster format, choosing an appropriate

colour table so to provide great immediacy even for not expert GIS users: unstable areas, characterized by low Safety Factor, are depicted in red; incipiently unstable areas, characterized by Safety Factor close to 1, are depicted in yellow; stable areas, characterized by Safety Factor greater than 1, are depicted in green.

A further map of particular importance is the “stability condition variation map”. It allows to distinguish the areas made unstable by a given rainfall event (represented in red in Figure 3.14b) from those which were unstable before that rainfall event (represented in blue in Figure 3.14) because of the particular hydro-geo-morphological conditions. In fact, note that IHG is a simplified model for landslides susceptibility analyses at 1:5000 scale, hence, it does not consider the possible presence of on-site stabilisation works.

IHG may consider the loads applied by structures, such as buildings, thanks to the DSM (Digital Surface Model) description and a load analysis, but this is not considered in the present contribution.

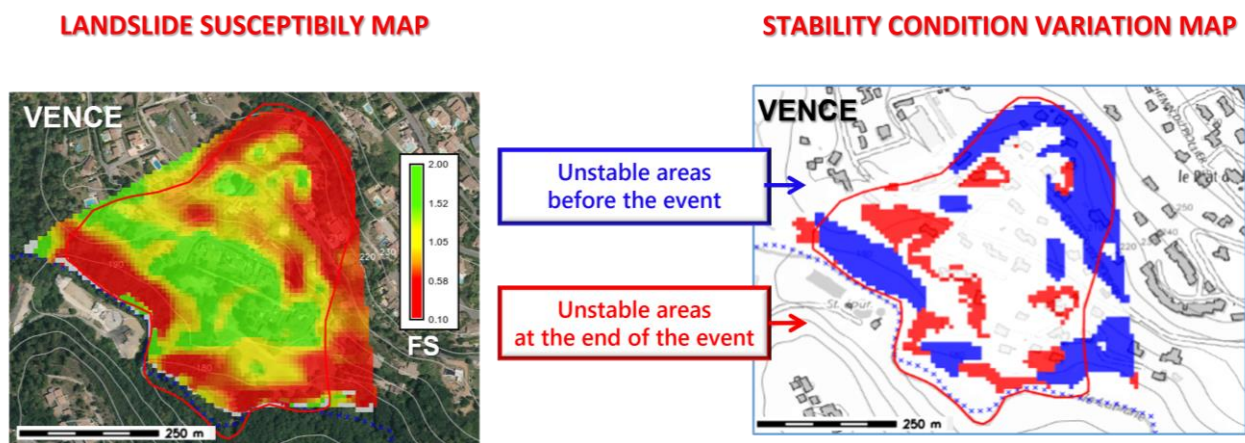


Figure 3.14. Vence (France). Example of the landslide susceptibility map (a) and stability condition variation map (b).

It is worth emphasising that the IHG model neglects the contact forces between the 3D elements in which the mass of the landslide is discretized. In literature, this assumption is not unusual. Among the LEM methods, some methods completely neglect contact forces, such as the one by Fellenius (1936), while other LEM methods only partially neglect these forces. For example, Janbu's method (1954) and Bishop's method (1955) only consider the normal components of the contact forces, but not tangential ones. It is worth noting that the results obtained under this assumption (i.e. neglecting contact forces) are in good agreement with the results of more sophisticated models (e.g. FEM) and with actual observations.

In the context of the analysis of large portions of land (as in applications of the IHG model), the above assumption is operative. Obviously, since reciprocal interactions between soil portions are not captured (e.g. the influence of upstream slope portions on downstream ones and vice versa), the results require careful interpretation.

The comparison of the results obtained using the IHG model with the results obtained with other methodologies (for example 3D FEM analyses) allowed to conclude that the IHG model allows for rapid analyses (compatible with near real time analysis) of significant landslide volumes by capturing the instabilities, which were also confirmed by on-site validation. In the following, this will be discussed, with particular reference to the case studies shown.

3.2. ASSESSMENT OF SOIL APPARENT COHESION (SAC) INDUCED BY PARTIAL SATURATION CONDITIONS

Slope stability is strongly influenced by soil hydraulic conditions, affected by the meteoric events to which the site is subject. With particular reference to shallow landslides triggered by rainfalls, the stability condition is influenced by the propagation of the saturation front inside the unsaturated zone. The soil shear strength varies in the vadose zone depending on the type of soil and the variations of soil moisture. Monitoring of the unsaturated zone can be done by measuring suction and/or water content. The measurement of the soil volumetric water content can be performed through the use of low-cost capacitive sensors distributed over the study area. Such sensors provide data in near-real time and are relatively easy to install and replace. However, it is strongly recommended to perform a laboratory soil-specific calibration of the instrumentation, that should take into proper account the characteristics of the soil, where the sensors are installed (Campora et al., 2020). In fact, previous work (Bovolenta et al., 2020) has shown that the factory settings may lead to inaccurate estimates of the actual volumetric soil water content.

The knowledge of soil water content allows the estimate of the suction, thanks to a Water Retention Curve (WRC), and consequently the definition of the soil shear strength in partly saturated conditions, throughout the apparent cohesion estimate. All the methodologies for landslide susceptibility assessment, based on the global Limit Equilibrium Method (LEM) or Finite Element Method (FEM), need the soil shear strength description in order to evaluate the slope stability conditions. Both in the recent literature (Escobar-Wolf et al., 2021; Moresi et al., 2020) and in the GRASS GIS software (GRASS Development Team, 2022), models are already proposed for shallow landslide susceptibility evaluation in GIS, based mainly on LEM (e.g.r.shalstab). However, these models do not usually consider the unsaturated soil behaviour, but at most take into account the strength contribution provided by the vegetation root systems.

In this section, a procedure, implemented by Python script in QGIS (QGIS Development Team, 2022) is proposed, that, starting from soil moisture monitoring data, allows a spatially distributed estimate of the soil shear strength in the vadose zone, that is essential for the landslide susceptibility assessment, especially in the case of shallow landslides. In fact, in reference to 2D or 3D modeling, this procedure may be directly integrated in slope stability analyses in GIS environment, or its results may be adopted in LEM/FEM analyses. Its usefulness is significant in the analysis of shallow landslides, taking advantage of the soil moisture measurements to improve the evaluation of the stability conditions over time, by analyzing the evolution of the saturation front according to the weather conditions. The monitoring of the water content in the soil can also be useful for the analysis of the evolution of soil shear strength over time after emergencies. In fact, the knowledge of the soil shear strength, calculated by the proposed procedure, is very important because landslide risk conditions may persist long after the officially issued alert has ceased. By the monitoring of the soil water content (provided that the sensors have not been damaged during the emergency) and by the soil shear strength evaluation, it would be possible to understand when people, subjected to evacuation, can return to their homes safely.

3.2.1 Soil shear strength

In the vadose zone, the soil shear strength is strongly related to the soil features and to the variation of soil moisture, in terms of suction. For this reason, it is postulated the existence of a relationship between the unsaturated soil shear strength and the soil-water characteristic curve (Vanapalli et al., 1996).

The use of Water Retention Curves (WRC) is probably the most widely employed method for defining the hydraulic characteristics of unsaturated porous media, such as soil. Indeed, the soil-water characteristic curve provides a conceptual and interpretative tool by which the behaviour of unsaturated soils can be understood (Vanapalli and Fredlund, 2000). However, as the definition of a site-specific WRC is not straightforward due to the requirement of specialized and expensive laboratory instrumentation, a variety of soil-water retention models have been proposed in literature. In this work, the described procedure for the definition of the WRC is based on the method proposed by Balzano et al. (2021), which employs the well-established pedotransfer function of Vereecken et al. (1989), built on a Van Genuchten (1980)-type function. The latter is based on a relationship directly linking volumetric water content and suction. It is worth underlining that the use of a pedotransfer function allows the use of empirical correlations between the water retention model and easily measurable physical soil properties. In particular, in the method here proposed, the Van Genuchten equation is related to intrinsic soil properties, (i.e. grain size distribution, dry density and carbon content). According to the Van Genuchten equation, the water retention curve of the reference soil can be written as follows:

$$\theta = \theta_r + (\theta_s - \theta_r) \frac{1}{1 + \left(\alpha \frac{s}{\gamma_w} \right)^n} \quad (3.64)$$

where:

θ = volumetric water content [-]

s =suction [kPa]

θ_s = saturated volumetric water content [-]

θ_r = residual volumetric water content [-]

γ_w = specific water weight= 10kN/m³

α = equation parameter [1/cm]

n = equation parameter [-]

The introduced parameters are related to the intrinsic soil properties, grain size distribution, dry density, and carbon content through the following relationships:

$$\theta_r = 0.015 + 0.005\%Clay + 0.014\%C \quad (3.65)$$

$$\theta_s = 0.81 - 0.283\rho_d + 0.001\%Clay \quad (3.66)$$

$$\alpha = \exp(-2.486 + 0.025\%Sand - 0.351\%C - 2.517\rho_d - 0.023\%Clay) \quad (3.67)$$

$$n = \exp(0.053 + 0.009\%Sand - 0.013\%Clay - 0.00015\%Sand^2) \quad (3.68)$$

where:

%Clay= clay fraction

%Sand = sand fraction

%C= carbon content

ρ_d = soil dry density [g/cm³]

The estimate of the dry density parameter is based on the assumption that the highest volumetric water content, θ_{max} , recorded on field in occasion of significant rainfalls corresponds to the fully saturated soil condition, thus coinciding with soil porosity. This assumption is expressed in terms of gravimetric water content, w_{max} :

$$\rho_d = \frac{\rho_w G_s}{1 + w_{max} G_s} \quad (3.69)$$

where:

G_s = specific gravity of soil grains [-]

ρ_w = water density= 1000 kg/m³

The application of this model, through the estimate of the parameters involved, allows the definition of the specific WRC. Consequently, at any investigated vertical of the monitoring network, for each installation depth, knowing the volumetric water content values recorded by the capacitive sensors, the pertinent suction value is estimated as follows:

$$s = \frac{\gamma_w}{\alpha} \left(\frac{\theta_s - \theta}{\theta - \theta_r} \right)^{1/n} \quad (3.70)$$

where the meaning of the different parameters is explained above. According to the Equation 3.71 proposed by Fredlund et al. (1978) and modified by Vanapalli et al. (1996), it is possible to estimate the value of unsaturated soil shear strength:

$$\tau_f = c' + (\sigma - u_a) \tan \varphi' + (u_a - u_w) \left(\frac{S - S_r}{S_{max} - S_r} \right) \tan \varphi' \quad (3.71)$$

where:

τ_f = shear strength of an unsaturated soil [kPa]

c' = effective cohesion [kPa]

φ' =effective stress soil friction angle [$^{\circ}$]

$(\sigma-u_a)$ = net normal stress on the plane of failure at failure [kPa]

(u_a-u_w) = matrix suction, corresponding to the parameter s in the procedure [kPa]

$\left(\frac{S-S_r}{S_{max}-S_r} \right)$ = effective degree of saturation [-]

The procedure, here described, is devoted to calculating the third addendum of Equation 3.71, i.e. the Soil Apparent Cohesion value, hereinafter called SAC, which is strictly related to unsaturated soil conditions. Its implementation in GIS environment is described in *Section 3.2.3*.

3.2.3 Soil Apparent Cohesion (SAC) procedure in GIS

An automatic procedure is proposed here in a GIS environment to describe the evolution of shear strength within the vadose zone based on weather-induced soil moisture measurements. The procedure adopts the method detailed in the *Section 3.2.1*, that, taking into account the unsaturated soil behaviour, allows to define a site-specific Soil Water Retention Curve, as proposed by Balzano et al. (2021), and then to evaluate the soil apparent cohesion and the associated soil shear strength, which is fundamental for the stability assessment, with particular reference to shallow landslides.

This procedure, called SAC, was implemented as a Python script for QGIS. It is open source and can be downloaded at the following Github address: <https://github.com/LabGeomatica/Unsaturated-soil-shear-strength.git>.

The implemented procedure is described in the flowchart in Figure 3.17 and detailed in Appendix B.

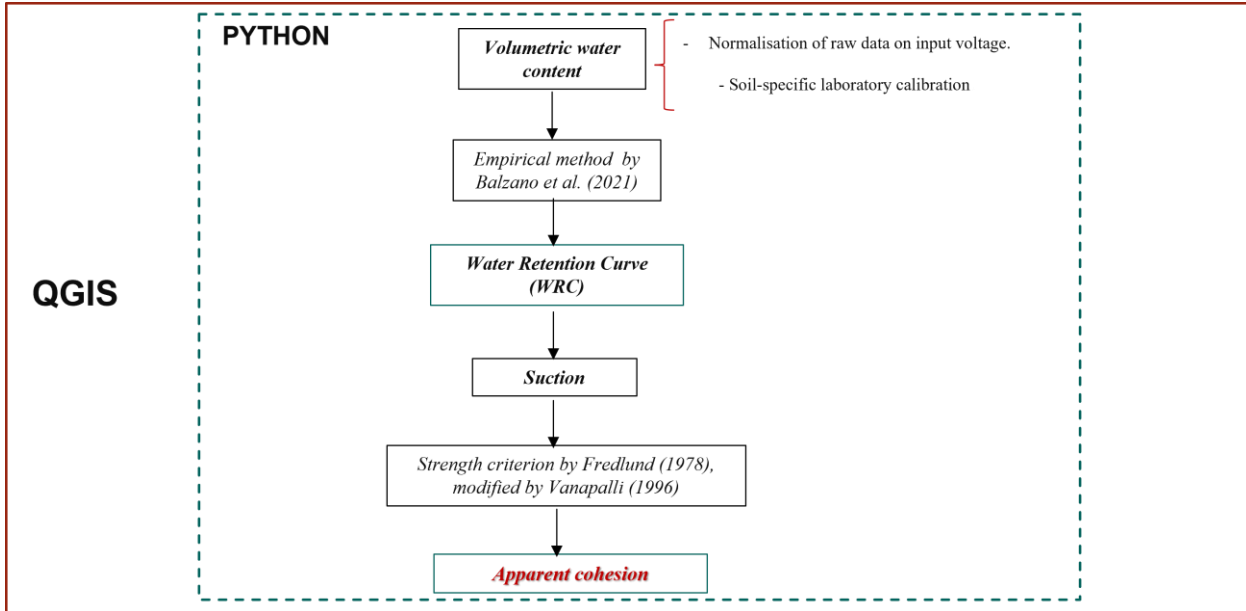


Figure 3.17. Procedure workflow diagram.

SAC procedure requires as input data the intrinsic soil properties and the maximum water content value (θ_{max}), corresponding to a fully saturated soil condition, registered on site by the monitoring network over all the period of measurements. The user must therefore provide as input the percentages of sand, clay, carbon content and θ_{max} . The implementation of the formulas allows the developed procedure to estimate the parameters involved (α , n , θ_s , θ_r , w_{max} and ρ_d) and consequently the definition of the site specific Soil-WRC.

Obviously, the Volumetric Water Content (VWC) values are requested in input, in order to calculate the pertinent soil shear strength values. VWC data can be provided as punctual data or in a raster format, by using maps obtained from point data interpolation or remote sensing product processing. In case of data provided by a monitoring network as punctual data, they can be stored in a geodatabase, and the user can choose the time scale to work with. Once the rainfall period to be analyzed is identified, the raw data at the different installation depths are extracted for each node composing the monitoring network. Otherwise, the user can provide a .csv or .txt input format containing data downloaded by the network.

Input VWC data can be either raw or already calibrated. In the case of VWC data requiring calibration, the procedure allows the user to enter the calibration parameters, according to a linear relationship.

By entering the relevant VWC values in the Soil-WRC curve, the automatic procedure performs the suction calculation at each node, by applying the Eq. 3.70 in *Section 3.2.1*, for each measurement depth, related to time step of the chosen time scale.

For each measurement depth, this information is spatialized, by applying the Delaunay triangulation interpolation between the nodes, the final products are surfaces of unsaturated shear strength over the investigated area.

If the VWC input data are already provided in raster format, i.e. already distributed over the study area, the previous formulas are applied to each cell of the raster, and spatial interpolation is not necessary.

The automatic procedure described above was fully developed in the PhD research described in this dissertation. It allows large portions of soil to be analysed quickly. The shear strength in partially saturated soils that depends on rainfall is evaluated. The procedure (which will be applied in the following) is a tool that can be used for the analysis of rainfall-induced surface landslides, which are unfortunately frequent.

3.2.4. Shallow landslide stability analyses

Superficial landslides are phenomena triggered by rainfall events of short duration and high intensity or long duration and medium-low intensity (Caine, 1980; Giannecchini, 2006; Giannecchini et al., 2012 and 2016). These phenomena affect the first layers of soil and are characterized by reduced thicknesses, generally in the order of 2 m. It is worth to underline that, among the different types of landslides, shallow landslides are one of the most damaging types due to their high frequency and their ability to evolve into destructive phenomena (Hung et al., [2001](#) and [2014](#); Sidle & Ochiai, [2006](#); Crosta et al., 2012).

The results of the described procedure can be used to evaluate the shallow landslide susceptibility, taking into account the soil behaviour under partial saturation conditions both in terms of apparent cohesion values and volumetric water content. The first term affects the slope stability in terms of strength contribution (Equation 3.77) the second affects the estimate of the weight per unit volume (Equation 3.78).

$$F_S = \frac{\tau_f}{\tau_m} = \frac{(c' + \Delta c_{app}) + (\gamma_{unsat} z \cos \beta \tan \varphi')}{(\gamma_{unsat} z \cos \beta \sin \beta)} \quad (3.77)$$

where:

$c' + \Delta c_{app}$ = shear strength contribution provided by effective and apparent cohesion values.

z = investigated depth

β = slope angle

φ' = soil friction angle

γ_{unsat} = unsaturated soil volume unit weight estimate through Equation 3.78

$$\gamma_{unsat} = \gamma_{dry} + \theta_v \gamma_{water} \quad (3.78)$$

γ_{dry} = dry soil volume unit weight

θ_v =volumetric water content

γ_{water} = water specific weight equal to 10 kN/m³

3.3. DATA SPATIALISATION IN GIS ENVIRONMENT

The IHG and SAC procedures, illustrated above, require the definition of physical surfaces and/or the spatialisation of parameters, defined in few points and then interpolated and/or extrapolated for the entire area under study.

Thanks to the experience acquired within the AD-VITAM project, the proper interpolation/extrapolation techniques and/or boundary conditions have been identified so to allow accurate and careful modelling of the landslide volume, as described in the following.

3.2.2 Soil properties and soil moisture monitoring

The Water Retention Curve estimate requires the definition of measurable intrinsic soil properties as input data. Laboratory tests conducted on site specific soil sample allows the determination of the soil features characterizing Equations 3.65-3.68. In fact, according to the BS EN ISO 17892-4:2016 guidelines, the grain size distribution by sieving and sedimentation for a soil sample can be conducted for the estimate of the percentage of clay and sand (i.e., %Clay and %Sand). Therefore, the percentage of soil carbon content is evaluated as 58% of the soil organic matter (Pribyl, 2010), determined in compliance with the standard ASTM D2974-20 (2020). The soil dry density, Equation 3.69, is function of the gravimetric water content and of the specific gravity of soil grains that is determined through of the pycnometer test, according to BS EN ISO 17892-3:2015.

In the assumption of fully saturated soil condition, the degree of saturation (S) is equal to 1. Since the volumetric water content θ_v and S are correlated by Equation 3.72a, it can be assumed that θ_{max} is equal to the porosity of the soil (n), as shown in Equation 3.72b. Then the gravimetric water content estimate is based on the mentioned hypothesis

$$\theta_v = S n \quad (a) \rightarrow \theta_{max} = n \quad (b)$$

It is possible to describe the relationship between gravimetric water content (w) and soil void ratio (e) through Equation 3.73 in terms of soil degree of saturation and specific gravity of soil grains:

$$Se = G_s w \quad (3.73)$$

By exploiting the relationship between soil void ratio and soil porosity in Equation (3.74)

$$e = \frac{n}{1 - n} \quad (3.74)$$

and the Equation 3.73, it is possible to express the gravimetric water content as function of θ_{max} , as follows:

$$w_{max} = \frac{\theta_{max}}{(1 - \theta_{max})G_s} \quad (3.75)$$

According to Equation 3.70, the suction is estimated in function of WRC and soil moisture measurements deriving from sensors network installed in site.

Soil moisture sensors can be installed in the soil at different depths and at different locations in the analysed area, thus creating a monitoring network. The network may consist of a series of devices, called Sensor Pup (Figure 3.16a), to which the capacitive sensors are plugged, and a receiver (called Retriever) collecting data from the network devices and connected to a Modem for remote data transmission (Figure 3.16b). Communication between the Sensor Pups and the Retriever could occur via radio. Each Sensor Pup, the modem and the Retriever can be powered by 5-Watt solar panels or connected to the mains through a power adapter.

Each Sensor Pup is usually connected to more than one soil moisture sensors, placed at different depths, so to provide information on soil water content along a vertical measuring line. Monitoring data can be provided at time intervals ranging from 5 to 60 minutes as needed and can be accessible and downloadable in .csv format through an internet portal (e.g. SpecConnect of Spectrum Tec.) and viewable through a mobile application (e.g. WatchDog Mobile).

The installation of the described monitoring network requires some operational precautions to ensure communication between devices, their integrity over time and the reliability of the obtained measurements. It is recommended to fence the measurement nodes and prevent the generation of preferential infiltration paths when the sensors are inserted into the ground (Iacopino et al., 2021).

Concerning the type of sensor, capacitive sensors are considered the most suitable to monitor soil moisture and its changes induced by rainfalls: they are relatively inexpensive, easy to install and replace, and provide an almost immediate response to moisture variation. In the context of the project AD-VITAM, sensor networks have been installed in the five sites, by choosing the capacitive sensors named WaterScout SM100 (Figure 3.15). The capabilities of the above-mentioned devices were analyzed by the University of Genoa both in test fields and in laboratory tests (Bovolenta et al., 2020b), in order to compare their capabilities with more complex sensors (i.e. Drill & Drop probes- Sentek Technologies).



Figure 3.15. WaterScout Sm100.



Figure 3.16 (a) Sensor Pup and (b) Retriever and Modem installed in the Ceriana_Mainardo site.

Concerning the VWC (Volumetric Water Content) value (i.e., θ_v), the monitoring sensor network installed on site provides raw data for which a soil-specific VWC calibration is needed. The calibration of soil moisture sensors is very important, and it has to be performed in laboratory, on soil samples taken directly from the study area where the sensors were installed, in order to define the correlation between the raw data and the actual volumetric water content (Bovolenta et al., 2020a). In particular, any soil sample has been divided into several specimens, which were then moistened with different amounts of water to simulate water content variations. This methodology has provided the VWC soil-specific calibration equation for the studied site by a linear regression of the laboratory data. The equation is defined as follows:

$$\theta_v = a \left(\frac{V_{out}}{V_{in}} \right) + b \quad (3.76)$$

where:

a, b = constants provided by the linear regression;

$\left(\frac{V_{out}}{V_{in}} \right)$ = normalised ratio between raw data (V_{out}) measured by the field sensors and the input voltage (V_{in}) of Sensor Pup.

This linear correlation allows the transition from the raw data, duly normalised to the Sensor Pup input voltage, to the estimated VWC value at any given depth.

3.3.1 Physical surfaces

The reconstruction of the stable layer or bedrock starts with the analysis of a proper number (depending on the expected complexity of the subsoil) of geotechnical investigations performed inside the landslide mass; the reconstruction of the groundwater table surface requires at least three spatially well distributed piezometers.

Several interpolation methods were tested to reconstruct such physical surfaces starting from a few known points: the Inverse Distance Weighted, the Spline and the Delaunay triangulation methods. After the performed tests, the algorithm suggested is the Delaunay triangulation, which generates a three-dimensional model consisting of triangular surfaces between the known data, without introducing fictitious trends.

The presence of observation points usually limited to the central zone of the landslide body requires the definition of model boundaries to spatialise the information over the entire studied area. The model boundaries can be fixed as follows: downstream and laterally to the landslide area, where a river is often present, the water table and the bedrock can be assumed to coincide with the DTM; in the upstream region of the study area, the slope of the water table and the bedrock depth can be assumed to be equal to the values observed inside the landslide body.

The characterisation of the Vence landslide volume is described below as an example. The generation of bedrock and groundwater table the 3D surfaces have been carried out by applying the general rules defined above.

The groundwater table surface (Figure 3.18) was defined by applying the Delaunay triangulation between the groundwater level depth, recorded at four piezometers. Hence, model boundaries conditions were defined downstream, in correspondence of the La Lubiane River, imposing coincidence between the river and the DTM elevations, while upstream imposing the constancy of the slope of the groundwater level defined between pairs of piezometers in the landslide body. In Figure 2.43 the imposed model boundaries in the upper part of the slope are named with the letters p, q, r, s, t.

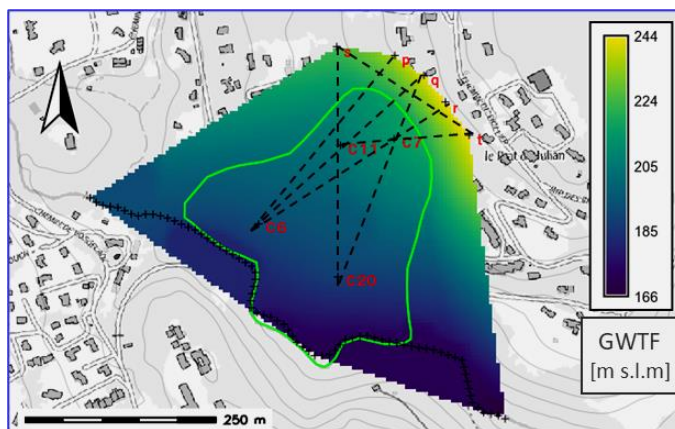


Figure 3.18. Vence (06, France). Example of water table obtained by interpolation of the piezometer observed data and extrapolation on the entire area by applying boundary conditions. Elevation is expressed in meters above the mean sea level.

The bedrock surface was generated firstly applying the Delaunay triangulation between 27 points where geotechnical investigations were available (Figure 3.19a). Then the interpolation was performed taking into account also lower and upper boundary conditions, i.e., the coincidence between DTM and bedrock in correspondence of La Lubiane River and the parallelism between DTM and bedrock in the upstream area (Figure 3.19b).

The above proposed interpolation procedure was applied on all sites analysed within the AD-VITAM project, allowing a good modelling of the landslide volumes.

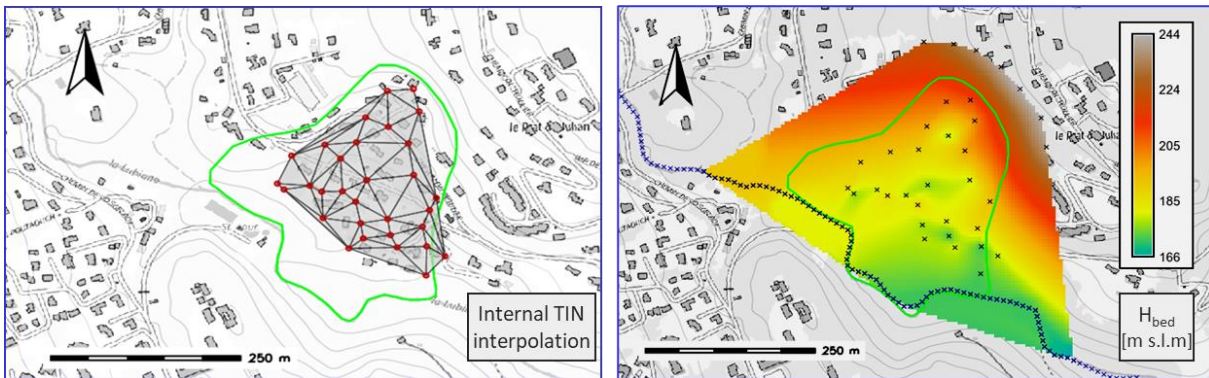


Figure 3.19. Vence (06, France): reconstruction of the three-dimensional triangular surfaces model between the spot points, using Delaunay algorithm (a) and the entire bedrock surface (b) obtained by interpolation and extrapolation of the data observed and model boundaries Elevation is expressed in meters above the mean sea level.

3.3.2 IHG parameters

Once the landslide volume is characterized in term of 3D physical surfaces (i.e., DTM, bedrock and groundwater table), the next step is the modelling of subsoil characterisation, and more specifically the soil effective porosity and the soil permeability. The spatialisation of these parameters, estimated by means of the point hydrological calibration described in *Section 3.1.2*, is strongly site dependent. For this reason, it is not possible to identify a general rule for the spatialisation of these parameters that can be applied to every site. However, the modelling carried out on the sites under study within the AD-VITAM project allowed the identification of two suitable methodologies for the spatialisation of point information over the entire study area, as follows:

- the definition of a linear correlation between blanket height and hydraulic soil parameters;
- the application of a “stratigraphic similarity” between hydraulic soil parameters and in situ stratigraphy.

A brief description of the modelling of the hydraulic parameters, referring to Mendatica and Vence sites is proposed below.

The linear correlation between blanket height and hydraulic soil parameters has been used to generate the soil permeability maps in Mendatica site. As detailed in section modelling of subsoil characterisation, and more specifically the soil effective porosity and the soil permeability. The spatialisation of these parameters, estimated by means of the point hydrological calibration described in *Section 3.1.2*, stratigraphic information highlighted the presence of different soil layer inside the slope mass (Figure 3.10), with

different geological and geotechnical features, that can affect the groundwater table response. Therefore, given the oscillation of the water table caused by rainfall, observed in 4 piezometers, different values of soil permeability were estimated and associated with the individual piezometer, in order to reproduce the observed oscillation as best as possible. The values of soil permeability and the blanket height in correspondence of the 4 piezometers are reported

in Table 3.2. An example of linear relationship between the four known values is represented in Figure 3.20a: the blanket thickness is plotted on the x-axis, and the soil permeability on the y-axis; the defined relation allows to spatialised soil permeability information over the entire study area (Figure 3.20b), thanks to the previous modelling of the blanket thickness in the whole area.

Piezometer	$k_s_{recharge}$ [m/s]	$z_{blanket}$ [m]
S6	2.25e-07	25
S4	1e-07	6
S3	3.53e-07	21
S11	1e-07	7

Table 3.2. Soil permeability values compared to the blanket depth assessed in the boreholes

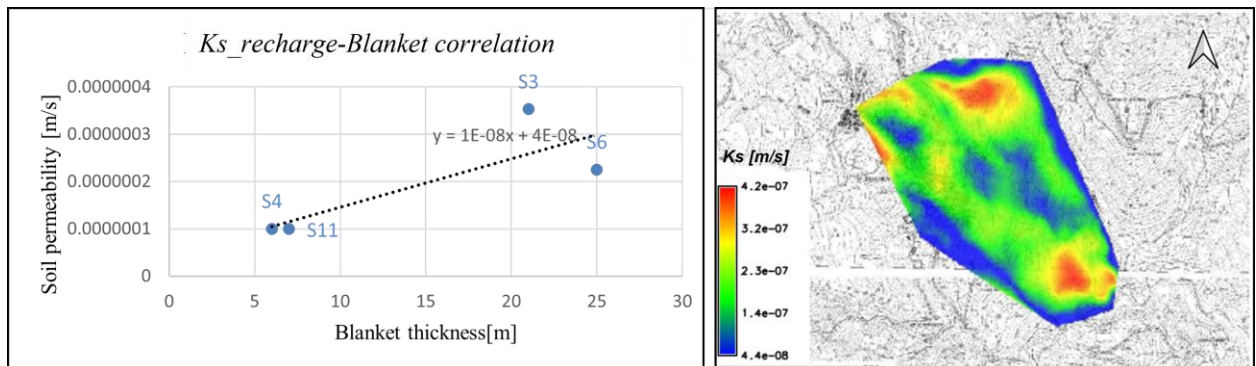


Figure 3.20. Mendatica, (IM, Italy). Soil permeability linear correlation defined for the GWT recharge phase(a), soil permeability final surface (b).

In addition, a different groundwater oscillation velocity was observed in Mendatica in the recharge and discharge phases; it required to estimate different values of soil permeability in the two phases, i.e., $k_{s_recharge}$ and $k_{s_discharge}$, making the modelling more complex. In fact, two different linear correlation between blanket height and hydraulic soil parameters were defined, for the two phases, in order to better reproduce the groundwater fluctuation (GWTF) velocity. Table 3.3 summarised the soil permeability values provided by applying the calibration on the GWT discharge values. The detected linear correlation and the soil permeability surface in GWT discharge conditions are showed in Figure 3.21.

Piezometer	$k_{s_discharge} [\text{m/s}]$
S6	3.29e-06
S4	9.48e-06
S3	7.85e-05
S11	1.02e-05

Table 3.3. Soil permeability values estimated in the loading and unloading phases

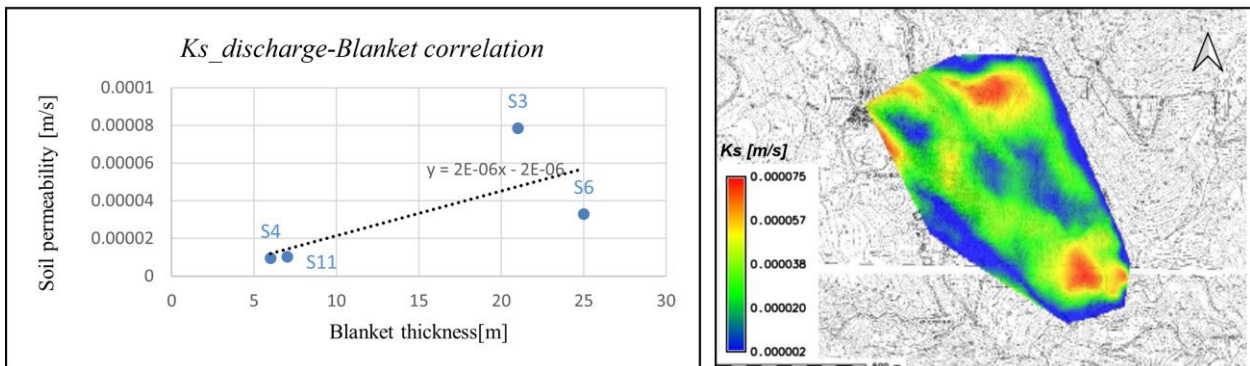


Figure 3.21. Mendatica, (IM, Italy). Soil permeability linear correlation defined for the GWT discharge phase(a), soil permeability final surface (b).

Concerning the “stratigraphic similarity” methodology, it consists in associating the values of effective porosity or soil permeability estimated in a few piezometers to all the boreholes characterised by the same stratigraphy. The final surface is modelled by spatialising the information over the whole area by applying different interpolation techniques (i.e. Inverse Distance Weighted and the Delaunay triangulation).

This technique was applied to model the effective soil porosity in Mendatica, where two different soil layers were observed to compose some areas of the Mendatica blanket. The effective soil porosity values, showed in Table 3.4, have been obtained performing the optimised calibration for the four piezometers available. According to Figure 3.21, n_{e1} represents the external layer, while n_{e2} represents the internal one.

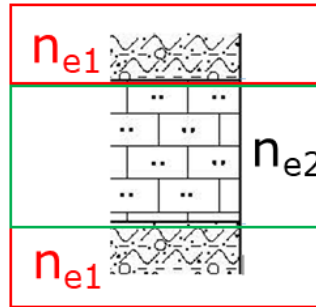


Figure 3.21. Mendatica (IM, Italy). Soil layer characterised by different effective porosity parameters

Piezometer	ne1 [-]	ne2 [-]
S6	0.021	
S4	0.02	0.05
S3	0.015	0.012
S11	0.046	

Table 3.4. Soil effective porosity values for the two soil layers

Since the values of effective porosity are only known in a few soundings, not sufficient to obtain an adequate characterisation of the site, the criterion of stratigraphic similarity was applied, associating the estimated values of ne to all the boreholes characterized with the same stratigraphy. Then, two maps, related to n_{e1} and n_{e2} , have been obtained by applying the Delaunay triangulation between 13 and 7 internal points respectively for n_{e1} and n_{e2} . Hence, the values have been extrapolated by using the nearest neighbour method for both maps. The outputs surfaces are shown in Figure 3.22.

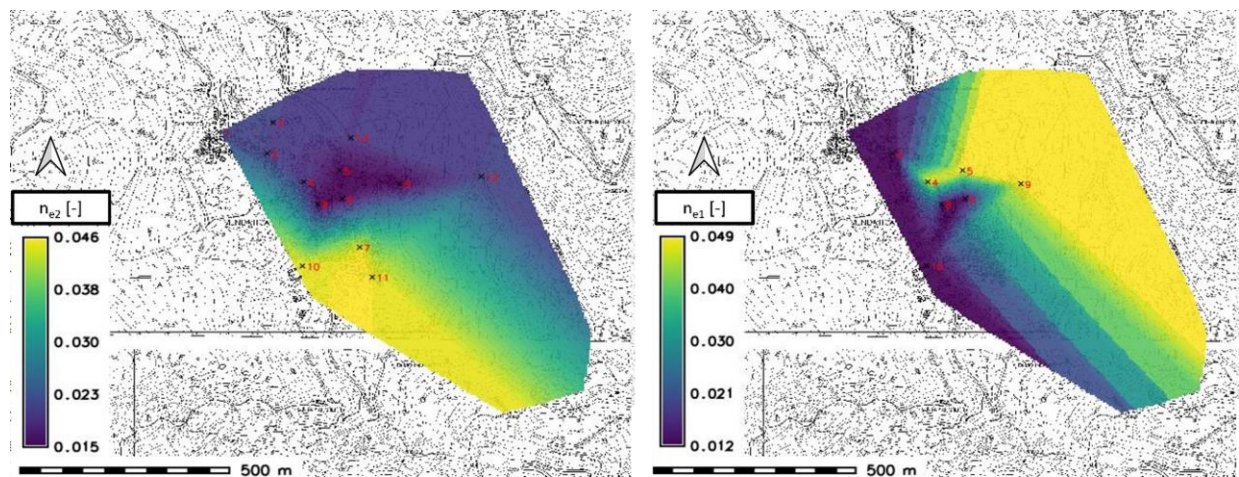


Figure 3.22. Mendatica, (IM, Italy). Effective porosity surfaces for the two different layers composing the blanket based on the “stratigraphic similarity” methodology

The same methodology has been applied for the generation of the hydraulic surfaces in Vence. The optimized calibration performed in correspondence of the four piezometers allowed the definition of the soil permeability in the recharge and discharge phases and of the effective porosity (in a unique layer), summarised in Table 3.5.

Optimized calibration

Piezometer	$ks_{recharge}$ [m/s]	$ks_{discharge}$ [m/s]	ne [-]
C6	4.55e-06	5.12e-06	0.100
C7	1.63e-05	3.07e-05	0.090
C11	4.0e-06	4.7e-06	0.105
C20	2.79e-06	3.79e-06	0.130

Table 3.5. Vence (06). Hydraulic soil parameters

Then, according to the stratigraphic similarity methodology, these parameters have been associated to the 27 boreholes present in the landslide body. A Delaunay triangulation was used to obtain the final maps inside the known points and the nearest neighbour method to extrapolate outside. Figures 3.23a and 3.23b show an example of soil porosity map and soil permeability for the loading GWT phase, respectively.

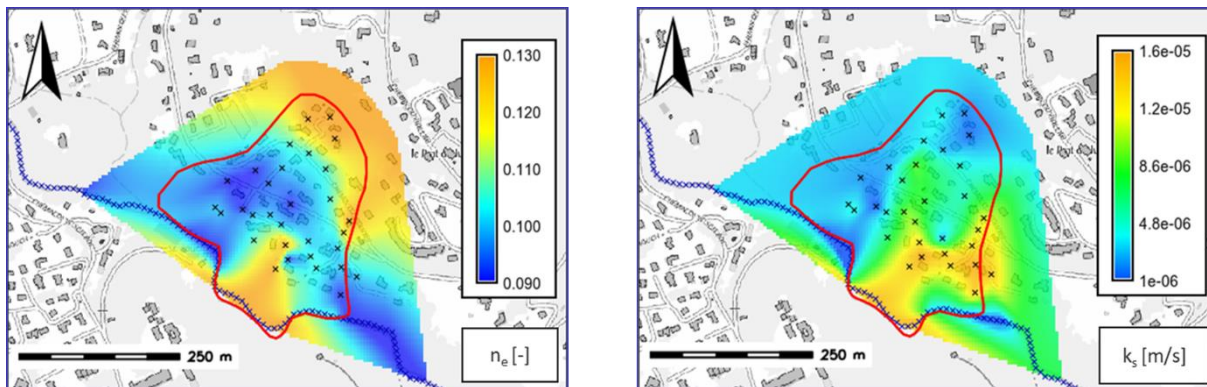


Figure 3.23. Vence (06, France). (a)Effective porosity surface and (b) soil permeability surface

Once the soil permeability map has been calculated by one of the two methods described above, it is possible to compute the discharge constant surface by applying Equation 3.16 of *Section 3.1.1*. An example of the lambda map is showed in Figure 3.24. Knowledge of this parameter allows the evaluation of the subsurface flow (according to Equation 3.28), which is fundamental in the hydrological balance.

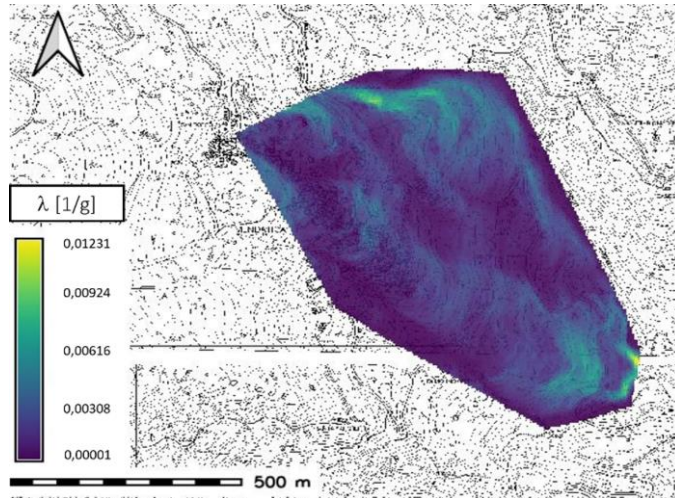


Figure 3.24. Mendatica, (IM, Italy). The discharge constant map

3.3.3 SAC spatial modelling

As detailed in *Section 3.2.3*, for each investigated depth, the outputs of the SAC automatic procedure are maps of suction and soil apparent cohesion, provided in a raster format by applying the Delaunay triangulation between the measurement points. In addition, if the VWC given in input to the procedure are not already spatialized, the procedure provides VWC raster maps. Figure 3.25 shows an example of suction map, referred to the Mendatica site, for a rainfall event occurred in 2021. The colour scale indicates variations in suction values ranging from blue, corresponding to the highest values (at M5) to red, corresponding to low suction values (minimum at M3). The map is referred to a depth of 10cm and it has been provided by the procedure by applying the TIN interpolation.

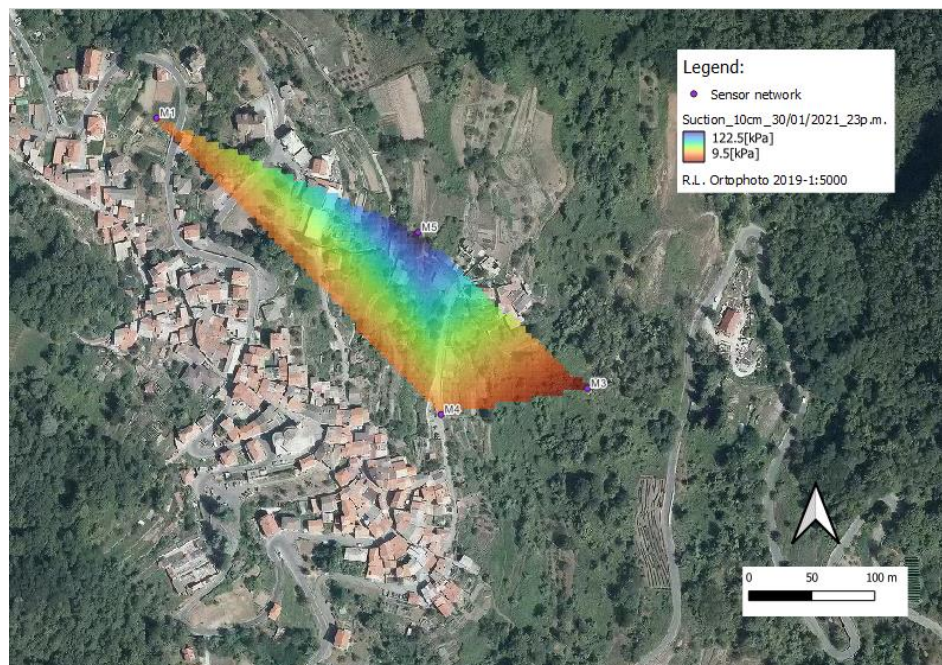


Figure 3.25. Mendatica, (IM, Italy). Hourly suction map related to the rainfall event occurred in January 2021

However, the extent of these surfaces is a function of the number of nodes installed on the site, usually 4 or 5, and for this reason it is necessary to define an interpolation methodology to cover the entire investigated area.

According to the Curve Number map generation, a similar procedure was defined to generate VWC, suction and apparent cohesion surfaces. The procedure is based on the association of VWC or apparent cohesion values to all areas that have the same characteristics in terms of land use and Hydrological Soil Group (HSG) class definition.

The land use map is reclassified in order to define homogeneous macro areas with the same land use characteristic (e.g., all the different types of woods are classified in only one class, named Woodland). On the other side, according to the stratigraphy of the first meters of soil, the HSG classes are associated to the site-specific soil to describe the infiltration capacity.

The reclassified land use map and the hydrological class map were then superimposed to obtain a single vector map containing all information on land use and soil infiltration capacity. Subsequently, with respect to the identified homogeneous areas, this map was compared with the location of the sensors on site. From this comparison it was then possible to associate the relevant sensor parameter (i.e. VWC, suction and apparent soil cohesion), which falls within a certain class, to all areas with the same characteristics.

All this information was then processed in GRASS-GIS by creating a vector containing the information related to the two maps and updating the database once with the VWC, once with that of apparent cohesion. Finally, according to the chosen time scale and for each investigated depth, through a rasterization process the output maps were generated. Figure 3.26 showed an example, related to an apparent cohesion map, of final product obtained by applying the described methodology.

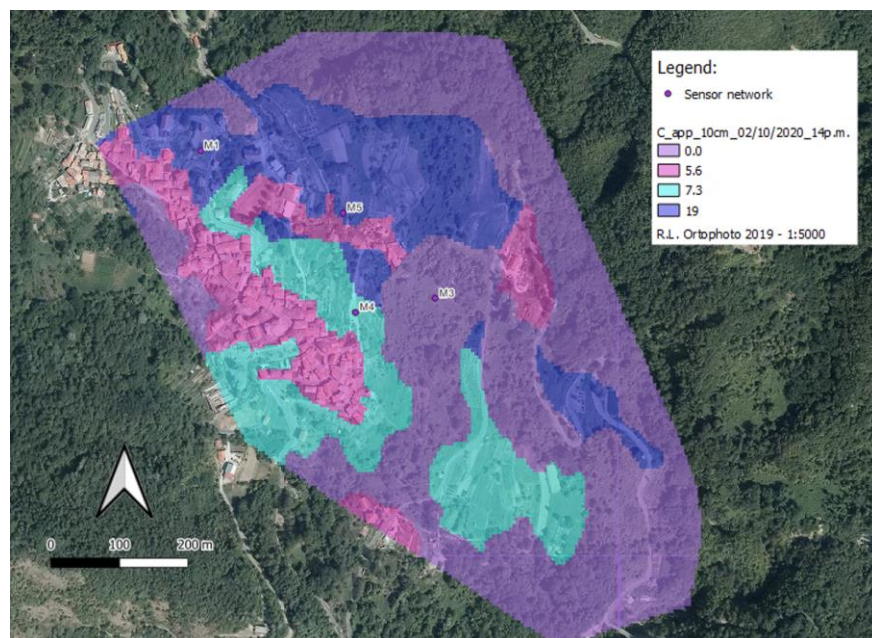


Figure 3.26. Mendatica (IM, Italy). VWC map obtained by applied the interpolation methodology

4. RESULTS AND DISCUSSION

In the first part of this chapter the IHG (Integrated Hydrological-Geotechnical) modeling applied to Mendatica and Vence sites is described. Due to their size, these landslides are among the most important for the Province of Imperia and for the PACA region, respectively. For this reason, attention has been focused on them and for each site two rainfall events are analyzed.

In accordance with the required phases of IHG modeling, first the hydrological calibration of the parameters is described. Next, the surfaces definitions and the spatialization of the parameters are presented; they represent the input data of the IHG modeling. Finally, the results obtained from the stability analysis are discussed and a critical analysis is provided too.

In the second part of this chapter, the application of the SAC (assessment of Soil Apparent Cohesion) modeling was applied to the Alex storm event in Mendatica. SAC allows shallow stability analyses in partial saturation conditions, estimating the soil Water Retention Curve and then, starting from the soil water content measurements provided by a sensor network, the suction values and the apparent cohesion. The SAC modelling was applied at the Alex storm on an hourly time scale in order to appreciate the evolution of the landslide phenomenon.

APPENDIXES A and B describe the IHG and SAC procedures outlined in this dissertation.

4.1. IHG APPLICATION IN MENDATICA

The results of the IHG model, applied to the Mendatica site, are here presented. Two rainfall events were analysed, both having a cumulative daily rainfall of more than 100 mm, chosen for their intensity that qualify them as critical events, according to the definition of rainfall thresholds proposed by Brunetti et al. (2010).

Considering a minimum Antecedent Dry Weather Period (ADWP) before precipitation of 48h, Figure 4.1 shows the defined rainfall events (337) for the Pornassio rain gauge.

These events can be compared with the green line, which represents the rainfall threshold identified by Brunetti et al. (2010) for the entire Italian territory. By entering the graph as a function of rainfall intensity and time duration, it is possible to define whether the rainfall event studied is critical (upper part of the graph). The red and blue lines indicate the rainfall events (2008 and 2019) and allow them to be defined as critical.

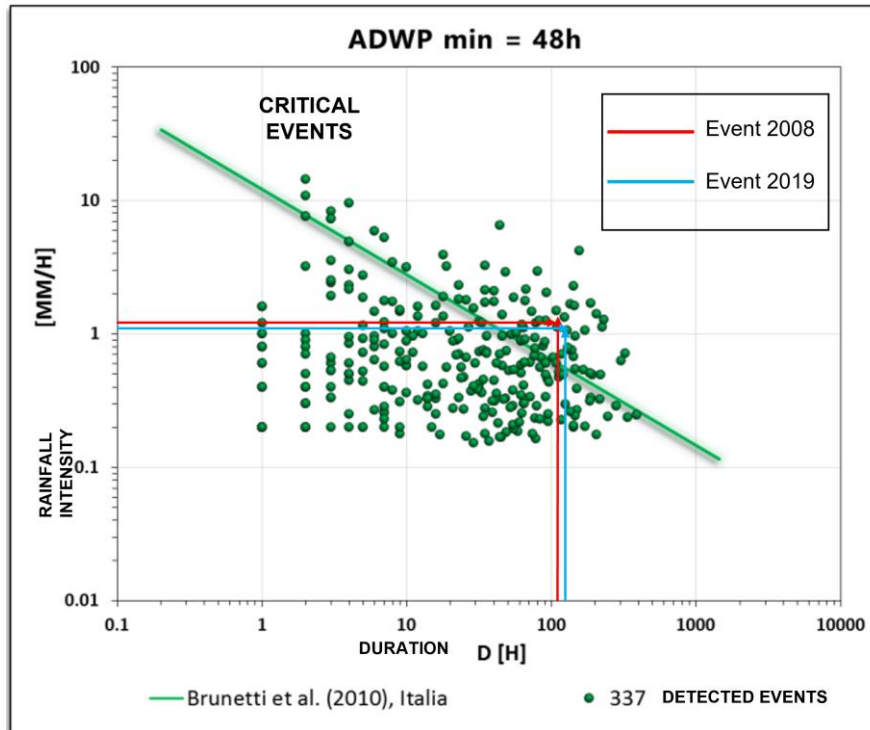


Figure 4.1. Detection of the 2008 and 2019 rainfall events as critical, based on the rainfall threshold (Brunetti et al., 2010) and the rainfall events identified for the Pornassio rain gauge for a 48-hour ADWP.

The first event occurred in 2008 (from 07/01/2008 to 19/01/2008), the second event occurred in 2019 (from 13/12/2019 to 25/12/2019).

The rainfall event occurred in January 2008 (Figure 4.2) was an intense rainfall event, with a cumulative rainfall equal to about 170 mm in two days (11/01/2008-12/01/2008). Due to the lack of a rain gauge on the Mendatica territory (installed later, in 2015), the data are referred to the rain gauge in Pornassio (IM). The choice of the reference rainfall station was made by performing a Thiessen tessellation between the closest rain gauges stations (i.e, Pornassio e Colle di Nava). Applying this procedure did not take into account the difference in elevation between the sites and meteorological and orographic variables: however, it can be a useful tool for analyses over wide-large areas. By setting the two rain gauges starting points, the programme does not provide an output, as at least three points are required. An additional point is then inserted at a suitable distance so as not to alter the tessellation around the area of interest. This procedure has shown that the municipality of Mendatica falls within the area of influence of the Pornassio rain gauge (Figure 4.3).

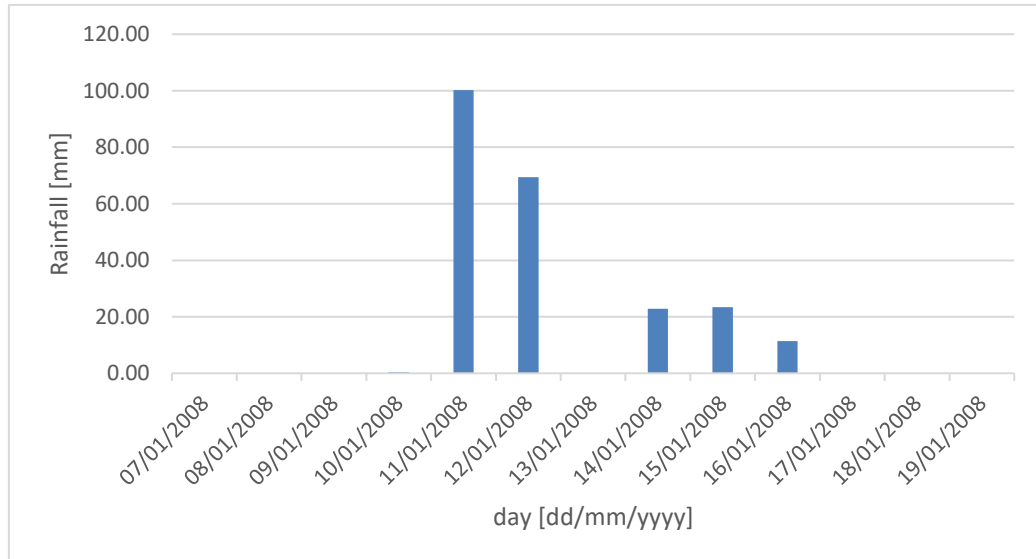


Figure 4.2. January 2008: event rainfall height

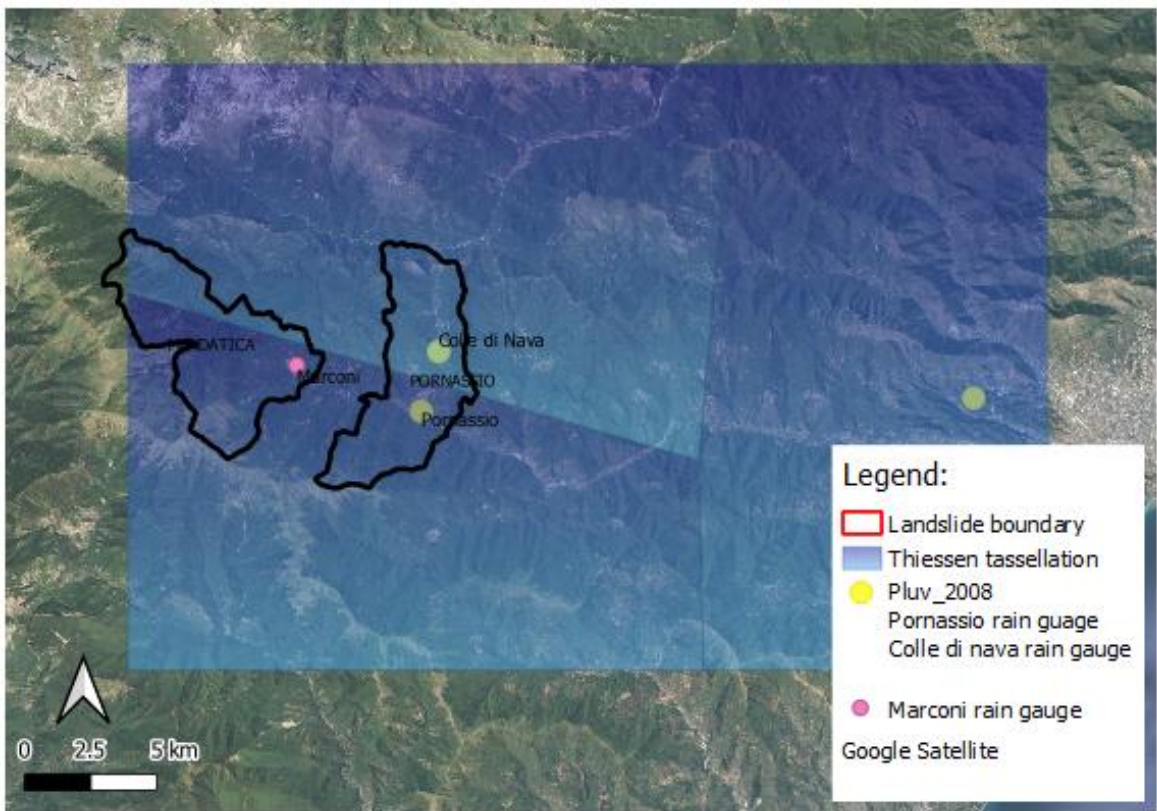


Figure 4.3. Thiessen tessellation between the rain gauges and their location

The second rainfall event occurred in December 2019 (Figure 4.4). The rainfall data are provided by the rain gauge, called “Marconi” (www.acronetworwitk.org), installed in the Mendatica village in 2015. The

instrument recorded a daily rainfall height of 138mm (on 20/12/2019) and cumulative rainfall of about 200 mm in four days.

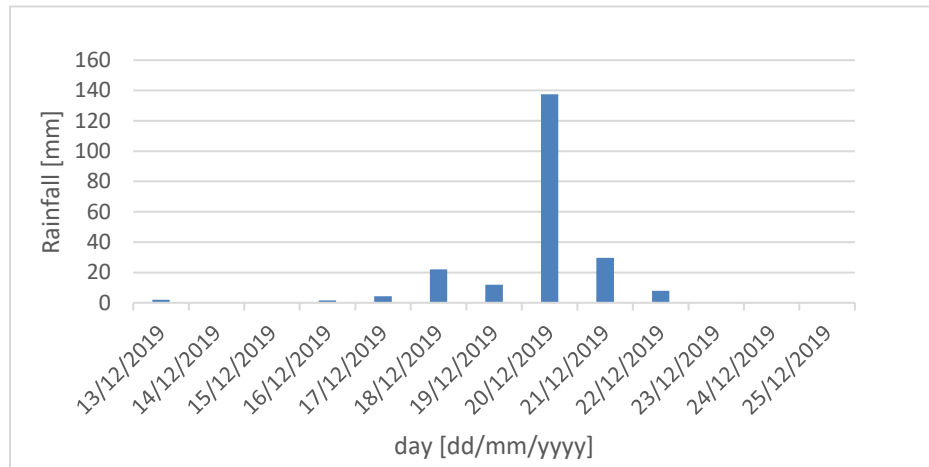


Figure 4.4. December 2019: event rainfall height

4.1.1 Physical surfaces

The IHG model requires in input the following cartographic layers, freely available from Liguria Region cartographic geoportal:

Raster data:

- Digital Terrain Model, at scale 1:5000 and resolution 5m (derived from Technical Regional Map 2007);
- Technical Regional Map 2007, at scale 1:5000 and resolution 5m.

Vector data:

- Land Use (2018), at scale 1:10000;
- Inventory of landslide phenomena in Italy (IFFI), at scale 1:10000

In addition, the following WMS services were used as background maps:

- RGB digital orthophoto (2019), at scale 1:5000.
- Centres of historical, artistic and environmental interest (1991) at scale 1:500.

The cartographic data provided by the Liguria Region geoportal are in the Roma40 reference system and Gauss-Boaga projection (EPSG code 3003). Figure 4.5 shows the boundaries of the Mendatica computational region and its cell resolution (*i.e. nsres and ewres*) equal to 5 m, according to the DTM resolution.

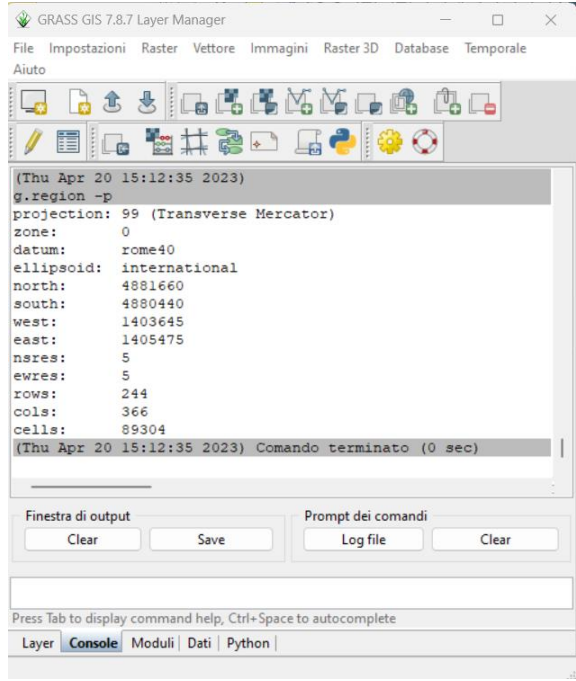


Figure 4.5. Boundaries of the geographical area of the Mendatica Mapset (*g. region*)

In addition to the Digital Terrain Model, the surfaces of bedrock and of the groundwater table have to be defined too. Moreover, the CN maps necessary to define the maximum storage capacity of the slope volume has to be calculated, as described in the following.

Bedrock surface generation:

The characterization of the slope volume first requires the generation of the *bedrock surface*. Indications on the bedrock depth were provided by the borehole loggings of the 13 investigated points and the results of the geophysical refraction test, during geognostic surveys conducted from 2006 to 2007, as detailed in *Section 2.1.2*.

The geographical position of the boreholes was indicated on an image present on the geological report Macciò et al., 2013, relative to the status of the monitoring network in 2013 (Figure 4.6). The blue dots represent the piezometers, the orange ones the inclinometers. The red crosses indicate the instruments that were no longer active at that date, while the pink arrows indicate the direction of the landslide movement according to the inclinometer measurements. For a better understanding of the site, a number of points of interest were identified (cemetery, sports field, municipal building and sewage treatment plant). This image was georeferenced in GIS, using as background layer the orthophoto at scale 1:5000 available as WMS layer, and then the cartographic coordinates of each instrument constituting the monitoring network were derived (Table 4.1).

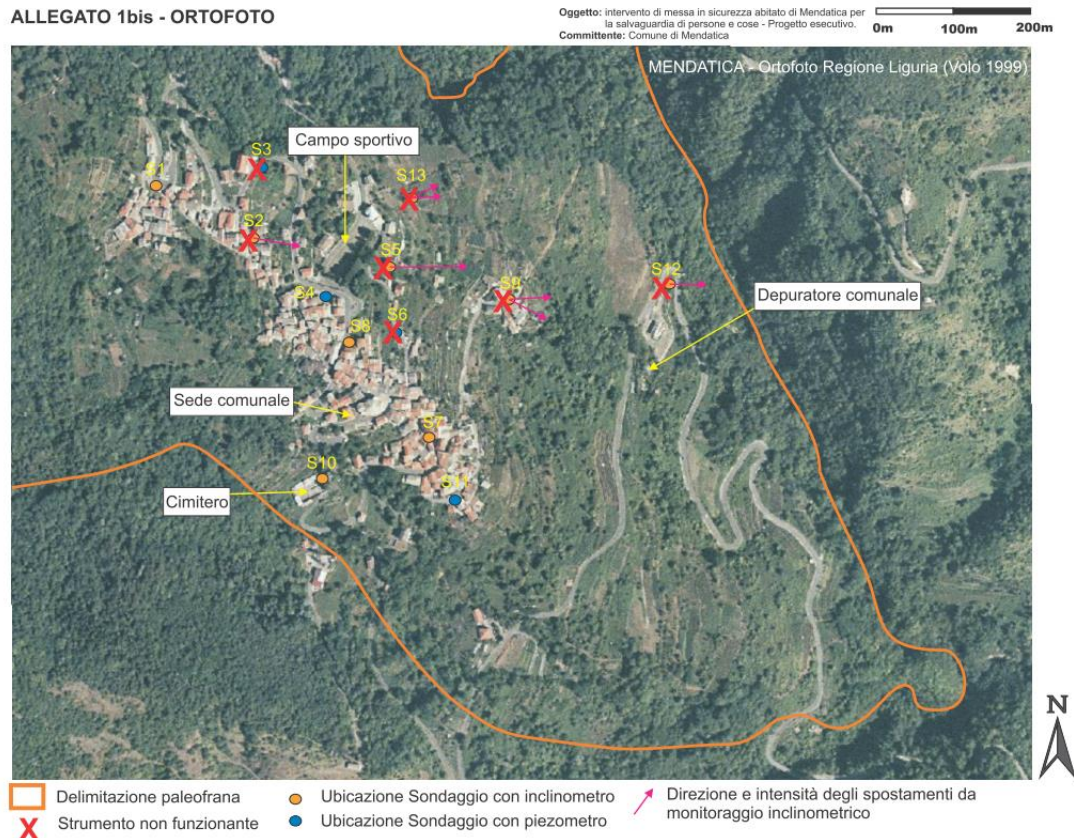


Figure 4.6. Orthophoto showing the monitoring network status in 2013, used in the georeferencing process. (Geological report, Macciò 2013)

Survey	Est	North
S1	1404150	4881341
S2	1404265	4881285
S3	1404279	4881366
S4	1404352	4881211
S5	1404437	4881241
S6	1404444	4881167
S7	1404485	4881040
S8	1404385	4881153
S9	1404580	4881206
S10	1404349	4880991
S11	1404515	4880962
S12	1404774	4881225
S13	1404464	4881326

Table 4.1. Projected coordinates of the boreholes, expressed in the ROMA40 reference system and Gauss-Boaga projection: zone 1 (west).

The position of the geophysical refraction test was derived by georeferencing the image in Figure 4.7, using as background layer the Chart of Artistic and Environmental Historical Interests at scale 1:500, supplied by Liguria Region geoportal as WMS service.

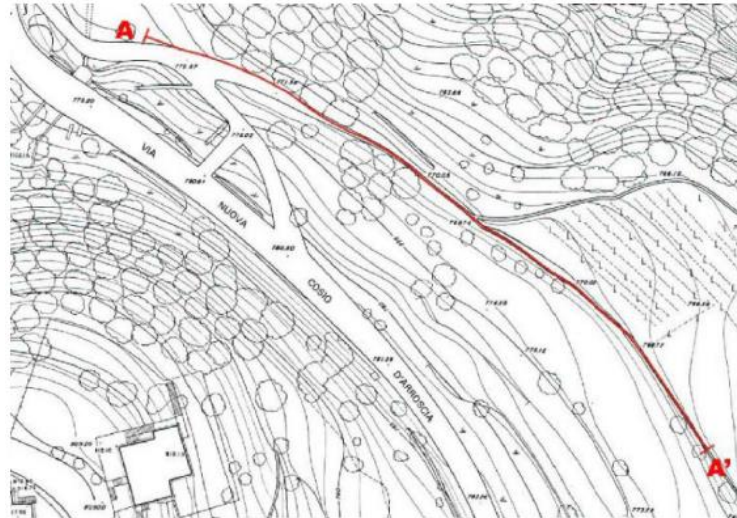


Figure 4.7. Position of the geophysical survey over the Chart of Artistic and Environmental Historical Interests at scale 1:500.

In order to extend the modelling analysis to a wider area than that in which the boreholes are located, model boundaries were introduced (as described in *Section 3.3.1*), in the lower and upper part of the slope, where watercourses with bedrock embedded riverbeds are present, imposing the coincidence of the DTM and the bedrock (Figure 4.8). A vector file containing the 3D position of the investigated points and of the model boundary conditions was thus created.

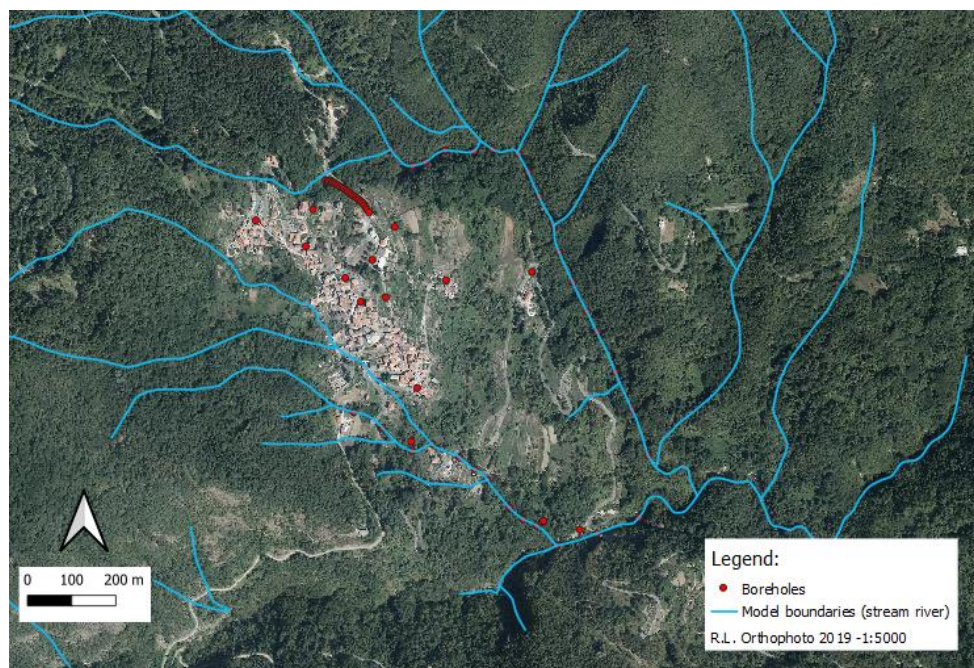


Figure 4.8. Survey borehole and model boundary condition for the bedrock surface generation.

TIN interpolation, based on a Delaunay algorithm, was identified as the most suitable technique to generate the bedrock surface (*Section 3.3.1.*). In particular, the GRASS GIS command `r.surf.nnbathy`, available as an extension of the standard version of the software, was applied using the linear algorithm (`alg=l`). The derived bedrock surface is shown in Figure 4.9.

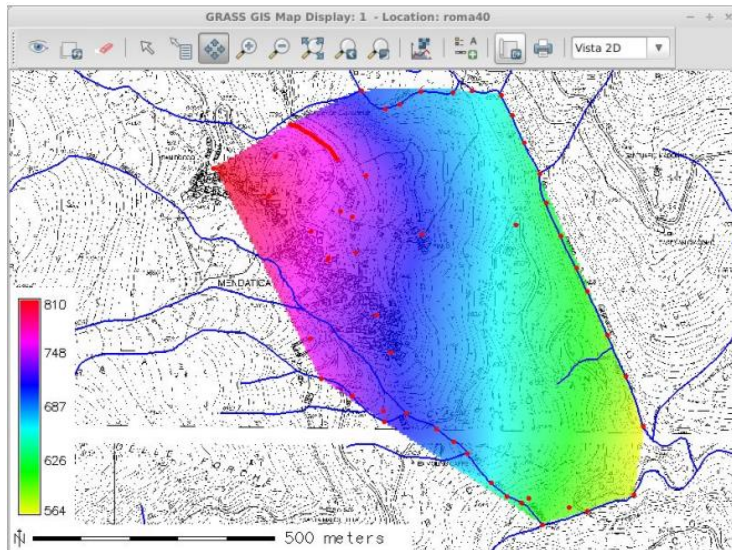


Figure 4.9. Bedrock surface [m a.s.l]

Groundwater table surface generation:

The knowledge of the groundwater level is the starting point for using the IHG model. In the following, the procedure for generating the average groundwater table surface in Mendatica is described. However, this procedure is valid for any water table investigated (maximum, minimum, 24hours).

The average water table values were obtained by averaging the piezometric records over the entire available historical series. Due to the fact that the landslide body is characterized by only four piezometers (S3, S4, S6, S11), model boundary and additional information associated to the in situ-boreholes are derived. Based on the comparison between GWT data at four piezometers and the stratigraphy loggings associated with them, indicative water table levels were associated to the seismic survey and some boreholes equipped with inclinometers (S1, S2, S9, S12, S13) too. Moreover, model boundaries were defined along the stream channels delimiting the landslide, imposing the coincidence between the DTM elevation and the groundwater table, according to the bedrock surface generation (Figure 4.9). Then, the surface generation has been carried out by applying the TIN interpolation, based on a Delaunay algorithm (Figure 4.10).

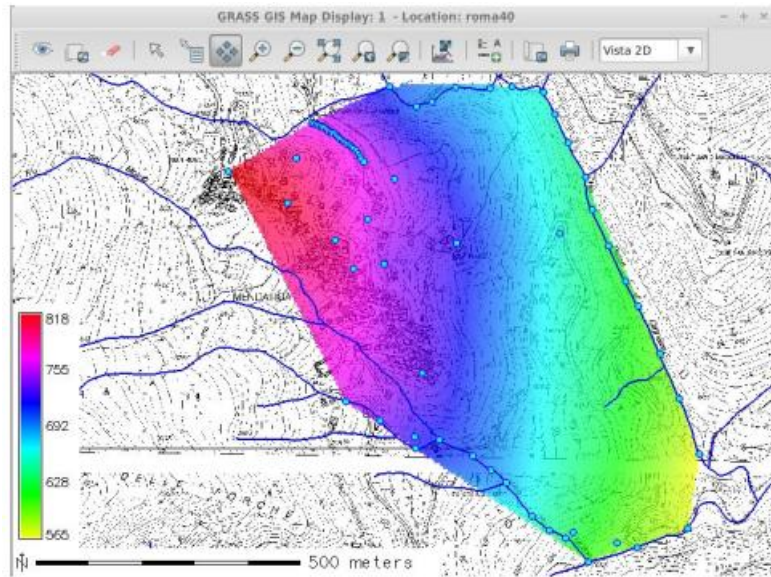


Figure 4.10. Average groundwater table surface [m a.s.l.]

Curve Number maps:

As detailed in *Section 3.1.1*, the generation of the CN maps is necessary to define the maximum storage capacity (S), which allows the runoff estimate (Equation 3.2) for each underground reservoir in which the landslide volume is schematized. Surfaces generation starts by defining the CN(II) map, describing intermediate soil wetting conditions, according to the soil Antecedent Moisture Condition (AMC) definition.

Input data are the Land Use map and the Hydrologic Soil Group (HSG) map, based on the geological knowledge.

The *Land Use map* is provided by the Liguria Region geoportal at a scale of 1:10000 (Figure 4.11). It describes the land use with minimum thematic unit of 0.5 ha and minimum polygon size of 10 m, and follows the standard CORINE 3th level legend, with peculiar specificities made explicit in the 4th level of the legend. Thus, according to the CORINE legend, the first number indicates the type (1= built-up area, 2= grassland, 3= woodland), while the subsequent numbers specify the characteristics (e.g. 1111= continuous and densely populated urban fabric, 1211= industrial areas, etc.).

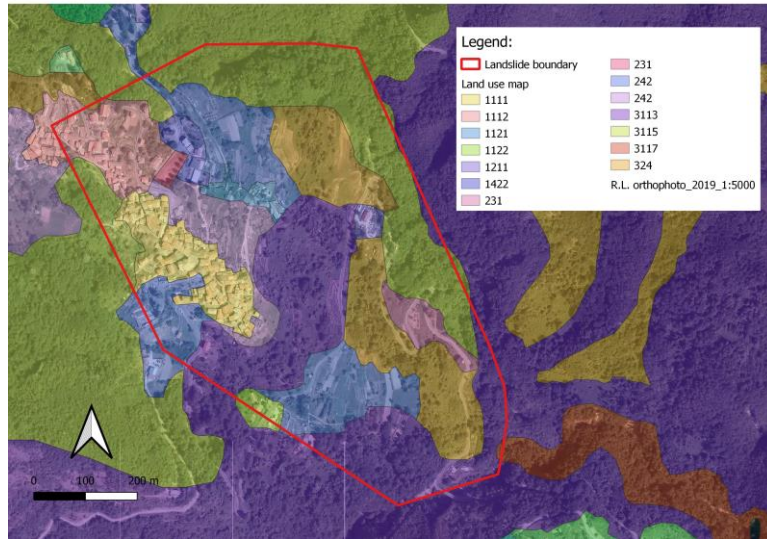


Figure 4.11. Land use map

According to the SCS method (1972-1975), four different CN values, functions of the different hydrological soil types, were assigned to each land-use class. The values, found in literature, are shown in Figure 4.12.

Cod.	Uso del suolo	A	B	C	D
1111	Tessuto urbano residenziale continuo e denso	61	75	83	87
1112	Tessuto urbano residenziale continuo mediamente denso	57	72	81	86
1121	Tessuto residenziale discontinuo e mediamente denso	57	72	81	86
1122	Tessuto residenziale discontinuo e sparso	51	68	79	84
1211	Aree industriali o artigianali	57	72	81	86
1422	Aree sportive (campo sportivo)	30	58	71	78
221	Vigneti	67	78	85	89
231	Prati stabili	30	58	71	78
242	Sistemi culturali e particellari complessi	62	71	78	81
243	Colture agrarie prevalenti con presenza di spazi naturali	62	71	78	81
3113	Bosco misto mesofilo	25	55	70	77
3115	Bosco a prevalenza di castagno	25	55	70	77
3117	Bosco di specie igrofile	25	55	70	77
312	Boschi di conifere	25	55	70	77
324	Aree a vegetazione boschiva ed arbustiva in evoluzione	45	66	77	83

Figure 4.12. Curve Number associated to each land use class.

In GRASS GIS, the database associated with the Land Use vector was updated with the introduction of four new columns of integer type (CN_II_A, CN_II_B, CN_II_C, CN_II_D), and then the automatic process of SQL instructions as follows:

(4.1)

The *HSG map* is representative of hydrological soil conditions and allows to associate a single characteristic Curve Number value to each area, defining the proper A-D hydrological type. It should be defined on the basis of soil geology, in accordance with the definition of hydrological classes described in paragraph 3.3.1. However, the Liguria Region geoportal does not provide the HSG map, hence it was created based on the results of the geognostic survey carried out in 2006-2007, looking at the stratigraphy of the first soil meters, as the CN value influences the runoff assessment. For boreholes characterized by sand and gravel mixtures (S4, S6, S7, S8, S10, S11), the hydrological Class A was associated; boreholes with silt and sand/gravel mixtures (S1, S2, S3, S5, S9, S13) were associated with type B, while borehole S12, characterized by clay silts, was associated with type C. No boreholes were associated to type D. The HSG map was then created by applying Thiessen's tessellation technique (*v.voronoi*) from the 13 boreholes, with subsequent fading to create homogeneous zones (*v.dissolve*) (Figure 4.13).

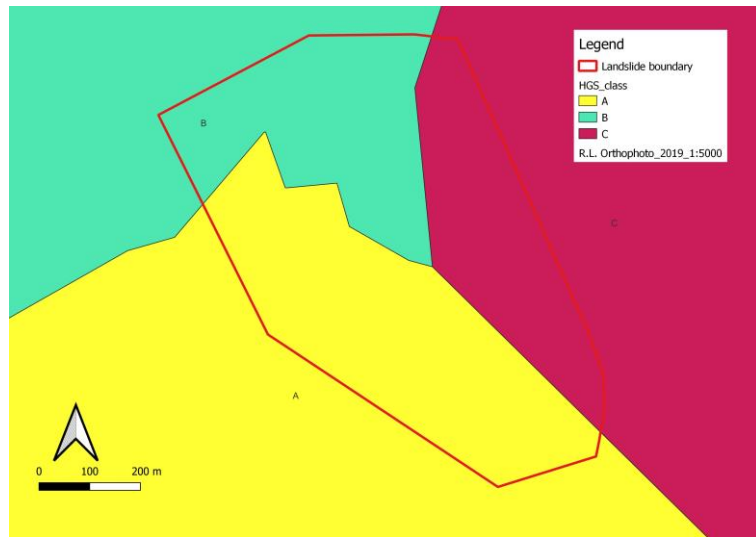


Figure 4.13. HSG map.

The overlap of the Land Use and HSG maps was performed, applying SQL instructions as follows:

```
db.execute UPDATE Vector Map SET CN_II=CN_II_A WHERE HGS_Type='A' (4.2)
```

Then the resulting vector layer was rasterized by using as attribute the new column CN_II. An example of *CN_II map* is showed in Figure 4.14.

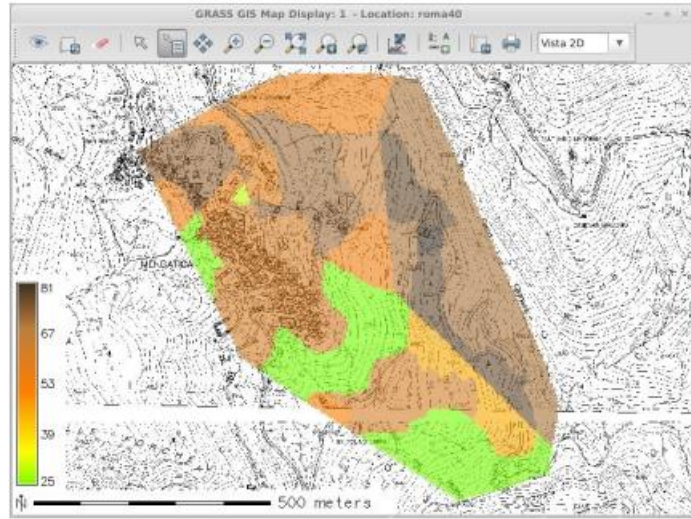


Figure 4.14. CN II map.

According to the soil Antecedent Moisture Condition (AMC) definition, the CN_I and CN_III maps, representing the dry (CN_I) and the wetting (CN_III) soil condition, are created by applying Equations (3.7) – (3.8), through the *r.mapcalc* command.

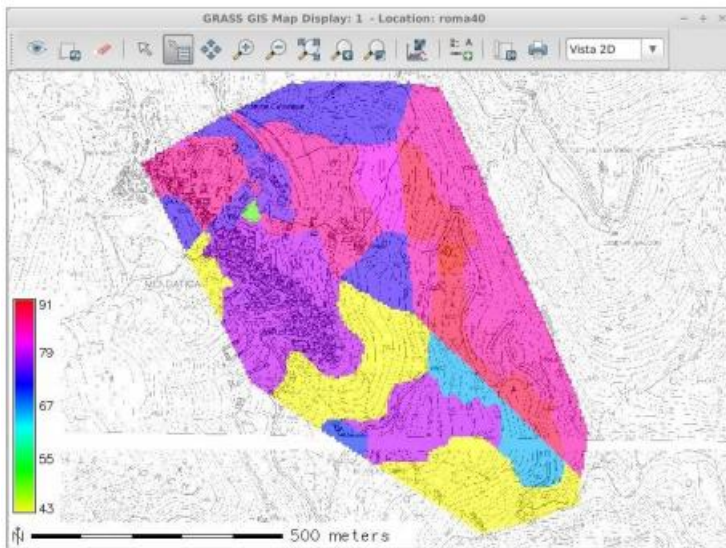


Figure 4.15. CN I map

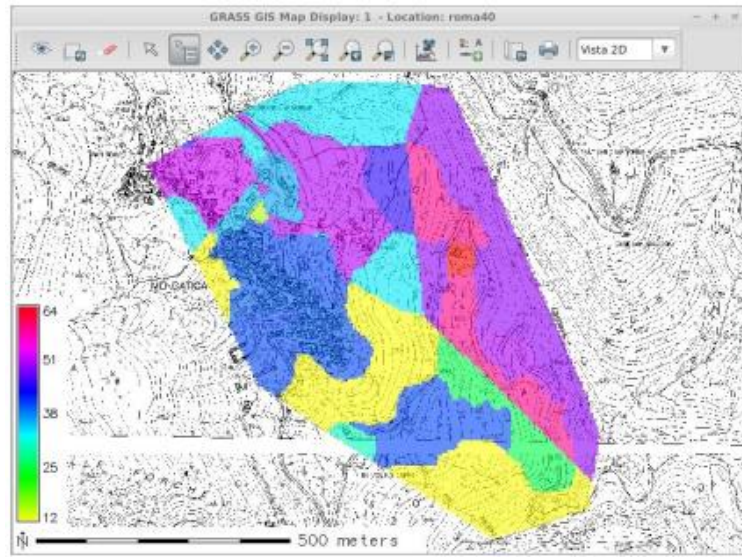


Figure 4.16. CN III map

Hence, three different S maps, relative to the maximum storage capacity in different soil Antecedent Moisture Condition (AMC), were created by applying Equation (3.6).

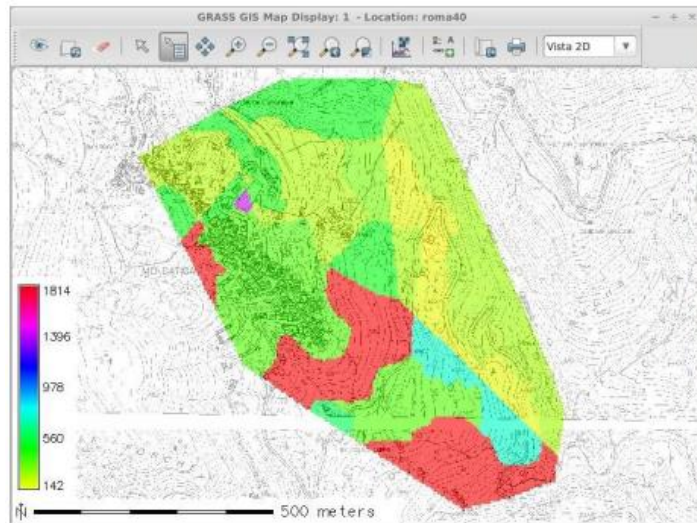


Figure 4.17. S I map

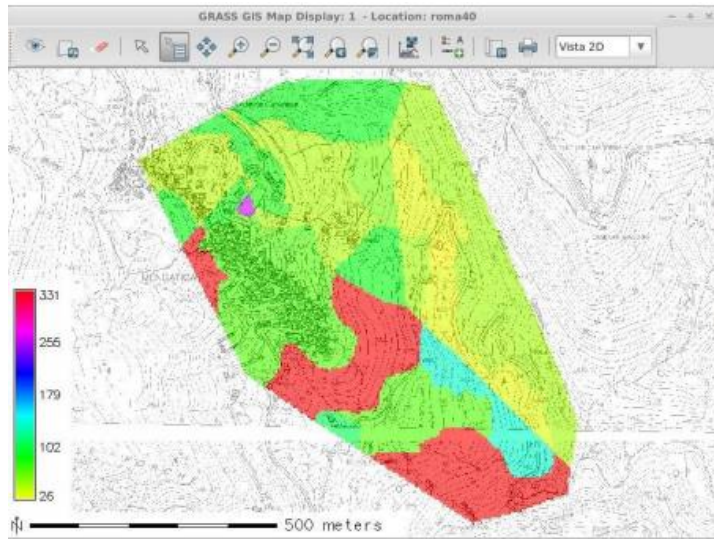


Figure 4.18. S II map

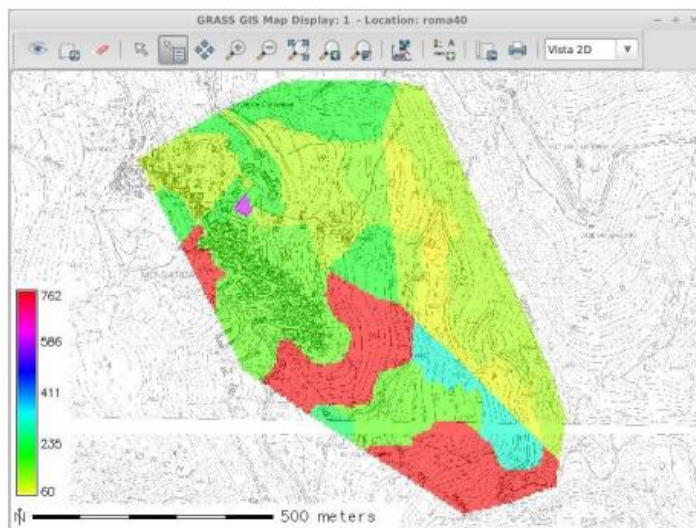


Figure 4.19. S III map

4.1.2. Calibration of the hydrological model

The modified CN hydrological model was calibrated with reference to the time series of groundwater level variations measured by the installed piezometers. This was implemented by means of four spreadsheets, one for each active piezometer (S3, S4, S6, S11).

Taking into account the measurement period of the piezometers, 14 rainfall events have been identified, here reported in Table 4.2.

	Beginning	End
Event 1	18/11/2007	21/11/2007
Event 2	07/01/2008	19/01/2008
Event 3	25/10/2008	09/11/2008
Event 4	05/04/2008	27/04/2008
Event 5	21/11/2008	04/12/2008
Event 6	06/12/2008	20/12/2008
Event 7	25/03/2009	08/04/2009
Event 8	13/04/2009	02/05/2009
Event 9	21/10/2007	29/10/2007
Event 10	19/12/2007	27/12/2007
Event 11	16/01/2009	23/01/2009
Event 12	26/11/2009	10/12/2009
Event 13	30/01/2009	10/02/2009
Event 14	17/06/2009	08/07/2008

Table 4.2 Time series rainfall events.

These events have been chosen for their strong intensity or their long-time duration. For each piezometer, the events have been divided in two classes, as reported in Table 4.3: events used to calibrate the model and events used for the validation. The validation of the events is performed by modelling and comparing the water table with the observed water table, using the hydraulic parametric estimated from the calibration phase.

Piezometer S6		Piezometer S3		Piezometer S4		Piezometer S11	
Calibration	Validation	Calibration	Validation	Calibration	Validation	Calibration	Validation
Event 1	Event 9	Event 1	Event 9	Event 1	Event 9	Event 1	Event 9
Event 2	Event 10	Event 2	Event 10	Event 2	Event 10	Event 2	Event 10
Event 3	Event 11	Event 3	Event 11	Event 3	Event 11	Event 3	Event 11
Event 4	Event 12	Event 4	Event 13	Event 4	Event 13	Event 4	Event 13
Event 5	Event 13	Event 5		Event 5	Event 14	Event 5	
Event 6	Event 14	Event 6		Event 6		Event 6	
Event 7		Event 7		Event 7			
Event 8		Event 8		Event 8			

Table 4.3 Rainfall events using in the calibration and validation phase

The calibration has been carried out in different steps, in order to provide the best results:

- 1) calibration with the initial H_{GWT} level equal to the average level, which is rainfall independent and easily known. In some cases, this condition significantly influences the results of the model showing a high deviation from the observed data.
- 2) Calibration with initial H_{GWT} level equal to groundwater table level recorded in the previous 24 hours. Usually an improvement in the model response is observed, but note that not always such data is available.
- 3) In order to improve the calibration phase, an optimisation of the effective porosity and of the permeability is introduced.

With regard to the effective soil porosity, the presence of the two soil layers with different characteristics observed in Mendatica (Figure 3.11) was taken into account in the calibration. Their position in correspondence of piezometer S6 and S4 and the effective porosity in each layer, derived from the calibration, are shown in Table 4.4. The calibration was performed by applying the objective function to both layers.

<i>S6</i>		<i>S4</i>	
$H_f < 15.5 \text{ m}$	$H_f > 18 \text{ m}$	$H_f < 28 \text{ m}$	$H_f > 33 \text{ m}$
Porosity	0.015	Porosity	0.012
$15.5 < H_f < 18 \text{ m}$		$28 < H_f < 33 \text{ m}$	
Porosity	0.012	Porosity	0.05

Table 4.4 Soil effective porosity for the different soil layers in the piezometer S6 (a) and S4 (b)

In addition, to correctly model daily runoff, a higher soil permeability is assigned on days when there is no rainfall, to facilitate groundwater subsurface flow. In the model, therefore, the calibrated permeability on all days is used only for rainy days, while the permeability on dry days is subject to a new calibration dedicated to dry days. The new soil permeability is detected for each of the four piezometers. (Table 4.5).

Piezometer	$ks_{recharge}$ [m/s]	$ks_{discharge}$ [m/s]
+S6	2.25e-07	3.29e-06
S4	1e-07	9.48e-06
S3	3.53e-07	7.85e-05
S11	1e-07	1.02e-05

Table 4.5. Soil permeability values derived by the optimized calibration

In Figure 4.20 a comparison of the observed and modelled GWT variations in the different calibration steps with reference to piezometer S6 and Event 1 (see Table 4.3) is shown. The blue line, representing the modelled GWT with reference to the average GWT value, has a shift in the order of 1.5 m compared to the

measured position (in red) at the beginning of the event. The grey line, representing the GWT level modelled on the 24-hour value, shows a better agreement with the red line in the initial phase. However, they are not able to reproduce the discharge phase in a satisfying way. The results of the optimized calibration are represented by the yellow line. The definition of two different soil permeability values, describing both the GWT charge phase and discharge phase ('no rainfall'), allows a more accurate modelling of the observed groundwater variations.

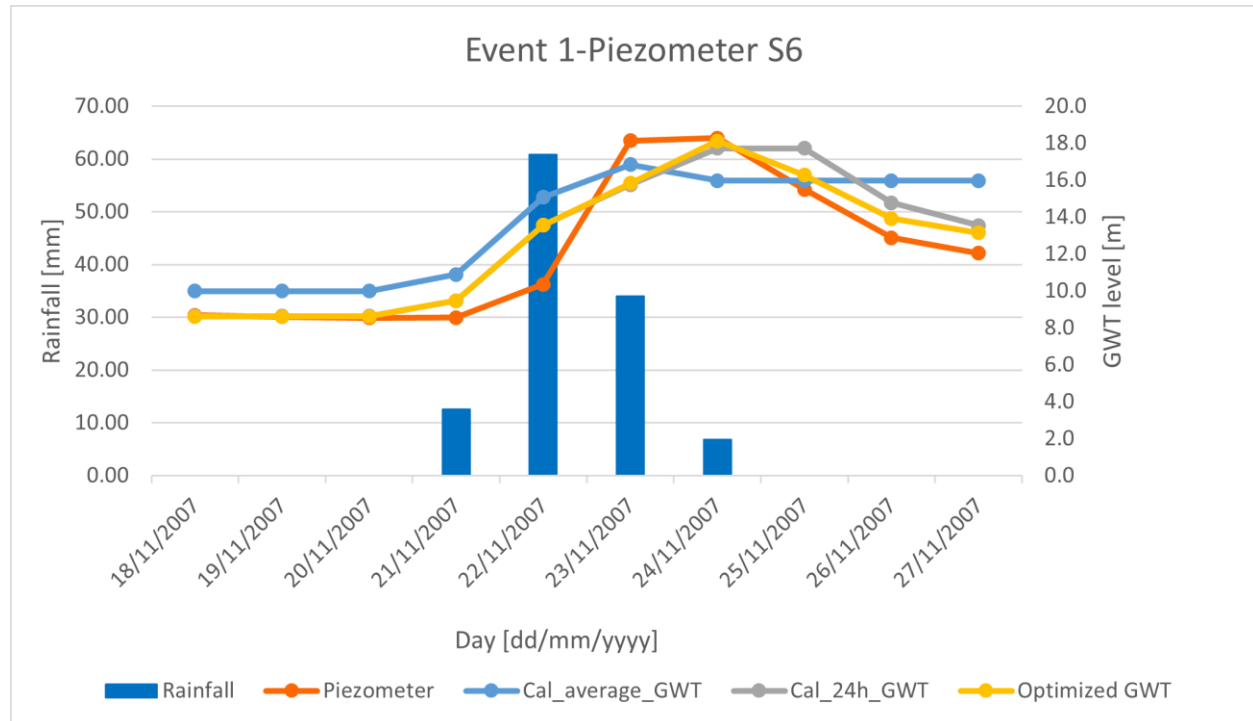


Figure 4.20. Optimised calibration GWT

The goodness of calibration is estimated according to the statistical indices defined in *Section 3.1.2*. Figure 4.21 shows the statistical indices calculated for the calibration step and the optimised step. The comparison shows a general growing of the correlation index, especially for S6 and S11, as well as a decreasing of the RMSE, from 4% to 3% for S6 piezometer, and PBIAS percentages, from 16% to 9% for S6 piezometer.

Performance indexes of the calibrated model

Calibrated event	Correlation [-]				RMSE [m]				PBIAS [%]			
	S3	S4	S6	S11	S3	S4	S6	S11	S3	S4	S6	S11
1	0,794	0,957	0,835	0,966	2,700	0,481	2,483	1,248	6,50%	1,05%	-10,03%	-3,49%
2	0,647	0,714	0,745	0,201	3,077	3,230	5,754	3,715	-7,80%	-8,64%	-14,97%	-10,06%
3	0,855	0,792	0,832	0,728	1,584	1,853	5,827	1,903	1,53%	-2,95%	-37,93%	-3,09%
4	0,876	0,802	0,780	0,451	1,385	0,768	2,617	1,352	2,87%	-0,73%	-9,01%	-3,00%
5	0,869	0,914	0,821	0,948	2,299	0,553	2,507	0,613	-8,67%	-0,92%	-13,95%	1,40%
6	0,795	0,820	0,828	0,398	2,309	3,995	6,691	5,105	0,88%	-9,97%	-15,50%	-13,43%
7	0,894	0,934	0,749		2,470	0,426	2,642		-9,25%	-0,62%	-9,93%	
8	0,818	-0,756	0,823		2,791	3,387	4,604		-8,90%	-7,42%	-15,41%	
Mean	0,819	0,647	0,802	0,615	2,327	1,836	4,141	2,323	-2,85%	-3,77%	-15,84%	-5,28%
Median	0,837	0,811	0,822	0,589	2,389	1,310	3,623	1,627	-3,46%	-1,93%	-14,46%	-3,29%
Dev.std	0,079	0,573	0,038	0,314	0,583	1,494	1,779	1,725	6,43%	4,25%	9,32%	5,43%

Performance indexes of the optimized model

Calibrated event	Correlation [-]				RMSE [m]				PBIAS [%]			
	S3	S4	S6	S11	S3	S4	S6	S11	S3	S4	S6	S11
1	0,749	0,898	0,914	0,873	2,668	0,638	1,667	0,815	6,20%	0,96%	-5,66%	-2,12%
2	0,751	0,694	0,878	0,408	2,474	1,809	2,657	1,976	3,46%	-4,81%	-3,35%	-5,26%
3	0,944	0,753	0,857	0,835	2,632	1,687	4,632	1,150	-8,69%	-3,06%	-28,73%	-1,33%
4	0,716	0,813	0,768	0,537	2,734	0,559	2,465	0,969	9,83%	-0,43%	-4,07%	-1,67%
5	0,633	0,803	0,885	0,888	1,959	0,595	1,771	0,995	-2,53%	-1,08%	-8,09%	2,68%
6	0,927	0,841	0,899	0,480	4,086	2,337	4,133	4,247	-10,07%	-6,18%	-7,28%	-11,39%
7	0,616	0,895	0,804		2,025	0,411	2,184		-4,31%	-0,66%	-5,64%	
8	0,918	-0,757	0,890		3,037	2,832	2,941		-8,09%	-6,31%	-7,62%	
Mean	0,782	0,618	0,862	0,670	2,702	1,358	2,806	1,692	-1,78%	-2,70%	-8,81%	-3,18%
Median	0,750	0,808	0,881	0,686	2,650	1,163	2,561	1,072	-3,42%	-2,07%	-6,47%	-1,89%
Dev.std	0,132	0,559	0,050	0,218	0,665	0,932	1,069	1,318	7,46%	2,80%	8,22%	4,75%

Figure 4.21. Comparison on statistical indices

Subsequently, a validation was carried out to verify the goodness of the estimation of hydraulic parameters in response to rainfall events not considered during calibration (Table 4. 3). In the Table 4.6 the standard deviation between the modelled GWT and the observed one in the available piezometers is reported. The highest values refer to piezometers where the groundwater table has high oscillation, hence the obtained standard deviation is acceptable.

Piezometer	ΔGWT [m]	$\sigma_{validation}$ [m]
S6	12.0	1.67
S4	2.52	0.52
S3	8.0	1.51
S11	2.15	0.46

Table 4.6. Validation: standard deviation between the modelled GWT and the observed one in four piezometers.

4.1.3 Hydraulic parameter mapping

As detailed in the *Section 3.1.2*, the calibration and optimization phases allowed to define the soil hydraulic parameters, i.e. the effective porosity and permeability, in correspondence of the piezometers, that are few points inside the landslide body. The most suitable techniques for data interpolation and extrapolation were then applied, as described in *Section 3.3.2*.

The *soil permeability map* has been generated through the definition of a linear relationship between the four known values of soil permeability and the blanket depth in correspondence of the piezometers. Two different linear relationships were defined in order to reproduce the groundwater recharging and discharging GWT phases (Figure 4.22 and 4.23).

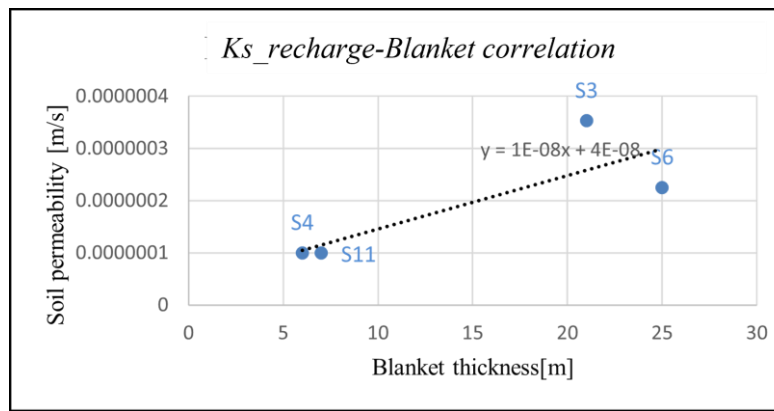


Figure 4.22. Linear regression between k_s and blanket thickness for the GWT recharging phase.

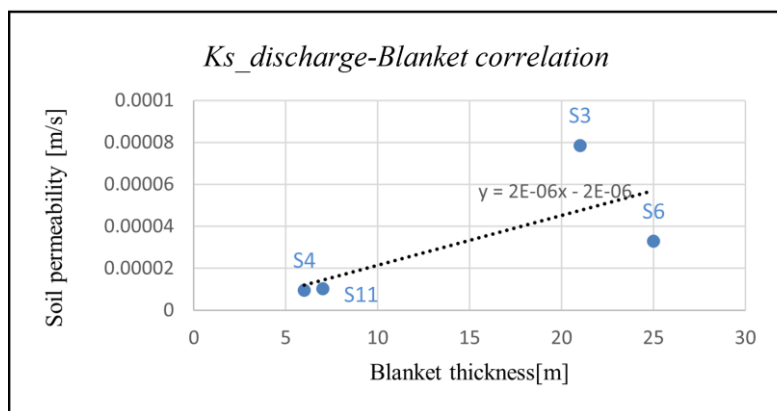


Figure 4.23. Linear regression between k_s and blanket thickness for the GWT discharging phase.

However, even if the soil permeability derived by these linear correlations is different from the optimized values for high blanket thickness, the effect on the ability of the IHG model to reproduce the GWT oscillation is small. Figure 4.23 shows the groundwater elevation calculated with both optimised and interpolated soil permeability values with reference to a rainfall event occurred in November 2011 for

piezometer S6. The graph shows good agreement between the interpolated GWT trend (yellow line) and the optimised GWT trend (grey line), also reproducing the piezometric level (blue line) correctly.

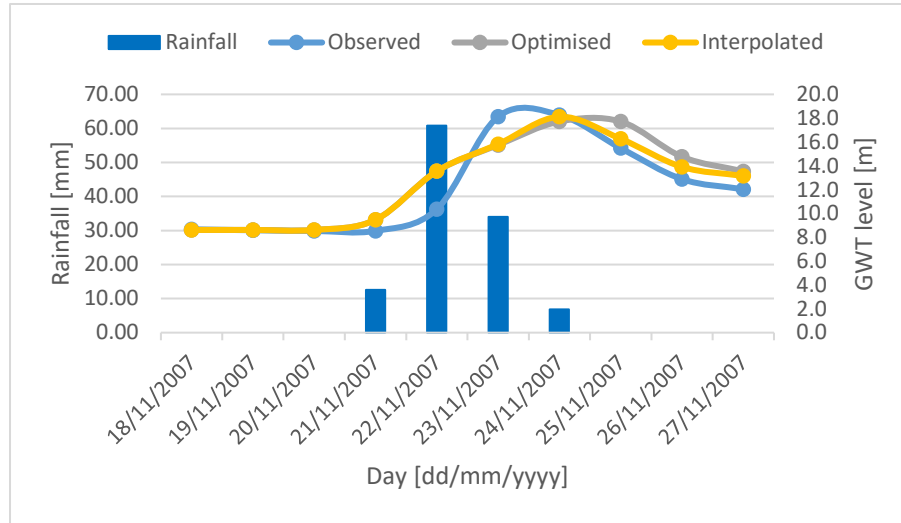


Figure 4.23. Comparison of GWT level calculated with interpolated and optimized soil permeability values

Applying the following linear regression equations:

$$K_{s_recharge} = 10^{-8}x + 4 \times 10^{-8} \quad (4.3)$$

$$K_{s_discharge} = 2 \times 10^{-6}x + 2 \times 10^{-6} \quad (4.4)$$

where the variable x represents the blanket depth, defined as the difference between the DTM and the groundwater surfaces, the soil permeability map can be calculated, are shown in Figure 4.24 and 4.25 for recharging and discharging phases.

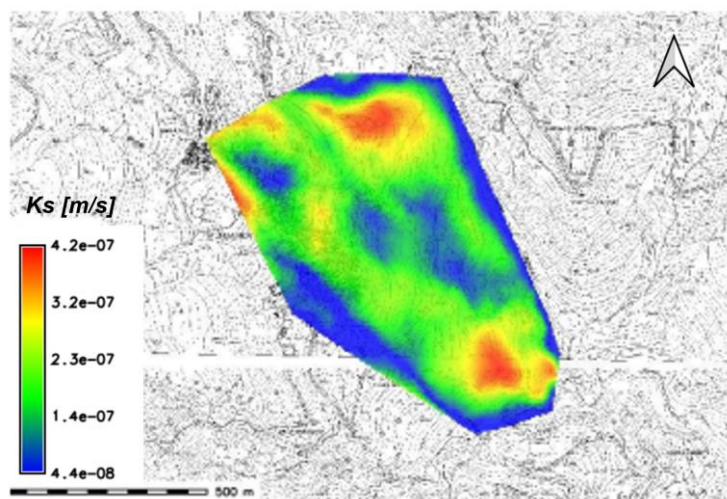


Figure 4.24. Soil permeability map for GWT recharging phase: (k_s _recharge)

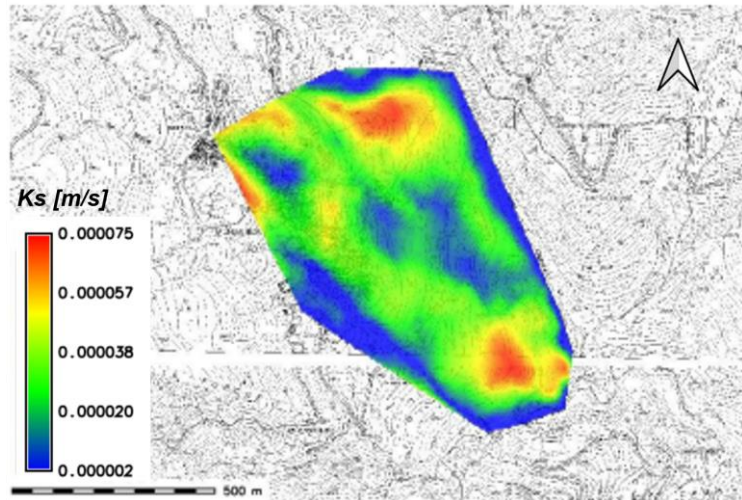


Figure 4.25. Soil permeability map for GWT discharging phase: (ks_discharge)

The soil permeability surfaces allow to compute the *discharge constant maps* λ by applying Equation 3.16, where ϑ is the maximum slope angle pertinent to each pixel, derived from the DTM (through *r.slope.aspect* command). To compute the Equation 3.16, the tangent of ϑ has to be calculated (through *r.mapcalc*). It is worth to underline that in the case of $\vartheta \approx 0$, extremely low values of the tangent are obtained, which can lead to subsequent numerical problems. To avoid this criticality, the tangent values is imposed equal to 0.01 where $\vartheta \approx 0$. When the hydrological analysis is conducted on a daily scale, the constant must be expressed in [1/day], hence the Equation 3.16 must be multiplied by 86400.

Two constant discharge maps are generated, relating respectively to the recharging (*Lambda_1*) and discharging (*Lambda_2*) GWT phases, as showed in Figure 4.26 and 4.27.

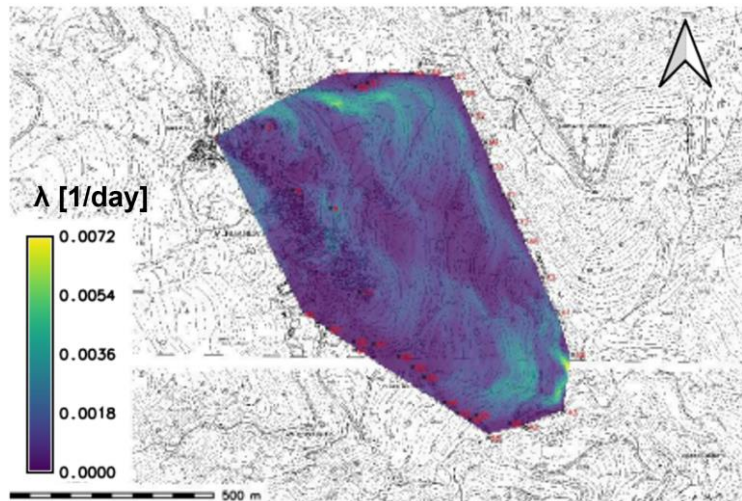


Figure 4.26. Discharge constant map for recharging phase (*Lambda_1*)

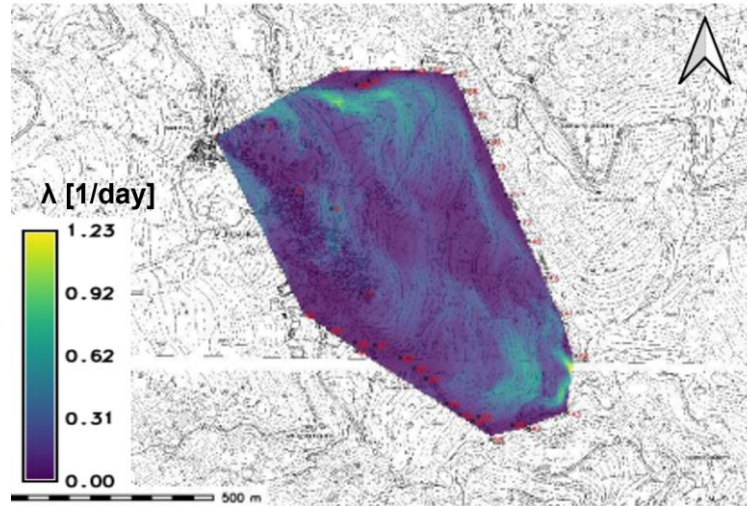


Figure 4.27. Discharge constant map for discharging phase (*Lambda_2*)

The effective soil porosity maps are generated by using the “stratigraphic similarity”, as detailed in Section 3.3.2. The “stratigraphic similarity” has been applied by comparing the borehole loggings of the 13 boreholes with the well-known soil effective porosity values (Table 4.7) in the piezometers (S3, S4, S6, S11). Because of the presence of two layers in Mendatica blanket (Figure 3.11), porosity data for the upper (and lower) layer, named n_{e1} , are shown in Tables 4.7, while data for the internal layer, named n_{e2} , are shown in Table 4.8 where present.

Borehole	Piezometer	n_{e1} [-]
S1	S3	0.021
S2	S3	0.021
S5	S6	0.02
S7	S11	0.046
S8	S6	0.015
S9	S6	0.015
S10	S11	0.046
S12	S3	0.021
S13	S4	0.02

Table 4.7. Soil effective porosity for the soil 1

Borehole	Piezometer	$n_{e2} [-]$
S2	S6	0.012
S5	S4	0.05
S8	S6	0.012
S9	S4	0.05
S10	S6	0.012

Table 4.9. Soil effective porosity for the internal soil layer

After defining the porosity values in the 13 surveys for the upper (and lower) layer and in the 7 boreholes for the inside layer, the surfaces were generated. The most suitable technique for creating the porosity maps of the two layers was the linear TIN method, based on the Delaunay algorithm inside the region between the known values at the boreholes, 13 in the case porosity map n_{e1} , 7 in the case of porosity map n_{e2} . Spatialisation over the entire area was performed using IDW (Inverse Distance Weighting) interpolation (through *r.surf.idw*, with *npoints*=1) starting from the boundary data of the TIN raster map. The final maps, named n_{e1} and n_{e2} , are illustrated in Figure (4.28).

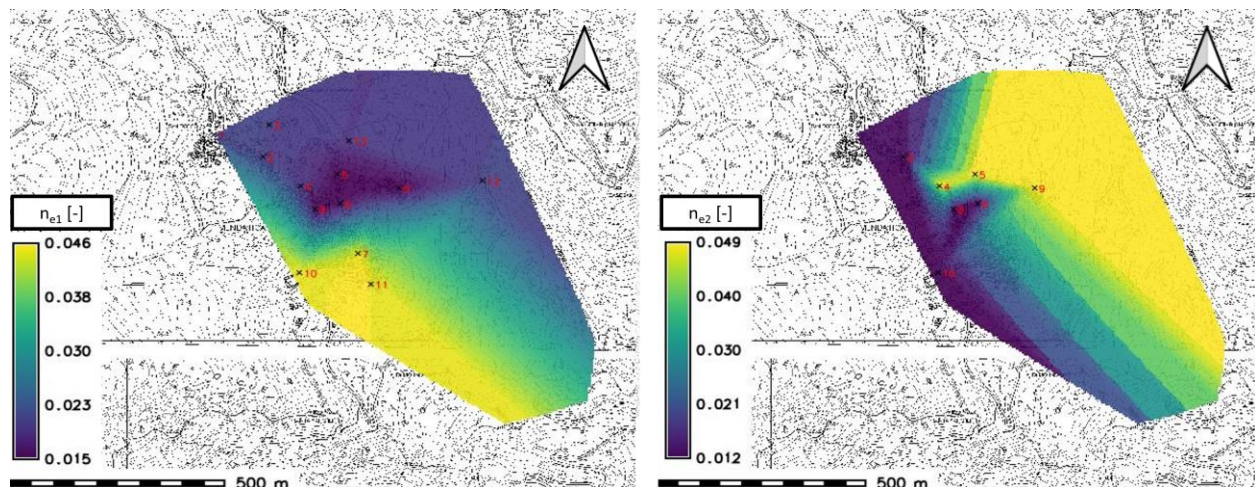


Figure 4.28. Soil effective porosity maps, for the soil 1based on the TIN interpolation between the 13 boreholes (a) and for the internal soil layer, based on the TIN interpolation between 7 points (b).

The spatialization of the soil hydraulic parameters, i.e. the effective porosity and permeability, allows to apply the integrated hydrological-geotechnical analysis for landslide susceptibility assessment in every cell of the landslide body.

4.1.4 Groundwater table evolution

The hydrologic modelling produces GWT height maps (H_f) every day of the analysed event.

The results relative to the two analysed events are here described as the goodness of modelling, estimated in terms of groundwater variation, by examining the GWT height maps at known points, i.e. the piezometers.

Event of January 2008

The modelled groundwater response was compared with S6 piezometric measurements in Figure 4.29. The variation of the modelled GWT (in orange) reproduces quite well the observed data (in grey), mimicking the GWT recharging and discharging phases, even if underestimating the initial peak. Some differences in the initial phase of the event are present, although the groundwater at day 0 was fixed as the level of the previous 24 hours. The difference of about 1.5 m can be related to the fact that the groundwater in a discharging phase due to a previous rainfall event, despite the fact that in the 48 hours before the first day of the event no rainfall occurred.

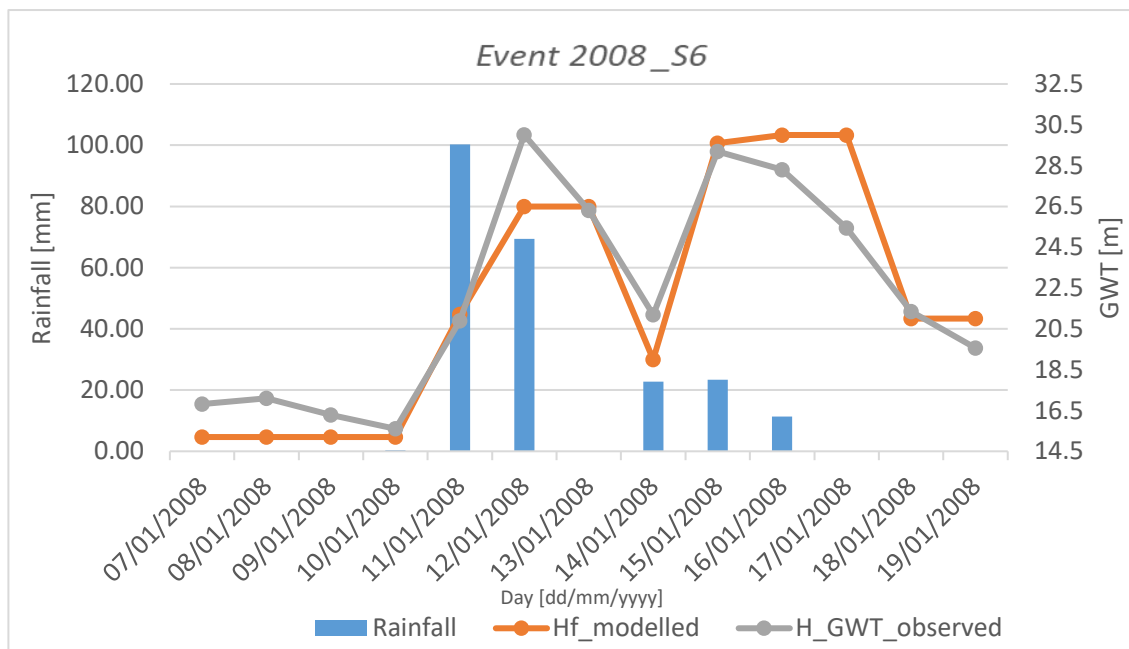


Figure 4.29. Comparison between GWT modelled (in orange) and the GWT recorded at piezometer S6.

The statistical indices (Table 4.10) calculated for IHG modelling show high correlation values between modelled and observed GWTS; the values of RMSE and PBIAS % are comparable with those obtained in the optimized calibration (Figure 4.21), confirming the goodness of modelling.

Piezometer S6

Correlation [-]	RMSE [m]	PBIAS [%]
0.941	1.98	-1.44

Table 4.10 Statistical indexes

Event of December 2019

The modelled groundwater response was compared with S11 piezometric measurements in Figure 4.30. The variation of the modelled GWT (in orange) tends to underestimate the observed trend (in grey). This may be due to the fact that the elaboration started from an average GWT value, that is about 70 cm lower than the observed value. Although 70 cm is a lower value than the initial gap observed when analysing the Event 2008, it should be noted that the blanket in S11 has a lower height than in S6, so lower oscillations usually occur in S11.

Statistical indexes show a good agreement between the GWT levels, comparable with the indexes detected during the calibration phase and in the previous analysed event.

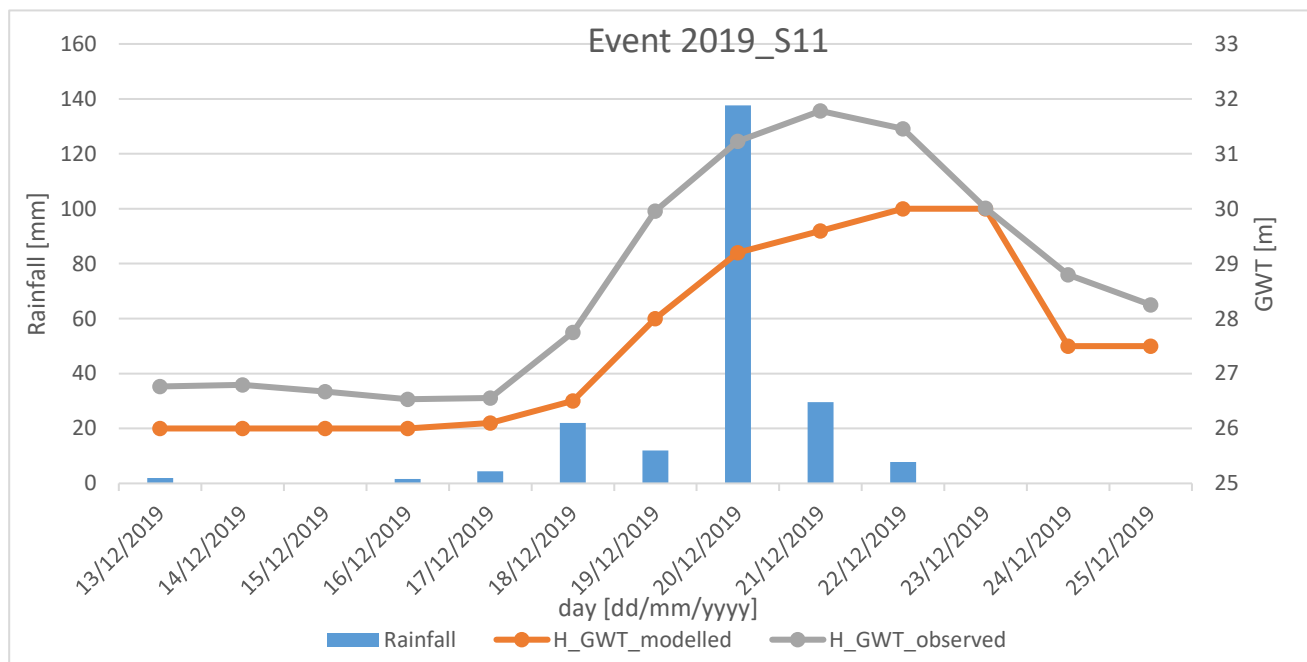


Figure 4.30. Comparison between GWT modelled (in orange) and the GWT recorded at piezometer S11

Piezometer S11

Correlation [-]	RMSE [m]	PBIAS [%]
0.954	1.26	-3.71

Table 4.11 Statistical indexes

4.1.5 Slope stability analysis

According to the slope stability analysis detailed in Section 3.1.3, the landslide susceptibility can be calculated by applying Equation 3.63, in occurrence of the chosen rainfall event that trigger the GWT oscillation.

In order to perform the stability analyses, geotechnical characterization of the study site was required. Both analyses were conducted using the geotechnical parameters detected by the results of laboratory tests

on samples, relating to the S4 and S11 boreholes, carried out by Macciò (2007). For the two boreholes, with reference to the investigated sample depth (z sample), the values of soil unit weight (γ), friction angle (φ') and effective cohesion (c') are summarized in Table 4.12.

Borehole	z sample [m]	γ [kN/m ³]	φ' [°]	c' [kPa]
S4	10.55-10.90	23.02	32.5	4.7
S4	17.65-18	22.29	29.-8	9.4
S13	5.65-6.0	23.11	-	-
S13	8.65-9.0	22.53	28	1.6
S13	16.35-16.7	22.42	28	5.1

Table 4.12. Soil physical-mechanical parameters

The friction angle was assumed to be 28° in favor of safety. The soil unit weight was assumed to be 23 kN/m³, while it was assumed equal to 10 kN/m³ for the water. For each of the previous parameters, a map of constant values was created in GRASS GIS.

The slope stability analysis requires, as input data, the definition of the parameter m to describe the groundwater table position in the 3D volume at the beginning of the rainfall event (*day 0*). m has to be spatially defined as the ratio of the water table height to the DTM with reference to the stable layer or bedrock (Equation 3.62), thus representing the daily GWT variation in each cell.

Based on the knowledge of the physical-mechanical parameters of the soil and the definition of the parameter m relative to the first day of the event, the landslide susceptibility map for the first day is calculated applying the Equation 4.5 as follows:

$$FS_{initial} = \frac{\tau_f}{\tau} = \frac{(\gamma - m\gamma_w) \tan \varphi'}{\gamma \tan \vartheta} \quad (4.5)$$

The same slope stability analysis must be applied to the subsequent days of the analysed event, given the level of GWT derived from the hydrological modelling as described above.

Event of January 2008

The GWT surface at the beginning of the 2008 Event was defined as equal to the level of the previous 24 hours. In Figure 4.31 each pixel represents the initial volume (V_o) of the 3D element, defined as the difference elevation between the initial GWT and the bedrock.

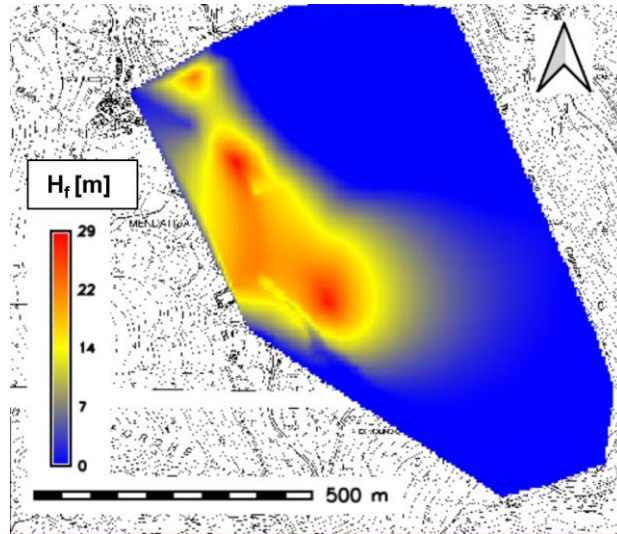


Figure 4.31. Groundwater table map at the beginning of the event (07/01/2008)

The safety factor derived by the slope stability analysis relative to the initial water volume (V_o) is shown for each pixel discretizing the study area (Figure 4.32). This map is fundamental for the creation of the stability condition variation map, which is one of the main outputs of the model.

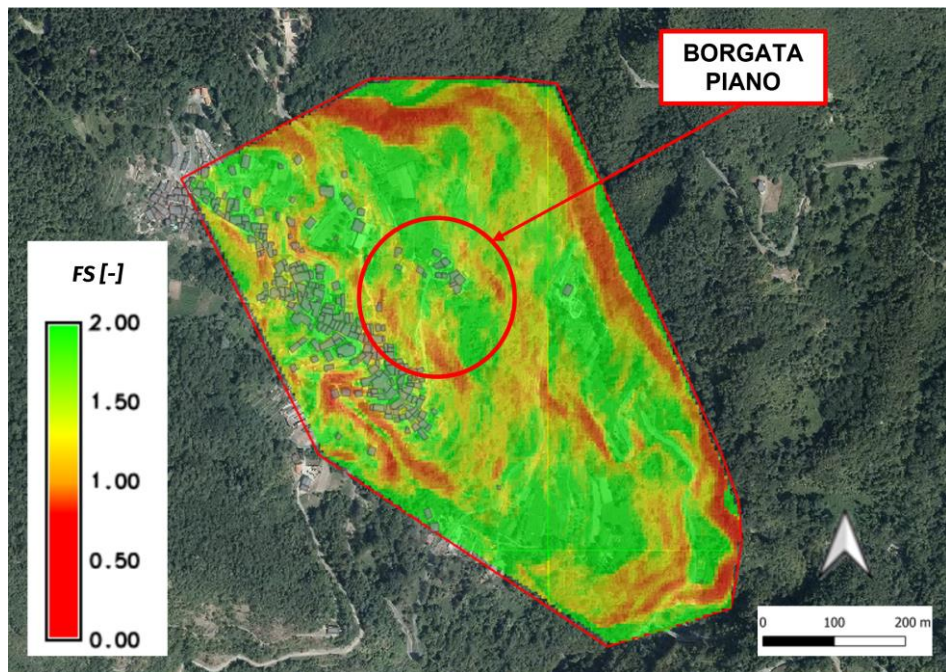


Figure 4.32. FS map at the beginning of the event (07/01/2008)

The most critical areas in Figure 4.32. are in the perimetral zones of the analysed area, due to the model boundaries along the riverbeds, which minimises the value of the m factor, making the factor of safety dependent only on the slope of each pixel, shown in Figure 4.33.

Moreover, some areas in the central part of the study area, corresponding to Borgata Piano, are confirmed to be unstable, in agreement with the geological report of Macciò (2007).

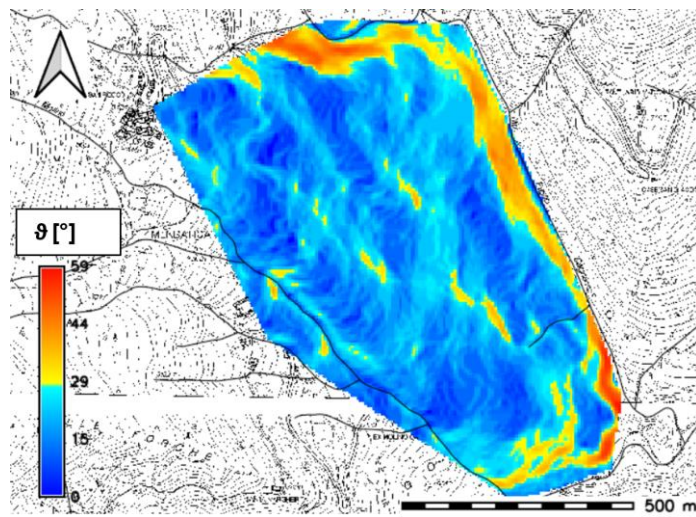


Figure 4.33. Slope map

Note again that the IHG modelling, at the scale of detail at which it works, does not take into account the possible presence of stabilising works (i.e. retaining walls). This leads to the identification of unstable areas, which are actually not unstable in the absence of critical rainfall events.

The daily IHG analysis allows us to appreciate the variation in slope stability due to GWT variations, in terms of safety factor. Figure 4.34 shows the most significant FS maps for the Event 2008. Green colour represented FS>1 (stable areas), yellow colour FS equals to 1 (area of incipient destabilization), while the critical areas, with FS<1, are depicted in red. According to the variation in rainfall intensity, there is an increase in the unstable areas (red areas), reaching a most critical condition on 12/01/2008, after a two-day cumulative rainfall of 170 mm. The map of stability conditions at the end of the rainfall event (19/01/2008), shows slight changes in the FS compared to the days of maximum rainfall (11-12/01/2008). This is in agreement with the rainfall history represented in Figure 4.30, which shows a cumulative precipitation of about 50 mm between 14/01/2008-16/01/2008.

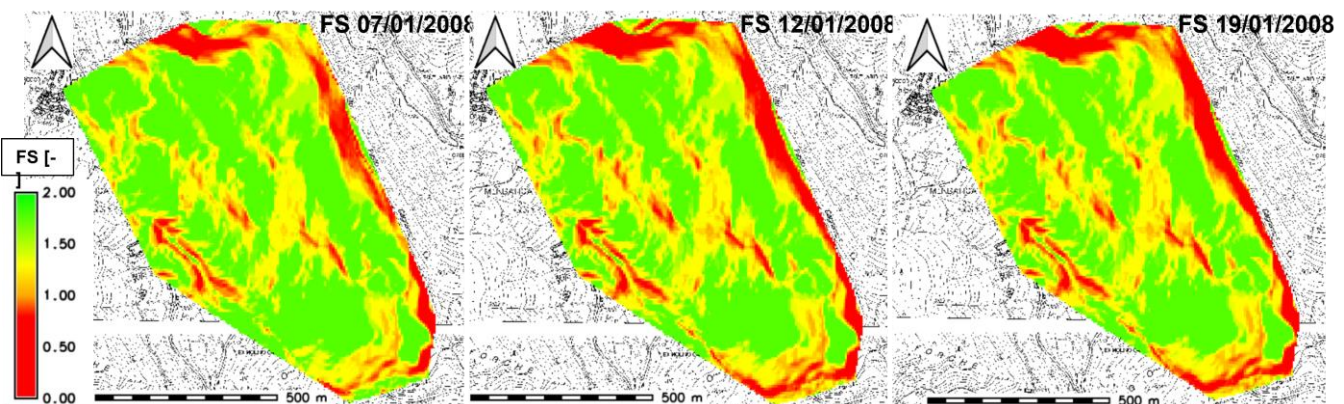


Figure 4.34. FS maps related to the most significant day of the Event 2008

These maps allow for a qualitative assessment of landslide susceptibility, identifying critical areas, but do not allow for highlighting areas that have become unstable due to the rainfall event alone. It is therefore recommended to create the stability condition variation map, which allows to distinguish between areas made unstable by the specific rainfall event (red areas) from those which were considered unstable before the rainfall event due to hydro-geo-morphological causes or because the presence of stabilisation works is not taken into account in this modelling (blue area). The stability condition variation map for the Event 2008 is showed in Figure 4.35. The percentages of cells that fall into the three classes described above were calculated (through *r.stats* in GRASS GIS) (Table 4.13).

Class	Class description	% Cells
0 (white)	Always stable	75.9
1 (red)	Unstable due to the current event	5.7
2 (blue)	Already unstable	18.4

Table 4.13. Percentage of cells belonging to the three different classes (cell area 25m²)

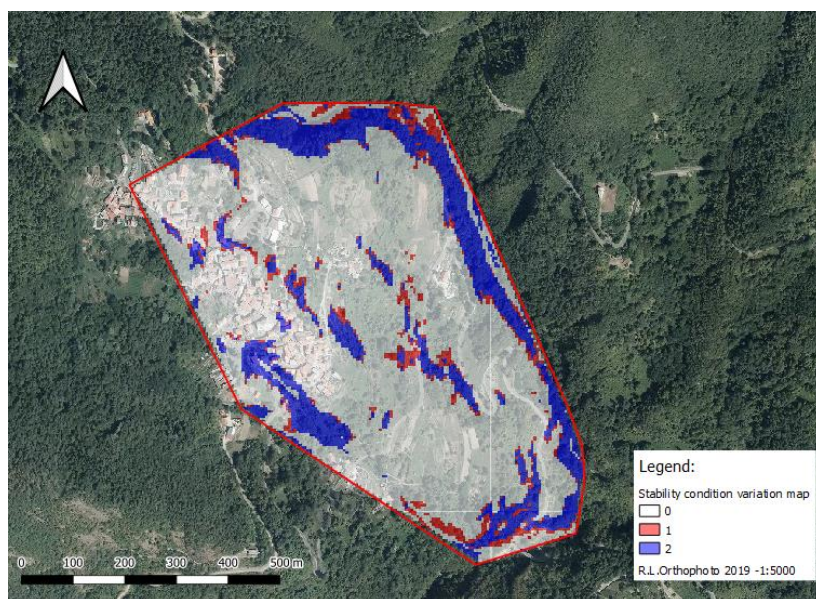


Figure 4.35. Stability condition variation map for the Event 2008

Event of December 2019

The initial GWT surface has been defined by spatialising the average values calculated in each piezometer, actually active in the landslide body. This choice is linked to the high number of piezometers active in 2019, which allow an accurate characterization of the average GWT level. Moreover, one of the goals to be achieved is the ability to carry out IHG modelling even in the absence of updated groundwater data, due to faults in the active instrumentation, starting the IHG modelling from the average GWT.

The average GWT table has been generated through a TIN interpolation between the known GWT values at 11 piezometers and the model boundaries on the landslide perimeter, previously described. The initial GWT is showed in Figure 4.36.

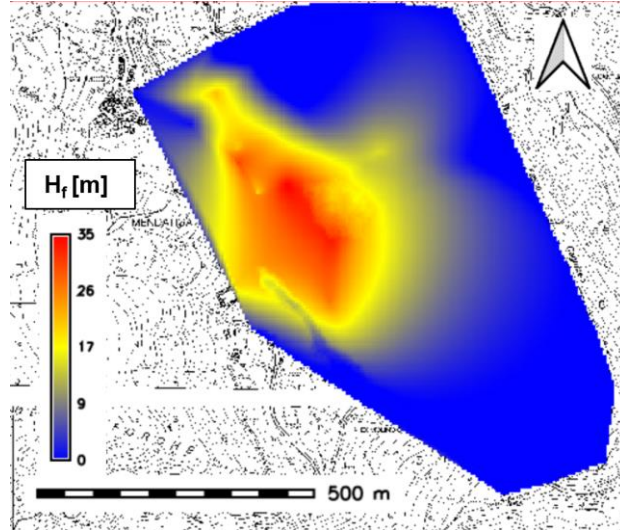


Figure 4.36. Groundwater table map at the beginning of the event (13/12/2019)

Compared to the initial GWT level for the 2008 event (Figure 4.31), it is possible to appreciate a more detailed spatialisation of groundwater height, which is linked to a wider knowledge about the groundwater behaviour in 2019. Obviously, proper modelling of the GWT is complex, as the water table fluctuates and levels may be separated or connected at different depths (Macciò, 2007).

Once the initial volume has been defined, the initial Safety Factor map may be calculated. The map in Figure 4.37 identifies the same critical zones as the map derived for the 2008 event, at the boundaries of the area and in Borgata Piano. However, in correspondence with this last zone, the area is more critical because the initial *GWT* in 2019 was higher than the one in 2008 (in blue and cyan respectively in Figure 4.38). This could be due to the lack of GWT data in 2008 with respect to 2019. In 2008 model boundaries could have influenced more the central area close to Borgata Piano lowering the groundwater heights (Figure 4.39). The difference can be appreciated also with reference to transversal cross section (Figure 4.40).

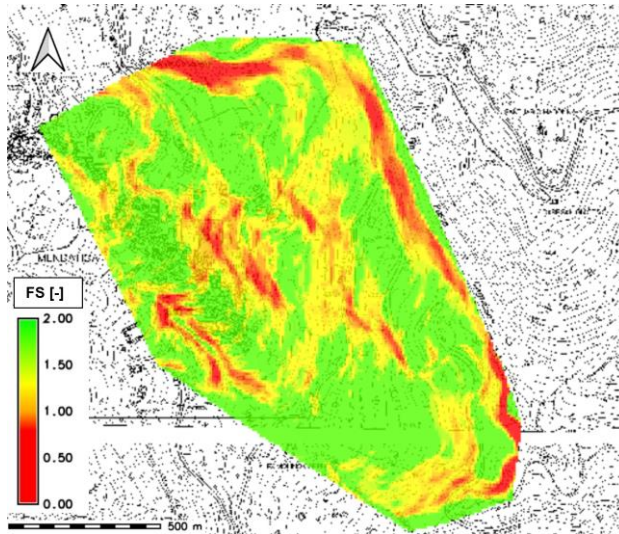


Figure 4.37. FS map at the beginning of the event (13/12/2019)

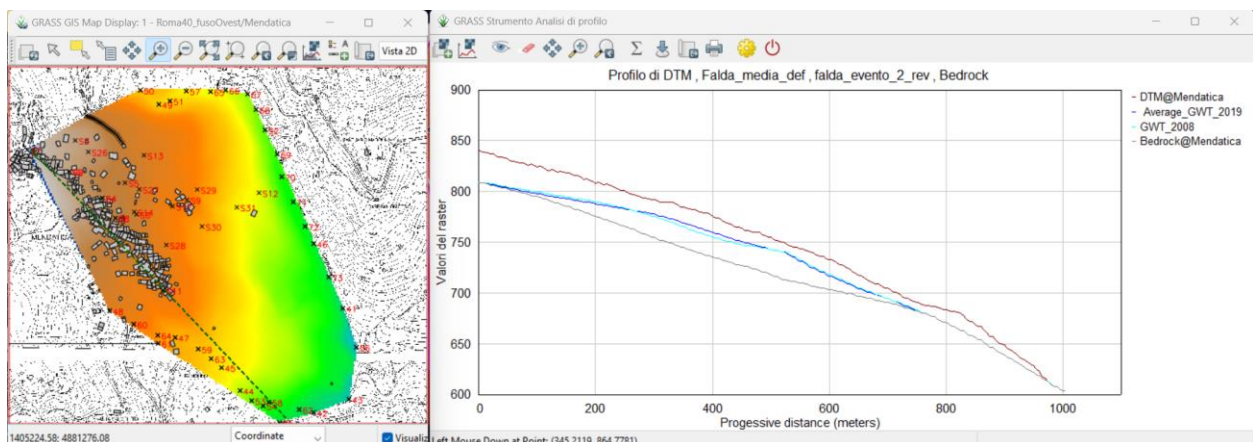


Figure 4.38. GWT_2019-2008 comparison along the cross-section AA

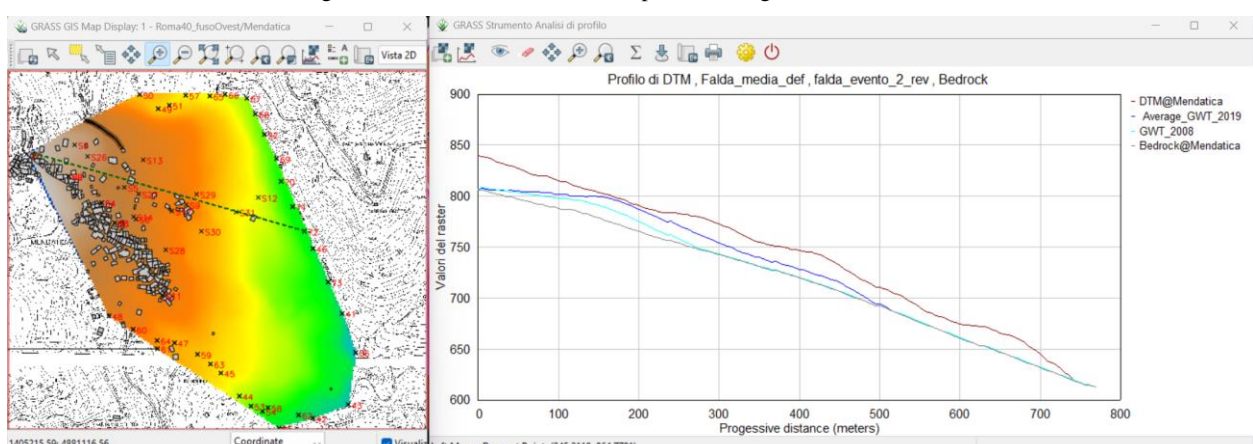


Figure 4.39. GWT_2019-2008 comparison along the cross-section CC

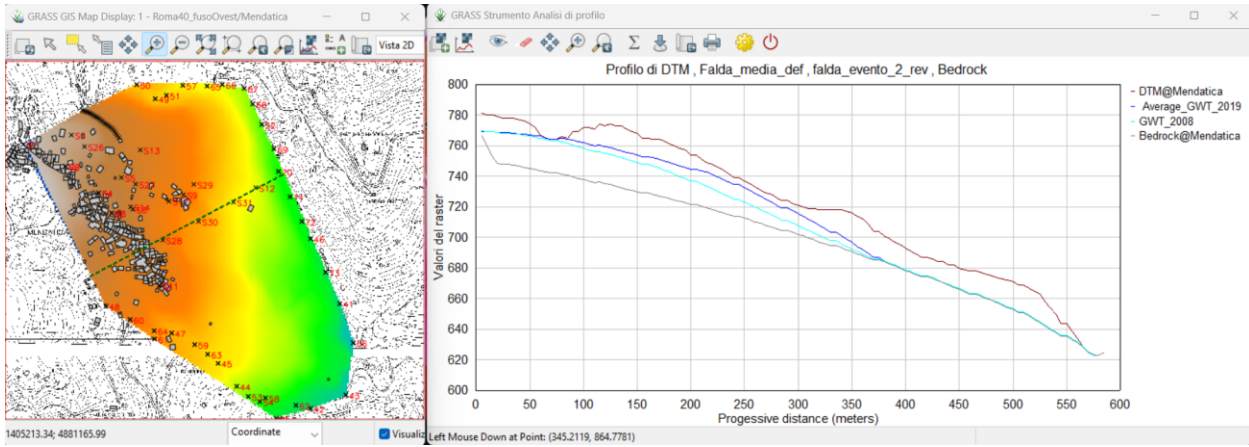


Figure 4.40. GWT_2019-2008 comparison along the transversal cross section

The daily analysis allows us to appreciate the variation in slope stability due to GWT variations, in terms of FS. Figure 4.41 shows the most significant FS maps for the 2019 event.

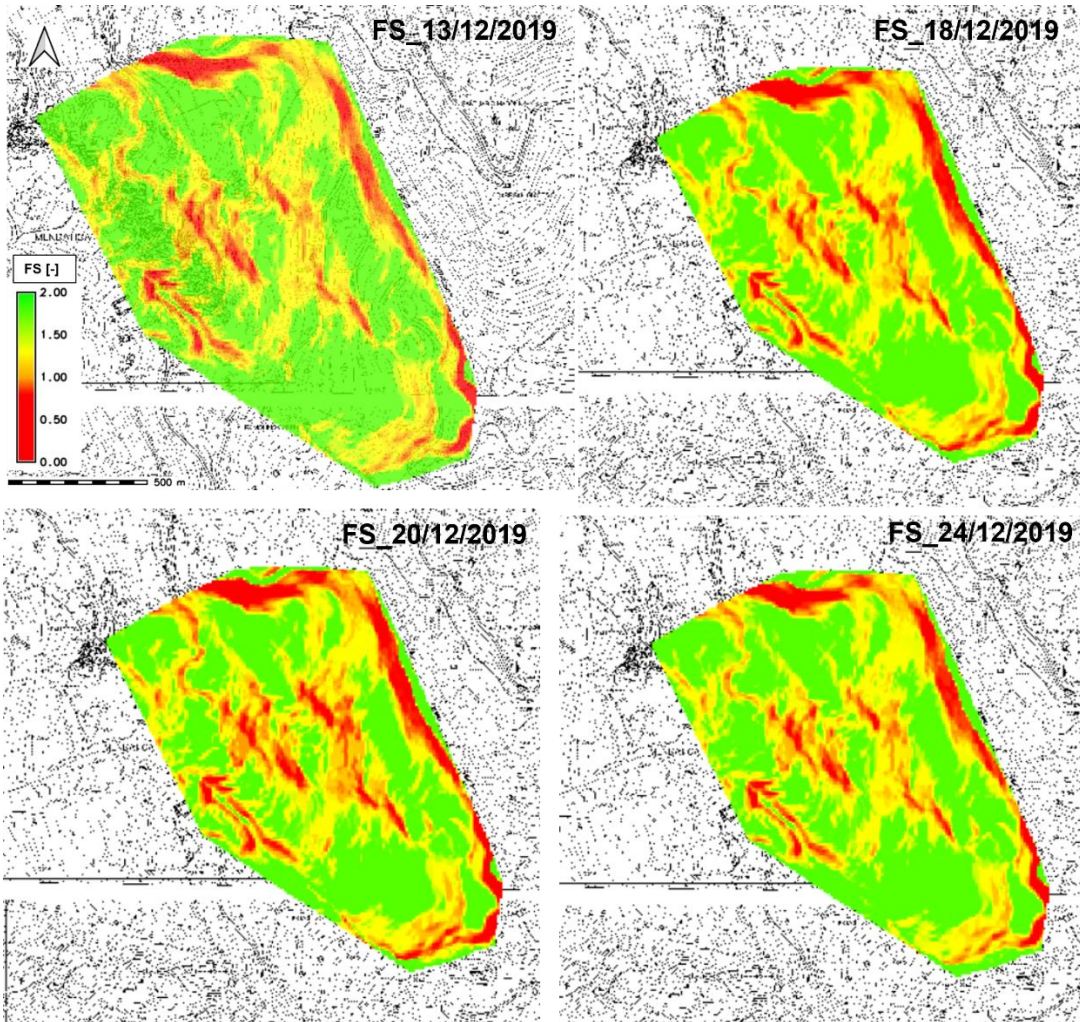


Figure 4.41. FS maps related to the most significant day of the Event 2019

According to the variation in rainfall intensity (Figure 4.3), there is a first important variation in stability condition on 18/12/2019, the increasing unstable areas reached a most critical condition on 20/12/2019, after the rainfall peak of 140 mm. Thereafter, an opposite trend is recorded, with safety factors increasing again. The number of unstable cells is detected in function of the stability variation map, as shown in Table 4.15.

Class	Class description	% Cells
0 (white)	Always stable	69.2
1 (red)	Unstable due to the current event	6.2
2 (blue)	Already unstable	24.6

Table 4.14. Percentage of cells belonging to the three different classes (cell area 25m²)

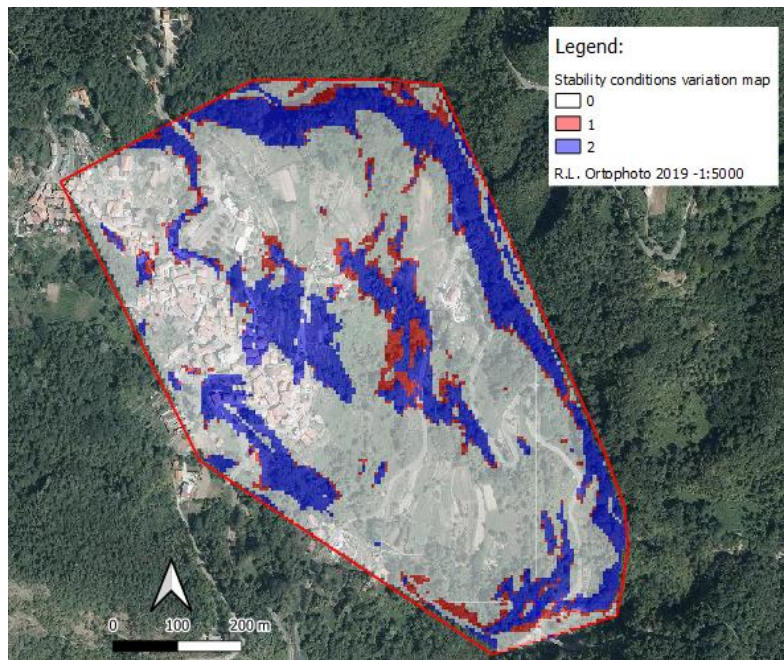


Figure 4.42. Stability condition variation map for the Event 2008

Comparison to Table 4.13 shows an increase of unstable cells (class 1) according to the differences detected in the initial FS_maps. This aspect affects also the number cells belonging to the class 2 and this is related to the fact that in the first case the strength contribution due to the cohesion is not taken into account and the instability is merely related to the pixel slope.

4.1.6 In situ validation

In the latter section, in accordance with the guidelines proposed by Fell et al. (2008), the results provided by the IHG model are validated by considering the on-site damages to the elements exposed to landslide risk. Before proceeding with the comparisons, attention has to be focused on the assumptions underlying

the procedure. It relates to the fact that the 3D discretization elements, as already underlined, are not assumed mechanically interacting. This means that any slope portion does not influence its contiguous portions and vice versa. Hence, a proper interpretation of the modelling results is necessary.

With reference to Borgata Piano, one of the areas most affected by the landslide reactivations over the years, the analyses carried out by the IHG model highlights the critical area, delimited by the blue circle in Figure 3.42. However, the criticality is not detected in the most upstream part (red circle). Therefore, if the cells were mechanically interacting, the instability of the downstream portion would affect the upstream one. To confirm this observation, please consider the evident fracture of a retaining wall located in the "green" zone (Figure 4.43)

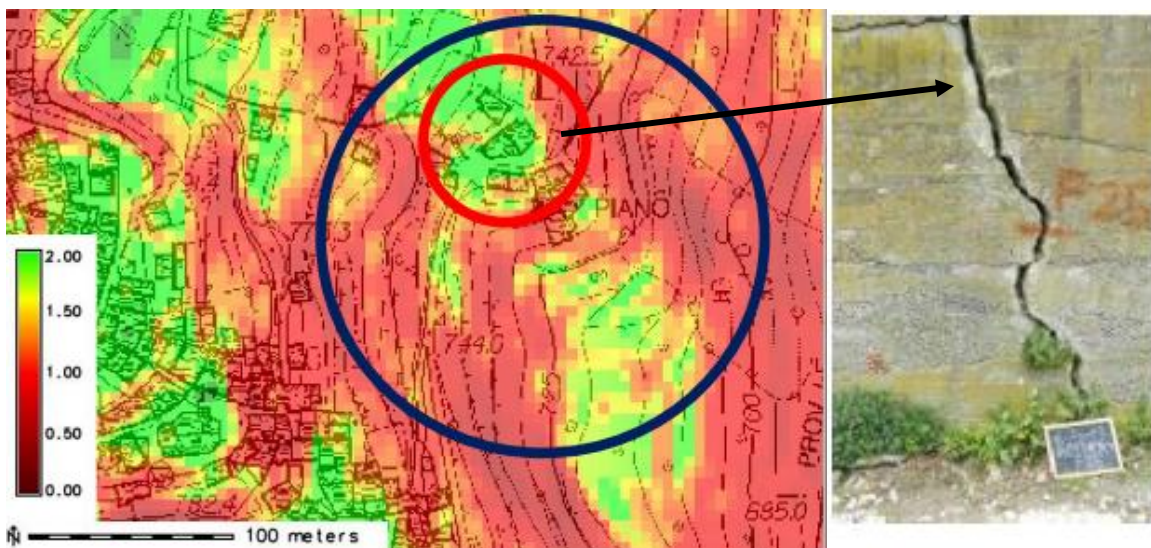


Figure 4.43. On-site criticality not detected by IHG modelling

However, the IHG Model is able to define unstable areas with a good degree of accuracy. A comparison between site survey and model results is presented in the following. Figure 4.44 shows an orthophoto on which the cross sections AA, BB and CC, identified by the local authorities as the most critical, and the images derived from a site survey were defined.

At the above-mentioned sections, the following was noted:

- in white, the areas where deep (Boumon, 2008) and shallow drains (and superficial) have been realised;
- in red, the critical zones within the urbanized area;
- in blue, the areas where criticalities were found outside the urbanized area.
- in green, photo of a lesioned building located in an area subject to damage during the rain event in 2013. A worsening of the crack pattern was not observed during the extreme event in 2016, as a deep drainage line was present (2014). The area is classified as stable by the IHG modelling pertinent to the 2019 rainfall event.

Some considerations regarding this comparison are given below. The first concerns the superficial drainage work (in white), in the terminal portion of the CC cross section. In that area, the roadway was damaged for a length of about 20m, and evident cracks were observed in the retaining walls at the side of the roadway.

In the area, $FS > 1$ provided by the analysis indicates a substantial condition of stability. However, pixels with factors less than 1 are present. This can be described as a consequence of the complexity of the groundwater characterising the landslide body, i.e., not continuous aquifer, but rather groundwater horizons in the most permeable soil layers, fed by infiltration during intense meteorological events. This aspect emerged from a further inspection (Carminati, 2017) where comparing flow measurement readings between several devices these were very different, at the same instant.

With reference to the blue zones, concordance between the model results can be observed, referring to the zone defined downstream of geological section AA, where the criticalities of the model are confirmed by the occurrence of landslide and in the terminal portion of section BB where landslides were observed in the wooded area, identifying slope instability.

Finally, the red zone identifies criticality within the urbanized zone, with particular reference to Borgata Piano, a very critical area, already subject to evacuation orders, following the 2013 rainfall event. The model shows an area with very low safety factors, confirming the criticality of the area. It can be stated that, although simplified, the IHG model succeeds in capturing the criticalities to which the Mendatica village is subjected. It is also true that the fact that the mechanical interaction between 3D elements is neglected results in a non-total agreement between reality and modelling. However, the IGH model is intended to be a simple model that can be used in landslide risk emergency management. If this assumption were to be nullified, then the computational effort would be greater as well as the numerical modelling. Furthermore, it should be pointed out that this procedure is unsuitable for more detailed studies. Therefore, for more detailed geotechnical analyses, the use of different numerical codes and the support of more geometric, hydrologic, and geotechnical information is recommended.

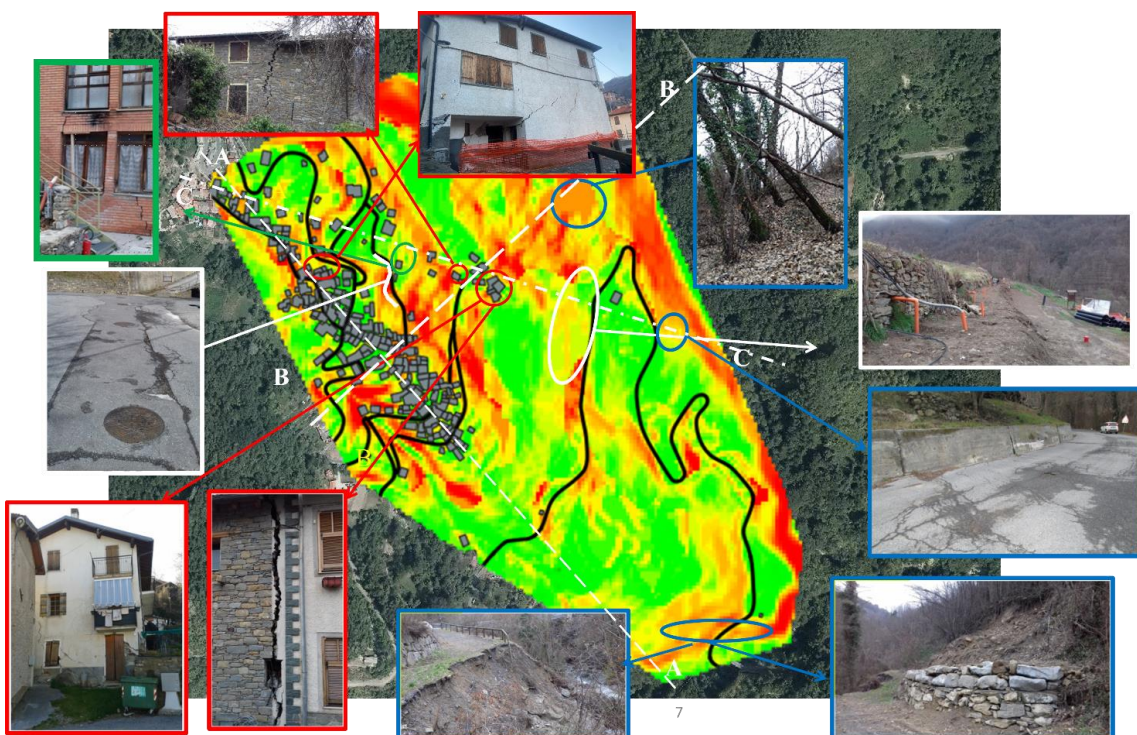


Figure 4.44. On-site validation of IHG modelling results.

The results obtained with the IHG model were compared with those obtained with other methodologies: the 3D LEM software named Slide3 by Rocscience and 3D FEM code PLAXIS 3D by Bentley.

For the sake of brevity, the above-mentioned modelling with LEM and FEM are not deeply discussed. However, the software and input data required to generate the 3D models of Mendatica are briefly described in the following.

Slide3 is a 3D LEM program for evaluating the safety factor of 3D failure surfaces in soil or rock slopes. Slide3 is based on the LEM method proposed by Cheng and Yip (2007). The software analyses the stability of 3-dimensional slip surfaces using vertical column limit equilibrium methods with a square cross-section, aligned to the x and y axes. Once all forces acting on the single column have been identified, the equilibrium of forces and moments are imposed for each column, while the sliding direction is globally defined for all columns. With these assumptions, a three-dimensional system of equations is produced.

It is possible to choose the maximum number of columns in x- or y-direction for the discretisation of each analysed sliding mass. The direction to which the maximum number of columns should be associated is automatically determined by the programme and depends on the shape of the sliding surface. Since all columns have a square section of equal area, specifying the number of columns in one direction automatically gives the number in the other direction. Consequently, the total number of columns that compose the entire sliding mass is set.

The sliding surfaces are defined using the *Grid Search* method, whereby the user can define a point grid representing the centre of n-spherical sliding surfaces. These surfaces are described by equispaced minimum and maximum radii, dependent on the slope geometry. In the stability analysis, the safety factor relative to each sliding surface is evaluated and the surface corresponding to the lowest safety factor is considered the critical one. In addition to this method for sliding surface definition, it is possible to use the *Cuckoo Search* and *Particle Swarm Search* methods, both based on the study of bird behaviour, which allow the generation of random sliding surfaces.

The stability analysis can be performed by LEM methods (e.g. simplified Bishop m., simplified Janbu m., Morgenstern-Price and Spencer's m.), respecting the assumptions on the intersection forces between the columns laid down in these methods. In the simplified Bishop and simplified Janbu methods, the resulting tangential components of the interslice forces between the columns are assumed to be zero. This assumption means that the resultants of the contact forces between the columns have a horizontal direction. In the Morgenstern-Price' method, the direction angle of the contact forces between the columns with respect to the horizontal is described by a function of x or y (by default, the programme has the sine function limited to one half-period), whereas in the Spencer' method, the direction angle of the contact forces between the columns with respect to the horizontal is considered constant and evaluated during the analysis.

On the other side, **Plaxis 3D** is FEM-based software that allows three-dimensional stability analyses to be performed. As already introduced in *Section 3.1.3*, stability analyses conducted with FEM-based software allow the evolution of the landslide phenomenon to be analysed, taking into account both equilibrium and compatibility equations. This methodology provides more accurate solutions than LEM methods, which are based on stronger assumptions. At the same time, numerical analyses are time-consuming both in terms of cost and modelling, especially for complex case studies.

The stability analysis by Plaxis 3D is performed through a phase called 'Safety', which provides the Safety Factor of the investigated site, based on the Phi-C reduction procedure which consists of reducing the soil shear strength parameters (i.e. $\text{tang}\varphi'$, c' and the undrained shear strength c_u) until collapse is reached. In this way, the programme automatically identifies the critical collapse mechanism, corresponding to the lowest Safety Factor. Each calculation step is a progressive approach to the collapse conditions, until a balanced and compatible solution is obtained. The incremental multiplier (Msf_i) through which the strength is progressively reduced must be sufficiently small, because under plastic conditions the solution depends on the stress path followed in the analysis.

The above described technique is called SSRT (*Shear Strength Reduction Technique*) and was proposed by Duncan (1996), who suggested that a slope is in a collapsed condition if the strength parameters take on values reduced by an amount equal to the FS. In this way, at the end of the step-by-step procedure, the incremental multipliers ($\sum_i Msf_i$), through which the strength parameters have been reduced, are added together to determine a collapse resistance mobilisation factor which correspond to the minimum Safety Factor for the global slope stability ($FS = \sum_i Msf_i$).

Since displacements and strains during the kinematism are taken into account, this procedure requires in input the knowledge of the stiffness parameters (i.e. Young's Modulus and Poisson's ratio), in addition to the knowledge of the soil strength parameters. Furthermore, the capacity of the software to analyse collapse conditions requires the introduction of a constitutive law for the soil, which allows it to be modelled with varying degrees of accuracy, from simple linear laws (i.e. linear elastic constitutive law) to more advanced behaviour models that take into account, for example, the stiffness dependency of the strain level or softening.

The use of such constitutive laws may require significant effort in both parameter definition and computation.

The models generated in Plaxis 3D and Slide3 for the Mendatica site are briefly described below.

Similar to the IHG model, both the modelling in PLAXIS 3D and Slide3 required, in input, the physical surfaces definition to characterise the landslide volume. The DTM, GWT and bedrock surfaces were then extracted from the GIS environment and imported. For the sake of brevity, all the steps required for surface generation are not here described. Figure 4.45 shows the triangular mesh surfaces with 150 m resolution generated and imported into the two models. The surfaces generated in AutoCAD Civil3D (2016 version) for the Plaxis 3D software, shown in Figure 4.44a, were also adopted in Slide3 Figure 4.44b. For a more detailed description, please refer to the relevant texts (Carminati, 2017 and Cavanna, 2017).

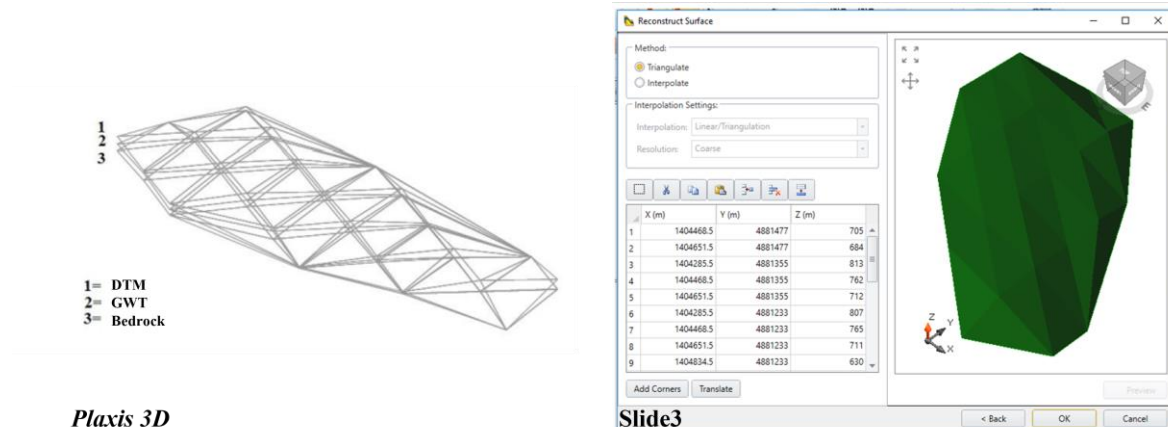


Figure 4.45. Triangular mesh surfaces with 150 m resolution used in the (a) FEM (Plaxis 3D), (b) LEM (Slide3) modelling for the generation of the Mendatica slope volume.

It is worth underlining that the physical model of the slope volume created does not have the same resolution as the model created in IHG. In fact, to avoid computational problems, it was necessary to switch from the 5m resolution of the IHG model to a resolution of 150m of the Slide3 and Plaxis 3D models. This shows that the area considered in the study carried out in the GIS environment is wider than the one considered in the studies carried out using Plaxis 3D and Slide3 due to this difference in resolution.

This stresses the advantage provided by the GIS environment for wide area slope modelling. In fact, by allowing the easy management of high-resolution maps, it is possible to investigate the same area with a higher resolution and thus a higher degree of accuracy. This allows even smaller areas of instability to be captured than in the studies conducted with Plaxis 3D and Slide3.

Once the physical surfaces were imported, it was necessary to define the volume of the area under study.

Concerning the modelling with Plaxis 3D, the slope volume definition requires the mesh generation. In the case of Mendatica, this point was carried out by assigning a coarseness factor of 0.5 in the area occupied by the blanket, and a value of 1 at the other edges. This operational choice makes it possible to 'thicken' and, consequently, make the analysis more accurate in the soil portion affected by the displacements. However, it was necessary to adopt *a very fine mesh* to meet the accuracy required by the programme during the calculation. In a time of approximately 15 minutes, 10-node triangular elements were generated. In this way, the model is composed by 257711 number of soil elements and 361290 nodes (Figure 4.46a).

In Slide3's modelling, after defining the external volume bounded by the physical surfaces, it was necessary to subdivide it into a number of volumes equal to the number of soil layers. In this modelling, two are the layers and therefore the volumes identified: Blanket and Bedrock (Figure 4.46b).

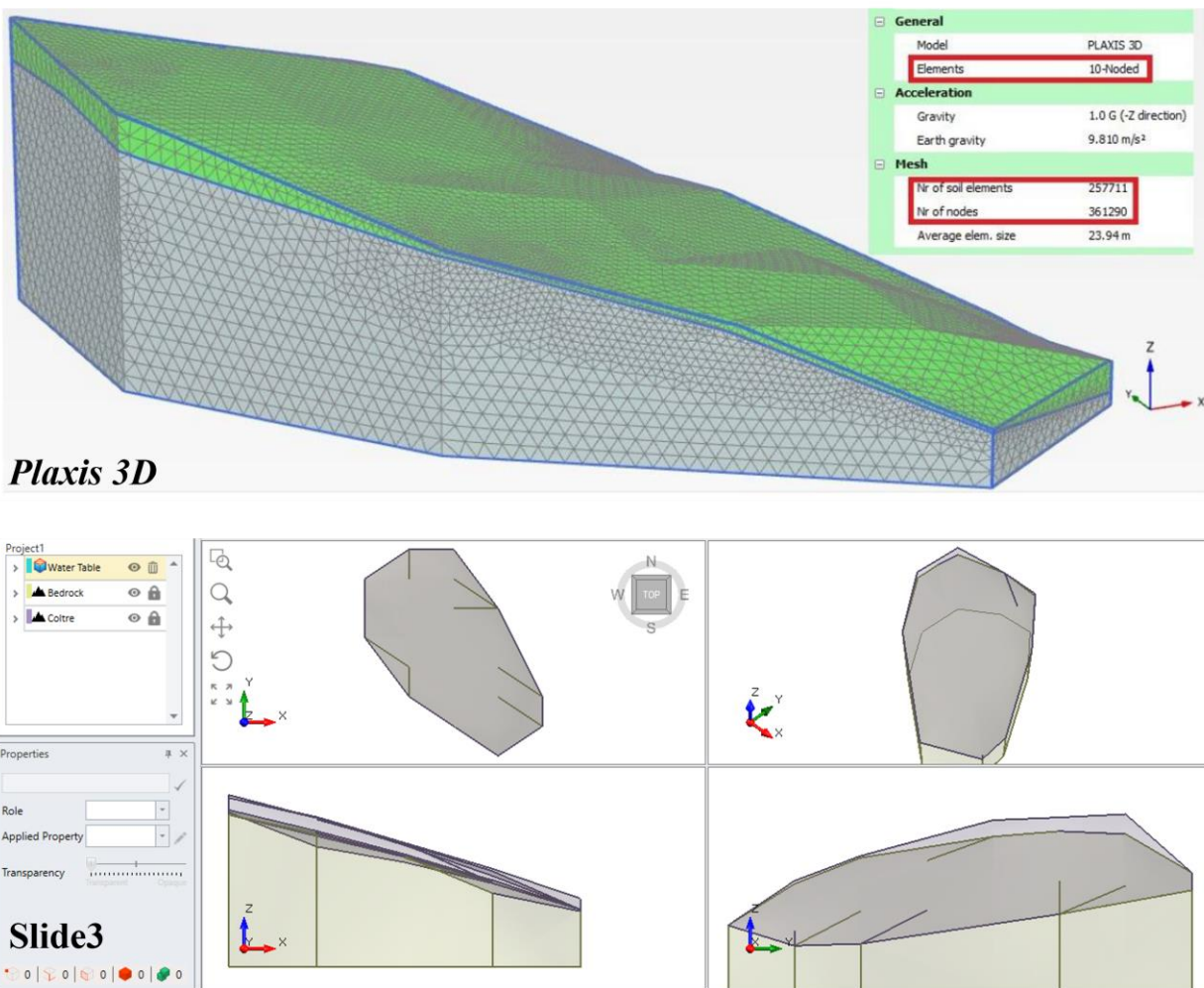


Figure 4.46. Mendatica slope volume provide by (a) FEM modelling (Plaxis 3D), (b) LEM modelling (Slide3).

In order to perform the stability analyses, the geotechnical characterisation of the study site was required. Both modelling was conducted using the geotechnical parameters introduced as input data in the IHG model, summarised in Table 4.12.

In addition, the Plaxis3D FEM model required the definition of a stress-strain constitution law. In this modelling, the elastic-perfectly plastic (Mohr-Coulomb) model was chosen, which required the definition of Poisson's coefficient and Young's modulus. According to formulas found in the literature (e.g., Cassinis 1979, Roccaforte et al., 2015), the definition of these values was performed using the data used from the geophysical investigations (compression or primary waves Vp), and the NSPT values derived from the Standard Penetration Test (SPT).

Characterised the 3D models in terms of both physical surfaces and physical-mechanical strength (and stiffness) parameters, stability analyses were performed.

The final step has been the comparison of the results obtained using the IHG model with the results obtained by the LEM and FEM methodologies. The comparison shown here refers to the average groundwater table, using Spencer's method for stability analysis in Slide3 (Figure 4.47).

In order to make the comparison easier, it was decided to highlight the unstable area detected by Slide3 in black and to circle the areas of instability provided by Plaxis 3D in red. These areas were then identified on the instability susceptibility map produced by the IHG modelling. The map resulting from the IHG modelling does not present the usual traffic light colour scale (red to green). In fact, to make the comparison more immediate, the default colour scale used by LEM and FEM software (red to blue) was chosen.

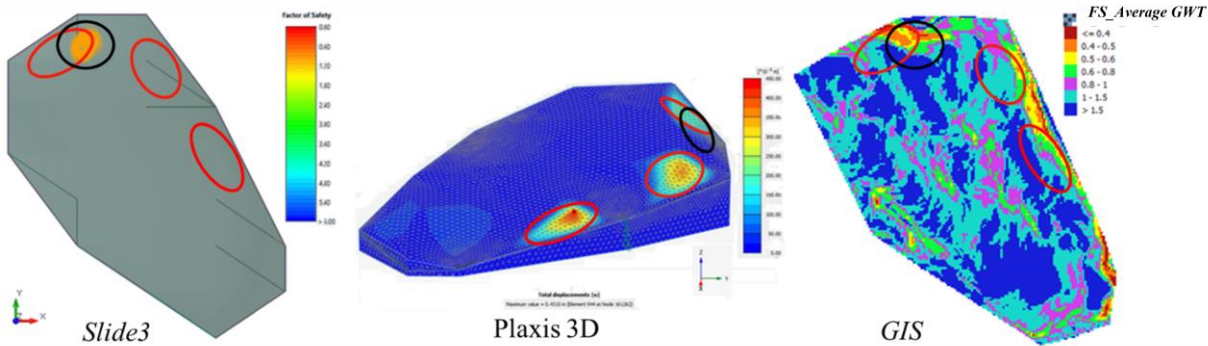


Figure 4.47. Comparison between LEM, FEM and IHG modelling results (Average GWT).

Regarding the instability zones defined by the three models, it can be observed that there is good accordance between the most unstable zones. Although the models in Slide3 and Plaxis 3D do not detect as unstable the central area of Borgata Piano. This difference may be related to the variation in the resolution of the physical surfaces, necessary to facilitate analysis times, which corresponds to slight modifications, smoothing, of the physical surfaces that do not allow the landslide instability of these areas to be captured.

With regard to the safety factors, referring to the overlapping critical areas, the minimum value resulting from the analysis with Slide3 is 0.98, that obtained with Plaxis 3D is 0.85, while those resulting from the IHG modelling are in the range of 0.4-0.6. The results obtained with Slide3 and Plaxis 3D are comparable, while those from IHG modelling are lower.

Compared to FEM modelling, this difference with the IHG model is due to the different modelling approach, which is more sofisticated in Plaxis 3D and allows taking into account both equilibrium and compatibility equations. For the same areal, more precise modelling, however, pays off in terms of both resolution and computation.

Compared to the 3D LEM modelling, the difference with the IHG model can be both in the analysis methodology used (i.e., Slide 3 takes into account interslice forces) and in the sliding surface definition methodology.

However, even if simplified, it is worth emphasising that IHG allows large portions of land to be analysed in less time than other 3D modelling techniques (e.g., in Slide3, the modelling computation time turned out to be about 45 minutes), capturing critical areas with a satisfactory degree of detail. It therefore appears promising.

4.2. IHG APPLICATION IN VENCE

The results of the IHG model applied to the Vence site are here presented. First, a comparison between rainfall data observed by a rain gauge and by a meteorological radar is proposed. Then the GIS modelling for the generation of the surfaces, the hydrological calibration phase and its optimization, and the GIS spatialization of the calibrated hydraulic parameters are described. Finally, the results of the groundwater table (GWT) modelling and of the stability analyses will be present and discussed.

The rainfall events were chosen for their intensity. The first event occurred in 2013, from 16 to 29 December. Two rainy days, with cumulative values exceeding 60 mm, occurred on 19 and 23 December; then the maximum daily rainfall, about 120 mm, was recorded on 25 December. The second event occurred in 2019, from 15 to 25 December. The maximum cumulative rainfall, about 80 mm, occurred on 20 December.

4.2.1. Rainfall data

Meteorological radar data were introduced as part of the AD-VITAM project in order to test landslide susceptibility modelling over large areas and in quasi real time. The collection of spatialized radar data concerned the radars of Mont Vial on the French side and Monte Settepani in Italy and were provided by the company Novimet thanks to the French partner BRGM, which purchased them and made them accessible to all AD-VITAM partners (Figure 4.48).

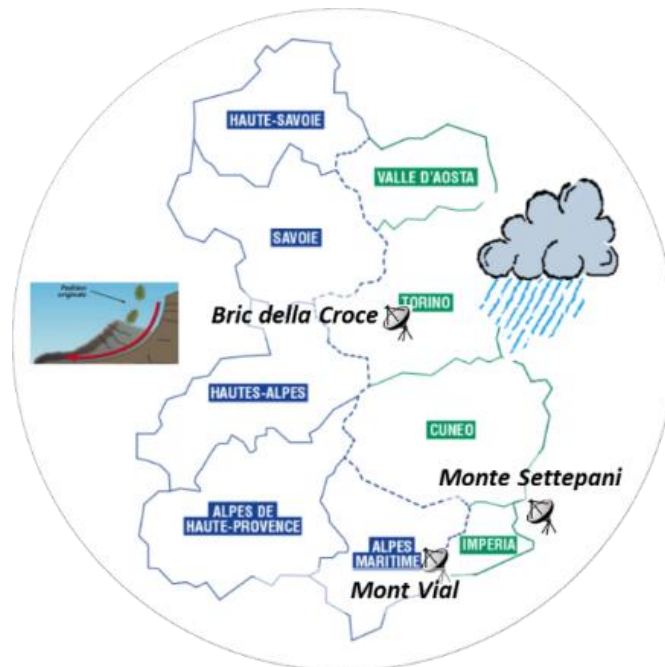


Figure 4.48. General overview

Radar maps have a spatial resolution of 1 km² and provide spatialized rainfall data at an hourly scale. Working at a daily scale, it was therefore necessary to sum the 24 raster maps for the rainfall day analysed. Figure 4.49 shows the final daily map for one day of the December 2013 event, which will be described

below. The spatialization of the data is described by polygons in a scale of reds describing the measured rainfall height. High rainfall polygons are described in dark red, while the colour fades in accordance with less intense rainfall variations.

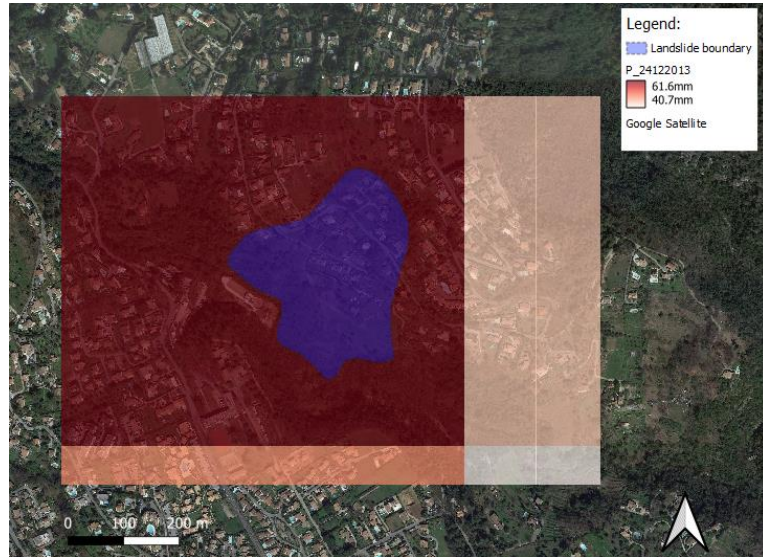


Figure 4.49. Rainfall spatialized information

With reference to the two analyzed rainfall events, here described, a comparison between rainfall data observed by a rain gauge and by a meteorological radar is proposed.

Regarding the 2013 event, no rain gauges was available at Vence, but in the village of Carros, about 15 km from Vence and at a comparable elevation (Vence is 322 m a.s.l. and Carros is 385 m a.s.l.). In 2019 "VP2" rain guage was active (since 2016), located about 4 km from Prat de Julian site in Vence.

The radar maps relative to December 2013 referred only to Mont Vial radar, while the radar maps relative to December 2019 were derived by merging Mont Vial and Monte Settepani radars. In Figure 4.50 an example of radar map from Mont Vial and the relative position of V2 and Carros rain gauges.

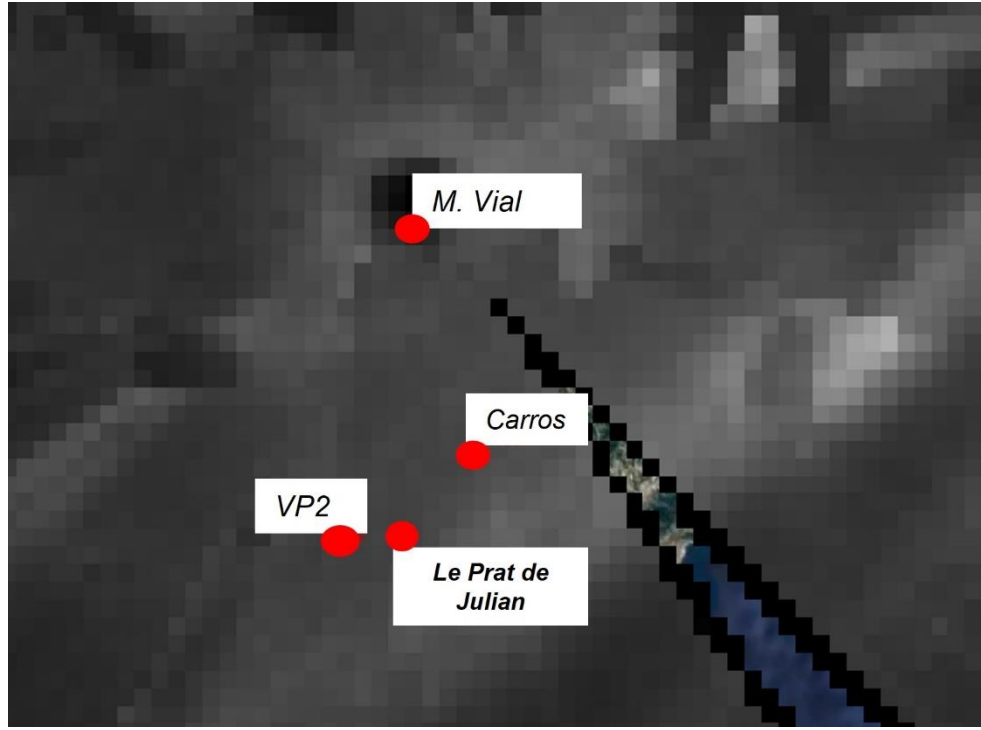


Figure 4.50. Representative image of the radar map derived from the Mont Vial radar.

The histogram in Figure 4.51 represents the rainfall measured by the Mont Vial radar in the cell over the landslide area of Prat de Julian and in the cell over Carros, compared with the “Carros” rain gauge measurements (in orange, yellow and grey respectively).

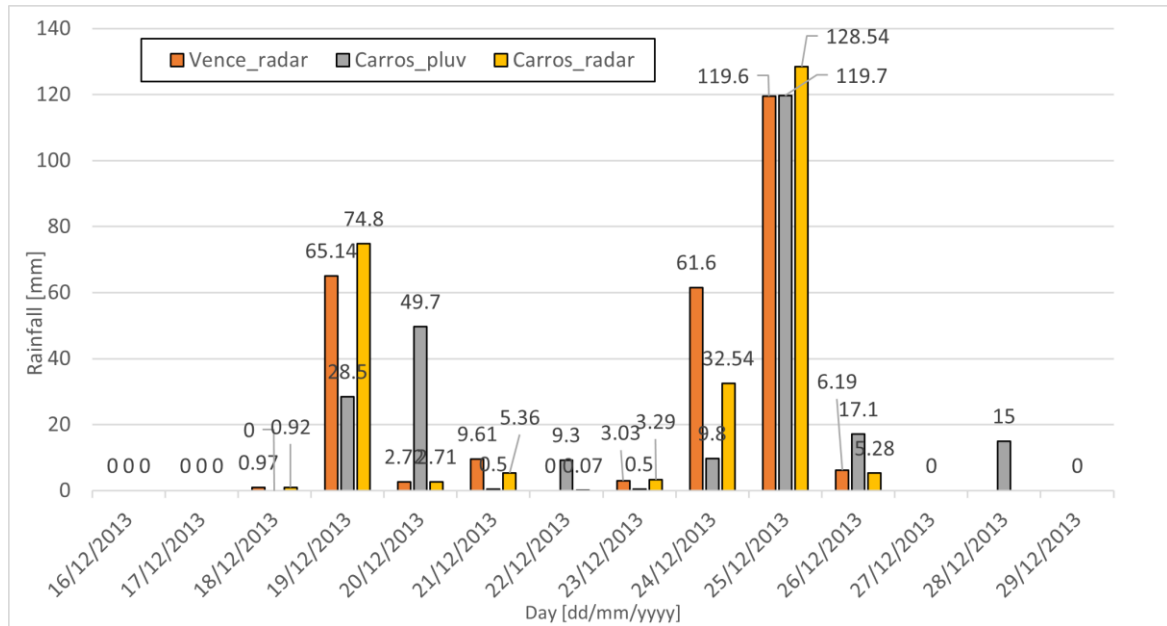


Figure 4.51. Comparison on rainfall heights for December 2013 event

The estimated heights show a good agreement with the radar measurements of Vence and Carros, while substantial differences emerge when compared with the rain gauge measurements. The small differences between the radar measurements are attributable to the different geographical position of Vence and Carros, but also to the fact that, even if rainfall can vary a lot in space and time, the radar data are average over 1 km². The differences between the rain gauge measurements and the radar ones in Carros highlight possible disagreement between the two different sensors, i.e the radar and the rain gauge.

Hence, the great advantage deriving from the use of spatialized radar data is confirmed but not its accuracy. Difficulty could arise where no rain gauge is present close to the landslide area, due to the possible over- or underestimation of rainfall derived by radar.

The same comparison was also made on the rainfall event on December 2019. Figure 4.52 shows the rainfall measured by radar in the cell over the landslide area of Prat de Julian and in the cell over VP2 rain gauge, compare with the “VP2” rain gauge measurements (in cyan, blue and orange respectively).

A good agreement is observed between all the data. The greatest difference is observed on the day of maximum rain (20/12/2019) and could be due to the difference between average data over 1 km² and very localized measurements.

In the following the slope stability analyses referred to rainfall data derived by radar maps, queried on the landslide area, while the calibration of the hydraulic parameters was performed using long time series derived by the rain gauge closest to the site.

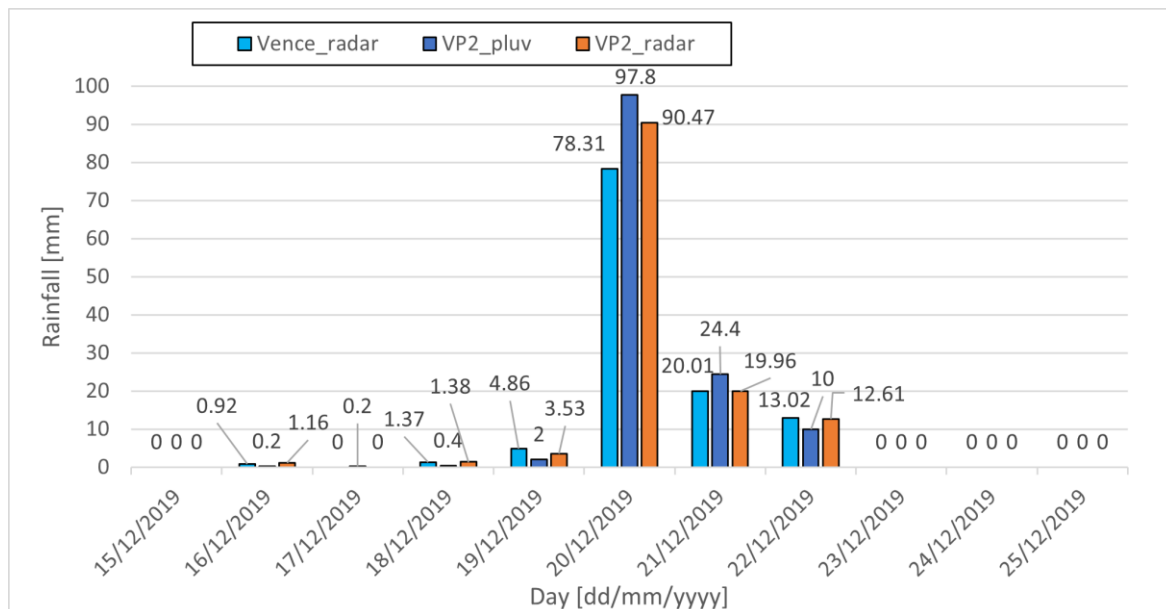


Figure 4.52. Comparison on rainfall heights for December 2019 event

4.2.2. Physical surfaces

The official Coordinate Reference System of the France cartography is the Reseau Geodesique Francais 1993, known as FRG93; the associated projection is the Lambert 93, that is a Conformal Conic projection (LCC). Table 4.15 shows the parameters for the proper creation of the *location* in GRASS GIS.

Reseau Geodesique Francais 1993 (RGF93)		Parameter
Projection	Lambert 93 (LCC)	
Coordinate system	2D ellipsoids – Lat, Long [°]	
Latitude false origins	46° 30' 00" N	
Longitude false origins	03° 00' 00" E	
Latitude first standard parallel	49° 00' 00" N	
Latitude second standard parallel	44° 00' 00" N	
False Easting	700000 m	
False Northing	6600000 m	

Table 4.15. FRG93 Datum parameters

The boundaries of the computational region are set to coincide with the geographical limits of the Prat de Julian site, while the resolution is set at 5 metres in accordance to the degree of detail of the available DTM (Figure 4.53).

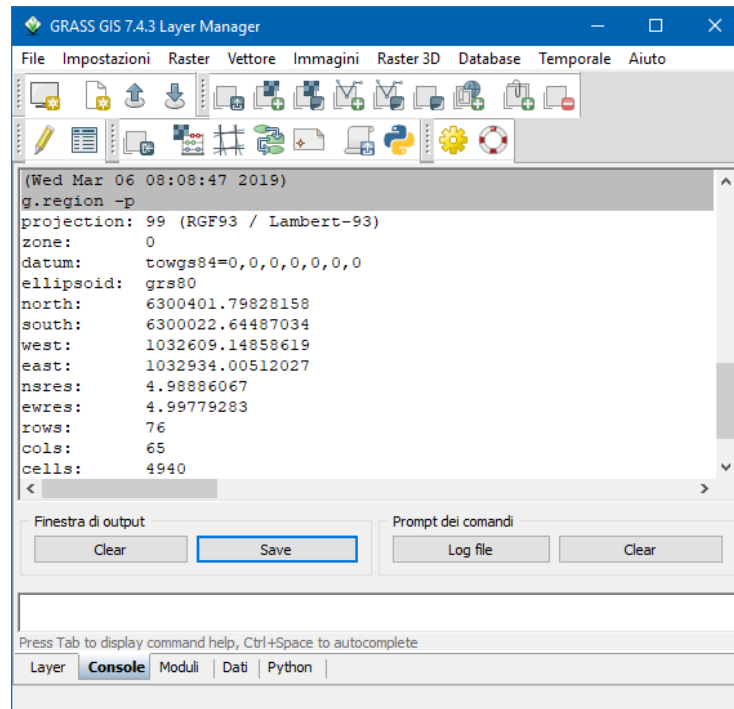


Figure 4.53. Mapset g.region

The cartography, provided within the AD-VITAM project by the French partners, consists of:

- Digital terrain model for the municipality of Vence, at resolution of 5m.
- MOS (Mode d'Occupation du Sol) land use map, year 2014, at resolution of 25m.
- Geological map, at scale 1:10000.
- Vector map of survey network positions.
- Vector map of buildings and infrastructure

In addition to the Digital Terrain Model, the surfaces of bedrock and of the groundwater table has to be defined too. Moreover, the CN maps necessary to define the maximum storage capacity of the slope volume has to be calculated as follow.

Bedrock surface generation:

The bedrock surface is created on the basis of the geotechnical investigations carried out in the Prat de Julian area. In particular, borehole loggings referring to 27 boreholes were analyzed. After a careful interpretation, it was possible to identify the bedrock depth for each measurement point. Once the bedrock elevation values were associated with the punctual data, the map was generated using the TIN interpolation. However, as in the case of the Mendatica site, the information available did not allow to cover the entire study area. For this reason, it was necessary to apply model boundaries, defined as follows:

- in the downstream region, in correspondence of the river La Lubiane the bedrock was considered coinciding with DTM.
- In the upper region, it was assumed that the bedrock surface remains mostly parallel to ground level, known the bedrock elevations detected in the boreholes closest to the upper limit. In Figure 4.54 the final surface together with the model boundaries, i.e the river (in blue crosses) and the 7 points in the upper part of the area, is showed.

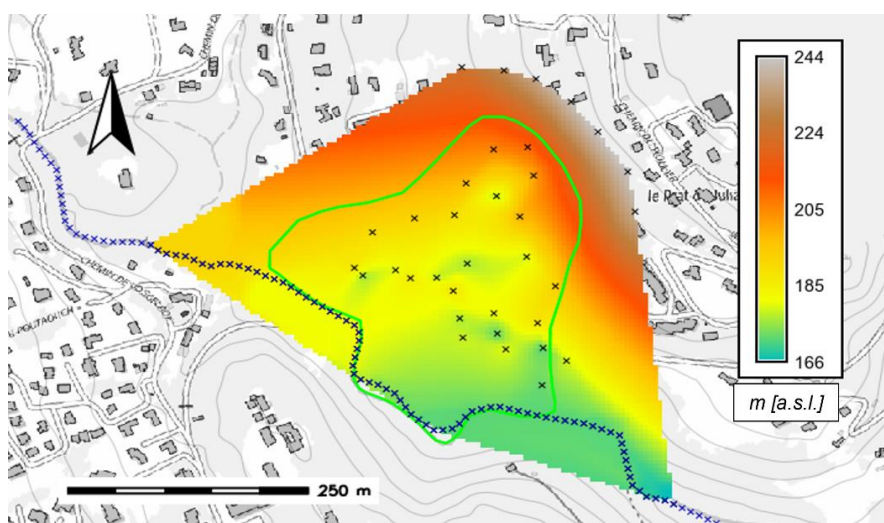


Figure 4.54. Bedrock surface

Groundwater table map:

The procedure for the generation the groundwater surfaces is similar to that applied for bedrock generation, with the major difference being the limited number of sampled points for spatial interpolation. In fact piezometric data are available only in four positions. The boundary conditions are given by the La Lubiane river, and by five points, labelled with the letters p, q, r, s, t, and located at the upper boundary of the landslide, in which the constancy of the slope of the GWT, defined between pairs of piezometers, is maintained as explained in Table 3.16. The final surface is shown in Figure 4.55.

<i>Model Boundary</i>	<i>GWT slope</i>
p	C6-C11
q	C6-C11
r	C6-C7
s	C20-C11
t	C7-C11

Table. 4.16. Identification of model boundaries, based on the GWT slope

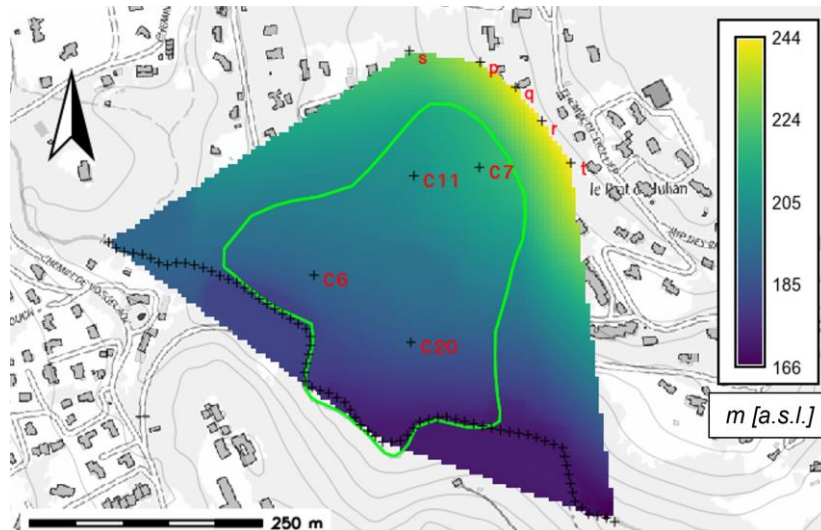


Figure 4.55. GWT surface

Curve Number maps:

The procedure for the Curve Number surfaces generation, already detailed in *Section 4.1.1* related to the Mendatica case study, is here briefly described.

Concerning the *land use* map, it is based on the Mode d'Occupation du Sol (MOS) model, derived by aerial photo-interpretation from the Direction Aménagement et Urbanisme Service Planning and promoted by the Istitut Metropole Nice cote d'Azur of the region of PACA. The map, produced in vector format, classifies the territory into 70 different categories, following the Corine Land Cover (CLC) specifications

proposed in the MOS by Autran (2007). The homogeneous land use areas are characterized by a minimum surface extension of 45 m^2 , comparable with the resolution adopted in this modelling (cell area 25 m^2), and sufficiently detailed in the field of hydrological modeling and analysis. The area of the Prat de Julian results to be described by 7 different classes.

The land use map, relative to 2014, was overlapped on an aerial photo relative to 2018, provided by the French IGN geoportal. The comparison showed a change in Land use in the *zone a*. In fact, as reported in *Section 2.2* following the modification of the PPRN which took place in 2015, the area was affected by changes in the land use due to the demolition of some houses in order to reduce the landslide risk.

Figure 4.56 shows how the dashed red area is classified in the MOS with the code 112 (low/medium density urbanized area), while at present, following the demolitions, it appears to be a grassland area. Consequently, the associated CN values has been modified passing from a value equal to 70 (describing the class 112) to 61 (referring to the class 231: meadows and cultivated land or grassland).

The MOS map was classified grouping the similar classes in a unique class (e.g. 313, 311 grouped in class 1 as forest), following this new classification:

- 1) Forests and shrubs;
- 2) Mixed forests;
- 3) Meadow, cultivated land;
- 4) Residential area;
- 5) Industrial and commercial areas.

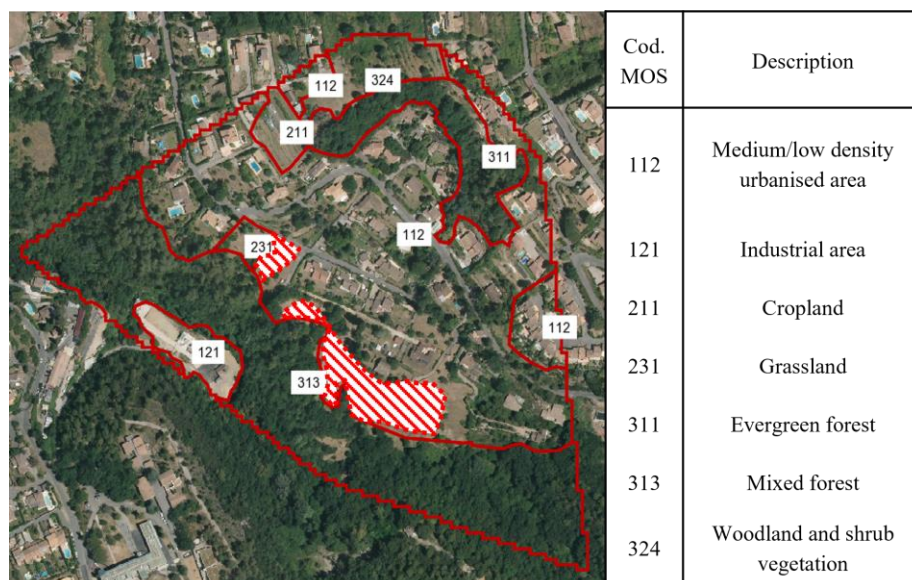


Figure 4.56. Land use classification according to the MOS model

In order to define the HSG classes (A, B, C and D), the *geological map* has been used (Figure 4.57). However, since a digital cartographic elaboration regarding the lithology of the site is not available, the information was obtained from the geological map of Vence reported in the study of Palis (2017), then

georeferenced using IGN cartography. The lithological zones inside the site were identified and associated to the HSG classes.

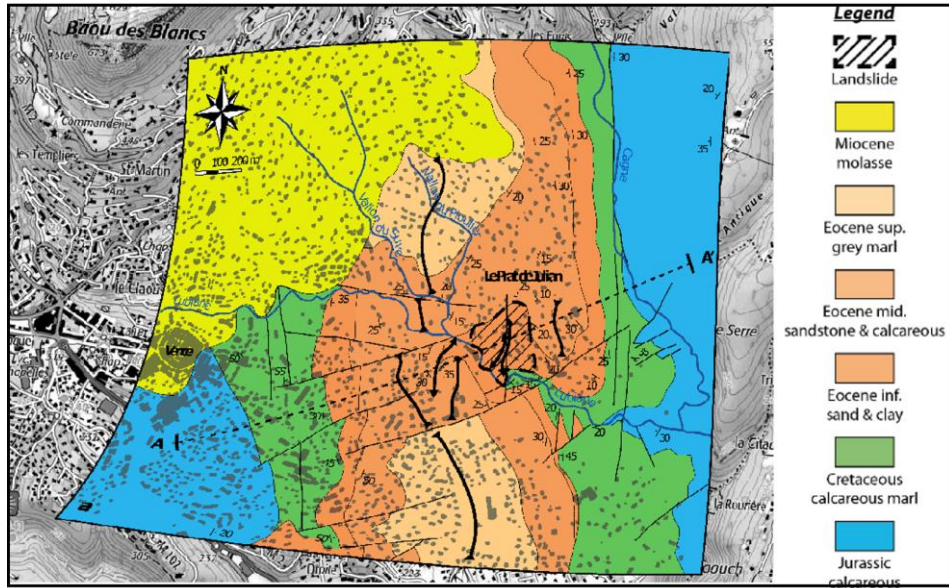


Figure 4.57. Geological map

Finally, a matrix (Table 3.17) was constructed on the basis of the SCS indications, in which different values of CN II are matched for each combination of soil type and land use.

CN II		LAND USE				
MOS		311-324	313	212	112	121
RICLASSIFICATION		1	2	3	4	5
HSG	A	25	45	39	54	89
	B	55	66	61	70	92
	C	70	77	74	80	94
	D	77	83	80	85	95

Table 4.17.CN values matrix

Table 4.17 was implemented in GRASS GIS and, through the procedure already describing in *Section 4.1.1*, the final CN_II was generated (Figure 4.58).

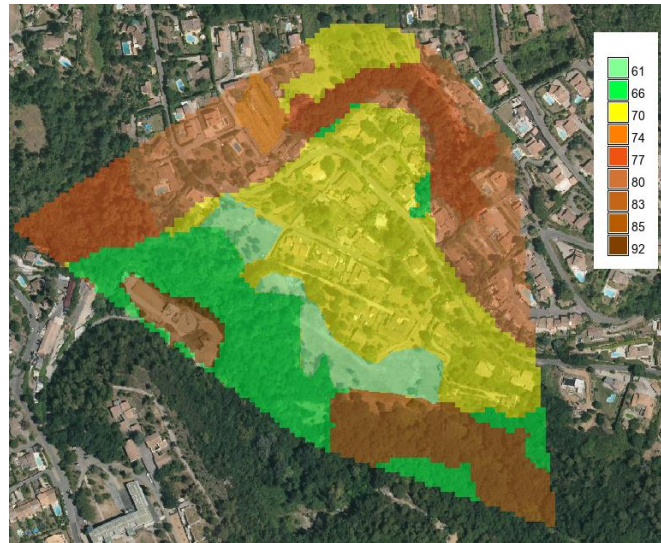


Figure 4.58. CN II Map

According to the Curve Number method detailed in *Section 3.1.1*, the CN_I map describing dry soil condition, and the CN III map, describing soil wetting condition, as well as the pertinent maps of maximum storage capacity (S_I, S_II, S_III), here not showed for sake of brevity, were produced.

4.2.3 Calibration of the hydrological model

The calibration phase concerning three piezometers, C6 and C20, located in the downstream area of the landslide body (*zone a*) and C11 located in the upper stream area (*zone c*). The decision to disregard the piezometer C7, located in *zone c*, is justified both by the relative duration of activity of the piezometer (2008-2010) and the insignificance of the readings, which show very small variations in the water table compared to the others in response to the rainfall and for a short time period (Figure 4.58). Hence piezometer C7 was merely considered as a known point for the creation of the groundwater surface, without calibrating the hydraulic parameters in it. Although the spatial characterization of the hydraulic parameters, derived by calibration, was less precise, it was possible to guarantee a sufficiently long-time interval in which significant weather events can be identified, to improve the parameter calibration.

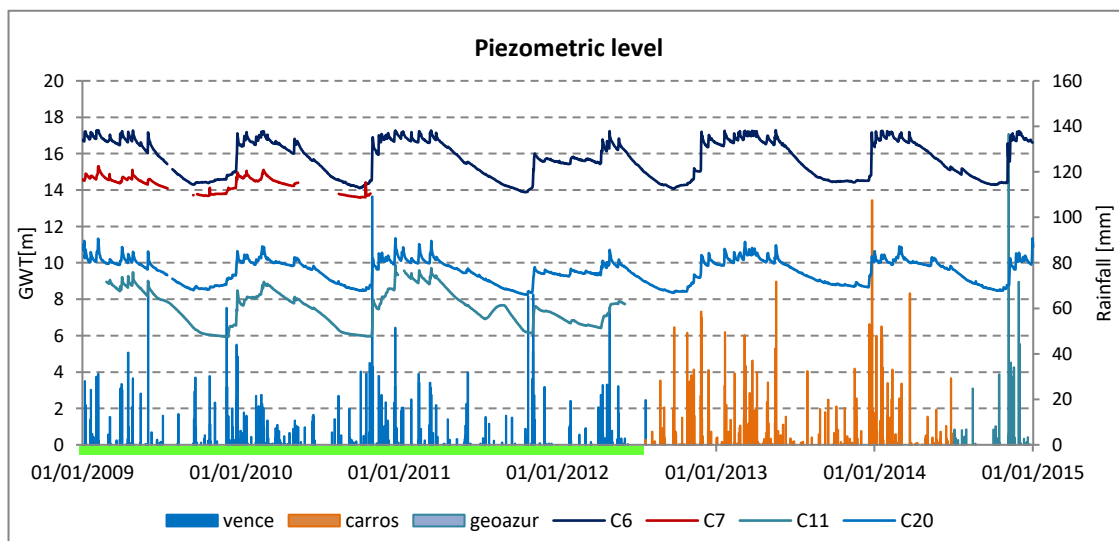


Figure 4.58. Time history of piezometric levels over the period of activity.

With reference to Figure 4.58, the green line shows the time period (09/12/2008 to 05/06/2012) in which C6, C11 and C20 present a continuous series of data. 18 rainfall events, on which the calibration was performed, were defined in this period (Table 4.18). The rainfall measurements used for the calibration refer to the Vence rain gauge as detailed in Section 2.2.

	Beginning	End
Event 4	25/03/09	04/04/09
Event 5	12/04/09	21/04/09
Event 6	23/04/09	29/04/09
Event 9	18/12/09	27/12/09
Event 10	14/02/10	26/02/10
Event 11	27/10/10	04/11/10
Event 12	11/11/10	03/12/10
Event 13	18/12/10	28/12/10
Event 14	11/02/11	22/02/11
Event 15	09/03/11	22/03/11
Event 17	30/10/11	11/11/11
Event 18	01/04/12	21/04/12
Event 19	26/04/12	08/05/12
Event 20	15/05/12	24/05/12
Event 21	22/11/12	02/12/12
Event 22	10/12/12	17/12/12
Event 23	16/01/13	25/01/13
Event 26	12/05/13	21/05/13

Table 4.18. Rainfall events selected for hydraulic calibration in Vence

The rainfall events were divided in two different classes: 11 events have been involved in the calibration phase, while 7 events have been used for the validation phase (Table 4.19).

Piezometer C6		Piezometer C11		Piezometer C20	
Calibration	Validation	Calibration	Validation	Calibration	Validation
Event 4	Event 10	Event 4	Event 10	Event 4	Event 10
Event 5	Event 15	Event 5	Event 15	Event 5	Event 15
Event 6	Event 20	Event 6	Event 20	Event 6	Event 20
Event 9	Event 21	Event 9	Event 21	Event 9	Event 21
Event 11	Event 22	Event 11	Event 22	Event 11	Event 22
Event 12	Event 23	Event 12	Event 23	Event 12	Event 23
Event 13	Event 26	Event 13	Event 26	Event 13	Event 26
Event 14		Event 14		Event 14	
Event 17		Event 17		Event 17	
Event 18		Event 18		Event 18	
Event 19		Event 19		Event 19	

Table 4.19. Rainfall events used for calibration and validation

The piezometric measurements were provided in continuous with a time step of 1 hour and the level was referred to the ground level. However, the comparison between modelled and observed data was referred to the bedrock level, so the groundwater table level was converted so to refer to the bedrock elevation, using the Equation 3.57. Then, for each piezometer, the calibration was performed on the Excel spreadsheet referred to the initial H_{GWT} recorded in the previous 24 hours.

In the preliminary phase (step_1), the hydrological analysis was carried out using reference values of the hydraulic parameters, established on the basis of the data available in literature, in accordance with the type of soil characterizing the landslide body. For all piezometer, soil effective porosity values equal to 0.15 and soil permeability values k_s equal to $3.4 \cdot 10^{-5}$ m/s were considered. Although the modelled GWT correctly represented the observed piezometric variations, the standard deviation was considerable, greater than one meter for all three piezometers.

Then, calibration based on the use of the objective function, by minimizing the difference between the modelled and observed GWT, was performed (step_2). Table 4.20 shows the calibrated parameters. The calibrated porosity values are lower than the preliminary one, but consistent. Moreover, a significant decrease in the standard deviation, ranging between 15 and 20 cm, was obtained.

Figure 4.59 shows the GWT trend for the piezometer C6 with reference to the Event 17, indicated in Table 4.20. The yellow line represents the GWT at the end of the step_2. A good agreement between the GWT at the end of the step_2 and the piezometric level (orange line) is detected, differently from the blue line that represent the GWT modelled in the step_1.

Piezometer	$n_e [-]$	$k_s [\text{m/s}]$
C6	0.100	$4.55 \cdot 10^{-6}$
C11	0.130	$3.93 \cdot 10^{-6}$
C20	0.090	$1.63 \cdot 10^{-5}$

Table 4.20. Hydraulic parameters

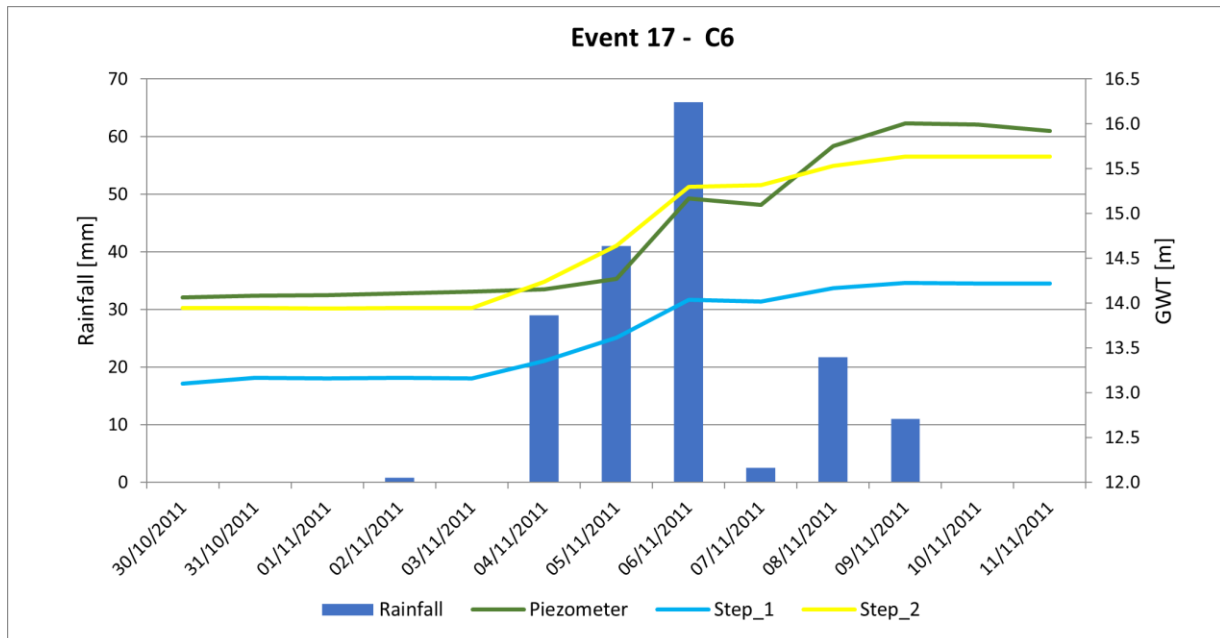


Figure 4.59. Comparison on GWT levels in different calibration phases

Step 2 provides good GWT modelling for intense rainfall events. However, the calibration seems to incorrectly interpret the non-rainfall phases within an intermittent rainfall event, underestimating the discharge phase and keeping groundwater levels constant in the absence of rainfall. The higher discharge is probably due to the presence of fractures in the bedrock and water exchanges between the superficial aquifer and the deep one, as highlighted by the ERT tomography (Lebourg et al., 2010). In order to improve the calibration phase, an optimisation was introduced for the soil permeability. The modelling was carried on by using the previously calibrated permeability for the rainy days and trying to optimize the soil permeability value calibrating it on the dry days. The new soil permeability was optimized for each of the piezometers. Final soil permeability values are shown in Table 4.20, while Figure 4.60 compares the piezometer C6 variation to the optimized GWT level, for the Event 12 (as defined in Table 4.19). The final soil permeability values are summarized in Table 4.21.

Piezometer	$ks_{recharge}$ [m/s]	$ks_{discharge}$ [m/s]
C6	$4.55 \cdot 10^{-6}$	$5.12 \cdot 10^{-6}$
C20	$1.63 \cdot 10^{-5}$	$3.07 \cdot 10^{-5}$
C11	$3.93 \cdot 10^{-6}$	$4.68 \cdot 10^{-6}$

Table 4.21. Final soil permeability values

With reference to C6 piezometer, Figure 4.60 shows the optimized GWT trend (green line) compared to the piezometric level (orange) and the GWT level modelled at the step 2 (in yellow). It should be noticed that, even if, the modelling implemented with the double soil permeability values underestimates the piezometric level, allows a more correct representation of groundwater levels in the case of intermittent rainfall events.

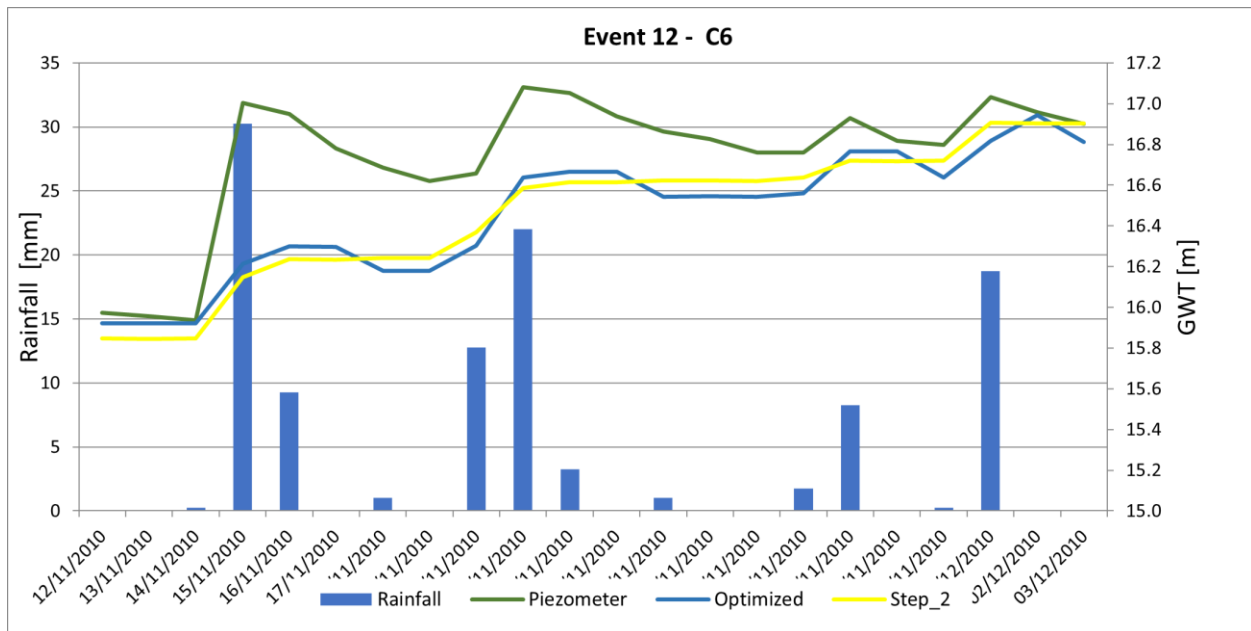


Figure 4.60. Piezometer C6. Optimised calibration GWT for the Event 12

The goodness of calibration is estimated according to the statistical indices defined in *Section 3.1.2* with satisfactory results. For the sake of brevity, the correlation values obtained for all rainfall events analysed are shown (Table 4.23). Overall, this index is high, demonstrating the good modelling capacity to reproduce the groundwater in the optimisation phase.

ρ_{xy}	C6	C11	C20
Evento 4	0.882	0.800	0.980
Evento 5	0.861	0.858	0.952
Evento 6	0.930	0.971	0.972
Evento 9	0.981	0.945	0.968

Evento 11	0.978	0.945	0.986
Evento 12	0.816	0.972	0.650
Evento 13	0.819	0.931	0.819
Evento 14	0.851	0.864	0.840
Evento 17	0.964	0.958	0.986
Evento 18	0.926	0.895	0.976
Evento 19	0.898	0.808	0.959

Table 4.23. Comparison on standard deviation with respect to the range of GWT fluctuations.

A validation was carried out to verify the goodness of the estimation of hydraulic parameters in response to rainfall events not considered during calibration (Table 4.19). In the Table 4.24 the standard deviation between the modelled GWT and the observed one in the available piezometers is reported. The values are quite small compared with the groundwater oscillation, hence the obtained standard deviations were acceptable.

Piezometer	ΔGWT [m]	$\sigma_{validation}$ [m]
C6	0.84	0.19
C11	0.87	0.15
C20	0.85	0.13

Table 4.24. Comparison on standard deviation with respect to the range of GWT fluctuations.

4.2.4 Hydraulic parameter mapping

The calibration and optimization phases allowed to define the soil hydraulic parameters, i.e. the effective porosity and permeability, in correspondence of the piezometers, that are few points inside the landslide body. Then, their spatialization was performed as described in *Section 3.3.2*.

The *effective soil porosity map* has been generated applying the "stratigraphic similarity" criterion to attribute the same porosity to other boreholes. Having established the range of variation of porosity between 0.09 and 0.13, the porosity value is attributed to each measuring point based on the percentage of sand and clay, considering the stratigraphy of the first meters of soil; the upper limit of the range is assigned to soils composed mainly of fine sands, while the lower value is assigned to soils composed mainly of clay. It should be emphasized that the decision to consider only the upper layers is due to the fact that the n_e parameter affects the rainfall infiltration process. Consequently, the deepest soil layers are not considered in this process.

The association of soil porosity values is summarized in Table 4.25.

Borehole	Piezometer	$n_e [-]$
C2	C20	0.09
C3	C20	0.09
C4	C11	0.13
C5	C6	0.10
C7	C11	0.13
C8	C6	0.10
C9	C6	0.10
C10	C11	0.13
C11	C11	0.13
C12	C20	0.09
C13	C20	0.09
C14	C6	0.10
C16	C11	0.13
C18	C6	0.10
C21	C20	0.09
C22	C6	0.10

Table 4.25. Soil effective porosity values due to stratigraphic similarity criterion

Once the porosity values for each measurement point have been determined, the model boundaries must be set on the landslide perimeter. Again, the points on the upper and lower contours are assigned values close to the nearest boreholes. The final map is generated by applying the TIN interpolation technique (Figure 4.61).

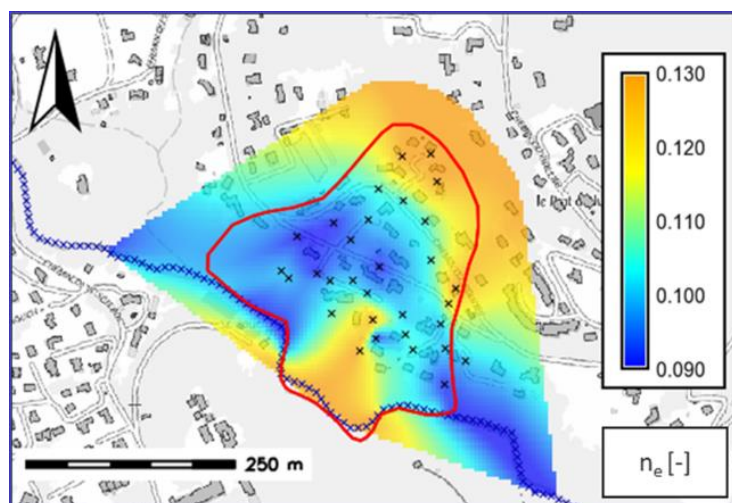


Figure 4.61. Soil effective porosity map

The goodness of the output map is validated by the comparison with the geological map provided by the technical report “Note technique glissement du Prat de Julian” (06 - Vence) produced by the EEG-Simecsol (Figure 4.62).

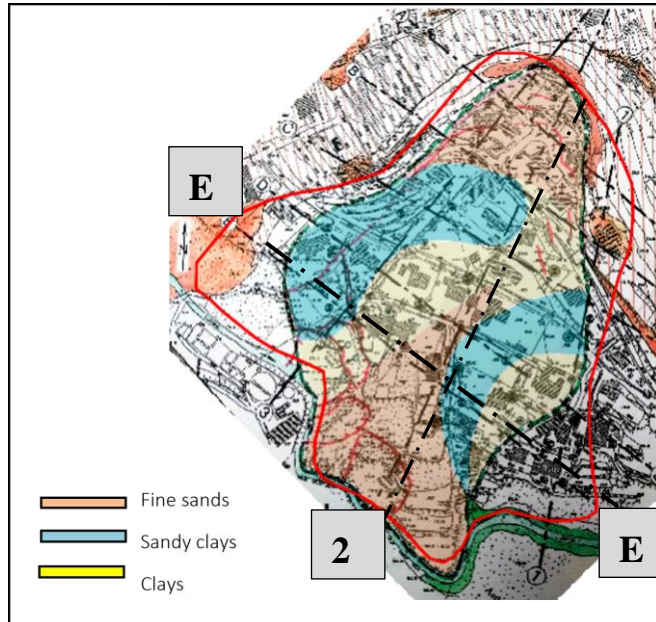


Figure 4.62. Geological map for comparison

The comparison between Figure 4.61 and Figure 4.62 shows a good agreement. In fact, the areas indicated as fine sands, in orange in the geological map, are associated to higher values of the modelled effective porosity in the upstream area and in the downstream part of the landslide body along the maximum slope line (axis 2 in the geological map).

The stratigraphic similarity criterion has been applied for the generation of the *soil permeability maps* too, following the same rules applied for the soil effective porosity generation. However, differently from the previous case, it was decided to consider the entire extent of the saturated blanket since the k_s coefficient is the basis of the sub-surface flow, affecting the deepest soil layers too.

The results, shown in Figure 4.63, allow to identify areas with higher permeability values in the downstream area, characterised by deep sandy soil layers.

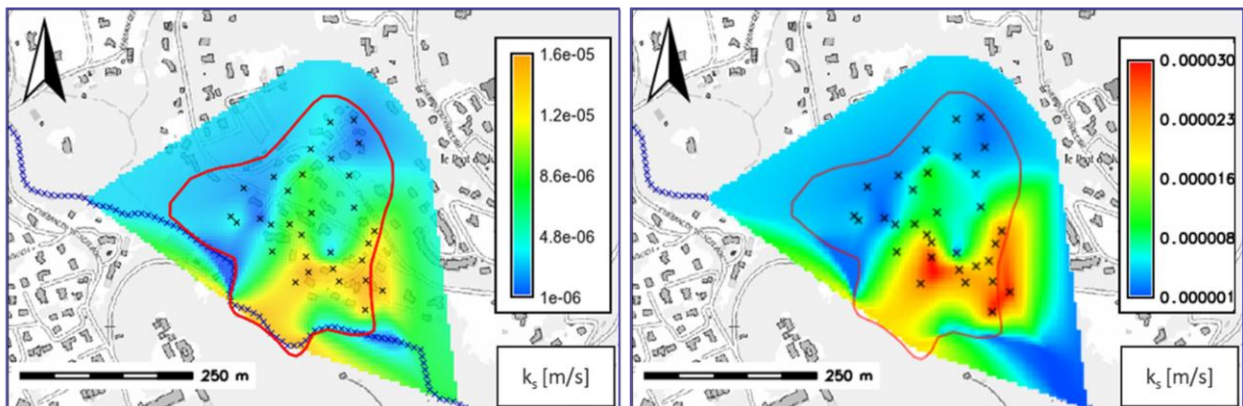


Figure 4.63. Soil permeability maps for recharging (a) and discharging GWT phases (b)

The soil permeability surfaces allow to compute the *discharge constant maps* by applying Equation 3.16. The λ map definition required the knowledge of the maximum slope angle (θ) pertinent to each pixel, i.e. the *slope map* calculated from the DTM through the *r.slope.aspect* command (Figure 4.64).

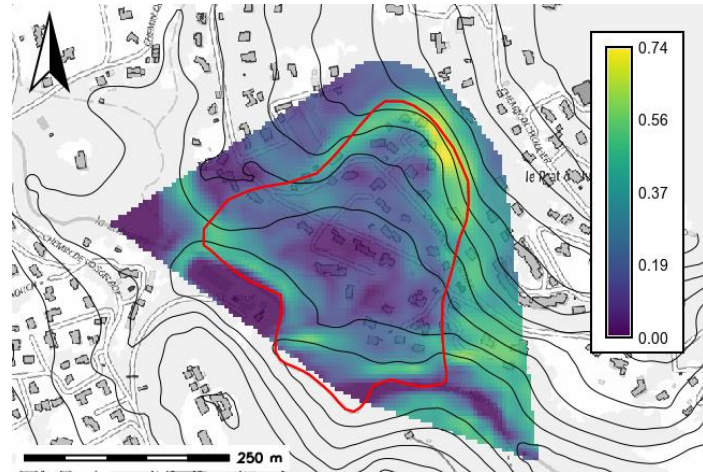


Figure 4.64. Slope map

The *discharge constant maps*, in Figure 4.65(b), presents an increase in the values of the constant in the south-eastern part of the slope at the highest values of hydraulic conductivity at the discharge phase.

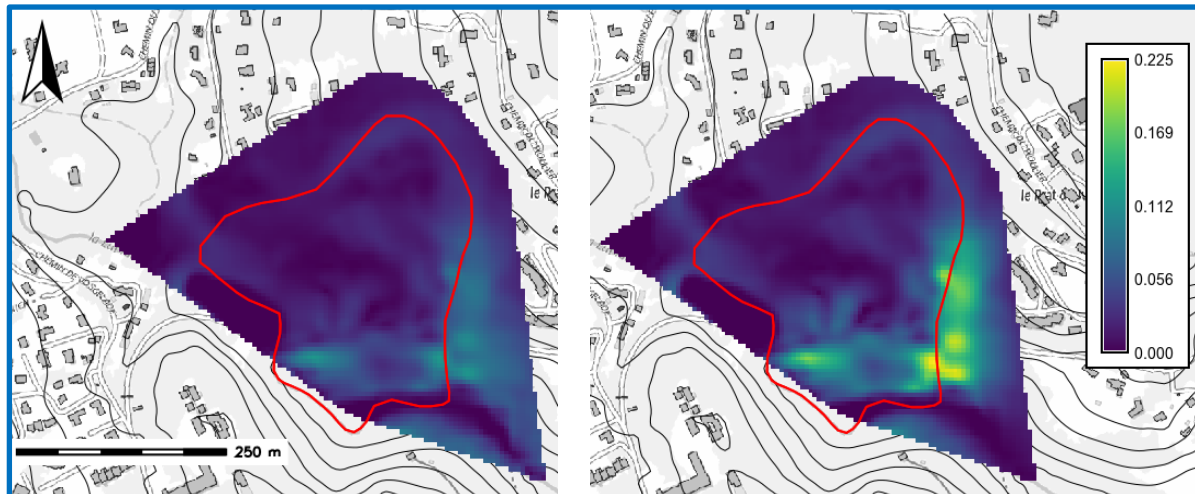


Figure 4.65. Discharge constant maps calculated for *Ks_recharge* (a) and *Ks_discharge* (b)

4.2.5 Groundwater table evolution

The hydrologic modelling produces GWT height maps (H_f) every day of the analysed event.

The results relative to the two analysed events are here described as the goodness of modelling, estimated in terms of groundwater variation, by examining the GWT height maps at known points, i.e. the piezometers.

Event December 2013:

The rainfall event analyzed is a long-time duration event. According to the definition of rainfall event (Brunetti, 2010 and 2015), the time period considered two days before the rainfall started, ranging from 16 to 29 December. December 25 turns out to be the day in which the maximum cumulative rainfall value was recorded, about 120 mm, however it shows also other two rainy days (12/19/2013 and 12/23/2013) with cumulative values above 60 mm. Rainfall data were derived by meteorological radar (Section 4.2.1).

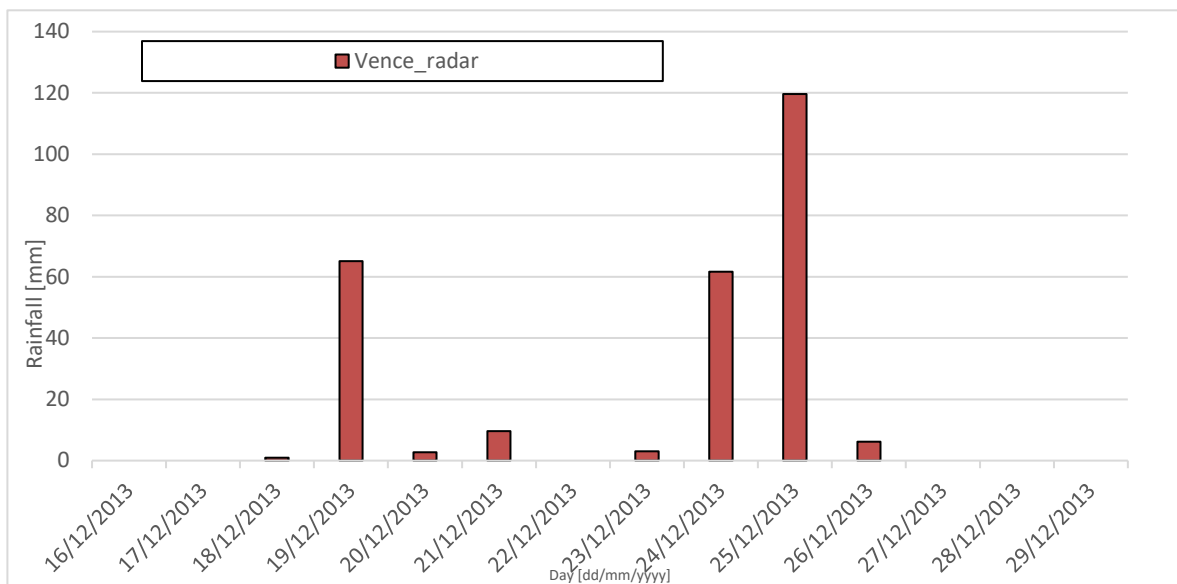


Figure 4.66. Time series of the December 2013 rainfall event

During the period of the considered event, the piezometers located in zone c, the upper part of the slope, are no longer active. Hence the average GWT surface (Figure 4.66) was obtained using the TIN interpolation between the piezometric measurements recorded by the monitoring network made up of the four piezometers C6, C11, C20 and C7, adding the model boundaries along La Lubiane river and in upper part of the landslide body.

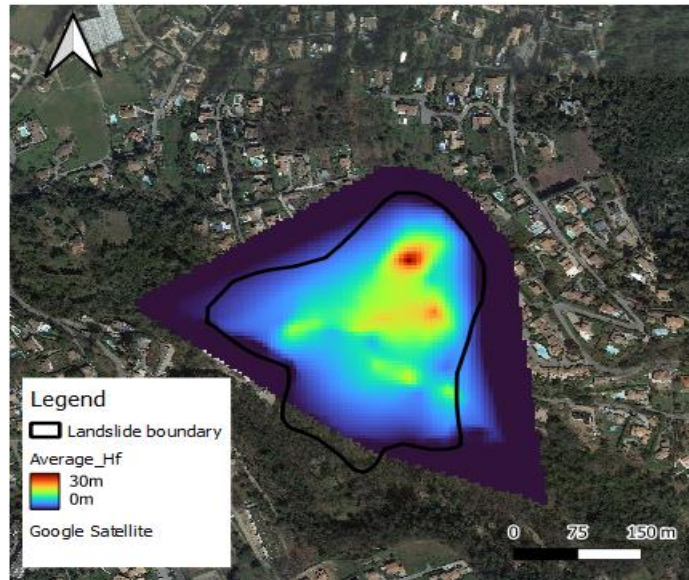


Figure 4.66. Average GWT

The modelled groundwater response was compared with C6 piezometric measurements in Figure 4.67. The comparison highlights a GWT difference equal to about 70 cm at the beginning of the event, due to the difference between the average GWT and the initial level. Furthermore, the discharge phase at the end of the rain event was not reproduced. However, the GWT modelling was able to reproduce the general trend of the observed one as showed by the statistical indexes (Table 4.26).

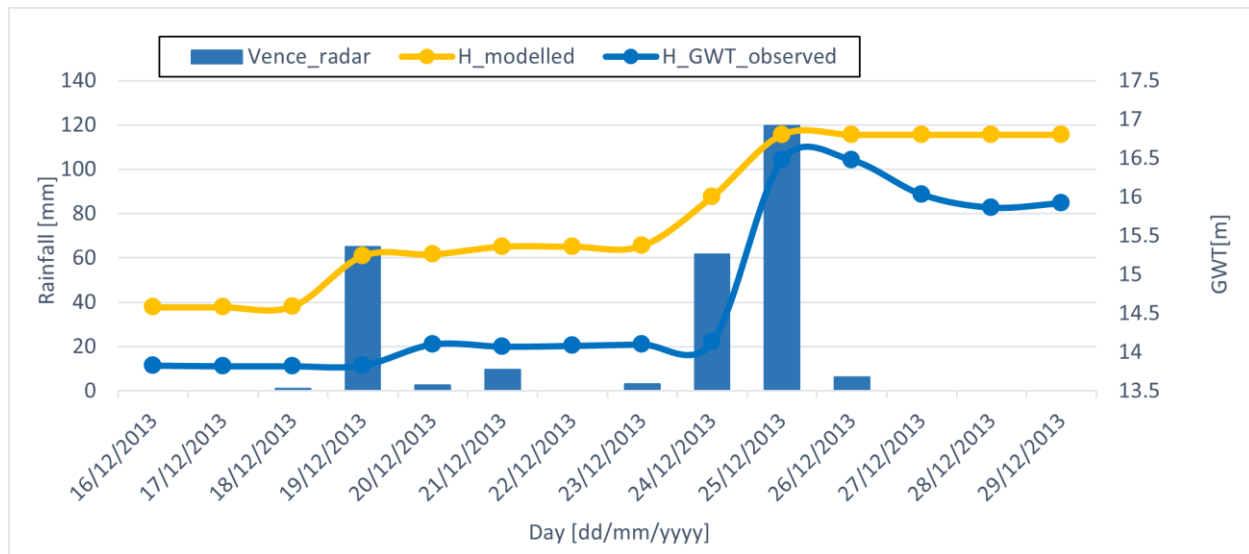


Figure 4.67. Comparison on GWT

The correlation value was high and comparable with those obtained for the C6 piezometer during the calibration optimization phase. The PBIAS highlights an overestimation of the aquifer, while the RMSE shows a difference in aquifer in the order of 1 meter.

Piezometer C6

Correlation [-]	RMSE [m]	PBIAS [%]
0.929	1.14	6.83

Table 4.26. Statistical indexes in C6 piezometer with respect to the Event 2013

Event December 2019:

The rainfall event occurred in 2019 is a short-intense event ranging from 15 to 25 December. The maximum cumulative rainfall occurs on 20 December, with about 80 mm of rainfall. Rainfall data was provided by raster radar (Figure 4.68).

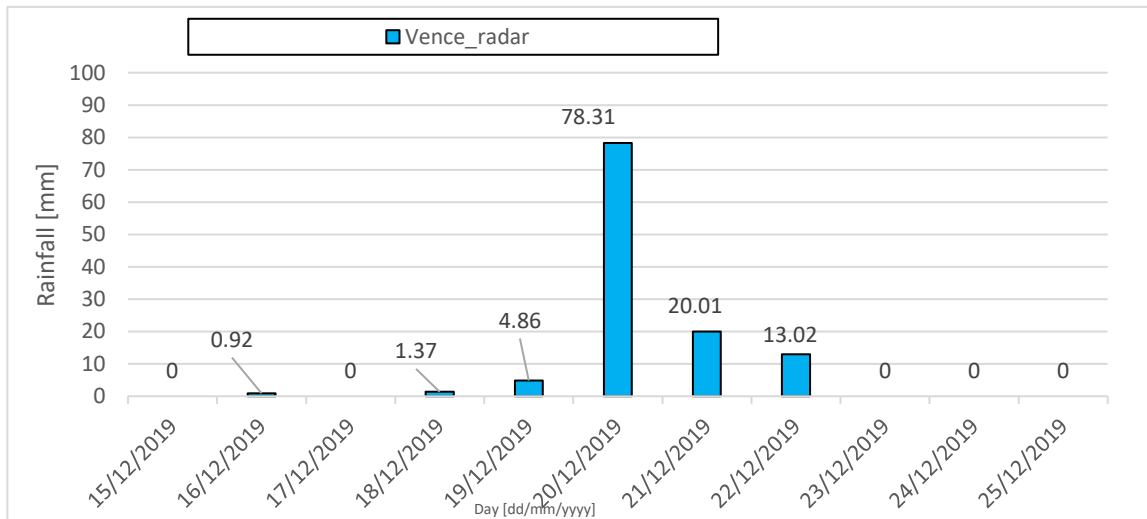


Figure 4.68. Rainfall event 2019

In the period analysed, the aforementioned monitoring network was no longer active. In fact, the C20 piezometer, although present, was damaged since 2015 and is no longer usable. Furthermore, in the upstream part the two piezometers (C11 and C7) are no longer active since 2010 and 2012, respectively.

A new piezometer, called C42, has been active since 2017. Therefore, the currently functioning monitoring network consists of two piezometers, (C6 and C42), positioned in the downstream area. For this reason, a new average GWT was defined, using the data recorded by active piezometers (2017-2019) and those relative to the old monitoring network. The modeling took place as already described. The new average GWT map is shown in Figure 4.69.

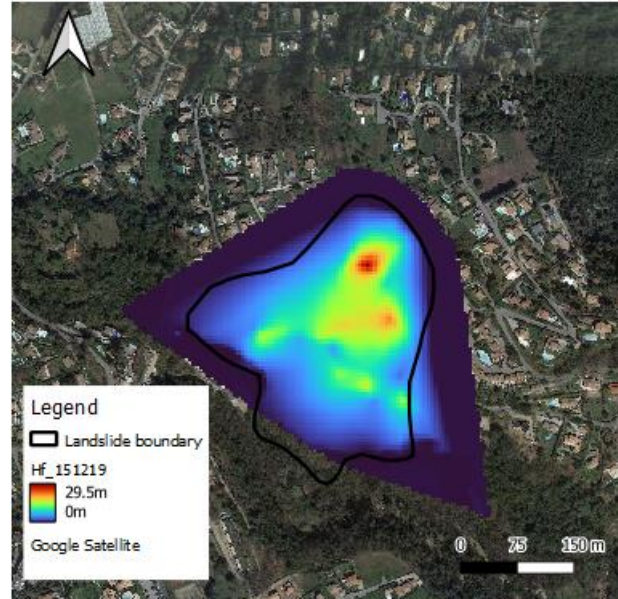


Figure 4.69. Average GWT_2019

As can be observed in the following figures, cross-sections of the landslide volume show that the two average GWT are almost coincident. Figures 4.70 and 4.71 show two cross-sections passing through pairs of piezometers, C11 and C6 and C7-C20, where the two groundwater tables are almost overlapping. The most substantial variations are observed at the cross section passing through zone a, for piezometers C6, C42 and C20. The presence of an additional measurement point makes it possible to grasp a minimal variation in the trend of the water table (Figure 4.72).

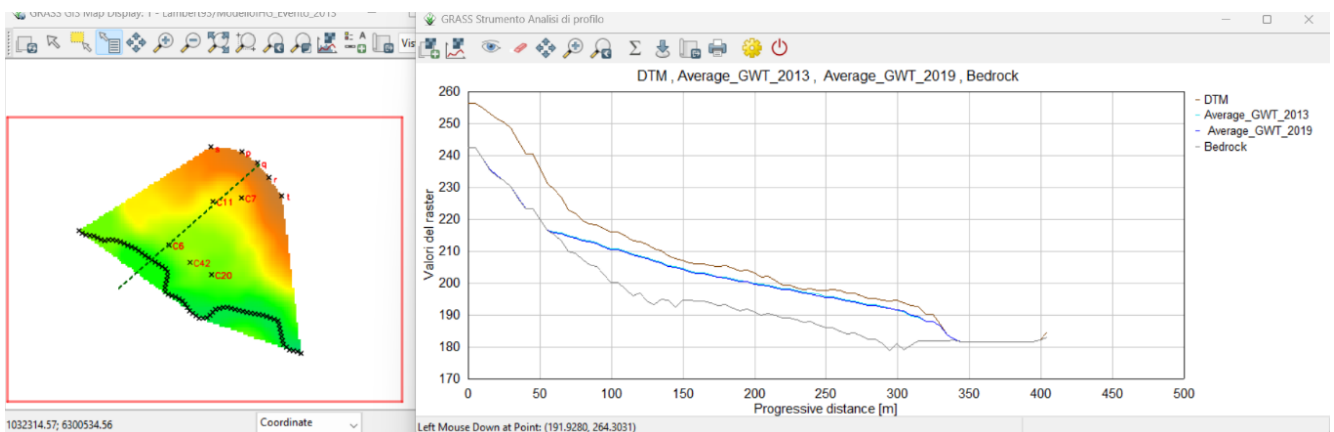


Figure 4.70. C6-C11 cross section

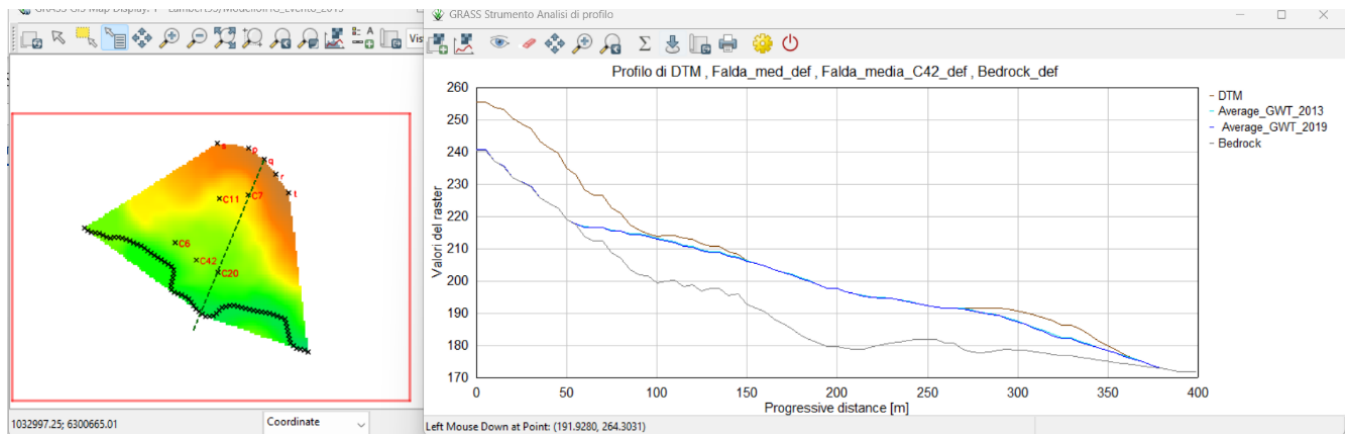


Figure 4.71. C7-C20 cross section

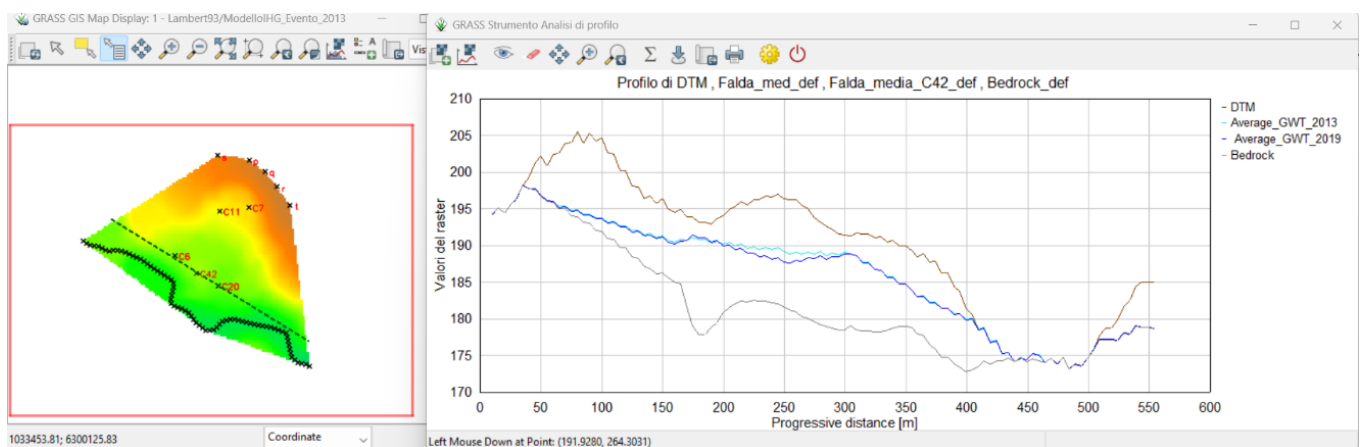


Figure 4.72. C6-C42-C20 transversal cross section

The modelled groundwater response was compared with C6 piezometric measurements in Figure 4.73 to evaluate its goodness. The initial difference between the two maps is about 75 cm, comparable with that estimated for the 2013 event. This confirms the coincidence of the modelled average water tables.

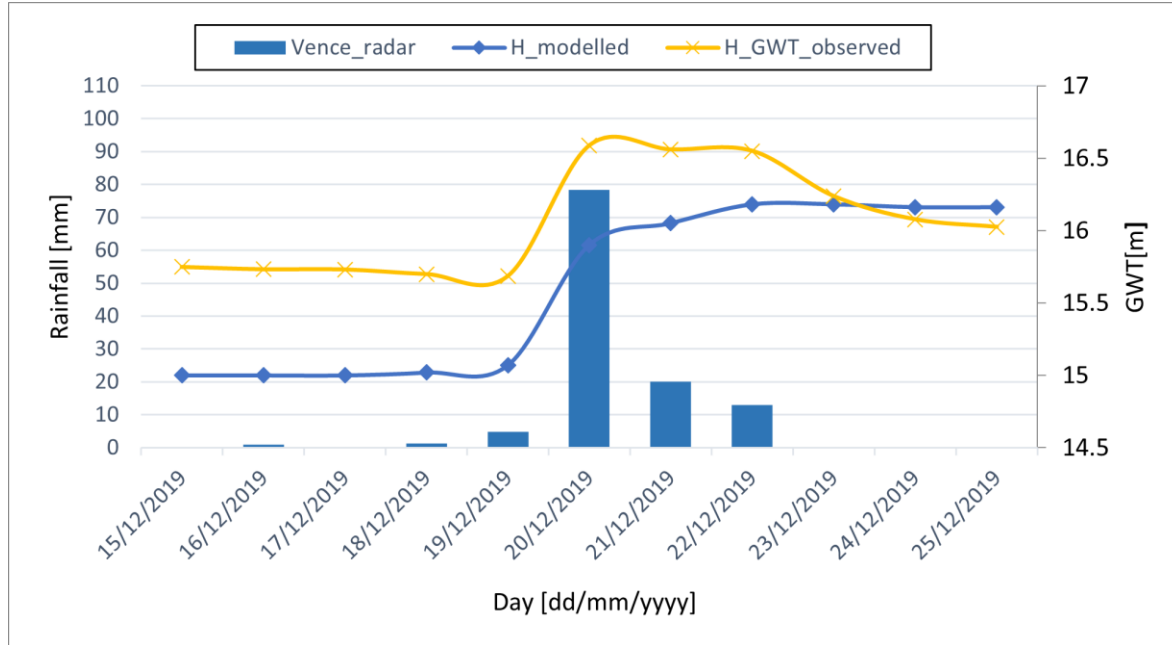


Figure 4.73. GWT heights variation in piezometer C6

The high correlation value indicates that the modelled GWT follows the trend of the measured one well and is consistent with the results of the optimisation phase. Although the value is underestimated (negative PBIAS), the overall RMSE is moderate (Table 4.27).

Piezometer C6

Correlation [-]	RMSE [m]	PBIAS [%]
0.82	0.3	-2.79

Table 4.27. Statistical indexes in C6 piezometer with respect to the Event 2019

4.2.6 Slope stability analysis

According to the slope stability analyses detailed in *Section 3.1.3*, the landslide susceptibility is detected by applying Equation 3.63 in occurrence of the chosen rainfall event that trigger the GWT oscillation. In order to perform the stability analyses, geotechnical characterization of the study site was required. The physical-mechanical parameters of the soil have been uniquely defined for both the analysed events.

With reference to the cross section in Figure 2.25 (*Section 2*), it was possible to classify the volume of Prat de Julian into two main types, characterized by different mechanical characteristics: the superficial layer consisting of sandy-clayey soil, coinciding with the unstable blanket, and the bedrock composed of alternating layers of soft sandstone and limestone.

The values, derived from preliminary analyses of studies carried out between 2001 and 2008 by groups of technicians involved in the study of the Prat de Julian landslide (i.e., EEG-Simecsol and IMS-Ingénierie des Mouvements du Sol et des Risques Naturels), are reported in Tables 4.28 and 4.29 for blanket and bedrock respectively.

Blanket layer	
γ [kN/m ³]	21
φ (simecsol) [°]	10
φ' (IMS) [°]	14
c' [kPa]	0

Table 4.28. Physical-mechanical parameter for blanket layer

Bedrock layer	
γ [kN/m ³]	21
φ [°]	40
c' [kPa]	50

Table 4.29. Physical-mechanical parameter for bedrock layer

Table 4.28 shows very low values that can be considered referred to a residual soil strength condition. Furthermore, this soil description does not appear to be consistent with the real slope stability conditions with reference to a minimum groundwater level. This statement is evident from preliminary analyses carried out based on the residual parameters at the minimum groundwater condition (Perata, 2018). With reference to the line of maximum slope, central to the landslide body (i.e., Section 2), Figure 4.74 shows FS which are diffusely lower than 1, in contrast with the actual slope stability conditions.

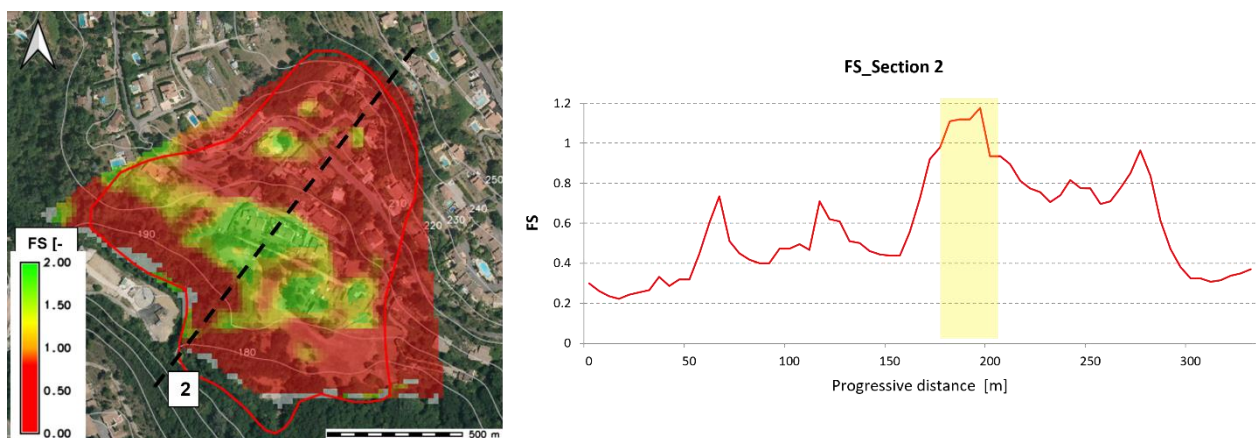


Figure 4.74. FS variation along the line of maximum slope (Section 2)

The only stable area with $FS > 1$ is in correspondence with the range between 170 and 200 meters (interval highlighted in yellow in Figure 3.74b) which represents the central area of the landslide. This area corresponds to the zone b, which was defined as stable in the geological report described in *Section 2.2*.

More representative values of the cohesion and friction angle parameters, defined in a previous master thesis work (Viaggio, 2018) through a back-analysis process on three significant cross sections of the landslide, were used. In addition, the assumption of effective cohesion equals to 0 is not reasonable in relation to the clayey composition of the surface layer. Thus, Table 4.30 summarized the geotechnical parameters characterizing the blanket, used in the stability analyses.

Blanket layer (<i>Slide 2D</i>)	
γ [kN/m ³]	21
φ	19
c' [kPa]	5

Table 4.30. Physical-mechanical parameter for bedrock layer

Event December 2013:

The first landslide susceptibility map, calculated by Equation 3.63, is referred to the average GWT (Figure 4.75). It is independent on the rain event considered, hence it allows to detect the most critical areas (red and yellow), located in the upstream (zone c) and downstream areas (zone a), because characterized by high slopes. On the contrary, the central area (zone b), characterized by low slopes, results stable, with $FS > 1$ (green area).

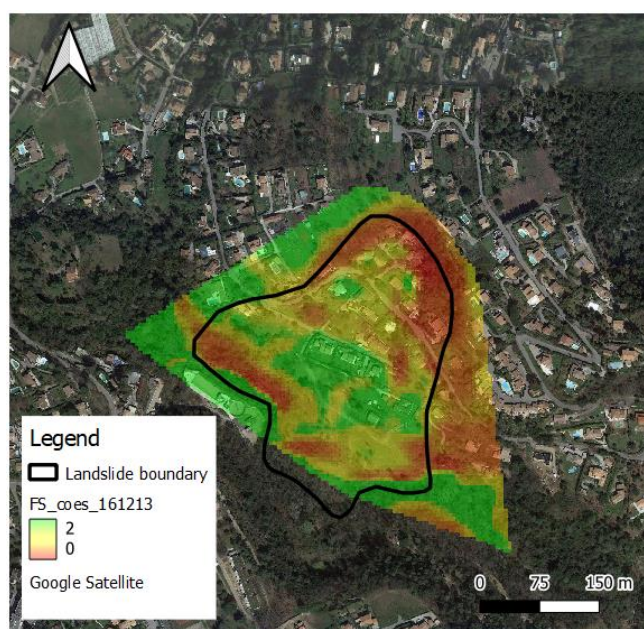


Figure 4.75. Initial FS map for the Event 2013

Figure 4.76 shows the landslide susceptibility variation in response to rainfalls for the most significant days of this event. A more marked variation of the stability conditions is observed in *zone a*, where an increase in critical areas (red and yellow areas) is particularly evident in the SE area of the slope.

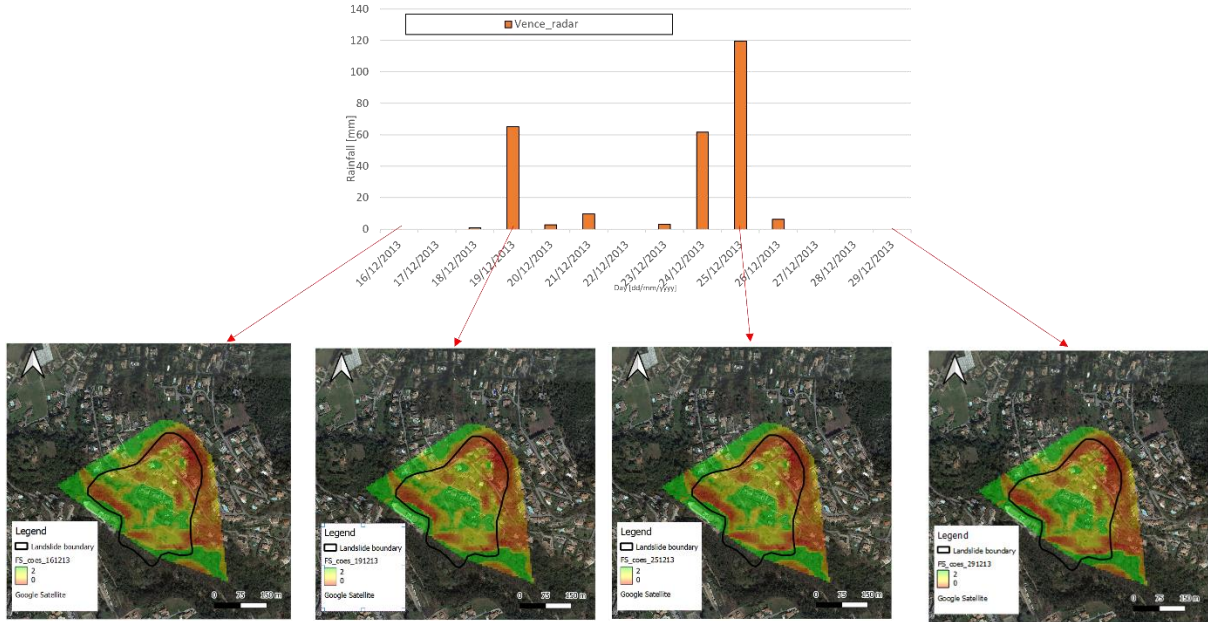


Figure 4.76. Landslide susceptibility evolution during Event 2013

A higher instability is observed in the considered most active area, due to the strong slopes and to the presence of the La Lubiane river which affects its stability at the foot.

The map representing the variation of the stability highlights the number of unstabilized cells by the rainfall event, in red in Figure 4.77 and in % in Table 4.31. These cells fall in the most critical areas of the landslide body, i.e. zone a zone c, highlighting the criticality of these areas. The central area, on the other hand, is confirmed to be stable.

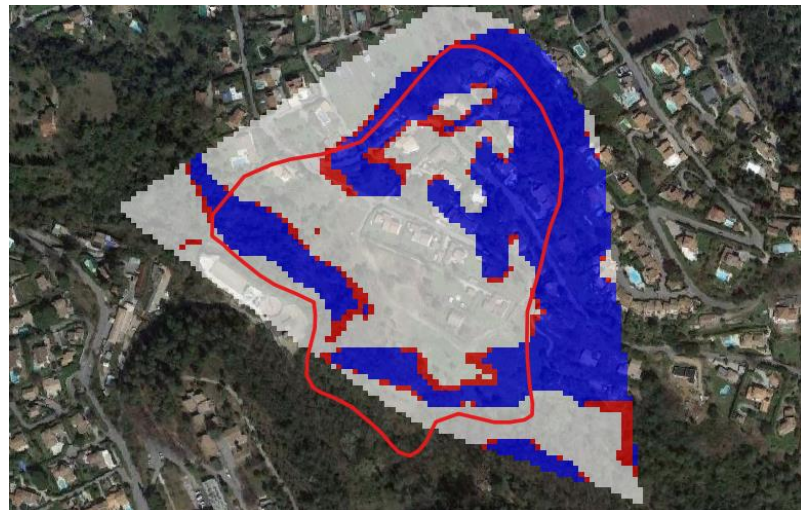


Figure 4.77. Stability condition variation map for the Event 2013

Class	Class description	% Cells
0 (white)	Always stable	53.7
1 (red)	Unstable due to the current event	5.7
2 (blue)	Already unstable	41

Table 4.31. %Cells belonging to the three different classes (cell area 25m²)

Event December 2019:

The landslide susceptibility map, considering the average GWT at the beginning of the event, is the same derived for the 2013 event. Three areas with different degrees of instability were highlighted: the stable central zone and the more critical a and c areas, due to steep slopes and the presence of the river downstream.

Figure 4.78 show the susceptibility variation on the most significant days of the event.

This event shows less variation in terms of susceptibility with respect to the 2013 event. A stability variation was observed only at the maximum rainfall days (20-21/12/2019), and it is also lower than what was observed during the 2013 event. The percentage of unstabilized cells (Figure 4.79) is summarised in Table 4.32.

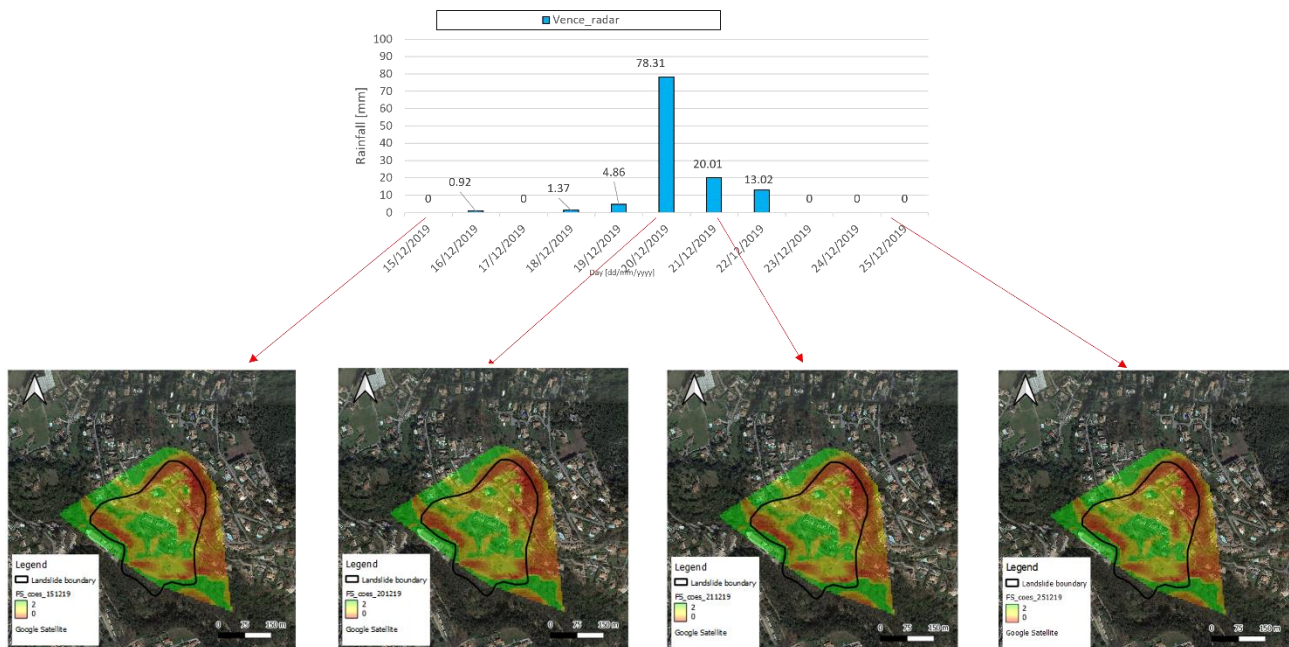


Figure 4.78. Landslide susceptibility evolution

Class	Class description	%Cells
0 (white)	Always stable	56.9
1 (red)	Unstable due to the current event	2.8
2 (blue)	Already unstable	40.4

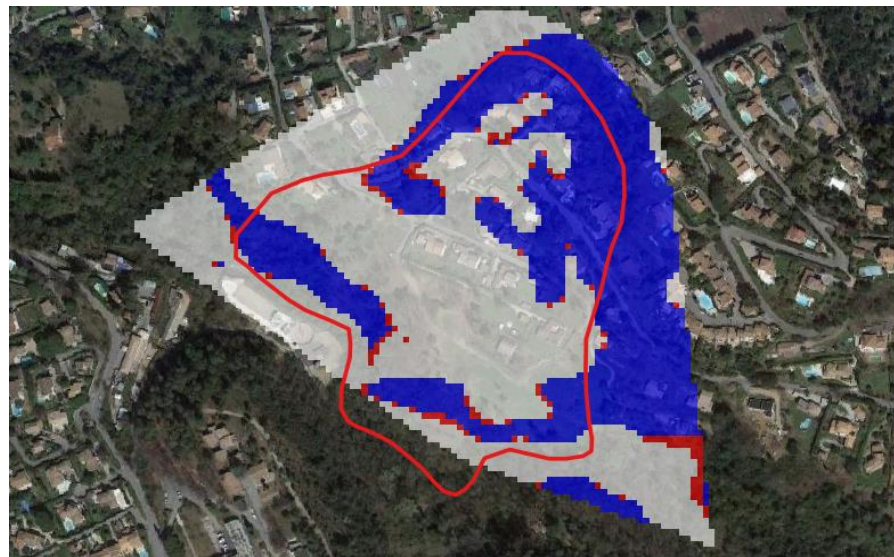
Table 4.32 %Cells belonging to the three different classes (cell area 25m²)

Figure 4.79 Stability variation conditions map for the Event 2019

Results comparison:

Stability condition variation maps allow to quantify the different response in terms of slope stability conditions to the Event 2013 (Figure 4.77) and the Event 2019 (Figure 4.79). The maps referring to the two events show unstable areas (belonging to class 1), which are almost coinciding. These areas, classified as unstable already from the initial groundwater levels, are mainly located at the foot of the landslide at the STEP sewage station and in the upper part, characterized by high slopes.

For the Event 2019, the critical, thus unstable, areas (in red) are reduced in extent and number (2.9%) compared to those detected for the Event 2013, and are located near areas belonging to class 1 (Table 4.31). This leads to state that reaching the typical GWT levels of the winter regime does not lead to a substantial degradation of stability conditions.

For the 2013 event, a higher number of cells are observed in the map in red colour (5.70%). These areas indicate higher criticality for both the downstream and upstream areas, confirming their high landslide susceptibility. They also highlight how, despite the water table reaching typical levels of the winter regime, an intense rain event of longer duration leads to greater slope instability.

4.2.7 In situ validation

The modelling results are compared with in situ observations, which show kinematism-related damage. This procedure is necessary in order to assess the goodness of the results and the validity of the model. The first comparison is made by superimposing the initial FS map (referring to the mean groundwater table) with the inventory map of landslide movements recorded from 1950 to 2001.

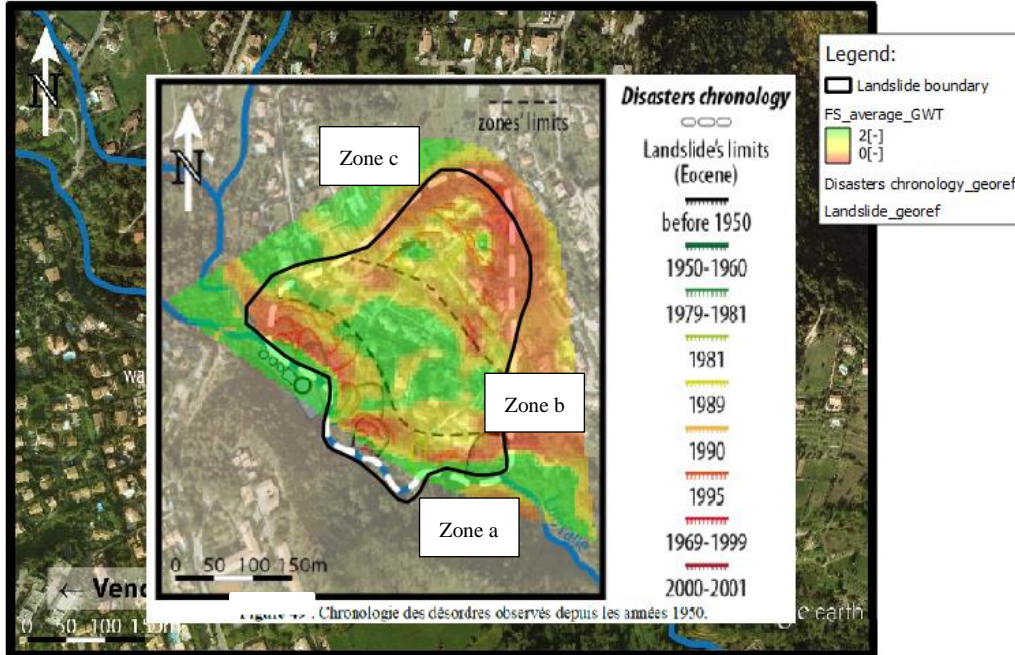


Figure 4.80. Comparison between the FS map and the disaster chronology image

Figure 4.80 shows that the kinematics surveyed between 1950 and 2001 correspond to the most critical areas ($FS < 1$, in red), which are classified as unstable already in correspondence with the groundwater levels of the winter regime.

With regard to the zones of the slope with different behaviour, identified in the geological report, some considerations can be made:

- Zone a, is where the most severe effects occurred following the rainfall event in the winter of 2000-2001 (Figure 4.81). The model correctly represents the criticality of the zone. In fact, Figure 4.80 shows that the observed slides are significant in number and size (red lines).



Figure 4.81. Landslide occurred in 2001 event in zone a.

- *Zones b.* No instability phenomena are documented, consistently the model reports values of the safety coefficient above unity (green areas).

- *Zone c.* It is coincident with the landslide crown, it is subject to diffuse larger instability.

Part of the in situ validation refers to the master thesis work carried out by Perata (2018). Stability variation conditions map was overlaid with georeferenced aerial photographs of the area, referring to 2018. The unstable areas were then compared with inventory maps of landslide movements recorded from 1950 to 2001 (Figure 34.82).

Three different zones were identified: zone A, divided into three sub-zones (A₁, A₂, A₃), zone B and zone C, located respectively at the base, centre and at the top of the landslide body. The report on the kinematics provides information up to 2001, however, by questioning the history of the photographic area (Google Maps) superimposed on the cadastral maps (French geoportal), it has been possible to observe the subsequent evolutions.

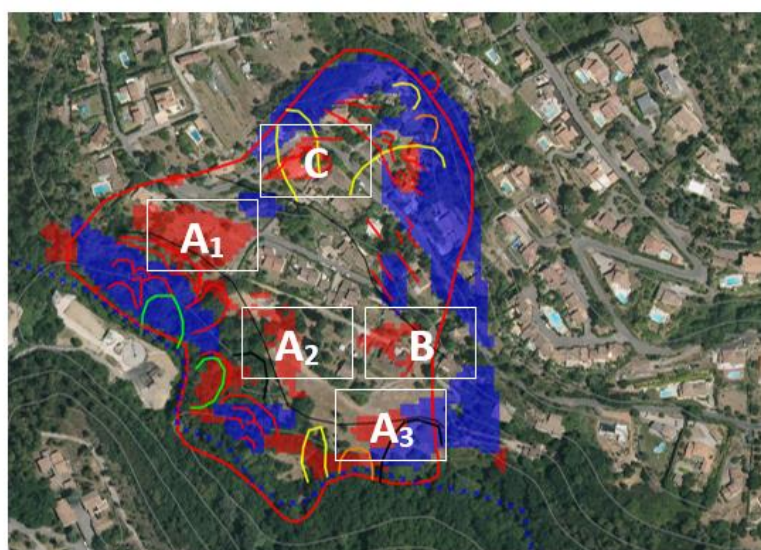


Figure 4.82. Landslide occurred in 2001 event.

Area A₁ (Figure 4.83): it can be considered the natural extension of the area at the foot of the landslide, characterized by severe criticality even in average groundwater conditions. In the cadastral map 308 (Figure 4.83a) the building was demolished in 2004. The separate building with the cadastral map 259 was demolished in compliance with the provisions contained in the modification of the PPRN referring to the year 2015. As a result of the kinematics recorded in 2001, the slope immediately downstream of the building suffered considerable ground failure, as shown in the photo from 03/2001 (Figure 4.83b).



Figure 4.83. Demolished buildings (a) and settlement of land parcel 259 (b).

Areas A2-A3 (Figure 4.84): in these areas, in accordance with the provisions of the PPRN, seven houses were demolished. With reference to Figure 3.80, where the FS map for average GWT is superimposed to the chronological damages map, it is possible to appreciate the concordance in the detecting hight landslide susceptibility areas.



Figure 4.84. Particular of buildings demolition referred to in zone A3

Area B: no kinematic mechanisms or demolitions of buildings were detected within zone B and this is in agreement with what emerges from the Figure 4.85. However, the model identifies this area as unstable, but currently no buildings are present in map 142.



Figure 4.85. Particular of the on-site comparison: “false” unstable area detected by IHG modelling

Area C: unstable zone due to the groundwater variations that affected the area during the rainfall events occurred in 1989-1990 and in 2000-2001. In this area, there are the ruins of the basement of an old building, known as "Maison Cavallin", demolished because of the displacements that occurred in 1950. In the surveyed area, this building represents the first building that have been affected by displacements such as to lead to its demolition .



Figure 4.86. Particular of in situ validation: “Maison Cavallin”

4.3. ASSESSMENT OF SOIL APPARENT COHESION (SAC) IN MENDATICA.

The SAC procedure was applied to the Mendatica site and an interesting example of analysis is described here. In the framework of the AD-VITAM project, soil moisture monitoring network was installed in December 2019, in Mendatica. The monitoring network (Figure 4.87), currently operational, consists of five measurement nodes (named M1, M2, M3, M4, M5) distributed over the study area, each bearing four soil moisture sensors positioned at different depths (-10, -35, -55 and -85 cm) along a vertical (Iacopino et al., 2021).

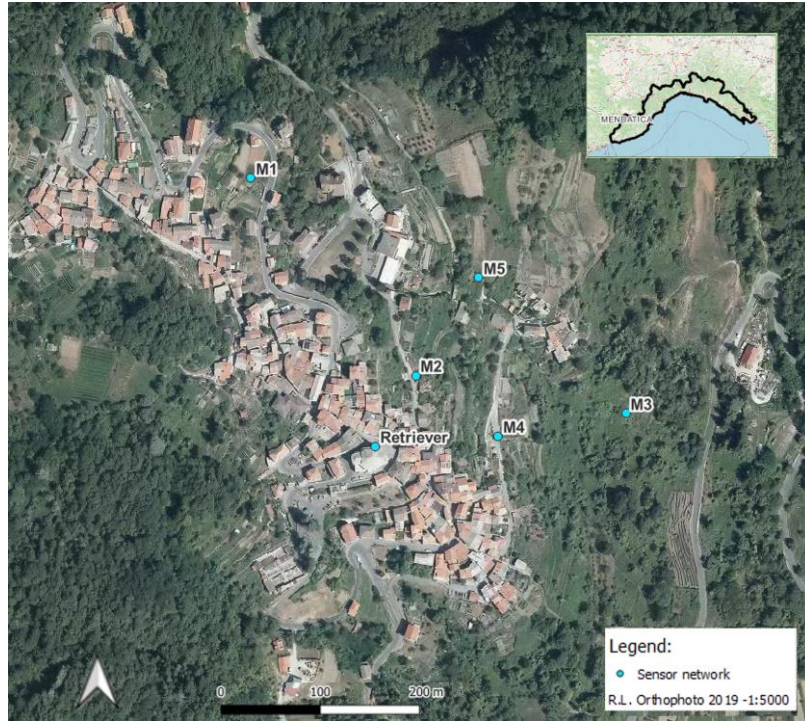


Figure 4.87. Soil moisture sensor network.

The rainfall event analyzed is the better-known storm named Alex (for brevity indicated as Alex Storm in the following), which occurred between 2 and 3 October 2020, triggering numerous landslides and causing considerable damage to the Mendatica village.

The SAC modelling described in *Section 3.2.3* was applied to the Alex storm on an hourly time scale in order to appreciate the evolution of the landslide phenomenon.

Rainfall data, relative to the 'Marconi' station placed in the center of the village, were downloaded. The rainfall histogram (Figure 4.88) shows hourly values between 50 and 60 mm, at the peak phase of the event. This phase is prolonged in time. The 24-hour cumulative rainfall is 556 mm.

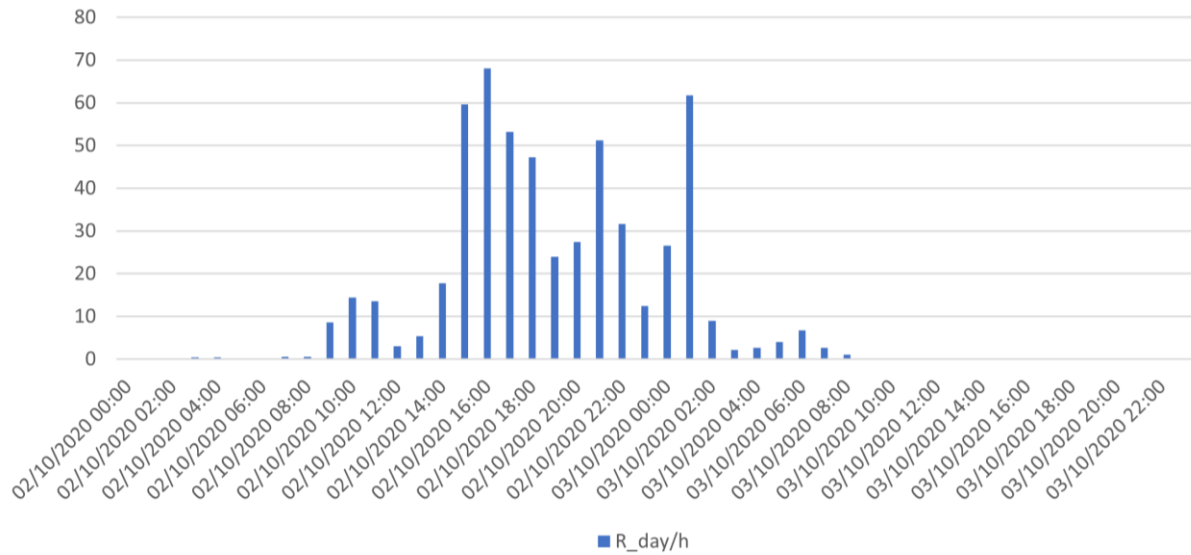


Figure 4.88 Hourly rainfall histogram for the “Alex Storm”

4.3.1. Input data preparation

According to the workflow explained in *Section 3.2.3*, the automatic procedure for the SAC definition requires the *Soil WRC* definition, built up on the intrinsic soil properties. These quantities were determined by performing laboratory tests on the Mendatica soil for the geotechnical characterization and laboratory calibration of the Waterscout measures. The grain size distribution by sieving and sedimentation for a soil sample at node M1 was conducted conforming to the guidelines proposed by BS EN ISO 17892-4:2016, showed in Figure 4.89 and tabled in Table 4.33.

Grain size distribution		
%Sand	%Silt	%Clay
[2-0.075mm]	[0.075-0.0025mm]	[<0.0025mm]
%	%	%
33.1	51.7	6.0

Table 4.33. % grain size distribution

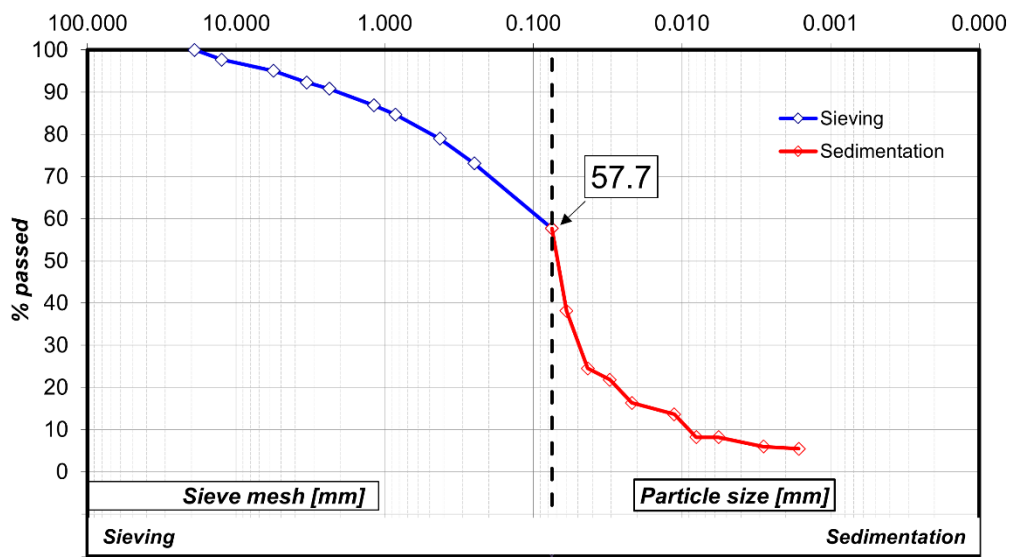


Figure 4.89. Soil grain distribution for the sample M1

In addition, the Atterberg limits have been detected and the values of Liquid Limit (37%) and the Plasticity index (10.3%) allow to define the soil as low plasticity-compressibility organic silt (ML), according to Casagrande classification.

Furthermore, with reference to a soil sample at the M1 node, the carbon content (%C) was calculated as 58% of the soil organic matter (Pribyl, 2010), determined in compliance with the standard ASTM D2974-20 (2020). Figure 4.90 shows some phases of the laboratory test: the sample was put in an ignition oven capable of producing constant temperatures of $440 \pm 40^\circ$, in order to dry it (a); soil sample is placed in a desiccator used to prevent the increase in moisture during cooling of the oven-dried sample (b). The %C results to be equal to 5.1%, confirming the organic soil nature.

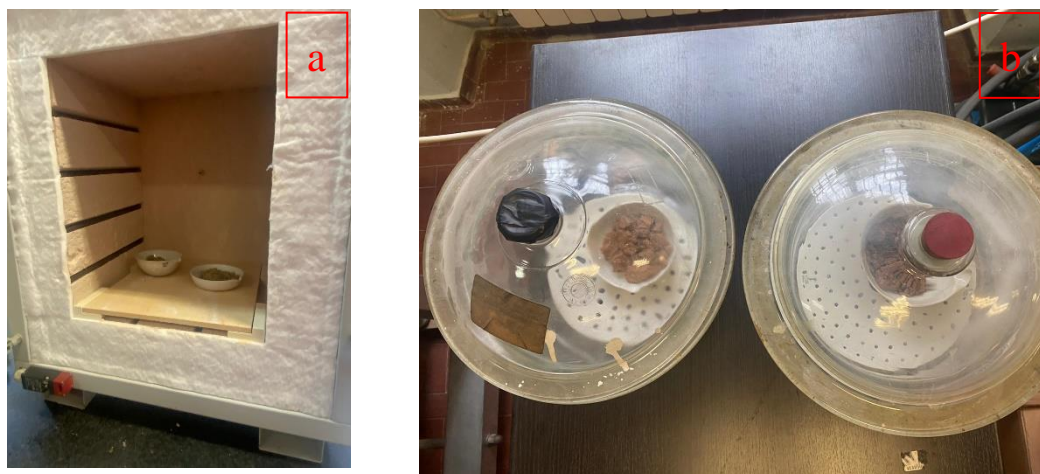


Figure 4.90. Phases for the soil organic matter determination: soil drying phase (a) soil cooling phase (b)

For the case study, G_s is equal to 2.7. and it was determined through of a picnometer test according to BS EN ISO 17892-3:2015.

The intrinsic soil properties values adopted as input in the automatic procedure for the WRC definition are summarized in Table 4.34.

Intrinsic soil properties			
%Sand	%Clay	%C	G_s
33.1	6.0	5.1	2.7

Table 4.34. Intrinsic soil properties for M1

The soil-specific calibration, detailed in *Section 3.2.2*, allows the raw data provided by the soil monitoring network to be transformed into Volumetric Water Content values (θ_v); this procedure was performed on soil sample M1 applying the following calibration equation:

$$\theta_v = 286.8 \left(\frac{V_{out}}{V_{in}} \right) - 89.3 \quad (4.6)$$

where the values 286.8 and 89.3 are the constants values. Equation 3.6 provided by the linear regression parameters for the Mendatica soil calibration.

By applying this equation on the maximum data measured by the network over the available period of measurement (i.e., December 2019-March 2022) the calibrated θ_{max} value results equal to 0.487 and it was detected during the Alex Storm. With reference to the calibrated θ_{max} adopted in the procedure, the calculated gravimetric water content value and the pertinent dry density value are equal to 0.351 and 1.386 g/cm³ respectively.

The analysis was carried out to an hourly time scale with reference to the period shown in the rainfall histogram. The calibrated VWC data have been provided for each node in a .csv format, loaded in QGIS, saved in .shp format and then given as input data to the SAC procedure.

4.3.2. Results

Once all input data were set, the implemented procedure performed the calculation of the WRC for the Mendatica soil. In Figure 4.91 suction (in kPa) is reported in abscissa on a logarithmic scale, in accordance with the literature representation, and θ_v (dimensionless) is indicated on the ordinate. The blue line represents the WRC obtained for the Mendatica soil type, the orange line represents the residual volumetric water content, θ_r , while the black dot is θ_s , corresponding to a fully saturated soil condition.

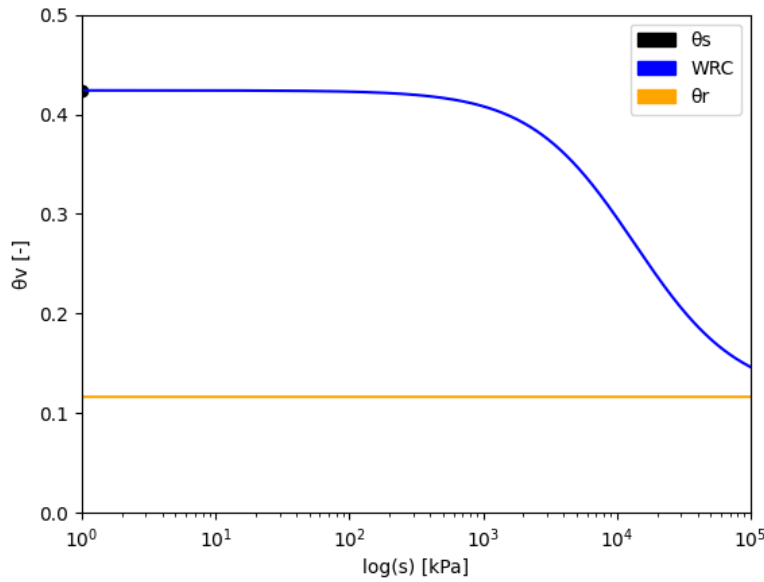


Figure 3.91. Soil WRC

Note that θ_s calculated by the procedure is equal to 0.424, hence it is lower than that recorded on site θ_{max} . This difference may be related to the fact that the latter was recorded at an extreme event. Moreover it is the result of an experimental calibration, described by a linear regression, that may be affected by a certain degree of uncertainty not evaluable a priori. On the other hand, the defined Soil WRC is based exclusively on empirical correlations and intrinsic parameters of the soil whose determination depends on laboratory tests, which also in this case may be influenced by errors. In addition, the SAC simplified procedure cannot reproduce some types of soil behaviour, such as hydraulic hysteresis (Balzano et al., 2021). However, it should be emphasised that the procedure described here is intended to be a useful tool to be provided to the competent authorities for landslide risk management. This aspect requires the elaboration of a tool which, even if simplified, is able to describe the soil behavior in partial saturation conditions. The WRC is able to describe the soil in an acceptable way and allows to estimate the suction and apparent cohesion values in a satisfactory manner.

For each θ_v datum the procedure provides suction and apparent cohesion values, according to Equation 3.70 and the third term of Equation 3.71. These outputs are provided in raster format and in vector format.

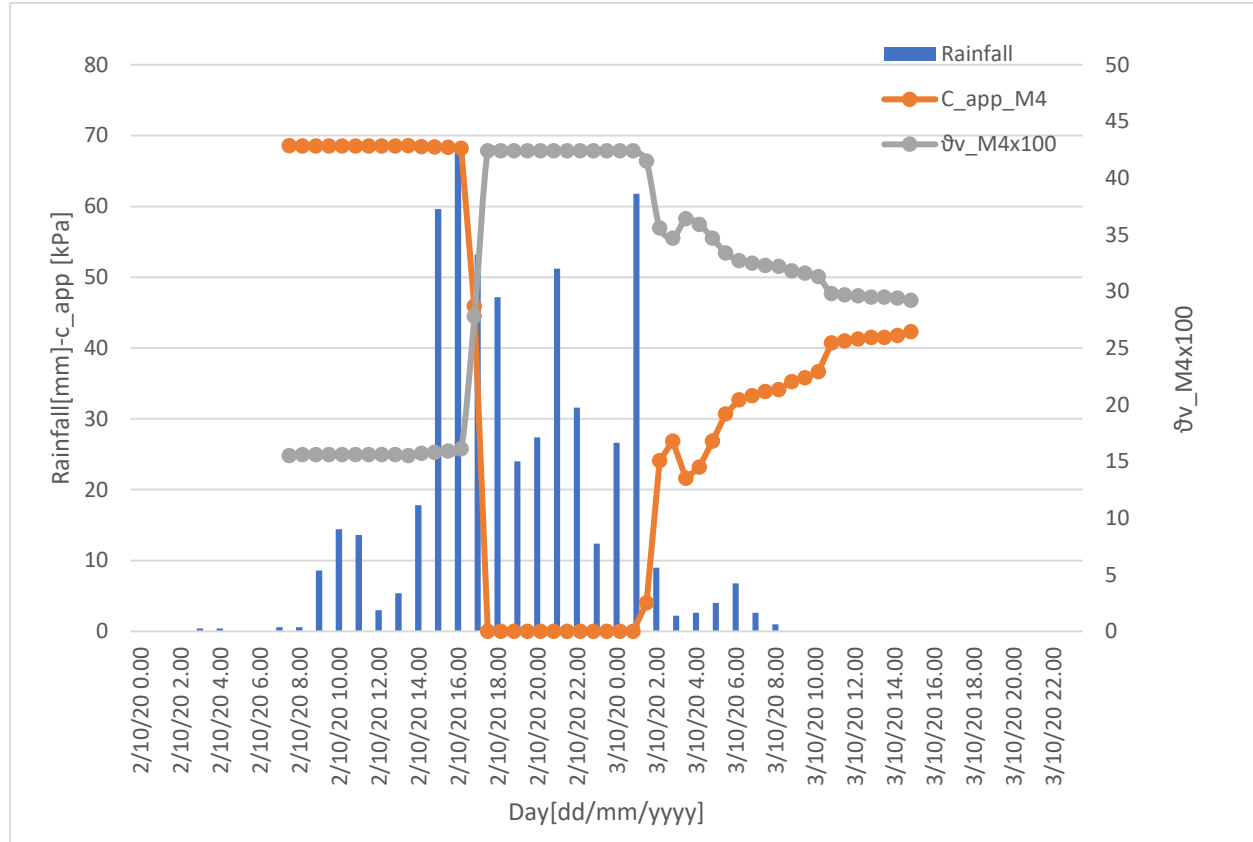


Figure 4.92. Comparison between the VWC and apparent cohesion trends.

Figure 4.92 shows the shear strength induced by partial saturation (in orange) with reference to each hour of the analyzed rainfall period (blue histogram), also compared with the monitored VWC values (in grey). The graph was obtained by querying the raster outputs of the automatic procedure at the -55 cm depth in the node M4. Note that, for a better comprehension of the parameters showed in the graph, the VWC values are multiplied by 100. With regard to the VWC trend, a good response to rainfall is evident, with high values during the hours on which the rainfall is intense (from 5p.m. of the 2nd October to 1a.m. of the 3rd October). Conversely, the shear strength shows a significant decrease when rainfall occurs, due to the variation in soil moisture content.

The results of this application show the magnitude of the shear strength variations during a rainfall event, which may strongly affect the slope stability.

4.3.3. Shallow landslide stability analyses

The results of the previous procedure can be used to evaluate the shallow landslide susceptibility, taking into account the soil behaviour under partial saturation conditions both in terms of apparent cohesion values and volumetric water content.

The shallow landslide stability analyses here carried out are referred to a soil depth equal to 85 cm, in order to be able to characterize the slope behaviour in the first metre of soil, according to the

definition of shallow landslide given above. The analyses have been carried out in GRASS GIS, through the *r.mapcalc* module.

Working on the surface depth, the geotechnical parameters used in the IHG modelling were too conservative for this modelling, as they were defined for much greater blanket depths. For this reason, a new friction angle was defined to describe the superficial stratum.

The friction angle, related to the superficial depth, was identified as a function of the results of the SPT tests performed during the geognostic survey. Based on the N_{spt} values referred to the most superficial layers, between 3 and 5m from ground level, and through the use of empirical formulas proposed in literature, the range of variation of this parameter was identified. With reference to the relationships proposed by the *Road Bridge Specification* and by *De Mello*, the range is between 18° and 30° . A back analysis was therefore carried out to identify the value of the significant friction angle for the first metre of soil Table 4.35.

The definition of the unit weight of dry soil, which characterises Equation 3.78, was found by averaging the value detected for a S13 sample (depth close to 6m) provided by the direct shear test result deduced from the geotechnical report (Macciò, 2007) and the value averaged for the M1 soil samples, used for laboratory calibration. Defined in accordance with Equation 4.7, γ_{dry} results to be a function of G_s , γ_w and the soil porosity of the specimens.

$$\gamma_{dry} = \frac{G_s * \gamma_{water}}{(1 - e)} \quad (4.7)$$

Table 4.35 summarized the geotechnical parameters, while the strength contribution due the effective cohesion has been neglected in this analysis.

$\phi' [^\circ]$	$\gamma_{dry} [\text{kN/m}^3]$
20	16.4

Table 4.35. Geotechnical parameters

The shallow landslide stability analyses require as input data the volumetric water content and the apparent cohesion maps. The procedure to generate these maps ad been detailed in *Section 3.3*. It is based on the association of VWC or apparent cohesion values to all areas that have the same characteristics in terms of land use and HSG classes definition.

Concerning the land use map, it was reclassified to obtain homogeneous areas (Figure 4.93), by identifying three different classes:

- urbanised area;
- woodland;
- grassland.

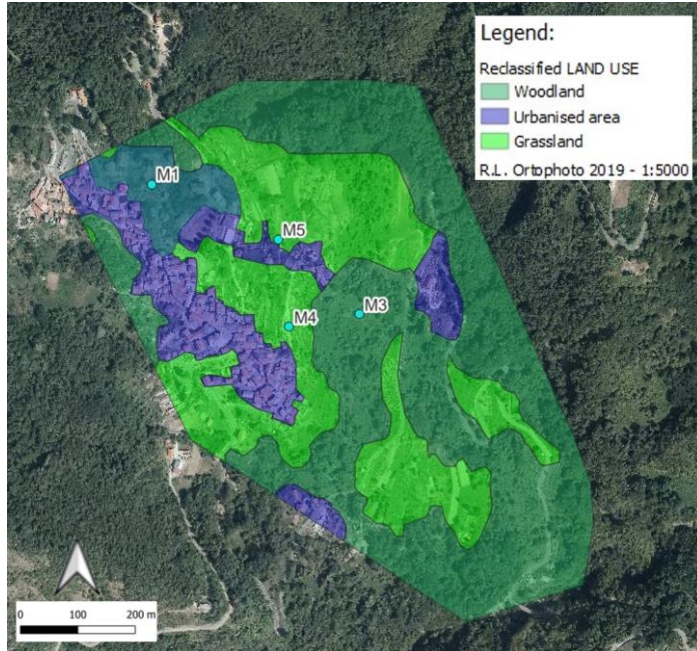


Figure 4.93. Reclassified Land use map

The obtained map was then superimposed on the hydrological classes map referred to the first meters of soil. Subsequently, with respect to the identified homogeneous areas, the derived map was compared with the location of the sensors on site. From this comparison it was therefore possible to associate the parameter of interest (i.e., VWC, apparent cohesion) to all the areas with the same characteristics (Figure 4.94).

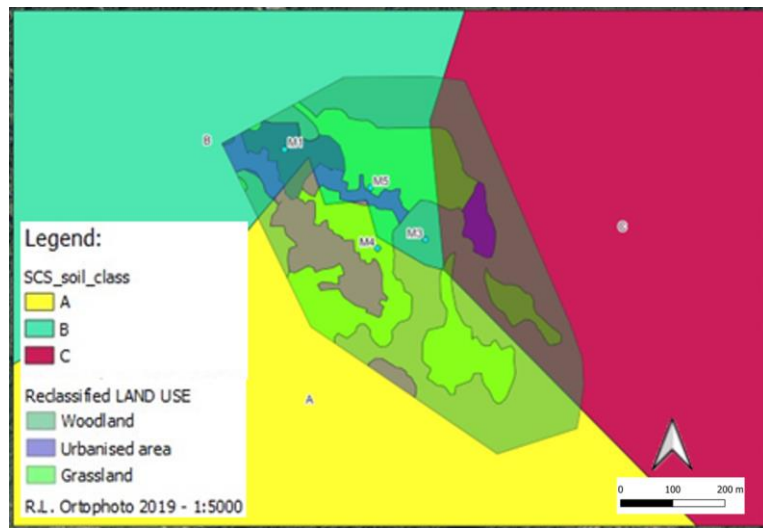


Figure 4.94. Comparison map of Land use/SCS soil/sensors position

The association was made as follows: the M1 sensor was associated with the urbanized area, the M3 sensor with the wooded area, the grassland area was divided according to the HSG class to the M4 sensor (zone A) and M5 (zone B and C).

All this information was then processed in GRASS-GIS by creating a vector containing the information related to the two maps and updating the database once with the volumetric content of water, once with the apparent cohesion. Given the amount of data processed, it was preferred to divide the information into two distinct vectors, so as to make the analyses faster.

Finally, through the rasterization process, the hourly maps of WVC (Figure 4.95) and apparent cohesion (Figure 4.96) were obtained.

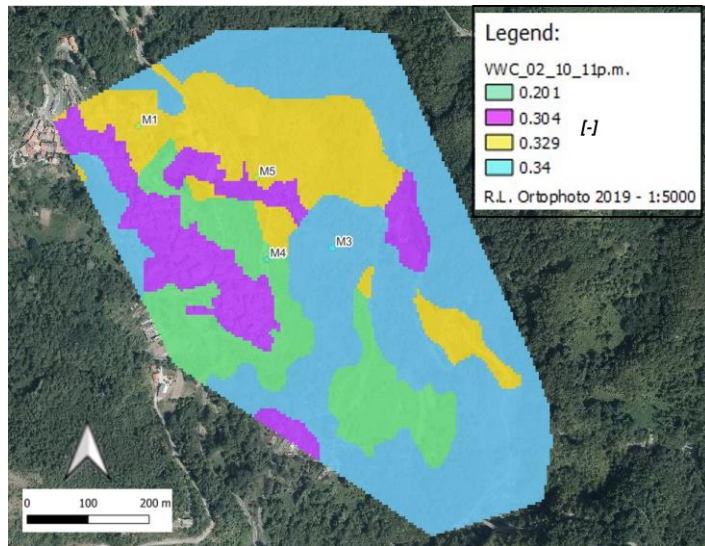


Figure 4.95. Volumetric Water content map related to the 02/01/2020 at 11 p.m.

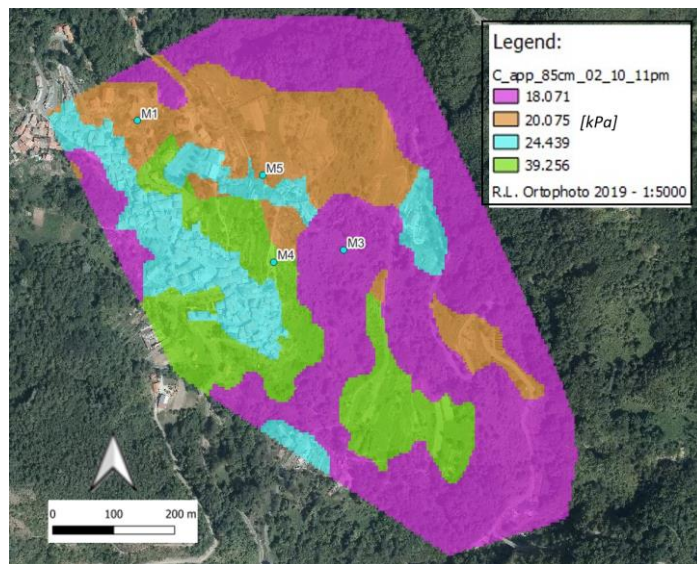


Figure 4.96. Apparent cohesion map related to the 02/01/2020 at 11 p.m.

For each hour of the rainfall event the landslide susceptibility map has been produced, based on the Safety Factor definition, according to Equation 3.77. These maps are represented in a traffic light colour scale, according to IHG modelling, varying from red colours (describing critical areas with $FS < 1$) to the green

colour (describing stable areas, with $FS > 1$). Yellow colours describe areas of incipient instability, characterised by FS close to 1. Figure 4.97 shows the FS variation over the rainfall hours. In the first hours of the rainfall event, the slope results to be stable, then at 2.00 p.m., the areas in the eastern part of the slope, classified from the hydrological point of view by class C, i.e. low infiltration capacity, are subjected to a decreasing of FS , and so to became unstable. From 6 p.m. to 2 a.m. the greatest criticalities were observed. Subsequently, the slope moves towards a stability condition, even if it still has unstable zones, especially in the areas to which hydrological class C is associated.

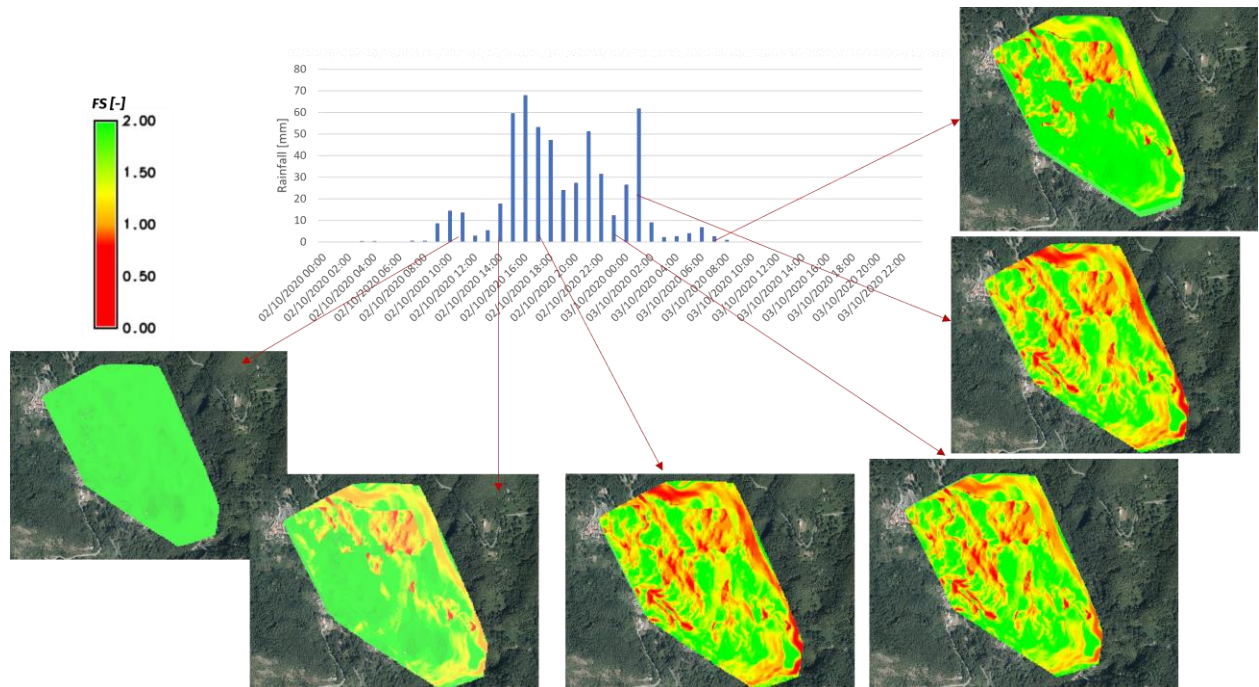


Figure 4.97. Stability analyses evolution

This type of analysis makes it possible to assess the stability conditions of a slope due to changes in the volumetric water content following a rainfall event.

The goodness of this analysis was estimated through indirect validations, both in situ and by comparison with the displacements recorded by the GNSS network.

The in-situ validation made it possible to verify whether real instability phenomena occurred at the critical zones estimated by the model. Figure 4.98 highlights this comparison. It emerges that, although simplified, this analysis made it possible to detect the areas where damage had actually occurred.

The data recorded by the GNSS network allow to identify the areas where important movements happen and in which direction (blue arrows for the planimetry and red arrows in altimetry in Figure 4.99), making possible to validate the criticalities in Borgata Piano identified by the landslide susceptibility map.

In fact, the displacements appear to be very intense, compared to those recorded in the pre-event (a) and post-event (b) periods.

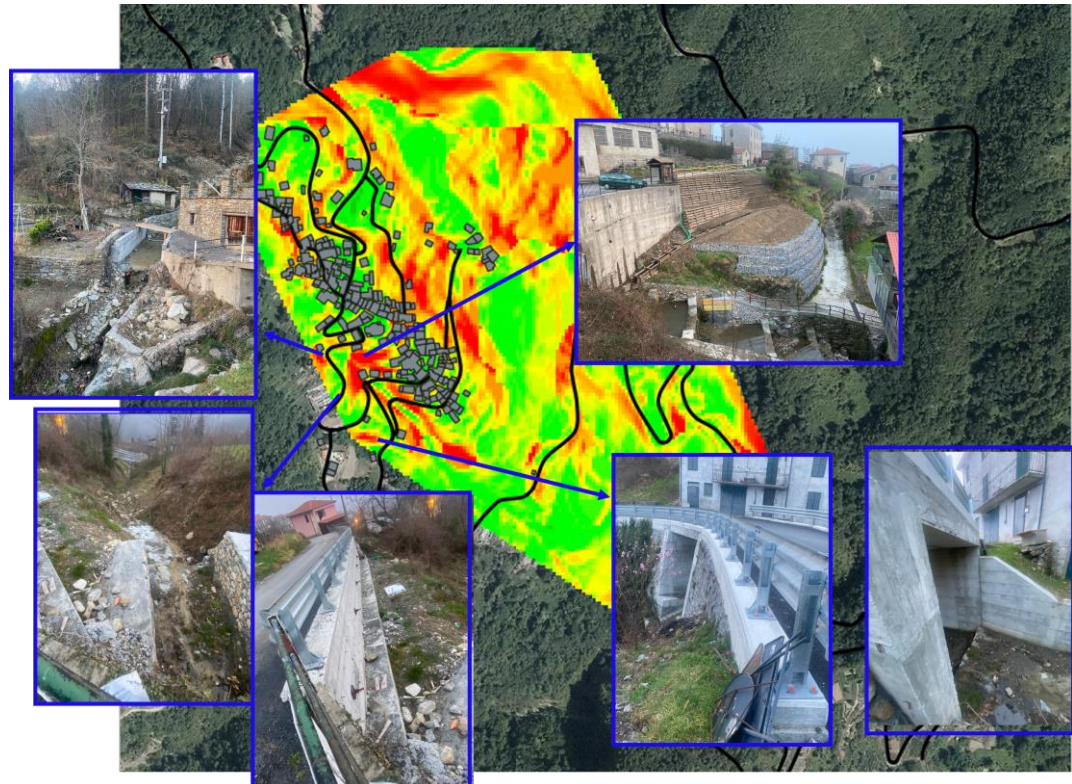


Figure 4.98. In situ validation: correspondence between some damage that occurred in 2020 and the critical zones defined by SAC modelling.

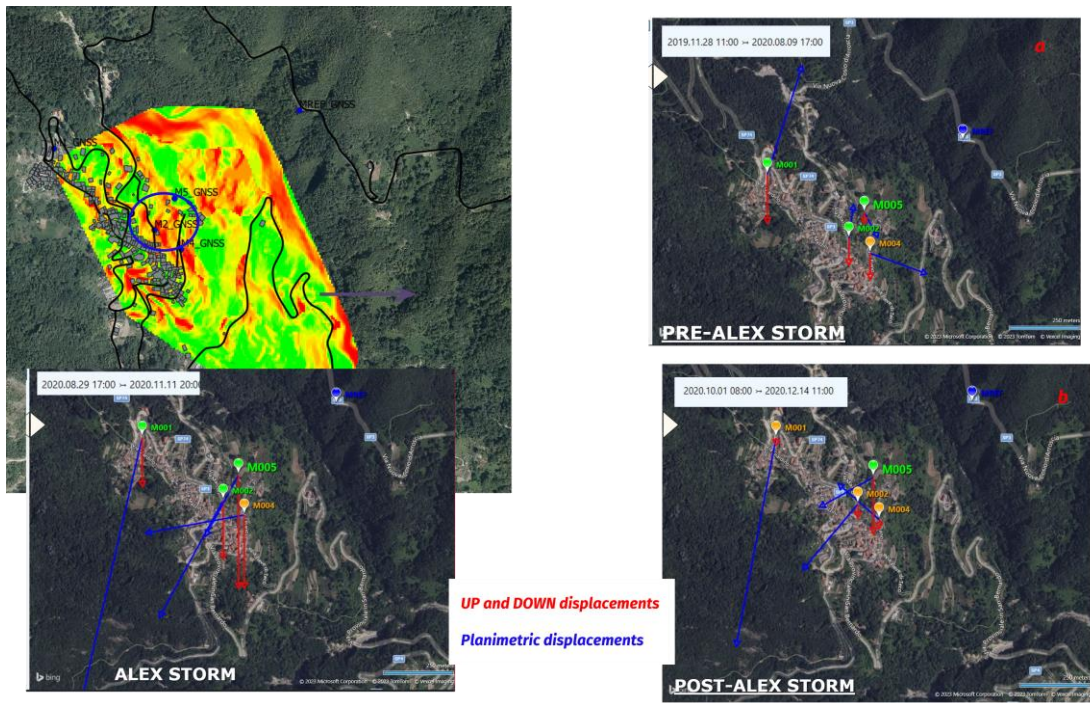


Figure 4.99. GNSS comparison validation of the criticalities in Borgata Piano, identified by the landslide susceptibility map, and displacements comparison in the pre-event (a) and post-event (b) periods.

5. CONCLUSIONS

Rainfall-induced landslides are natural hazards that often generate a large number of fatalities and economic losses. Over the years, the occurrence of increasingly intense rainfalls, human activities, including often uncontrolled urbanisation, and land abandonment, which have led to massive changes in land cover and land use, have affected and still affect slope stability. More and more often, the authorities in charge have to deal with landslide risks management without having appropriate tools. Landslide risk mitigation generally involves landslide mapping, warning systems and regional planning. The most effective approaches include a combination of these strategies, with good coordination between the scientific, engineering and planning communities (Gori et al., 2003).

Desirably, the estimate of landslide susceptibility requires the development of 3D models to characterise the typically three-dimensional nature of the slopes. Critical analysis of existing models in the literature has shown that the development of three-dimensional LEM methodologies for estimating landslide susceptibility over areas of a few square kilometres, typically at the scale 1:5000, is an open challenge. The difficulty lies in the design and development of 3D modelling procedures that, although simplified, can represent a useful tool for landslide risk management.

Such operational models must allow information to be managed in a simple and user-friendly manner in both input and output, they must return results spatialised over the entire area under study although the input information is often very localised, and they must be computationally light. This can be achieved by working in a GIS environment.

With regard to rain-induced landslides, this dissertation focused on the development of automatic procedures for mapping susceptibility to landslides due to: (i) groundwater fluctuations and/or (ii) changes in soil water content.

With reference to the landslide susceptibility due to groundwater oscillations, the application of the physically-based IHG model to two case studies (Mendatica and Vence, in Italy and France respectively) was described and discussed.

In the first modelling phase, the calibration and optimisation of the hydrological model, based on the Modified CN method, was performed at the local scale, referring only to the cells of the domain where the piezometric stations were located. The calibration and optimisation procedures allow to determine the values of effective soil porosity and soil permeability characteristic of the site, so to represent with good accuracy the groundwater fluctuations compared to the piezometer measurements.

The second phase of the procedure consisted in the spatial modelling of surfaces and parameters, with particular attention on the criticalities inherent in the discretization of rather large areas with good resolution and computational speed has been discussed.

Then, slope stability analyses, based on the limit equilibrium method, was performed on the entire study areas, obtaining landslide susceptibility maps. The application of the IHG model to the case studies highlight the potential of this methodology of analysis. In fact, it is worth emphasising that IHG allows large portions of land to be analysed in less time than other 3D modelling techniques (3D LEM and 3D FEM), capturing critical areas with a satisfactory degree of detail. It therefore appears promising.

Recent improvements to the IHG procedure as part of my doctoral research allow both an optimal geometric reconstruction of the model and the spatialisation of hydrological-geotechnical parameters by interpolation/extrapolation of local measurements. Moreover, the procedure was automatized thanks to a QGIS plugin, based on a Python script, that, starting from the input data allows to perform the landslide susceptibility analyses.

The study of landslide susceptibility due to change in soil water content represents the most innovative aspect of this dissertation. In fact, knowledge of unsaturated soil behavior is essential for the landslide susceptibility assessment, especially in the case of shallow landslides. Hence, an automatic procedure, named SAC (assessment of Soil Apparent Cohesion), for shallow stability analyses in partial saturation conditions has been implemented.

Input data are soil moisture monitoring data, provided by a network of sensors or by a raster map derived from previous data processing/spatialization or remote sensing products. In case of point data, a properly structured table in a geodatabase must be populated. If soil moisture data are not already calibrated, the laboratory-defined soil-specific sensor calibration equation can be applied in the procedure to automatically pass from raw sensor data to soil water content data. Then, the automatically obtained Water Retention Curve equation is applied to estimate the suction and apparent soil cohesion induced by the partially saturated soil condition. Apparent cohesion can be automatically estimated for each depth at which soil moisture is given. If input data comes from a monitoring network, the output values must be spatialized over the entire area of interest, through appropriate interpolation techniques.

Shallow landslide susceptibility assessment is based on the limit equilibrium method, where the shear strength contribution provided by the soil under partial saturation conditions is considered in the definition of the Factor of Safety FS (in the determination of which the weight of the soil at a given moisture content is also taken into account).

The innovative aspect of the SAC procedure lies not only in being an operational model, allowing processing at a punctual scale, but also in the fact that it allows spatial mapping of outputs, useful to characterize the entire area under study. Knowledge of unsaturated soil behavior is essential for the

landslide susceptibility assessment, especially in the case of shallow landslides. With reference to the Mendatica site, the procedure was presented and discussed. The preparation of the input data, based on standard laboratory tests, the working scale at which the landslide phenomenon can be analysed, the possibility of choosing the time scale at which to work, the empirical method underlying the procedure, and the data spatialisation techniques represent key points to which attention has been paid in this dissertation. It is precisely the attention devoted to these points that has allowed the development of a methodology that can be useful in landslide risk management.

It is worth underlining that the described procedure can be usefully employed (also in other landslide modelling approaches, in which it can be integrated) to improve the assessment of stability conditions over time, by analysing the evolution of the saturation front as a function of weather conditions.

Fell et al. (2008) emphasised the need to test the results of GIS modelling on field; this is crucial for understanding the goodness of a model and for estimating how well the maps reflect field reality.

In the present dissertation, the comparison between the modelled landslide susceptibility maps and on-site observation was carried out for both the developed procedures (i.e. IHG and SAC procedures). Despite the simplifications introduced in the modelling, given the need to develop operationally simple models that can be used in landslide risk management, the results obtained from the model show a strong correspondence with on-site observations. As discussed, generally, the areas classified as high susceptible by the model correspond well to actual damaged zones (e.g., soil settlement, building cracking). In addition, displacements measured by topographic or GNSS techniques have been used for further validation.

Therefore, it can be concluded that the IHG and SAC automatic procedures can enable geotechnical analyses in GIS environment, to assess landslide susceptibility due to changes in groundwater or in soil water content in near-real time over areas of a few square kilometers, typically at the 1:5000 scale, in a short time. Therefore, they can be a useful tool for landslide risk mitigation and management.

REFERENCES

- Aleotti, P., 2004. A warning system for rainfall-induced shallow failures. *Engineering geology*, 73(3-4), 247-265.
- Alvioli, M. and Baum, R., 2016. Parallelization of the {TRIGRS} model for rainfall-induced landslides using the message passing interface. *Environmental Modelling & Software*, 81:122 – 135.
- AA.VV. Note technique glissement du Prat de Julian, Vence (06); Progetto AD – VITAM, INTEREGGV-A, FRANCE-ITALIE.
- Anagnosti, P. 1969. Three dimensional stability of fill dams. Proceeding of 7th International Conference on Soil Mechanics and Foundation Engineering, Mexico, 275-280.
- Autran J., 2007. "Extension de la nomenclature "Corine Land Cover" pour la description de l'occupation du sol à grande échelle", in: Les ontologies: Mythes, réalités et perspectives, Actes JFO, Sousse 2007, No.7, 115-134,http://liris.cnrs.fr/gom/JFO_2007/7.pdf
- Azzouz, A., Baligh M., 1978. Three-dimensional Stability of Slopes. Alexandria, VA, USA.
- Balestrero D., 2015. Procedura in ambiente GIS per l'analisi della suscettibilità al dissesto franoso dovuto ad eventi meteorici: il caso studio di Mendatica (IM). Department of Civil, Chemical and Environmental Engineering, University of Genoa. Master Thesis.
- Baligh, M., Azzouz A., 1975. End Effects on Stability of Cohesive Slopes. *Journal of Geotechnical Engineering Division*, 101(11), 1105-1117.
- Balzano, B., Bruno, A. W., Denzer, H., Molan, D., Tarantino, A., Gallipoli, D., 2021. REAL-TIME quality check of measurements of soil water status in the vadose zone. *Physics and Chemistry of the Earth, Parts A/B/C*, 121, 102918. DOI: [ht- tps://doi.org/10.1016/j.pce.2020.102918](https://doi.org/10.1016/j.pce.2020.102918).
- Baum RL, Savage WZ, Godt JW, 2002. TRIGRS—A fortran program for transient rainfall infiltration and grid-based regional slope-stability analysis. U.S. Geological Survey Open-File Report 02-0424 (<http://pubs.usgs.gov/of/2002/ofr-02-424/>)
- Baum, R.L., Savage, W.Z., and Godt, J.W., 2008, TRIGRS - A Fortran program for transient rainfall infiltration and grid-based regional slope-stability analysis, version 2.0: U.S. Geological Survey Open-File Report, 2008-1159, 75
- Baum, R. L., Godt, J. W., and Savage, W. Z., 2010. Estimating the timing and location of shallow rainfall-induced landslides using a model for transient, unsaturated infiltration, *J. Geophys. Res.*, 115, F03013, doi:10.1029/2009JF001321.
- Besson J, Durville J. 2012. Glissement du Prat de Julian - Risques de mouvements de terrain sur le site du Prat de Julian, commune de Vence. Conseil Général de L'environnement et du développement durable. Rapport n. 007951-01. cgedd.documentation.developpement-durable.gouv.fr

- Bishop, A. W., 1955. The Use of The Slip Circle in the Stability Analysis of Earth Slope," Geotechnique, 5(1), 7-17.
- Bomont S, 2008 Back experience of deep drainage for landslide stabilization through lines of siphon drains and electro-pneumatics drains: a French railway slope stabilization example. In: Chen et al (eds) Landslides and Engineered Slopes. From the Past to the Future. Taylor & Francis Group, CRC Press Balkema, vol 1, pp 1713–1720
- Boni A., Vanossi M., 1972. Carta geologica dei terreni compresi tra il Brianzese ligure s.l. ed il Flysch ad Elmintoidi s.s. Atti Ist. geol. Univ. Pavia, 23.
- Bovolenta R., Passalacqua R., Federici B., & Sguerso D., 2016. LAMP Landslide Monitoring and Predicting for the analysis of landslide susceptibility triggered by rainfall events. 12th International Symposium on Landslides (ISL2016) 12th-19th June in Naples, Italy, Vol.2, pp. 517-522.
- Bovolenta, R., Federici, B., Berardi, R., Passalacqua, R., Marzocchi, R., Sguerso, D., 2017. Geomatics in support of geotechnics in landslide forecasting, analysis and slope stabilization. In GEAM, Geoingegneria Ambientale e Mineraria - ISSN: 1121-9041, 151(2), 57–62.
- Bovolenta, R., Iacopino, A., Passalacqua, R., Federici, B., 2020a. Field measurements of soil water content at shallow depths for landslide monitoring. In Geosciences (Switzerland) - ISSN: 2076-3263, 10(10), 409. DOI:10.3390/geosciences10100409.
- Bovolenta, R., Passalacqua, R., Federici, B., Sguerso, D., 2020b. Monitoring of Rain-Induced Landslides for the Territory Protection: The AD-VITAM Project. In Lecture Notes in Civil Engineering - ISSN: 2366-2557. 40, 138–147. DOI:10.1007/978-3-030-21359-6_15.
- Caine N., 1980. The rainfall intensity-duration control of shallow landslides and debris flows. Geografiska Annaler, Series A 62(1-2), 23-27.
- Brunetti M.T., Peruccacci S., Roccati A., Melillo M., Gariano S.L., Guzzetti F., 2015. Aggiornamento di soglie pluviometriche regionali e sub-regionali e definizione di nuove soglie topografiche per la Liguria. Convenzione tra Commissario Delegato per il superamento dell'emergenza derivante dagli eventi alluvionali occorsi nel novembre 2012-Regione Liguria e IRPI del CNR.
- Brunetti M.T., Peruccacci S., Rossi M., Luciani S., Valigi D., Guzzetti F., 2010. Rainfall thresholds for the possible occurrence of landslides in Italy. Nat. Hazards Earth Syst. Sci., 10, 447–458.
- Campora, M., Palla, A., Gnecco, I., Bovolenta, R., Passalacqua, R., 2020. The laboratory calibration of a soil moisture capa- citance probe in sandy soils. Soil and Water Research - ISSN:1801-5395, 15(2), 75–84. DOI: 10.17221/227/2018-SWR.
- Carminati P., 2017. Modellazione idrologica e geotecnica del corpo frana di Mendatica: analisi numeriche di infiltrazione delle precipitazioni e delle condizioni di stabilità del versante. Department of Civil, Chemical and Environmental Engineering, University of Genoa. Master Thesis.

- Cavanna S., 2017. Analisi di stabilità 3D condotte con il Metodo dell'Equilibrio Limite Globale: il caso studio di Mendatica (IM). Department of Civil, Chemical and Environmental Engineering, University of Genoa. Master Thesis.
- Cavounidis, S., 1987. On the Ratio of Factor of Safety in Slope Stability Analyses. *Geotechnique*, 37(2), 207-210.
- Cavounidis, S., Kalogeropoulos H., 1992. End Effects on the Stability of Cuts in Normally Consolidated Clays. *Rivista Italiana di Geotecnica*, 2, 85-93.
- Chen, R., Chameau J., 1983a. Three-dimensional Limit Equilibrium Analysis of slopes. *Geotechnique*, 32(1), 31-40.
- Chen, R. Chameau J., 1983b. Discussion Three-dimensional Limit Equilibrium Analysis of Slopes. *Geotechnique*, 33(1), 215-216.
- Cheng, Y., Yip C., 2007. Three-Dimensional Asymmetrical Slope Stability Analysis. Extension of Bishop's, Junbu's, and Morgenstern-Price's Techniques. *Journal of Geotechnical and Geoenvironmental Engineering*, 133(12), 1544-1555.
- de Mello, V. F. B., 1967. Considerações sobre os ensaios de penetração e sua aplicação a problemas de fundações rasas. University Thesis.
- Dennhardt M., Forster W., 1985. Problems of Three Dimensional Slope Stability. Proceeding of the 11th International Conference in Soil Mechanics and Foundation Engineering, Part 2, San Francisco, 427-431
- Du Bois, L., Levato, L., Besnard, J., Marchant, R., Olivier, R., Ouwehand, M., Sellami, S. & Wagner, J.-J. 1990: Aspects particuliers du traitement sismique des profils alpins suisses du PNR-20. In: Deep structure of the Alps (Ed. by Roure, F., Heitzmann, P. & Polino, R.). *Mém. Soc. géol. Fr.* 156; *Mém. Soc. Géol. Suisse* 1; *Soc. geol. ital.*, Vol. spec. 1, 47-54.
- Duncan, J. M., 1996. State of The Art: Limit Equilibrium and Finite-Element Analysis of Slopes. *Journal of Geotechnical Engineering*, 557-596
- Escobar-Wolf, R., Sanders, J., Vishnu, C., Oommen, T., Sajinkumar, K., 2021. A GIS tool for infinite slope stability analysis (GIS-TISSA). *Geoscience Frontiers*, 12(2), 756–768.
- Federici PR, Capitani M, Chelli A, Del Seppia N, Serani A. (2007). Atlante dei centri abitati instabili della Liguria. Volume IV-Provincia di Imperia. Tipografia Nuova Ata, Genova.
- Federici B., Bovolenta R., Passalacqua R., 2014. From rainfall to slope instability: an automatic GIS procedure for susceptibility analyses over wide areas, *Geomatics, Natural Hazards & Risk*, Volume 6, 2015-Issue 5-7: The Role of Geomatics in Hydro-geological Risk. ISSN: 1947-5713, doi: 10.1080/19475705.2013.877087.
- Fell, R., Corominas, J., Bonnard, C., Cascini, L., Leroi, E., Savage, W. Z., 2008. Guidelines for landslide susceptibility, hazard and risk zoning for land use planning. *Engineering geology*, 102(3-4), 85-98

- Fellenius, W., 1936. Calculation of the Stability of Earth Dams. Proceeding of the Second Congress on Large Dams, Washington, DC, 445-463.
- Fredlund, D. G., 1984. Analytical Methods for Slope Stability Analysis. Proceeding of the Fourth International Symposium on Landslides, State-of-the-Art, Toronto, Canada, 229-250.
- Fredlund, D., Morgenstern, N. R., Widger, R., 1978. The shear strength of unsaturated soils. Canadian geotechnical journal, 15(3), 313–321. DOI: <https://doi.org/10.1139/t78-029>.
- Fredlund, D.G., Krahn J., 1977. Comparison of slope stability methods of analysis. Canadian Geotechnical Journal, 16, 121-139.
- Gafurov, Z., Eltazarov, S., Akramov, B., Yuldashev, T., Djumaboev, K., & Anarbekov, O. (2018). Modifying hargreaves-samani equation for estimating reference evapotranspiration in dryland regions of Amudarya River Basin. Agricultural Sciences, 9(10), 1354.
- Gens, A., Hutchinson, J., Cavounidis S., 1988. Three-dimensional Analysis of Slides in Cohesive Soils. Geotechnique, 38(1), 1-23.
- Giammarino, S., Capponi, G., Crispini, L., Giglia, G., & Piazza, M. (2002). Carta Geologica della LIGURIA – Scala 1: 200.000. LAC (Firenze). <https://doi.org/10.13140/RG.2.2.14791.50081>
- Giannecchini, R., Galanti, Y., Avanzi, G. D. A., & Barsanti, M., 2016. Probabilistic rainfall thresholds for triggering debris flows in a human-modified landscape. *Geomorphology*, 257, 94-107.
- Giannecchini, R., Galanti, Y., & D'Amato Avanzi, G., 2012. Critical rainfall thresholds for triggering shallow landslides in the Serchio River Valley (Tuscany, Italy). *Natural Hazards and Earth System Sciences*, 12(3), 829-842.
- Giannecchini, R., 2006. Relationship between rainfall and shallow landslides in the southern Apuan Alps (Italy). *Natural hazards and earth system sciences*, 6(3), 357-364.
- Godt JW, Baum RL, Chleborad AF, 2006. Rainfall characteristics for shallow landsliding in Seattle, Washington, USA. *Earth Surf Process Landforms* 31:97–110
- Gori, P. L., Jeer, S. P., and Highland, L. M., 2003. Enlisting the support of land-use planners to reduce debris-flow hazards in the United States. Debris-flow hazards mitigation: Mechanics, Prediction and Assessment, edited by: Rickenmann, D. and Chen, C., Millpress, Rotterdam, 1119–1127.
- GRASS Development Team, Geographic Resources Analysis Support System (GRASS) Software, Version 7.8. Open Source Geospatial Foundation (2020), <https://grass.osgeo.org>, last accessed on 30/04/2023.
- Hargreaves G. H, Samani Z. 1982. Estimating potential evapotranspiration. *Journal of irrigation and drainage engineering*, Vol. 108, Issue 3, pp. 223-230. ASCE library.
- Hongjun, L., Longtan S., 2011. Three-Dimensional Finite Element Limit Equilibrium Method for Slope Stability Analysis Based on the Unique Sliding Direction. *Geotechnical Special Publication*, 216, 48-55.
- Huang, C. C., Tsai and C. C., 2000. New Method for 3D and Asymmetrical Slope Stability Analysis. *Journal of Geotechnical and Geoenvironmental Engineering*, 126(10), 917-927.

- Huang, C. C., Tsai, C. C., Chen Y. H., 2002. Generalized Method for Three-Dimensional Slope Stability Analysis. *Journal of Geotechnical and Geoenvironmental Engineering*, 128(10), 836-848.
- Hungr O, Leroueil S, Picarelli L. 2014. The Varnes classification of landslide types, an update. *Landslides*. 1:167–194
- Hungr O, Evans SG, Bovis M, Hutchinson JN. 2001. Review of the classification of landslides of the flow type. *Environ Eng Geosci*. 7:221–238.
- Hungr, O., 1987.n Extension of Bishop's Simplified Method of Slope Stability Analysis to Three Dimensions. *Geotechnique*, 37(1), 113-117.
- Hungr, O., Salgado, F., Byrne, P., 1989. Evaluation of a three-dimensional method of slope stability analysis. *Canadian Geotechnical Journal*, 26, 679-686.
- Iacopino, A., Viaggio, S., Bovolenta, R., 2021. Monitoraggio delle frane mediante una rete di sensori: la misura del contenuto d'acqua nel terreno. *Atti del XXVII Convegno Nazionale Geotecnica*, Vol. 2, 807-814.
- Iverson RM., 2000. Landslide triggering by rain infiltration. *Water Resources Research*. 36 (7): 1897-1910.
- Janbu, N., 1954. Application of composite Slip Surface for Stability Analysis. Proceeding of the Conference on Stability of Earth Slopes, Part. 3, Stockholm, Sweden, 43-49
- Jiang, J. C., Yamagami T., 2004. Three-dimensional Slope Stability Analysis using an Extended Spencer Method," *Journal of the Japanese Geotechnical Society of Soils and Foundations*, 44(4), 127-135.
- Johnson, A. I., 1967. Specific yield: compilation of specific yields for various materials (No. 1662). US Government Printing Office.
- Kalatehjari, R., Ali, N., 2013. A review of three-dimensional slope stability analyses based on limit equilibrium method. *Electronic Journal of Geotechnical Engineering*, 18, 119-134.
- Kopacsy, J., 1957. Three-dimensional Stress Distribution and Slip Surfaces in Earth Works at Rupture. Proceeding of the 4th International Conference on Soil Mechanics and Foundation Engineering, London, England, 339-342.
- Lam, L., Fredlund D., 1993. A General Limit Equilibrium Model for Three-Dimensional Slope Stability Analysis. *Canadian Geotechnical Journal*, 30, 905-919.
- Lebourg, T., Hernandez, M., Zerathe, S., El Bedoui, S., Jomard, H., & Fresia, B. (2010). Landslides triggered factors analysed by time lapse electrical survey and multidimensional statistical approach. *Engineering Geology*,114(3-4), 238-250.
- Leshchinsky, D., Huang C. C. 1992a. Generalized Slope Stability Analysis: Interpretation, Modification, and Comparison," *Journal of Geotechnical Engineering*, 118(10), 1559-1576.
- Leshchinsky, D., Huang C. C. 1992b. Generalized Three-Dimensional Slope Stability Analysis. *Journal of Geotechnical Engineering*, 118(11), 1748-1764.

- Leshchinsky, D., Mullett T., 1988a. Design Charts for Vertical Cuts. *Journal of Geotechnical and Geoenvironmental Engineering*, 114(3), 337-344.
- Leshchinsky, D., Mullett T., 1988b. Stability of Vertical Corner Cuts. Proceeding of the Sixth International Conference on Numerical Methods in Geomechanics, Innsbruck, Austria: AA Balkema, 1249-1256.
- Leshchinsky, D., Baker R., 1986. Three-dimensional Slope Stability: End Effects. *Soils and Foundations*, 26(4), 98-110.
- Leshchinsky, D., Baker, R., Silver M., 1985. Three Dimensional Analysis of Slope Stability. *International Journal for Numerical and Analytical Methods in Geomechanics*, 9, 199-223.
- Lu, N., and Godt, J., 2008. Infinite slope stability under steady unsaturated seepage conditions, *Water Resour. Res.*, 44, W11404, doi:10.1029/2008WR006976.
- Lugeon, M. (1902). Les grandes nappes de recouvrement des Alpes du Chablais et de la Suisse. *Bull. Soc. Géol. France.*, 4, 723.
- Macciò R., 2007. Relazione geologica illustrativa. Realizzazione di una campagna di indagini geognostiche-geotecniche, predisposizione di una rete di monitoraggio del dissesto che interessa il centro abitato del capoluogo del Comune di Mendatica e progettazione preliminare/definitiva degli interventi prioritari finalizzati alla mitigazione del rischio.
- Macciò R., 2013. Relazione tecnica illustrativa. Evoluzione del movimento franoso che coinvolge un settore dell'abitato del capoluogo di Mendatica e della Borgata Piano.
- Macciò R., De Silvestri T, Fusini F., 2013. Relazione geologica e di pericolosità sismica. Interventi di mitigazione del rischio su movimento franoso in Località Capoluogo del Comune di Mendatica.
- Macciò R., 2015. Relazione geologica e di pericolosità sismica: Interventi di mitigazione del rischio di frana nell'abitato di Mendatica.
- Maino M., Seno S, 2016 The thrust zone of the Ligurian Penninic basal contact (Monte Fronté, Ligurian Alps, Italy), *Journal of Maps*, 12:sup1, 341-351, DOI:10.1080/17445647.2016.1213669
- Mangan, C., 1982. Géologie et hydrogéologie karstique du bassin de la Brague et ses bordures (Alpes-Maritimes, France). University of Nice Sophia-Antipolis, 182 pp
- Mockus, V. (1971). SCS national engineering handbook, section 4, hydrology.
- Morgenstern, N. and V. Price, 1965. The Analysis of the Stability of General Slip Surfaces. *Geotechnique*, 15(1), 79-93.
- Montgomery D, Dietrich W., 1994. A physically based model for the topographic control on shallow landsliding. *Water Resources Research*. 30 (4): 1153–1171.
- Montrasio, L., & Valentino, R., 2008. A model for triggering mechanisms of shallow landslides. *Natural Hazards and Earth System Sciences*, 8(5), 1149-1159.

- Moresi, F., Maesano, M., Collalti, A., Sidle, R., Matteucci, G., Scarascia Mugnozza, G., 2020. Mapping landslide prediction through a GIS-based model: A case study in a catchment in southern Italy. *Geosciences*, 10(8), 309.
- Occelli F., 2008. Comune di Mendatica (IM). Indagini archeologiche preventive.
- Oudin, L., Hervieu, F., Michel, C., Perrin, C., Andréassian, V., Anctil, F., & Loumagne, C., 2005. Which potential evapotranspiration input for a lumped rainfall–runoff model?: Part 2—Towards a simple and efficient potential evapotranspiration model for rainfall–runoff modelling. *Journal of hydrology*, 303(1-4), 290-306.
- Palis E., 2017. Étude du comportement post-rupture de versants instables par l'observation et l'instrumentation. École doctorale Sciences Fondamentales et Appliquées Unité de recherche : Géoazur. l'Université Côte d'Azur. www.theses.fr/2017AZUR4014
- Passalacqua R., 2002. Vulnerabilità territoriale da frane e crolli in roccia, Prog. UE INTERREG II – Cooperazione transfrontaliera Italia-Francia: Progetto GE.RI.A., Dossier Tematico n° 8, Collana Territorio e Ambiente, Edizioni del Delfino Moro, Albenga (SV), December 2002, ISBN 88-88397-05-1, pp 1-37 (in italiano).
- Passalacqua R., Bovolenta R. Spallarossa D., De Ferrari R, 2013. Geophysical site characterization for a large landslide 3-D modeling, Proc. of the Fourth Int. Conference on Geotechnical and Geophysical Site Characterization (ISC'4 2012), held at Porto de Galinas – Pernambuco – Brasil from 17 to 21 september 2012, © 2013 Taylor & Francis Group, London (UK), ISBN 978-0-415-62136-6, pp. 1765-1771.
- Passalacqua, R., Bovolenta, R., Federici, B., 2015. An integrated hydrological-geotechnical model in GIS for the analysis and prediction of large-scale landslides triggered by rainfall events. *Engineering Geology for Society and Territory - Volume 2: Landslide Processes* 1 January 2015, Pages 1799-1803.
- Passalacqua R., Bovolenta R., 2015. Landslides' susceptibility on large surfaces triggered by rain histories, Proc. of the XVIth European Conference on Soil Mechanics & Geotechnical Engineering (ECSMGE), Edinburgh (UK) 13-17 September 2015, ICE Publishing 2015, ISBN 978-0-7277-6067-8, doi:10.1680/ecsmge.60678, pp. 1831-1836.
- Passalacqua R., Bovolenta R., Federici B., Balestrero D., 2016. A physical model to assess landslide susceptibility on large areas: recent developments and next improvements. *Italian Conference of Researchers in Geotechnical Engineering (CNRIG)*, Bologna, 22-23 September 2016, *Procedia Engineering*, Vol 158, pp. 487-492, doi: 10.1016/j.proeng.2016.08.477, ISSN: 1877-7058.
- Passalacqua, R., Bovolenta, R., Spallarossa, D., De Ferrari, R., 2012. Geophysical site characterization for a large landslide 3-D modeling. In Proceedings of the Fourth International Conference on Geotechnical and Geophysical Site Charac- terization ISC'4 - ISBN:9780415621366. 2, 1765–1771.
- Pepe, G., Cevasco, A., Piazza, M., Macciò, R., Arrighetti, F., & Casagli, N. (2021). On the efficiency and effectiveness of automatic deep drainage systems during an extreme rainfall event: the Mendatica landslide case study (western Liguria, Italy). *Landslides*, 18(12), 3799-3820.

- Pepe G, Piazza M, Cevasco A, 2015. Geomechanical characterization of a highly heterogeneous flysch rock mass by means of the GSI method. *Bull Eng Geol Env* 74:465–477. <https://doi.org/10.1007/s10064-014-0642-4>
- Perata E., 2018. Modellazione integrata idrologico-geotecnica 3D in ambiente GIS per la valutazione della suscettibilità al dissesto franoso: il caso studio di Prat de Julian a Vence. Department of Civil, Chemical and Environmental Engineering, University of Genoa. Master Thesis.
- Pfiffner, O.A. 2009. Geologie der Alpen (in German). Bern/Stuttgart/Wien: Haupt Verlag. ISBN 978-3-8252-8416-9.
- Pribyl, D. W., 2010. A critical review of the conventional SOC to SOM conversion factor. *Geoderma*, 156(3-4), 75–83. DOI: <https://doi.org/10.1016/j.geoderma.2010.02.003>.
- QGIS Development Team, 2022. QGIS Geographic Information System. <https://www.qgis.org>, last accessed on 11 May 2023.
- Qiu, C., Esaki, T., Xie, M., Mitani, Y., Wang, C., 2007. Spatio-temporal estimation of shallow landslide hazard triggered by rainfall using a three-dimensional model. *Environmental Geology*, 52, 1569-1579.
- Ricou, L. E., Dercourt, J., Geyssant, J., Grandjacquet, C., Lepvrier, C., & Biju-Duval, B., 1986. Geological constraints on the Alpine evolution of the Mediterranean Tethys. *Tectonophysics*, 123(1-4), 83-122.
- Sidle, R., & Ochiai, H., 2006. Processes, prediction, and land use. *Water resources monograph. American Geophysical Union, Washington*, 525.
- Schmid, S. M., Fügenschuh, B., Kissling, E., & Schuster, R., 2004. Tectonic map and overall architecture of the Alpine orogen. *Eclogae Geologicae Helvetiae*, 97, 93-117.
- Schmid, S.M.; Pfiffner, O.A.; Froitzheim, N.; Schönborn, G.; Kissling, E., 1996. Geophysical-geological transect and tectonic evolution of the Swiss-Italian Alps" (PDF). *Tectonics*.15 (5): 1036. Bibcode:1996Tecto15.1036S. doi:10.1029/96TC00433.
- Schmidt, C. 1907. Ueber die Geologie des Simplongebietes und die Tektonik der Schweizeralpen. Winter.
- Sentek Technologies, Inc.2011. Calibration manual for Sentek soil moisture sensors. Version 2.0, Sentek Sensor Technologies, Stepney, SA, Australia.
- Shioi, Y., Fukui, J., 1982. Application of N-value to design of foundation in Japan. Proceeding of the Second European Symposium on Penetration Testing. Amsterdam, Vol.1, 159-164.
- Skempton A.W., De Lory F.A., 1957. "Stability of natural slopes in London Clay", in: Proc. 4th Int. Conf. on Soil Mechanics & Foundation Engineering, vol. 2, 378-381.
- Spencer, E., 1967. A Method of Analysis of the Stability of Embankments Assuming Parallel Inter-Slice Forces. *Geotechnique*, 17(1), 11-26.
- Spencer, E., 1973. Thrust line criterion in embankment stability analysis. *Geotechnique*, 23(1): 85-100.
- Soil Conservation Service 1972. "Hydrology", in: National Engineering Handbook, sec. 4, U.S. Dept. of Agriculture, Washington D.C.

- Soil Conservation Service 1975. "Urban hydrology for small watersheds", Tech. Rel. No. 55, U.S. Dept. Of Agriculture, Washington D.C.
- Soloperto A. 2016. Modellazione 3D dell'oscillazione di falda relativa al dissesto franoso: calibrazione su eventi meteorici critici e applicazione in ambiente GIS per il caso studio di Mendatica. Department of Civil, Chemical and Environmental Engineering, University of Genoa. Master Thesis.
- Sun, G., Zheng, H., Jiang, W., 2012. A global Procedure for Evaluating Stability of Three-Dimensional Slopes. *Natural Hazards*, 61(3): 1083-1098.
- Ugai, K., 1985. Three Dimensional Stability Analysis of Vertical Cohesive Slopes. *Soils and Foundations*, 25(3): 41-48.
- Van Genuchten, M. T., 1980. A closed-form equation for predicting the hydraulic conductivity of unsaturated soils. *Soil science society of America journal*, 44(5), 892–898. DOI: <https://doi.org/10.2136/sssaj1980.03615995004400050002x>.
- Vanapalli, S., Fredlund, D., 2000. Comparison of different procedures to predict unsaturated soil shear strength. 195–209. DOI:[https://doi.org/10.1061/40510\(287\)13](https://doi.org/10.1061/40510(287)13).
- Vanapalli, S., Fredlund, D., Pufahl, D., Clifton, A., 1996. Model for the prediction of shear strength with respect to soil suction. *Canadian geotechnical journal*, 33(3), 379–392. DOI:<https://doi.org/10.1139/t96-060>
- Vanossi, M., Corte Sogno, L., Galbiati, B., Messiga, B., Piccardo, G., & Vannucci, R., 1984. Geologia delle Alpi Liguri: dati, problemi, ipotesi. *Memorie della Società Geologica Italiana*, 28, 5-75.
- Vereecken, H., Maes, J., Feyen, J., Darius, P., 1989. Estimating the soil moisture retention characteristic from texture, bulk density, and carbon content. *Soil science*, 148(6), 389–403. DOI:10.1097/00010694-198912000-00001.
- Viaggio, S., Iacopino, A., Bovolenta, R., & Federici, B., 2022. Landslide Susceptibility Assessment: Soil Moisture Monitoring Data Processed by AN Automatic Procedure in GIS for 3D Description of the Soil Shear Strength. *The International Archives of Photogrammetry, Remote Sensing and Spatial Information Sciences*, 48, 517-523.
- Viaggio S., 2018. Il movimento franoso di Prat de Julian a Vence, (France): caratterizzazione e analisi delle condizioni di stabilità. Department of Civil, Chemical and Environmental Engineering, University of Genoa. Master Thesis.
- Yamagami, T., Jiang J. C., 1996. Determination of the sliding direction in three-dimensional slope stability analysis," Proceedings of the 2nd International Conference on Soft Soil Engineering, Part 1, Nanjing: Hohai University Press, 567-572.
- Yamagami, T., Jiang J. C., 1997. A Search for the Critical Slip Surface in Three-dimensional Slope Stability analysis. *Soils and Foundations*, 37(3), 1-16.
- Yapo, P. O., Gupta, H. V., & Sorooshian, S., 1996. Automatic calibration of conceptual rainfall-runoff models: sensitivity to calibration data. *Journal of hydrology*, 181(1-4), 23-48.

- Wright, S., Kulhawy, E., Duncan J., 1973. Accuracy of Equilibrium Slope Stability Analysis. Journal of Soil Mechanics and Foundations Division, 99(10), 783-791.
- Wu, W., & Sidle, R. C. (1995). A distributed slope stability model for steep forested basins. Water resources research, 31(8), 2097-2110, <https://doi.org/10.1029/95WR01136>.Zheng, H., 2009. Eigenvalue Problem from the Stability Analysis of Slopes. Journal of Geotechnical and Geoenvironmental Engineering, 135(5), 647-656

6. APPENDIX A

The IHG procedure, described in this thesis, is here reported, as a script in GRASS GIS.

It was implemented as a Python script too; it is open source and can be downloaded at the following Github address: [https://github.com/LabGeomatica/Unsaturated-soil-shear-strength/soil_evolution_analysis_\(2\).zip.git](https://github.com/LabGeomatica/Unsaturated-soil-shear-strength/soil_evolution_analysis_(2).zip.git) (the user have to chose the IHG.py script).

```
#INTEGRATED HYDROLOGICAL GEOTECHNICAL MODEL (IHG)#
#For a generic rainfall event
#create the rainfall event mapset
#generate initial groundwater surface and create the Diff_GWT_bedrock map
#Input: rainfall and evapotranspiration data
#Input:hydraulic soil permeability and effective porosity surfaces
#Execute IHG.sh

r.mapcalc --o <<EOF
Gamma = soil gamma
coes = soil effective cohesion
tan_phi= tan(effective friction angle)
CN_I = round(4.2*CN/(10-0.058*CN))
CN_III = round((CN*23)/(10+0.13*CN))
EOF

r.mapcalc --o <<EOF
S_II = round((1000.00/CN-10)*25.4)
S_I = round((1000.00/CN_I-10)*25.4)
S_III = round((1000.00/CN_III-10)*25.4)
EOF

## Safety factor in the absence of GWT
r.mapcalc --o <<EOF
Fs_nw = tan_phi/tan_b
EOF

## Start of analysis
#day_0
r.mapcalc --o <<EOF
D_0 = Diff_GWT_bedrock * 1000 * (1 - exp(-(lambda_1)))
m_0 = Diff_GWT_bedrock/ Diff_DTM_bedrock
FS_0 = if(((Gamma - (m_0 * 10)) / Gamma) * (tan_phi/ tan_b) < 25, ((Gamma - (m_0 * 10)) / Gamma) * (tan_phi/ tan_b), 25)
FS_0_coes = if((coes + ((Gamma - (m_0 * 10)) * Diff_DTM_bedrock * (cos_b ^ 2) * tan_phi)) / (Gamma * Diff_DTM_bedrock * sin_b * cos_b) < 50, (coes + (Gamma - (m_0 * 10)) * Diff_DTM_bedrock * (cos_b ^ 2) * tan_phi) / (Gamma * Diff_DTM_bedrock * sin_b * cos_b), 50)
EOF
r.colors map=FS_0
rules=/home/utente/GIS/G_base/color_rules/fs_color
```

The creation of susceptibility maps follows the colour rule, in RGB, based on a traffic light colouring from red (unstable zones) to green (stable zones), via yellow, which describes zones with FS close to unity.

```
0 255:0:0 (red)
0.8 255:0:0
1 255:167:0 (orange)
1.3 255:255:0 (yellow)
2 0:255:0 (green)
25 0:204:0
50 45:255:0
200 0:204:102(forest gree)
```

```
#day_1
r.mapcalc --o <<EOF
P_1 = rainfall_day_1
E_1 = evapotranspiration_day_1
R_1 = if(P_1 > 0.2*S_I, ((P_1 - 0.2*S_I)^2)/(P_1 + 0.8*S_I), 0)
Pf_1 = if((P_1 - R_1 - D_0) < 0.2 * S_I, P_1 - R_1 - D_0, (0.04 * (S_I)^2
+ 0.8 * S_I * (P_1 - R_1 - D_0)) / (1.2 * S_I - (P_1 - R_1 - D_0)))
V_1 = Diff_GWT_bedrock*1000 - E_1 - D_0 + (P_1 - R_1)/n_eff
D_1 = V_1 * (1 - exp(-(lambda_1)))
Dc_1 = D_0 + D_1
Hf_1 = if((V_1/1000) > Diff_DTM_bedrock, Diff_DTM_bedrock, V_1/1000)
m_1 = Hf_1 / Diff_DTM_bedrock
FS_1 = if(((Gamma - (m_1 * 10)) / Gamma) * (tan_phi/tan_b) < 25,
((Gamma - (m_1 * 10)) / Gamma) * (tan_phi/tan_b), 25)
FS_coes_1 = if((coes + ((Gamma - (m_1 * 10)) * Diff_DTM_bedrock * (cos_b
^ 2) * tan_phi)) / (Gamma * Diff_DTM_bedrock * sin_b * cos_b) < 50, (coes
+ (Gamma - (m_1 * 10)) * Diff_DTM_bedrock * (cos_b ^ 2) * tan_phi) /
(Gamma * Diff_DTM_bedrock * sin_b * cos_b), 50)
Diff_FS_1 = FS_1 - FS_0
Diff_FS_coes_1 = FS_coes_1 - FS_coes_0
EOF
r.colors map=FS_1 rules=/home/utente/GIS/G_base/color_rules/fs_color
```

```
#day_2
r.mapcalc --o <<EOF
P_2 = rainfall_day_2
E_2 = evapotranspiration_day_2
S_2 = if(P_2 + P_1 < 5, S_I, if((P_2 + P_1 )>100,S_III,S_II))
Pc_2 = P_2 + Pf_1
Rc_2 = if(Pc_2 > 0.2*S_2, ((Pc_2 - 0.2*S_2)^2)/(Pc_2 + 0.8*S_2), 0)
Pfc_2 = if((Pc_2 - Rc_2 - D_1) < 0.2 * S_2, Pc_2 - Rc_2 - D_1, (0.04 *
(S_2^2 + 0.8 * S_2 * (Pc_2 - Rc_2 - D_1)) / (1.2 * S_2 - (Pc_2 - Rc_2 -
D_1))))
V_2 = Diff_GWT_bedrock*1000 - E_2 - D_1 + (Pc_2 - Rc_2 + D_0)/n_eff
D_2 = V_2* (1 - exp(-(lambda_1)))
Dc_2 = Dc_1 + D_2
Hf_2 = if((V_2/1000) > Diff_DTM_bedrock, Diff_DTM_bedrock, V_2/1000)
m_2 = Hf_2 / Diff_DTM_bedrock
FS_2 = if(((Gamma - (m_2 * 10)) / Gamma) * (tan_phi/tan_b) < 25, ((Gamma
- (m_2 * 10)) / Gamma) * (tan_phi/tan_b), 25)
FS_coes_2 = if((coes + ((Gamma - (m_2 * 10)) * Diff_DTM_bedrock * (cos_b
^ 2) * tan_phi)) / (Gamma * Diff_DTM_bedrock * sin_b * cos_b) < 50, (coes
```

```

+ (Gamma - (m_2 * 10)) * Diff_DTM_bedrock * (cos_b ^ 2) * tan_phi) /
(Gamma * Diff_DTM_bedrock * sin_b * cos_b), 50)
Diff_FS_2 = FS_2 - FS_0
Diff_FS_coes_2 = FS_coes_2 - FS_0
EOF
r.colors map=FS_2 rules=/home/utente/GIS/G_base/color_rules/fs_color

#day_3
r.mapcalc --o <<EOF
P_3 = rainfall_day3
E_3 = evapotranspiration_day_3
S_3 = if(P_3 + P_2 + P_1 < 5, S_I, if((P_3 + P_2 + P_1)>100,S_III,S_II))
Pc_3 = P_3 + Pfc_2
Rc_3 = if(Pc_3 > 0.2*S_3, ((Pc_3 -0.2*S_3)^2)/(Pc_3+0.8*S_3),0)
Pfc_3 = if((Pc_3 - Rc_3 - D_2) < 0.2 * S_3, Pc_3 - Rc_3 - D_2, (0.04 *
(S_3)^2 + 0.8 * S_3 * (Pc_3 - Rc_3 - D_2)) / (1.2 * S_3- (Pc_3 - Rc_3-
D_2)))
V_3 = Diff_GWT_bedrock*1000 - E_3 -D_2 + (Pc_3 - Rc_3 + Dc_1)/n_eff
D_3 = V_3* (1 - exp(-(lambda_1)))
Dc_3 = Dc_2 + D_3
Hf_3 = if((V_3/1000) > Diff_DTM_bedrock, Diff_DTM_bedrock, V_3/1000)
m_3 = Hf_3 / Diff_DTM_bedrock
FS_3 = if(((Gamma - (m_3 * 10)) / Gamma) * (tan_phi/tan_b ) < 25, ((Gamma
- (m_3 * 10)) / Gamma) * (tan_phi/ tan_b ), 25)
FS_coes_3 = if((coes + ((Gamma - (m_3 * 10)) * Diff_DTM_bedrock * (cos_b
^ 2) * tan_phi)) / (Gamma * Diff_DTM_bedrock * sin_b * cos_b) < 50, (coes
+ (Gamma - (m_3 * 10)) * Diff_DTM_bedrock * (cos_b ^ 2) * tan_phi) /
(Gamma * Diff_DTM_bedrock * sin_b * cos_b), 50)
Diff_FS_3 = FS_3 - FS_0
Diff_FS_coes_3 = FS_coes_3 - FS_0
EOF
r.colors map=FS_3 rules=/home/utente/GIS/G_base/color_rules/fs_color

#day_4
r.mapcalc --o <<EOF
P_4 = rainfall_day4
E_4 = evapotranspiration_day4
S_4 = if(P_4 + P_3 + P_2 + P_1 < 5, S_I, if((P_4 + P_3 + P_2 +
P_1)>100,S_III,S_II))
Pc_4 = P_4 + Pfc_3
Rc_4 = if(Pc_4 > 0.2*S_4, ((Pc_4 -0.2*S_4)^2)/(Pc_4 + 0.8*S_4),0)
Pfc_4 = if((Pc_4 - Rc_4 - D_3) < 0.2 * S_4, Pc_4 - Rc_4 - D_3, (0.04 *
(S_4)^2 + 0.8 * S_4 * (Pc_4 - Rc_4 - D_3)) / (1.2 * S_4 - (Pc_4 - Rc_4 -
D_3)))
V_4 = Diff_GWT_bedrock*1000 - E_4 -D_3 + (Pc_4 - Rc_4 + Dc_2)/n_eff
D_4 = if(P_4 > 0, V_4* (1 - exp(-(lambda_1))), V_4* (1 - exp(
(lambda_2))))
Dc_4 = Dc_3 + D_4
Hf_4 = if((V_4/1000) > Diff_DTM_bedrock, Diff_DTM_bedrock, V_4/1000)
M_4 = Hf_4 / Diff_DTM_bedrock
FS_4 = if(((Gamma - (M_4 * 10)) / Gamma) * (tan_phi/tan_b ) < 25, ((Gamma
- (m_4 * 10)) / Gamma) * (tan_phi/ tan_b ), 25)
FS_coes_4 = if((coes + ((Gamma - (m_4 * 10)) * Diff_DTM_bedrock * (cos_b
^ 2) * tan_phi)) / (Gamma * Diff_DTM_bedrock * sin_b * cos_b) < 50, (coes
+ (Gamma - (m_4 * 10)) * Diff_DTM_bedrock * (cos_b ^ 2) * tan_phi) /
(Gamma * Diff_DTM_bedrock * sin_b * cos_b), 50)

```

```

Diff_FS_4 = FS_211210 - FS_0
Diff_FS_coes_4 = FS_coes_4 - FS_0
EOF
r.colors map=FS_4 rules=/home/utente/GIS/G_base/color_rules/fs_color

#day_5
r.mapcalc --o <<EOF
P_5 = rainfall day5
E_5 = evapotranspiration day5
S_5 = if(P_4 + P_3 + P_2 + P_1 + P_5 < 5, S_I, if((P_4 + P_3 + P_2 + P_1 + P_5) > 100, S_III, S_II))
Pc_5 = P_5 + Pfc_4
Rc_5 = if(Pc_5 > 0.2 * S_5, ((Pc_5 - 0.2 * S_5)^2) / (Pc_5 + 0.8 * S_5), 0)
Pfc_5 = if((Pc_5 - Rc_5 - D_4) < 0.2 * S_5, Pc_5 - Rc_5 - D_4, (0.04 * (S_5)^2 + 0.8 * S_5 * (Pc_5 - Rc_5 - D_4)) / (1.2 * S_5 - (Pc_5 - Rc_5 - D_4)))
V_5 = Diff_GWT_bedrock * 1000 - E_5 - D_4 + (Pc_5 - Rc_5 + Dc_3) / n_eff
D_5 = if(P_5 > 0, V_5 * (1 - exp(-(lambda_1))), V_5 * (1 - exp(-(lambda_2))))
Dc_5 = Dc_4 + D_5
Hf_5 = if((V_5 / 1000) > Diff_DTM_bedrock, Diff_DTM_bedrock, V_5 / 1000)
m_5 = Hf_5 / Diff_DTM_bedrock
FS_5 = if(((Gamma - (M_5 * 10)) / Gamma) * (tan_phi / tan_b) < 25, ((Gamma - (M_5 * 10)) / Gamma) * (tan_phi / tan_b), 25)
FS_coes_5 = if((coes + ((Gamma - (m_5 * 10)) * Diff_DTM_bedrock * (cos_b^2) * tan_phi)) / (Gamma * Diff_DTM_bedrock * sin_b * cos_b) < 50, (coes + ((Gamma - (M_5 * 10)) * Diff_DTM_bedrock * (cos_b^2) * tan_phi)) / (Gamma * Diff_DTM_bedrock * sin_b * cos_b), 50)
Diff_FS_5 = FS_5 - FS_0
Diff_FS_coes_5 = FS_coes_5 - FS_0
EOF
r.colors map=FS_5 rules=/home/utente/GIS/G_base/color_rules/fs_color

#day_6
r.mapcalc --o <<EOF
P_6 = rainfall day6
E_6 = evapotranspiration day6
S_6 = if(P_4 + P_3 + P_2 + P_6 + P_5 < 5, S_I, if((P_4 + P_3 + P_2 + P_6 + P_5) > 100, S_III, S_II))
Pc_6 = P_6 + Pfc_5
Rc_6 = if(Pc_6 > 0.2 * S_6, ((Pc_6 - 0.2 * S_6)^2) / (Pc_6 + 0.8 * S_6), 0)
Pfc_6 = if((Pc_6 - Rc_6 - D_5) < 0.2 * S_6, Pc_6 - Rc_6 - D_5, (0.04 * (S_6)^2 + 0.8 * S_6 * (Pc_6 - Rc_6 - D_5)) / (1.2 * S_6 - (Pc_6 - Rc_6 - D_5)))
V_6 = Diff_GWT_bedrock * 1000 - E_6 - D_5 + (Pc_6 - Rc_6 + Dc_4) / n_eff
D_6 = if(P_6 > 0, V_6 * (1 - exp(-(lambda_1))), V_6 * (1 - exp(-(lambda_2))))
Dc_6 = Dc_5 + D_6
Hf_6 = if((V_6 / 1000) > Diff_DTM_bedrock, Diff_DTM_bedrock, V_6 / 1000)
m_6 = Hf_6 / Diff_DTM_bedrock
FS_6 = if(((Gamma - (m_6 * 10)) / Gamma) * (tan_phi / tan_b) < 25, ((Gamma - (m_6 * 10)) / Gamma) * (tan_phi / tan_b), 25)
FS_coes_6 = if((coes + ((Gamma - (m_6 * 10)) * Diff_DTM_bedrock * (cos_b^2) * tan_phi)) / (Gamma * Diff_DTM_bedrock * sin_b * cos_b) < 50, (coes + ((Gamma - (m_6 * 10)) * Diff_DTM_bedrock * (cos_b^2) * tan_phi)) / (Gamma * Diff_DTM_bedrock * sin_b * cos_b), 50)

```

```

Diff_FS_6 = FS_6 - FS_0
Diff_FS_coes_6 = FS_coes_6 - FS_coes_0
EOF
r.colors map=FS_6 rules=/home/utente/GIS/G_base/color_rules/fs_color

#day7
r.mapcalc --o <<EOF
P_7 = rainfall day7
E_7 = evapotranspiration day7
S_7 = if(P_4 + P_3 + P_7 + P_6 + P_5 < 5, S_I, if(( P_4 + P_3 + P_7 + P_6
+ P_5 )>100, S_III, S_II))
Pc_7 = P_7 + Pfc_6
Rc_7 = if(Pc_7 > 0.2*S_7, ((Pc_7 - 0.2*S_7)^2)/(Pc_7+0.8*S_7), 0)
Pfc_7 = if((Pc_7 - Rc_7 - D_6) < 0.2 * S_7, Pc_7 - Rc_7 - D_6, (0.04 *
(S_7)^2 + 0.8 * S_7 * (Pc_7 - Rc_7 - D_6)) / (1.2 * S_7 - (Pc_7 - Rc_7 -
D_6)))
V_7 = Diff_GWT_bedrock * 1000 - E_7 - D_6 + (Pc_7 - Rc_7 + Dc_5)/n_eff
D_7 = if(P_7 > 0, V_7* (1 - exp(-(lambda_1))), V_7* (1 - exp(
(lambda_2))))
Dc_7 = Dc_6 + D_7
Hf_7 = if((V_7/1000) > Diff_DTM_bedrock, Diff_DTM_bedrock, V_7/1000)
m_7 = Hf_7 / Diff_DTM_bedrock
FS_7 = if(((Gamma - (m_7 * 10)) / Gamma) * (tan_phi/tan_b) < 25, ((Gamma
- (M_7 * 10)) / Gamma) * (tan_phi/ tan_b), 25)
FS_coes_7 = if((coes + ((Gamma - (m_7 * 10)) * Diff_DTM_bedrock * (cos_b
^ 2) * tan_phi)) / (Gamma * Diff_DTM_bedrock * sin_b * cos_b) < 50, (coes
+ (Gamma - (M_7 * 10)) * Diff_DTM_bedrock * (cos_b ^ 2) * tan_phi) /
(Gamma * Diff_DTM_bedrock * sin_b * cos_b), 50)
Diff_FS_7 = FS_7 - FS_0
Diff_FS_coes_7 = FS_coes_7 - FS_coes_0
EOF
r.colors map=FS_7 rules=/home/utente/GIS/G_base/color_rules/fs_color

#day_8
r.mapcalc --o <<EOF
P_8 = rainfall day8
E_8 = evapotranspiration day8
S_8 = if(P_5 + P_8 + P_7 + P_8 + P_6 < 5, S_I, if(( P_4 + P_8 + P_7 + P_6
+ P_5 )>100, S_III, S_II))
Pc_8 = P_8 + Pfc_8
Rc_8 = if(Pc_8 > 0.2*S_8, ((Pc_8 - 0.2*S_8)^2)/(Pc_8+0.8*S_8), 0)
Pfc_8 = if((Pc_8 - Rc_8 - D_7) < 0.2 * S_8, Pc_8 - Rc_8 - D_7, (0.04 *
(S_8^2 + 0.8 * S_8 * (Pc_8 - Rc_8 - D_7)) / (1.2 * S_8 - (Pc_8 - Rc_8 -
D_7))))
V_8 = Diff_GWT_bedrock*1000 - E_8 - D_7 + (Pc_8 - Rc_8 + Dc_6)/n_eff
D_8 = if(P_8 > 0, V_8* (1 - exp(-(lambda_1))), V_8* (1 - exp(
(lambda_2))))
Dc_8 = Dc_7 + D_8
Hf_8 = if((V_8/1000) > Diff_DTM_bedrock, Diff_DTM_bedrock, V_8/1000)
m_8 = Hf_8 / Diff_DTM_bedrock
FS_8 = if(((Gamma - (M_8 * 10)) / Gamma) * (tan_phi/tan_b) < 25, ((Gamma
- (M_8 * 10)) / Gamma) * (tan_phi/ tan_b), 25)
FS_coes_8 = if((coes + ((Gamma - (m_8 * 10)) * Diff_DTM_bedrock * (cos_b
^ 2) * tan_phi)) / (Gamma * Diff_DTM_bedrock * sin_b * cos_b) < 50, (coes
+ (Gamma - (m_8 * 10)) * Diff_DTM_bedrock * (cos_b ^ 2) * tan_phi) /
(Gamma * Diff_DTM_bedrock * sin_b * cos_b), 50)

```

```

Diff_FS_8 = FS_8 - FS_0
Diff_FS_coes_8 = FS_coes_8 - FS_coes_0
EOF
r.colors map=FS_8 rules=/home/utente/GIS/G_base/color_rules/fs_color

#day_9
r.mapcalc --o <<EOF
P_9 = rainfall day9
E_9 = evapotranspiration day9
S_9 = if(P_9 + P_8 + P_7 + P_6 + P_5 < 5, S_I, if(( P_9 + P_8 + P_7 + P_6
+ P_5 )>100,S_III,S_II))
Pc_9 = P_9 + Pfc_8
Rc_9 = if(Pc_9 > 0.2*S_9, ((Pc_9 - 0.2*S_9)^2)/(Pc_9+0.8*S_9),0)
Pfc_9 = if((Pc_9 - Rc_9 - D_8) < 0.2 * S_9, Pc_9 - Rc_9 - D_8, (0.04 *
(S_9)^2 + 0.8 * S_9 * (Pc_9 - Rc_9 - D_8)) / (1.2 * S_9 - (Pc_9 - Rc_9 -
D_8)))
V_9 = Diff_GWT_bedrock*1000 - E_9 - D_8 + (Pc_9 - Rc_9 + Dc_7)/n_eff
D_9 = if(P_9 > 0, V_9* (1 - exp(-(lambda_1))), V_9* (1 - exp(
(lambda_2))))
Dc_9 = Dc_8 + D_9
Hf_9 = if((V_9/1000) > Diff_DTM_bedrock, Diff_DTM_bedrock, V_9/1000)
m_9 = Hf_9 / Diff_DTM_bedrock
FS_9 = if(((Gamma - (m_9 * 10)) / Gamma) * (tan_phi/tan_b) < 25, ((Gamma
- (M_9 * 10)) / Gamma) * (tan_phi/tan_b), 25)
FS_coes_9 = if((coes + ((Gamma - (m_9 * 10)) * Diff_DTM_bedrock * (cos_b
^ 2) * tan_phi)) / (Gamma * Diff_DTM_bedrock * sin_b * cos_b) < 50, (coes
+ (Gamma - (M_9 * 10)) * Diff_DTM_bedrock * (cos_b ^ 2) * tan_phi) /
(Gamma * Diff_DTM_bedrock * sin_b * cos_b), 50)
Diff_FS_9 = FS_9 - FS_0
Diff_FS_coes_9 = FS_coes_9 - FS_0
EOF
r.colors map=FS_9 rules=/home/utente/GIS/G_base/color_rules/fs_color

#day_10
r.mapcalc --o <<EOF
P_10 = rainfall day10
E_10 = evapotranspiration day10
S_10 = if(P_9 + P_8 + P_7 + P_6 + P_10 < 5, S_I, if(( P_9 + P_8 + P_7 + P_6
+ P_10 )>100,S_III,S_II))
Pc_10 = P_10 + Pfc_9
Rc_10 = if(Pc_10 > 0.2*S_10, ((Pc_10 - 0.2*S_10)^2)/(Pc_10+0.8*S_10),0)
Pfc_10 = if((Pc_10 - Rc_10 - D_9) < 0.2 * S_10, Pc_10 - Rc_10 - D_9,
(0.04 * (S_10)^2 + 0.8 * S_10 * (Pc_10 - Rc_10 - D_9)) / (1.2 * S_10 -
(Pc_10 - Rc_10 - D_9)))
V_10 = Diff_GWT_bedrock*1000 - E_10 - D_9 + (Pc_10 - Rc_10 + Dc_8)/n_eff
D_10 = if(P_10 > 0, V_10* (1 - exp(-(lambda_1))), V_10* (1 - exp(
(lambda_2))))
Dc_10 = Dc_9 + D_10
Hf_10 = if((V_10/1000) > Diff_DTM_bedrock, Diff_DTM_bedrock, V_10/1000)
m_10 = Hf_10 / Diff_DTM_bedrock
FS_10 = if(((Gamma - (M_10 * 10)) / Gamma) * (tan_phi/tan_b) < 25,
((Gamma - (M_10 * 10)) / Gamma) * (tan_phi/tan_b), 25)
FS_coes_10 = if((coes + ((Gamma - (m_10 * 10)) * Diff_DTM_bedrock * (cos_b
^ 2) * tan_phi)) / (Gamma * Diff_DTM_bedrock * sin_b * cos_b) < 50,
(coes + (Gamma - (M_10 * 10)) * Diff_DTM_bedrock * (cos_b ^ 2) * tan_phi)
/ (Gamma * Diff_DTM_bedrock * sin_b * cos_b), 50)

```

```
Diff_FS_10 = FS_10 - FS_0
Diff_FS_coes_10 = FS_coes_10 - FS_coes_0
EOF
r.colors map=FS_10 rules=/home/utente/GIS/G_base/color_rules/fs_color

#day_11 .....
```



```
#stability condition variation map estimate
r.mapcalc --o <<EOF
stability condition variation map =if( FS_coes_0 <=1,2,if( FS_coes_0>1 &&
FS_coes_10 <=1,1,0))
EOF
r.colors map=stability condition variation map
rules=/home/utente/GIS/G_base/color_rules/criteriol_colori
```

The RGB color rule to describe the three classes composing the stability conditions variation map is the following:

```
1 255:0:0 (red)
2 0:255 (blue)
0 255:255:255 (white)
```

```
# GWT variation at the end of the rainfall event
r.mapcalc --o <<EOF
Delta_GWT = Hf_10 - Hf_1
EOF
```

7. APPENDIX B

The SAC procedure, described in this thesis, is here reported.

It was implemented as a Python script for QGIS. It is open source and can be downloaded at the following Github address: [https://github.com/LabGeomatica/Unsaturated-soil-shear-strength-soil_evolution_analysis_\(2\).zip.git](https://github.com/LabGeomatica/Unsaturated-soil-shear-strength-soil_evolution_analysis_(2).zip.git) (the user have to chose the Cohesion.py script).

```
# -*- coding: utf-8 -*-
"""
Created on Fri Jun 3 14:21:52 2022

@author: Stella-Maria
"""

from qgis.core import QgsProcessing
from qgis.core import QgsProcessingAlgorithm
from qgis.core import QgsProcessingMultiStepFeedback
from qgis.core import QgsProcessingParameterNumber
from qgis.core import QgsProcessingParameterMapLayer
from qgis.core import QgsProcessingParameterFolderDestination
from qgis.core import QgsProcessingParameterEnum
from qgis.PyQt.QtCore import QApplication
from qgis.core import QgsVectorLayer, QgsVectorLayerUtils,
QgsProcessingUtils, QgsMapLayer
import processing
import numpy as np
import matplotlib.pyplot as plt
import matplotlib.patches as mpatches

class Cohesion(QgsProcessingAlgorithm):

    def initAlgorithm(self, config=None):
        #Definition of the parameters
        self.addParameter(QgsProcessingParameterEnum('type_input','Type of
input data', options = ['raw vector data','calibrated vector data','VWC
map','calibrated VWC map'], allowMultiple = False, defaultValue=None))
        self.addParameter(QgsProcessingParameterMapLayer('Data', 'Input
data',defaultValue=None))
        self.addParameter(QgsProcessingParameterNumber('a', 'a',
type=QgsProcessingParameterNumber.Double, minValue=0, maxValue=10000,
defaultValue=276.5))
        self.addParameter(QgsProcessingParameterNumber('b', 'b',
type=QgsProcessingParameterNumber.Double, minValue=-1000, maxValue=10000,
defaultValue=-87.8))
        self.addParameter(QgsProcessingParameterNumber('Vin', 'Vin',
type=QgsProcessingParameterNumber.Double, minValue=0, maxValue=10000,
defaultValue=3.0))
```

```

        self.addParameter(QgsProcessingParameterNumber('Gs', '\n\nSpecific
gravity of soil grains (Gs)', type=QgsProcessingParameterNumber.Double,
minValue=0, maxValue=10000, defaultValue=2.6))
        self.addParameter(QgsProcessingParameterNumber('C', 'Carbon
content (C)', type=QgsProcessingParameterNumber.Double, minValue=0,
maxValue=100, defaultValue=3.0))
        self.addParameter(QgsProcessingParameterNumber('Sand', 'Sand
fraction (Sand)', type=QgsProcessingParameterNumber.Double, minValue=0,
maxValue=100, defaultValue=47.9))
        self.addParameter(QgsProcessingParameterNumber('Clay', 'Clay
fraction (Clay)', type=QgsProcessingParameterNumber.Double, minValue=0,
maxValue=100, defaultValue=29.0))
        self.addParameter(QgsProcessingParameterNumber('tan_phi', 'Tangent
of the effective angle of shearing resistance for an unsaturated soil
(tan(φ))', type=QgsProcessingParameterNumber.Double, minValue=0,
maxValue=1, defaultValue=0.522))
        self.addParameter(QgsProcessingParameterNumber('teta_max',
'Highest volumetric water content (θmax)', type=QgsProcessingParameterNumber.Double,
minValue=0, maxValue=10000, defaultValue=0.478))

self.addParameter(QgsProcessingParameterFolderDestination('Output_Folder',
'\n\nFolder for download all the results'))

def processAlgorithm(self, parameters, context, model_feedback):
    feedback = QgsProcessingMultiStepFeedback(1, model_feedback)
    results = {}
    outputs = {}

    folder = QgsProcessingUtils.tempFolder()

    ##Calculation of constants
    wmax = parameters['teta_max'] / ((1-
parameters['teta_max']) * parameters['Gs'])
    rhod = ((1000 * parameters['Gs']) / (1 + wmax * parameters['Gs'])) / 1000
    alpha = np.exp(-2.486 + 0.025 * parameters['Sand'] -
0.351 * parameters['C'] - 2.617 * rhod - 0.023 * parameters['Clay'])
    n = np.exp(0.053 + 0.009 * parameters['Sand'] -
0.013 * parameters['Clay'] - 0.00015 * (parameters['Sand'] ** 2))
    teta_r = 0.015 + 0.005 * parameters['Clay'] + 0.014 * parameters['C']
    teta_s = 0.81 - 0.283 * rhod + 0.001 * parameters['Clay']

    s = [0.001, 0.05, 0.075, 0.1, 0.25, 0.5, 0.75, 1, 1.5, 2, 2.5, 3,
3.5, 4, 4.5] + [5*i for i in range(1,20000)]

    results['wmax']=wmax
    results['ρd']=rhod
    results['α']=alpha
    results['n']=n
    results['θr']=teta_r
    results['θs']=teta_s

```

```

#Writting of the .txt file which contain constants
file =
open(parameters['Output_Folder'].replace('/', '\\')+'\\WRC_params.txt',
      "w")
file.write('wmax = '+str(wmax)+'\n'+ 'pd = '+str(rhod)+'\n'+ 'α = '
          +str(alpha)+'\n'+ 'n = '+str(n)+'\n'+ 'θr = '+str(teta_r)+'\n'+ 'θs = '
          +'str(teta_s)')
file.close()

if parameters['type_input']==0:           #if input is raw vector data
    #Recovery of the data, the list of fields names and the values
of z
    data = self.parameterAsLayer(parameters, 'Data', context)
    fields = data.fields().names()
    z_value = QgsVectorLayerUtils.getValues(data, 'z_ground')[0]
    z_value = list(set(z_value))

input_0 = parameters['Data']
for i in range(len(fields)-4):          # for each date
    cal = 'Cal_' + fields[i+4][0:6]

    #Calibration of the data
    formule = (''+str(parameters['a'])+'*' + fields[i+4] + '/' +
    +str(parameters['Vin'])+'+'+str(parameters['b']))/100'
    formule_suite =
    'if('+formule+'<=' +str(teta_r)+', '+str(teta_r+0.001)+', '+formule+')'
    alg_params = {
        'INPUT': input_0,
        'FIELD_NAME': cal,
        'FIELD_TYPE': 0, # Flottant
        'FIELD_LENGTH': 10,
        'FIELD_PRECISION': 3,
        'FORMULA': formule_suite,
        'OUTPUT': QgsProcessing.TEMPORARY_OUTPUT
    }
    outputs[cal] = processing.run('native:fieldcalculator',
alg_params, context=context, feedback=feedback, is_child_algorithm=True)
    results[cal] = outputs[cal]['OUTPUT']

    #Calculation of s_eff
    input_0 = outputs[cal]['OUTPUT']

    s_eff = 'seff_'+ fields[i+4][0:6]
    formule = ('' + cal + '-' + str(teta_r) + ') / (' +
    str(parameters['teta_max'])) + '-' + str(teta_r) + ')'
    alg_params = {
        'INPUT': input_0,
        'FIELD_NAME': s_eff,
        'FIELD_TYPE': 0, # Flottant
        'FIELD_LENGTH': 10,
        'FIELD_PRECISION': 3,
        'FORMULA': formule,

```

```

        'OUTPUT': QgsProcessing.TEMPORARY_OUTPUT
    }
    outputs[s_eff] = processing.run('native:fieldcalculator',
alg_params, context=context, feedback=feedback, is_child_algorithm=True)
    results[s_eff] = outputs[s_eff]['OUTPUT']

    #Calculation of the suction
    input_0 = outputs[s_eff]['OUTPUT']

    suc = 's_' + fields[i+4][0:6]
    formule = '(10/' + str(alpha) + '*10^(-2))*((((' +
str(teta_s) + '-' + cal + '))/("' + cal + '-' + str(teta_r) + ')')^(1/' +
str(n) + ')'
    alg_params = {
        'INPUT': input_0,
        'FIELD_NAME': suc,
        'FIELD_TYPE': 0, # Flottant
        'FIELD_LENGTH': 10,
        'FIELD_PRECISION': 3,
        'FORMULA': formule,
        'OUTPUT': QgsProcessing.TEMPORARY_OUTPUT
    }
    outputs[suc] = processing.run('native:fieldcalculator',
alg_params, context=context, feedback=feedback, is_child_algorithm=True)
    results[suc] = outputs[suc]['OUTPUT']

    #Calculation of the cohesion
    input_0 = outputs[suc]['OUTPUT']

    if i != len(fields)-5:      #if not the last date save in
temporary file
        outname = folder.replace('/', '\\')+ '\\deltaC' +str(i)+ '.shp'
    else :                      #else save in the output
folder
        outname = parameters['Output_Folder']+ '\\Results.shp'
    dC ='dC_' + fields[i+4][0:6]
    formule = '"' + suc + '*' + s_eff + '*' +
str(parameters['tan_phi']))
    alg_params = {
        'INPUT': input_0,
        'FIELD_NAME': dC,
        'FIELD_TYPE': 0, # Float
        'FIELD_LENGTH': 10,
        'FIELD_PRECISION': 3,
        'FORMULA': formule,
        'OUTPUT':outname,
    }
    outputs[dC] = processing.run('native:fieldcalculator',
alg_params, context=context, feedback=feedback, is_child_algorithm=True)
    results[dC] = outputs[dC]['OUTPUT']
    input_0 = outputs[dC]['OUTPUT']

```

```

#Export the results in a spreadsheet
alg_params = {
    'FORMATTED_VALUES': False,
    'LAYERS': outputs[dC]['OUTPUT'],
    'OVERWRITE': True,
    'USE_ALIAS': False,
    'OUTPUT': parameters['Output_Folder']+ '\\table.csv'
}
outputs['tableur'] =
processing.run('native:exporttospreadsheet', alg_params, context=context,
feedback=feedback, is_child_algorithm=True)

#for each z ground
for z in z_value:

    #Selection of the attributes with the same value of z
    selected = 'select_'+str(z)+'_'+fields[i+4]
    alg_params = {
        'INPUT': input_0,
        'FIELD': 'z_ground',
        'METHOD': 0, # New selection
        'OPERATOR': 0, # equal to
        'VALUE': z
    }
    outputs[selected] =
processing.run('qgis:selectbyattribute', alg_params, context=context,
feedback=feedback, is_child_algorithm=True)

    #Saving selected features in a temporary file
    extracted = str(z)+'_'+fields[i+4]
    alg_params = {
        'INPUT': input_0,
        'OUTPUT': folder.replace('/', '\\')+ '\\'+fields[i+4].replace('/', '-').
        +'__Extracted_'+str(z)+'.shp'
    }
    outputs[extracted] =
processing.run('native:saveselectedfeatures', alg_params, context=context,
feedback=feedback, is_child_algorithm=True)
    results[extracted]= outputs[extracted] ['OUTPUT']

#Interpolation of the VWC with raw data between the
selected features
field_number = i+4
int_name = 'VWC_raw_'+str(z)+'_'+fields[i+4]
rect = QgsVectorLayer.extent(data)

extent=str(rect.xMinimum())+', '+str(rect.xMaximum())+', '+str(rect.yMinimum())
(), '+str(rect.yMaximum())+' ['+str(QgsVectorLayer.sourceCrs(data))[-10:-1]+']'

```

```

        int_data
='{}:{}:{}:{}:{}:{}:{}:{}'.format(folder.replace('/', '\\')+ '\\' + fields[i+4]
].replace('/', '-')+'__Extracted_'+str(z)+'.shp', '0', str(field_number),
'0')
        out_name =
parameters['Output_Folder']+ '\\' +'VWC_raw___'+str(z) +'___'+fields[i+4].rep
lace('/', '-')+'.tif'
        alg_params = {
            'EXTENT' : extent,
            'INTERPOLATION_DATA' : int_data,
            'METHOD' : 0,
            'OUTPUT' : out_name,
            'PIXEL_SIZE' : 5
        }
        outputs[int_name] =
processing.run('qgis:tininterpolation', alg_params, context=context,
feedback=feedback, is_child_algorithm=True)
        results[int_name] = outputs[int_name]['OUTPUT']

        #Interpolation of the VWC with calibrated data between
the selected features
        field_number = len(fields)+4*i
        int_name = 'VWC_cal_'+str(z) +'_'+fields[i+4]
        rect = QgsVectorLayer.extent(data)

extent=str(rect.xMinimum())+', '+str(rect.xMaximum())+', '+str(rect.yMinimum
())+', '+str(rect.yMaximum())+' ['+str(QgsVectorLayer.sourceCrs(data))[-
10:-1]+']'
        int_data
='{}:{}:{}:{}:{}:{}:{}:{}'.format(folder.replace('/', '\\')+ '\\' + fields[i+4]
].replace('/', '-')+'__Extracted_'+str(z)+'.shp', '0', str(field_number),
'0')
        out_name =
parameters['Output_Folder']+ '\\' +'VWC_cal___'+str(z) +'___'+fields[i+4].rep
lace('/', '-')+'.tif'
        alg_params = {
            'EXTENT' : extent,
            'INTERPOLATION_DATA' : int_data,
            'METHOD' : 0,
            'OUTPUT' : out_name,
            'PIXEL_SIZE' : 5
        }
        outputs[int_name] =
processing.run('qgis:tininterpolation', alg_params, context=context,
feedback=feedback, is_child_algorithm=True)
        results[int_name] = outputs[int_name]['OUTPUT']

        #Interpolation of the suction between the selected
features
        field_number = len(fields)+(i+1)*4-2
        int_name = 'Inter_'+str(z) +'_'+fields[i+4]
        rect = QgsVectorLayer.extent(data)

extent=str(rect.xMinimum())+', '+str(rect.xMaximum())+', '+str(rect.yMinimum
())

```



```

#Recovery of the data, the list of fields names and the values
of z
data = self.parameterAsLayer(parameters, 'Data', context)
fields = data.fields().names()
z_value = QgsVectorLayerUtils.getValues(data, 'z_ground')[0]
z_value = list(set(z_value))

input_0 = parameters['Data']
for i in range(len(fields)-4):      # for each date

    #Calculation of s_eff
    s_eff = 'seff_'+fields[i+4][0:6]
    formule = ('(' + fields[i+4] + '"-' + str(teta_r) + ')/('
    + str(parameters['teta_max']) + '-' + str(teta_r) + ')'
    alg_params = {
        'INPUT': input_0,
        'FIELD_NAME': s_eff,
        'FIELD_TYPE': 0, # Flottant
        'FIELD_LENGTH': 10,
        'FIELD_PRECISION': 3,
        'FORMULA': formule,
        'OUTPUT': QgsProcessing.TEMPORARY_OUTPUT
    }
    outputs[s_eff] = processing.run('native:fieldcalculator',
alg_params, context=context, feedback=feedback, is_child_algorithm=True)
results[s_eff] = outputs[s_eff]['OUTPUT']

    #Calculation of the suction
    input_0 = outputs[s_eff]['OUTPUT']

    suc = 's_'+fields[i+4][0:6]
    formule = '(10/' + str(alpha) + '*10^(-2))*((( ' +
str(teta_s) + ' -" + fields[i+4] + "))/(" + fields[i+4] + '" -' +
str(teta_r) + '))^((1/' + str(n) + '))'
    alg_params = {
        'INPUT': input_0,
        'FIELD_NAME': suc,
        'FIELD_TYPE': 0, # Float
        'FIELD_LENGTH': 10,
        'FIELD_PRECISION': 3,
        'FORMULA': formule,
        'OUTPUT': QgsProcessing.TEMPORARY_OUTPUT
    }
    outputs[suc] = processing.run('native:fieldcalculator',
alg_params, context=context, feedback=feedback, is_child_algorithm=True)
results[suc] = outputs[suc]['OUTPUT']

    #Calculation of the cohesion
    input_0 = outputs[suc]['OUTPUT']

```

```

        if i != len(fields)-5:      #if not the last date save in
temporary file
            outname = folder.replace('/', '\\')+'\\deltaC' +str(i)+'.shp'
        else :                      #else save in the output
folder
            outname = parameters['Output_Folder']+ '\\Results.shp'
dC = 'dC_'+fields[i+4][0:6]
formule = '"" + suc + "*" + s_eff + "*" +
str(parameters['tan_phi'])
alg_params = {
    'INPUT': input_0,
    'FIELD_NAME': dC,
    'FIELD_TYPE': 0, # Flottant
    'FIELD_LENGTH': 10,
    'FIELD_PRECISION': 3,
    'FORMULA': formule,
    'OUTPUT':outname,
}
outputs[dC] = processing.run('native:fieldcalculator',
alg_params, context=context, feedback=feedback, is_child_algorithm=True)
results[dC] = outputs[dC]['OUTPUT']
input_0 = outputs[dC]['OUTPUT']

#Export the results in a spreadsheet
alg_params = {
    'FORMATTED_VALUES': False,
    'LAYERS': outputs[dC]['OUTPUT'],
    'OVERWRITE': True,
    'USE_ALIAS': False,
    'OUTPUT': parameters['Output_Folder']+ '\\table.csv'
}
outputs['tableur'] =
processing.run('native:exporttospreadsheet', alg_params, context=context,
feedback=feedback, is_child_algorithm=True)

for z in z_value:          #for each value oh z ground

    #Selection of the attributes with the same value of z
selected = 'select_'+str(z)+'_'+fields[i+4]
alg_params = {
    'INPUT': input_0,
    'FIELD': 'z_ground',
    'METHOD': 0, # New selection
    'OPERATOR': 0, # equal to
    'VALUE': z
}
outputs[selected] =
processing.run('qgis:selectbyattribute', alg_params, context=context,
feedback=feedback, is_child_algorithm=True)

#Saving selected features in a temporary file
extracted = str(z) +'_'+fields[i+4]
alg_params = {

```



```

        'EXTENT' : extent,
        'INTERPOLATION_DATA' : int_data,
        'METHOD' : 0,
        'OUTPUT' : out_name,
        'PIXEL_SIZE' : 5
    }
    outputs[int_name] =
processing.run('qgis:tininterpolation', alg_params, context=context,
feedback=feedback, is_child_algorithm=True)
    results[int_name] = outputs[int_name]['OUTPUT']

    #Interpolation of the cohesion between the selected
features
    field_number = len(fields)+(i+1)*3-1
    int_name = fields[i+4] + '__Inter__'+str(z)
    rect = QgsVectorLayer.extent(data)

extent=str(rect.xMinimum())+', '+str(rect.xMaximum())+', '+str(rect.yMinimum())
()+' , '+str(rect.yMaximum())+' ['+str(QgsVectorLayer.sourceCrs(data))[-10:-1]+']'
    int_data
='{}::~::{}::~::{}::~::{}'.format(folder.replace('/', '\\')+ '\\' +fields[i+4]
].replace('/', '-')+'__Extracted__'+str(z)+'.shp', '0', str(field_number),
'0')
    out_name =
parameters['Output_Folder']+ '\\'+ 'Cohesion__'+str(z)+ '__'+fields[i+4].re
place('/', '-')+'.tif'
    alg_params = {
        'EXTENT' : extent,
        'INTERPOLATION_DATA' : int_data,
        'METHOD' : 0,
        'OUTPUT' : out_name,
        'PIXEL_SIZE' : 5
    }
    outputs[int_name] =
processing.run('qgis:tininterpolation', alg_params, context=context,
feedback=feedback, is_child_algorithm=True)
    results[int_name] = outputs[int_name]['OUTPUT']

if parameters['type_input']==2:      #if type input is a calibrated
VWC map

    #Recovery of the map
    data = self.parameterAsLayer(parameters, 'Data', context)

    #Calibration of the data
    formule = '('+str(parameters['a'])+'*'+ data.name()+
'@1')/'+str(parameters['Vin'])+'+'+str(parameters['b'])+')/100'
    alg_params = {
        'EXPRESSION':formule,

```

```

    'LAYERS':[parameters['Data']],
    'CELLSIZE':0,
    'EXTENT':None,
    'CRS':None,
    'OUTPUT':QgsProcessing.TEMPORARY_OUTPUT
}
outputs['Calibration']=processing.run("qgis:rastercalculator",
alg_params, context=context, feedback=feedback, is_child_algorithm=True)
results['Calibration']=outputs['Calibration']['OUTPUT']

#Calculation of s_eff
cal =
QgsProcessingUtils.mapLayerFromString(outputs['Calibration']['OUTPUT'],
context)
formule = ('"' + QgsMapLayer.name(cal) + '@1"-'+ str(teta_r) +
')/(' + str(parameters['teta_max']) + '-' + str(teta_r) + ')'
alg_params = {
    'EXPRESSION':formule,
    'LAYERS':[parameters['Data'],cal],
    'CELLSIZE':0,
    'EXTENT':None,
    'CRS':None,
    'OUTPUT': folder.replace('/', '\\\\') + '\\\\s_eff.tif'
}
outputs['s_eff']=processing.run("qgis:rastercalculator",
alg_params, context=context, feedback=feedback, is_child_algorithm=True)
results['s_eff']=outputs['s_eff']['OUTPUT']

s_eff =
QgsProcessingUtils.mapLayerFromString(outputs['s_eff']['OUTPUT'], context)

#Calculation of the suction
out_name =
parameters['Output_Folder']+ '\\'+data.name().replace('/','-'
)+ '_Suction.tif'
formule = '(10/' + str(alpha) + '*10^(-2))*(((' + str(teta_s) +
'"' + QgsMapLayer.name(cal) + '@1")/("' + QgsMapLayer.name(cal) + '@1"-'
+ str(teta_r) + '))^(1/' + str(n) + '))'
alg_params = {
    'EXPRESSION':formule,
    'LAYERS':[parameters['Data'],cal],
    'CELLSIZE':0,
    'EXTENT':None,
    'CRS':None,
    'OUTPUT':out_name
}
outputs['suc']=processing.run("qgis:rastercalculator",
alg_params, context=context, feedback=feedback, is_child_algorithm=True)
results['suc']=outputs['suc']['OUTPUT']

suc =
QgsProcessingUtils.mapLayerFromString(outputs['suc']['OUTPUT'], context)

```

```

        #Calculation of the cohesion
        out_name =
parameters['Output_Folder']+ '\\'+data.name().replace('/', '-'
')+ '_Inter.tif'
        formule = '''+'+ QgsMapLayer.name(suc)+ '@1**'+
QgsMapLayer.name(s_eff)+ '@1**'+str(parameters['tan_phi']))
        alg_params = {
            'EXPRESSION':formule,
            'LAYERS':[parameters['Data'],cal,suc,s_eff],
            'CELLSIZE':0,
            'EXTENT':None,
            'CRS':None,
            'OUTPUT':out_name
        }
        outputs['Delta_C']=processing.run("qgis:rastercalculator",
alg_params, context=context, feedback=feedback, is_child_algorithm=True)
results['Delta_C']=outputs['Delta_C']

if parameters['type_input']==2:      #if type input is a VWC map

        #Recovery of the map
        data = self.parameterAsLayer(parameters, 'Data', context)

        #Calculation of s_eff
        cal =
QgsProcessingUtils.mapLayerFromString(outputs['Calibration']['OUTPUT'],
context)
        formule = '((' +data.name() + '@1-' + str(teta_r) + ')/(' +
str(parameters['teta_max']) + '-' + str(teta_r) + ')'
        alg_params = {
            'EXPRESSION':formule,
            'LAYERS':[parameters['Data']],
            'CELLSIZE':0,
            'EXTENT':None,
            'CRS':None,
            'OUTPUT': folder.replace('/', '\\') + '\\s_eff.tif'
        }
        outputs['s_eff']=processing.run("qgis:rastercalculator",
alg_params, context=context, feedback=feedback, is_child_algorithm=True)
results['s_eff']=outputs['s_eff']['OUTPUT']

        s_eff =
QgsProcessingUtils.mapLayerFromString(outputs['s_eff']['OUTPUT'], context)

        #Calculation of the suction
        out_name =
parameters['Output_Folder']+ '\\'+data.name().replace('/', '-'
')+ '_Suction.tif'
        formule = '(10/' + str(alpha) + '*10^(-2))*((((' + str(teta_s)
+ ')-' + data.name() + '@1')/(' +data.name() + '@1-' + str(teta_r) +
'))^(1/' + str(n) + '))'

```

```

alg_params = {
    'EXPRESSION':formule,
    'LAYERS':[parameters['Data']],
    'CELLSIZE':0,
    'EXTENT':None,
    'CRS':None,
    'OUTPUT':out_name
}
outputs['suc']=processing.run("qgis:rastercalculator",
alg_params, context=context, feedback=feedback, is_child_algorithm=True)
results['suc']=outputs['suc']['OUTPUT']

suc =
QgsProcessingUtils.mapLayerFromString(outputs['suc']['OUTPUT'], context)

#Calculation of the cohesion
out_name =
parameters['Output_Folder']+('\\'+data.name().replace('/','-')
')+'__Inter.tif'
formule = ''''+ QgsMapLayer.name(suc)+'@1***'+QgsMapLayer.name(s_eff) +'@1**'+str(parameters['tan_phi'])
alg_params = {
    'EXPRESSION':formule,
    'LAYERS':[parameters['Data'],suc,s_eff],
    'CELLSIZE':0,
    'EXTENT':None,
    'CRS':None,
    'OUTPUT':out_name
}
outputs['Delta_C']=processing.run("qgis:rastercalculator",
alg_params, context=context, feedback=feedback, is_child_algorithm=True)
results['Delta_C']=outputs['Delta_C']

# Function to calculate teta for a list of values s given
def calc_teta(teta_r, teta_s, alpha, n, s):
    teta = []
    for i in s:
        teta.append(teta_r + (teta_s - teta_r)/(1 +
(alpha*i/10)**n))
    return teta

# Drawing of the WRC
plt.figure()
plt.plot(s, calc_teta(teta_r, teta_s, alpha, n, s), 'b')
plt.plot(s, [teta_r for i in range(len(s))], 'orange')
plt.scatter(1, teta_s, color='black')
plt.xscale("log")
plt.axis([1,100000,0,0.5])
plt.xlabel('log(s) [kPa]')
plt.ylabel('θv [-]')
black_patch = mpatches.Patch(color='black', label='θs')
blue_patch = mpatches.Patch(color='blue', label='WRC')
orange_patch = mpatches.Patch(color='orange', label='θr')

```

```
plt.legend(handles=[black_patch, blue_patch, orange_patch])
plt.savefig(parameters['Output_Folder']+ '\\WRC.png')

return results

def name(self):
    return 'Cohesion'

def displayName(self):
    return 'Cohesion'

def tr(self, string):
    return QCoreApplication.translate('Processing', string)

def shortHelpString(self):
    return self.tr("The script will give you the Soil Water Retention
Curve (SWRC) and the unsaturated soil shear strength under partial
saturation conditions.\n\nThe input data must be designed as follows:\n-
Vector data .shp file with sensor name, coordinates (E and N),
installation depth (named z_ground) and for the volumetric water content a
number of columns corresponding to the number of days to be analysed,
named with the daily date\n-Raster data can be Volumetric Water Content
maps\n\na and b are the values used to calibrate the raw data with the
equation data_calibrated = a*raw_data/Vin + b")

def createInstance(self):
    return Cohesion()
```